SURFEX SCIENTIFIC DOCUMENTATION

P. Le Moigne

May 19, 2009

Editor : P. Le Moigne

Contributing authors :

A. Boone [1], J.-C. Calvet [1], B. Decharme [1], S. Faroux [1], A.-L. Gibelin [1], C. Lebeaupin [2], P. Le Moigne [1], J.-F. Mahfouf [1], E. Martin [1], V. Masson [1], D. Mironov [3], J. Noilhan [1], P. Tulet [1], B. Van Den Hurk [4]

[1] : CNRM/GAME, Météo-France/CNRS, Toulouse, France

[2] : Laboratoire de Météorologique Dynamique, Ecole Polytechnique, Palaiseau, France

[3] : German Weather Service, Offenbach am Main, Germany

[4] : KNMI, The Netherlands

Dissemination Level : public

ISSUE No	DATE	PAGES	DESCRIPTION OF CHANGE
1	11 MAY 2009	1 - 211	ORIGINAL

SURFEX

Part I

SURFACE PROCESSES SCHEME

Chapter 1

Introduction: a brief description of the SURFEX system

Surface modelling in numerical weather prediction has always held an important place in the activities of the Centre National de Recherches Météorologiques (CNRM hereafter). In the late 80's, Isba (*Noilhan et al.* [1989], *Noilhan and Mahfouf* [1996]), a soil vegetation atmosphere transfer scheme (Interaction between Soil Biosphere and Atmosphere) has been developed and it aimed to better simulate the exchanges of energy and water between the land surface and the atmosphere just above. Isba model has been designed to be simple and efficient in order to be put into operations at Météo-France. Isba scheme computes the exchanges of energy and water between the continuum soil-vegetation-snow and the atmosphere above. In its genuine version, the evapotranspiration of the vegetation is controlled by a resistance like proposed by *Jarvis* [1976] . A more recent version of the model named Isba-A-gs (*Calvet* [1998]) accounts for a simplified photosynthesis model where the evaporation is controlled by the aperture of the stomates, the component of the leaves that regulates the balance between the transpiration and the assimilation of CO2. Nowadays, Isba land surface scheme is used in the French operational and research forecast models. Thanks to the efforts made by the research community at CNRM, French numerical weather prediction models have always been at the forefront of research in terms of surface modelling. More recently, the modelling of urban areas has began to be of great interest in the research community. In 2000, TEB (Town Energy Balance) model, specially designed to represent the exchanges between a town and the atmosphere has enabled advanced studies in this direction (*Masson* [2000]). The TEB model is based on the canyon concept, where a town is represented with a roof, a road and two facing walls with characteristics playing a key role in the town energy budget. More especially, the ability, of the canyon to trap a fraction of the incoming solar and infrared radiation is taken into account in the model. A special effort has been made this last years to externalize the surface scheme from the embedded surface-atmosphere Meso-NH model. The main idea was to gather all the developments and improvements made in surface schemes in order to make them available for as many people as possible. Not only physical parameterizations have been externalized, but also the preparation of specific surface parameters needed by physical schemes and the initialization of all state variables of the different models: SURFEX (stands for surface externalisée) system was born. Moreover, the surface representation has been improved and thus Surfex system has been enhanced with the specific treatment for water surfaces. Indeed, up to now, the exchanges of energy between water surfaces and the atmosphere were treated in a very simple way, while now a physically based model have been introduced to build a more complex but accurate surface model, available for all atmospheric models. There are two possibilities to compute fluxes over marine surfaces. The simplest one consists in using Charnock's approach to compute the roughness length and fluxes with a constant water surface temperature. Secondly, a one-dimensional ocean mixing

layer model has been introduced (*Lebeaupin* [2006]) in order to simulate more accurately the sea surface temperature (SST hereafter) and the fluxes at the sea/air interface. This model based on *Gaspar* [1990] , will be very helpful especially at meso-scale to better represent diurnal cycle of SST. At meso-scale, a good representation of lakes is of great interest especially for Northern countries. In order to improve the treatment of lake areas, the simple but robust Flake model (*Mironov* [2005]) has been implemented within Surfex system. It allows to have an evolving lake surface temperature and a good description of the energy exchanges within water.

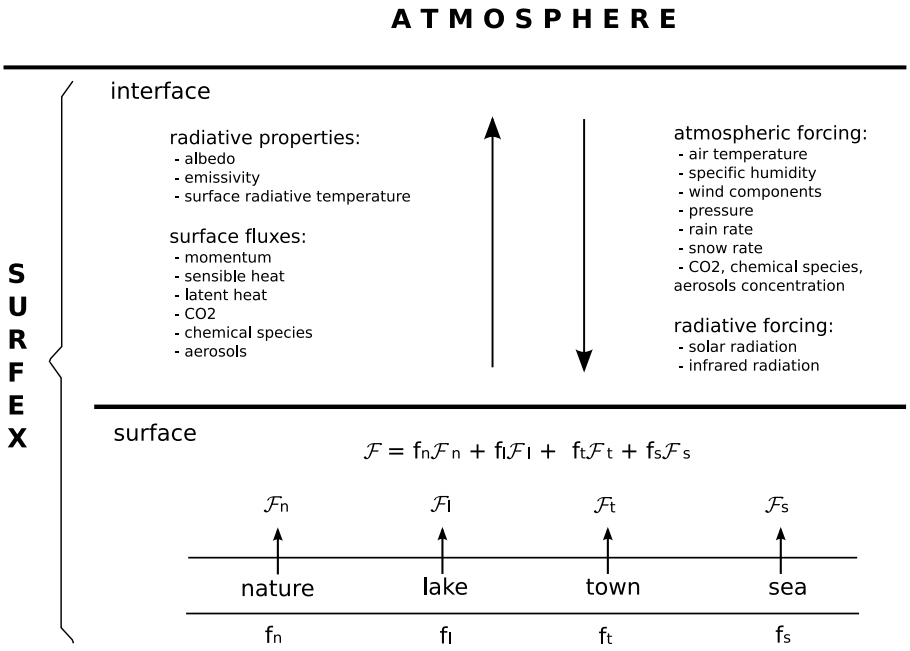

Figure 1.1: Description of the exchanges between an atmospheric model sending meteorological and radiative fields to the surface and Surfex composed of a set of physical models that compute tiled variables $\mathcal{F}_*$ covering a fraction f_* of a unitary grid box and an interface where the averaged variables $\mathcal{F}$ are sent back to the atmosphere

In Surfex, the exchanges between the surface and the atmosphere are realized by mean of a standardized interface (*Polcher et al.* [1998], *Best et al.* [2004]) that proposes a generalized coupling between the atmosphere and surface. During a model time step, each surface grid box receives the upper air temperature, specific humidity, horizontal wind components, pressure, total precipitation, long-wave radiation, short-wave direct and diffuse radiations and possibly concentrations of chemical species and dust. In return, Surfex computes averaged fluxes for momentum, sensible and latent heat and possibly chemical species and dust fluxes and then sends these quantities back to the atmosphere with the addition of radiative terms like surface temperature, surface direct and diffuse albedo and also surface emissivity.
All this information is then used as lower boundary conditions for the atmospheric radiation and turbulent schemes. In Surfex, each grid box is made of four adjacent surfaces: one for nature, one for urban areas, one for sea or ocean and one for lake. The coverage of each of these surfaces is known through the global ECOCLIMAP database (*Masson et al.* [2003]) , which combines land cover maps and satellite information. The Surfex fluxes are the average of the fluxes computed over nature, town, sea/ocean or lake, weighted by their respective fraction.

Chapter 2

Water surfaces

Contents

2.1 Simple parameterization

2.1.1 Free water surfaces

For ocean surfaces and over inland waters, all the prognostic variables are kept constant.
The surface fluxes are calculated using Eqs. 4.127, 4.128, 4.130 and Eqs. 4.153, 4.154, 4.155 of Isba, taking the relative humidity of the ocean $hu = 1$, and $veg = p_{sn} = 0$. The roughness length is given by Charnock's relation:

$$z_{0sea} = 0.015\frac{u_*^2}{g} \tag{2.1}$$

2.1.2 Sea ice

Sea ice is detected in the model when sea surface temperature (SST) is two degrees below 0°C (i.e. 271.15 K). In this case, in order to avoid an overestimation of the evaporation flux, the calculations are performed with the roughness length of flat snow surfaces:

$$z_{0ice} = 10^{-3}m \tag{2.2}$$

In the same manner, the sea ice albedo is set equal to the fresh snow albedo instead of the free water albedo. This leads to a much brighter surface. This has no effect on the sea ice cover (since there is no evolution of the sea surface parameters), but modifies the lower boundary shortwave flux input for the atmospheric radiative scheme.

2.2 Sea surface turbulent fluxes

In this section, we introduce the various sea surface fluxes parameterizations available in the SURFEX surface scheme. In addition to the direct parameterization from Louis (1979), we present two iterative parameterizations: the COARE3.0 (*Fairall et al.* [2003]) and ECUME (*Belamari* [2005]) parameterizations.

2.2.1 Bulk equations

Bulk parameterizations estimate the surface fluxes from mean meteorological gradients in the atmospheric boundary layer. This method 's aim is to determine the transfer coefficients that directly link the surface flux with the meteorological gradients between the surface and a "measurement's height" (*Liu et al.* [1979]).
The surface turbulent fluxes, *i.e.* the stress or the momentum flux τ_{sea}, the sensible heat flux H_{sea} and the latent heat flux LE_{sea} are expressed by:

$$\left\{ \begin{array}{l} |\vec{\tau}|_{sea} = \rho_a \overline{w'u'} = -\rho_a u_*^2 \\ H_{sea} = \rho_a c_{p_a} \overline{w'\theta'} = -\rho_a c_{p_a} u_* \theta_* \\ LE_{sea} = \rho_a \mathcal{L}_v \overline{w'q'} = -\rho_a \mathcal{L}_v u_* q_* \end{array} \right. \tag{2.3}$$

where u', θ' and q' are the vertical perturbations of wind, temperature potential and specific humidity, u_*, θ_* and q_* are the characteristic scale parameters from Monin-Obukhov.
Considering the bulk parameterizations using transfer coefficients:

$$\left\{ \begin{array}{l} |\vec{\tau}|_{sea} = -\rho_a C_D U^2 \\ H_{sea} = \rho_a c_{p_a} C_H U (\theta_s - \theta_a) \\ LE_{sea} = \rho_a \mathcal{L}_v C_E U (q_s - q_a) \end{array} \right. \tag{2.4}$$

s indicates sea surface variables whereas a indicates atmospheric variables at first level. U is the mean value of the relative wind. Here, we choose the atmospheric convention, *i. e.* fluxes are defined positive in case of energy benefit for the atmosphere.
From equations (2.3) and (2.4), we can write:

$$\left\{ \begin{array}{l} C_D = \left(\frac{u_*}{U}\right)^2 \\ C_H = \frac{u_* \theta_*}{U(\theta_a - \theta_s)} \\ C_E = \frac{u_* q_*}{U(q_a - q_s)} \end{array} \right. \tag{2.5}$$

In a general way, the transfer coefficient for the X variable is:

$$C_X = \frac{\overline{w'x'}}{U \Delta X} \tag{2.6}$$

with X equal D for drag, H for heat and E for evaporation and ΔX is the gradient of x ($= u$, θ or q) between the ocean surface and the atmospheric low level.
Each coefficient is divided in two components:

$$C_X = c_x^{\frac{1}{2}} c_d^{\frac{1}{2}} \tag{2.7}$$

that could be expressed following the Monin-Obukhov's similitude theory as a function of the first atmospheric level height z, of atmospheric stratification with a parameter ζ, of roughness lengths (z_0, z_{0_t} and z_{0_q}) and of the Von Karman's constant κ:

$$c_x^{\frac{1}{2}}(\zeta) = C_{x10n}^{\frac{1}{2}} F_x(\zeta, \kappa, C_{x10n}^{\frac{1}{2}}) \tag{2.8}$$

$$C_{x10n}^{\frac{1}{2}} = \frac{\kappa}{\ln(\frac{z}{z_{0x}})} \tag{2.9}$$

Roughness lengths are generally computed thanks to the *Smith* [1998]'s relationship:

$$z_0 = \frac{\alpha u_*^2}{g} + \frac{\beta \nu}{u_*} \tag{2.10}$$

where α (also called the Charnock 's constant) and β are numerical constants and ν is the dynamical viscosity.

Each of the following parameterizations uses its own closure hypothesis with a theoretical method or resulting from experimentation to determine the exchange coefficients from neutral transfer coefficients at 10m $C_{D_{10n}}$, $C_{H_{10n}}$ and $C_{E_{10n}}$ (*i.e.* for $\zeta = 0$) and from a stability function F_x and roughness lengths (*Lebeaupin Brossier* [2007]) .

2.2.2 *Louis* [1979]'s parameterization

The closure relationship allows to determine the exchanges coefficients at the air-sea interface from the neutral transfer coefficients at 10 meters and the *Louis* [1979]'s functions that depend on the stability evaluates from the Richardson number Ri. According to the equation 2.8, exchanges coefficients C_D and C_H are:

$$\begin{aligned} C_D &= C_{D10n} \times \mathcal{F}_D^2(Ri, z, z_0) \\ C_H &= C_{D10n}^{\frac{1}{2}} C_{H10n}^{\frac{1}{2}} \times \mathcal{F}_D(Ri, z, z_0)\mathcal{F}_H(Ri, z_t, z_{0_t}) = C_{D10n}^{\frac{1}{2}} C_{H10n}^{\frac{1}{2}} \times (\mathcal{F}'_H(Ri, z, z_t, z_0, z_{0_t}))^2 \end{aligned} \tag{2.11}$$

The exchange coefficient for evaporation C_E is here equal to the heat coefficient C_H.

Louis's functions $\mathcal{F}_D$ and $\mathcal{F}'_H$ are:

$$\mathcal{F}_X(Ri, z, z_t, z_0, z_{0_t}) = \begin{cases} \left(\mathcal{A} - \frac{b_X Ri}{1 + c_X\sqrt{-Ri}}\right)^{\frac{1}{2}} & for\ Ri \leq 0 \\ \left(\frac{\mathcal{A}}{1 + b'_X \frac{Ri}{\sqrt{1 + c'_X Ri}}}\right)^{\frac{1}{2}} & for\ Ri > 0 \end{cases} \tag{2.12}$$

Numerical values of constants $\mathcal{A}, b,\ b',\ c,\ c'$ for $\mathcal{F}_D$ are (*Mascart et al.* [1995], *Giordani et al.* [1996]) :

$$\begin{cases} \mathcal{A} = 1 \\ b_D = b'_D = 10 \\ c'_D = 5 \\ c_D = b_D C_{D_{10n}} CM_* \left(\frac{z}{z_0}\right)^{PM} \\ CM_* = 6.8741 + 2.6933\ ln\left(\frac{z_0}{z_{0_t}}\right) - 0.3601\ ln\left(\frac{z_0}{z_{0_t}}\right)^2 + 0.0154\ ln\left(\frac{z_0}{z_{0_t}}\right)^3 \\ PM = 0.5233 - 0.0815\ ln\left(\frac{z_0}{z_{0_t}}\right) + 0.0135\ ln\left(\frac{z_0}{z_{0_t}}\right)^2 - 0.0010\ ln\left(\frac{z_0}{z_{0_t}}\right)^3 \end{cases} \tag{2.13}$$

and for $\mathcal{F}'_H$ are:

$$\begin{cases} \mathcal{A} = \frac{ln(z/z_0)}{ln(z_t/z_0)} \\ b_H = b'_H = 15 \\ c'_H = 5 \\ c_H = b_H C_{D_{10n}} CH_* \left(\frac{z_t}{z_{0_t}}\right)^{PH} \\ CH_* = 3.2165 + 4.3431\ ln\left(\frac{z_{0_t}}{z_0}\right) + 0.5360\ ln\left(\frac{z_{0_t}}{z_0}\right)^2 - 0.0781\ ln\left(\frac{z_{0_t}}{z_0}\right)^3 \\ PH = 0.5802 - 0.1571\ ln\left(\frac{z_{0_t}}{z_0}\right) + 0.0327\ ln\left(\frac{z_{0_t}}{z_0}\right)^2 - 0.0026\ ln\left(\frac{z_{0_t}}{z_0}\right)^3 \end{cases} \tag{2.14}$$

Neutral transfer coefficients at 10m ($C_{D_{10n}}$ and $C_{H_{10n}}$) are given by Eq. 2.9, where roughness lengths z_0 and z_{0_t} are estimated with a distinction between the free sea water and the sea ice by a temperature criterion with a threshold at -2C (Tab. 2.1). In sea ice case, roughness length are the same than for the snow. Over free seawater, roughness lengths are reduce to the *Charnock* [1955]'s relationship (*i.e.* $\alpha = 0.015$ and $\beta = 0$ in Eq (2.10)).

	$z_0 \ (m)$	$z_{0_t} = z_{0_q} \ (m)$
$T \leq -2C$	$z_{0_{seaice}} = z_{0_{snow}} = 10^{-3}$	$z_{0_{Tseaice}} = z_{0_{Tsnow}} = 10^{-4}$
$T > -2C$	$0.015\frac{u_*^2}{g}$	$0.015\frac{u_*^2}{g}$

(2.15)

Table 2.1: Roughness lengths in Louis'sparameterization.

The Richardson's number is defined for a layer Δz as the fraction of its potential energy and its kinetic energy:

$$Ri = \frac{g\mathcal{B}\Delta T\Delta z}{U^2} = \frac{g\mathcal{B}(T_s - T_a)z_t}{U^2} \tag{2.16}$$

where g is the gravity and $\mathcal{B} = -\frac{1}{\rho_a}\frac{\partial \rho_a}{\partial T}$ is the thermal expansion coefficient.

2.2.3 Iterative parameterizations

Bulk equations could be resolve with iterative methods on the stability parameter and the characteristic scale parameters from Monin-Obukhov. Convergence criteria vary according to the parameterizations. They also differ in the representation of various processes as waves effects, sea spray, seawater salinity effect on evaporation, wind gusts and especially in the calculation of the roughness lengths or of the transfer coefficients (*Brunke et al.* [2003]) .

The *Liu et al.* [1979]'s algorithm is the most used iterative algorithm for the turbulent air-sea fluxes computation and was also a base for new parameterizations developments [for example, COARE (*Fairall et al.* [1996b], *Mondon and Redelsperger* [1998]) or the ECUME parameterization (*Belamari* [2005])].

The COARE parameterization

The COARE (Coupled Ocean-Atmosphere Response Experiment) algorithm development was developed during the TOGA (Tropical Ocean and Global Atmosphere) experiment and several versions were produced since then. The 2.5b version (*Fairall et al.* [1996b]) in particular was successfully used during several measurement campaigns in several location overall the globe.

The COARE parameterization is based on the LKB model. The details of equations could be found in *Fairall et al.* [1996b,a] and *Gosnell et al.* [1995] for the 2.5b version. The *Mondon and Redelsperger* [1998]'s parameterization available in SURFEX sea scheme is a declination of this COARE algorithm version with different numerical values for the Businger's functions and in the gustiness correction computation.

Taking into account air-sea interaction data from the NOAA/ETL dataset and the HEXMAX data reanalysis, the algorithm validation had been extended leading to the last version 3.0 of the COARE algorithm (*Fairall et al.* [2003]) that is available in the SURFEX sea surface scheme (*Lebeaupin Brossier et al.* [2008a]) .

The COARE 3.0 parameterization main characteristic are:

1. Functions F_X in Eq. 2.8 are defined by:

$$F_X(\zeta) = \frac{1}{\left(1 - \frac{C_{x10n}^{\frac{1}{2}}}{\kappa}\psi_x(\zeta)\right)} \qquad \zeta = z/L \tag{2.17}$$

with similitude functions from Monin-Obukhov:

$$C_X = \frac{u_* X_*}{U \Delta X}$$

$$C_X = c_x^{\frac{1}{2}} c_d^{\frac{1}{2}} = C_{x10n}^{\frac{1}{2}} F_x C_{D10n}^{\frac{1}{2}} F_d$$

$$so \quad \frac{u_* X_*}{U \Delta X} = \frac{\kappa^2}{ln\left(\frac{z}{z_{0x}}\right) ln\left(\frac{z}{z_0}\right)} F_x F_d$$

$$\begin{cases} \frac{u_*}{U} = \frac{\kappa}{ln\left(\frac{z}{z_0}\right) - \psi_m(z/L)} \\ \frac{\theta_*}{\theta_s - \theta_a} = \frac{\kappa}{ln\left(\frac{z}{z_{0_t}}\right) - \psi_h(z/L)} \\ \frac{q_*}{q_s - q_a} = \frac{\kappa}{ln\left(\frac{z}{z_{0_q}}\right) - \psi_q(z/L)} \end{cases} \tag{2.18}$$

where ψ_m, ψ_h and $\psi_q = \psi_h$ are modified Businger 's stability functions that depend on Monin-Obukhov parameter $\zeta = \frac{z}{L}$ and that correct the logarithmic wind, temperature and humidity profiles in the atmospheric boundary layer according to its stability.

$\zeta = \frac{z}{L}$	$\psi_m(\zeta) =$	$\psi_h(\zeta) =$
stable	$-(1+\zeta) - \frac{2}{3}\frac{(\zeta - 14.28)}{exp(\Gamma)} - 8.525$	$-(1+\frac{2}{3}\zeta)^{1.5} - \frac{2}{3}\frac{(\zeta - 14.28)}{exp(\Gamma)} - 8.525$
($\zeta \geq 0$)	$\Gamma = min(50, 0.35\zeta)$	
unstable:	$(1-f)\psi_{mK} + f\psi_{mC}$	$(1-f)\psi_{hK} + f\psi_{hC}$
($\zeta < 0$)	$f = \frac{\zeta^2}{(1.0+\zeta^2)}$	
Kansas	$\psi_{mK} = 2ln(\frac{1+x}{2}) + ln(\frac{1+x^2}{2}) - 2arctan(x) + \frac{\pi}{2}$ with $x = (1-15\zeta)^{\frac{1}{4}}$	$\psi_{hK} = 2ln(\frac{1+x}{2})$ with $x = (1-15\zeta)^{\frac{1}{2}}$
Convective	$\psi_{mC} = \frac{3}{2}ln(\frac{y^2+y+1}{3}) - \sqrt{3}arctan(\frac{2y+1}{\sqrt{3}}) + \frac{\pi}{\sqrt{3}}$ with $y = (1-10.15\zeta)^{\frac{1}{3}}$	$\psi_{hC} = \frac{3}{2}ln(\frac{y^2+y+1}{3}) - \sqrt{3}arctan(\frac{2y+1}{\sqrt{3}}) + \frac{\pi}{\sqrt{3}}$ with $y = (1-34.15\zeta)^{\frac{1}{3}}$

and

$$L^{n+1} = \frac{T}{\kappa g} \frac{{u_*^n}^2}{\theta_*^n + 0.61 T q_*^n}$$

2. Transfer coefficients are estimated from characteristic scale parameters of Monin-Obukhov (u_*, θ_* and q_*) and from atmospheric gradients according to Eq. 2.5. Scale parameters and roughness lengths are computed by iterations.

$$u_*^{n+1} = \frac{\kappa S}{ln(\frac{z}{z_0}) - \psi_m(\zeta^{n+1})} \tag{2.19}$$

$$\theta_*^{n+1} = \frac{\kappa(\theta_a - \theta_s)}{ln(\frac{z}{z_0}) - \psi_h(\zeta^{n+1})} \tag{2.20}$$

$$q_*^{n+1} = \frac{\kappa(q_a - q_s)}{ln(\frac{z}{z_0}) - \psi_h(\zeta^{n+1})} \tag{2.21}$$

The iterations number is reduced to three due to a better background of the stability parameter with a bulk Richardson's number Ri_b (*Grachev and Fairall* [1997]) (Eq. 2.16).

3. In z_0 expression (Eq.2.10), β is 0.11 and the Charnock's parameter is a wind dependent parameter (*Hare et al.* [1999]) :

$$\begin{array}{ll} \alpha = 0.011 & if\ \ U \leq 10\ m.s^{-1} \\ \alpha = 0.011 + (0.018 - 0.011)(U - 10) & if\ \ U \leq 18\ m.s^{-1} \\ \alpha = 0.018 & if\ \ U > 18\ m.s^{-1} \end{array} \tag{2.22}$$

Then, z_{0_q} and z_{0_t} are directly obtained by the formulae:

$$z_{0_q} = z_{0_t} = MIN\left(1.15\ 10^{-4}, 5.5\ 10^{-5}\left(\frac{\nu}{z_0 u_*}\right)^{0.6}\right)$$

4. A reduction of 2% of the specific humidity at saturation is applied due to a reduction of saturated vapor pressure linked to the seawater salinity [i. e. 34 ppth *Kraus* [1972]]:

$$q_s = 0.98 \times q_{sat}(\theta_s) \tag{2.23}$$

where q_{sat} is the specific humidity at saturation.

5. The relative wind could be increased by a correction due to gustiness w_g:

$$U = \sqrt{|\vec{v}|^2 + w_g^2} \tag{2.24}$$

where

$$w_g = \beta_{gust}(bf.z_{bl})^{\frac{1}{3}} \tag{2.25}$$

$$bf = MAX\left(0, \frac{g u_* T_{v*}}{T}\right)$$

$$T_{v*} = T_*\left\{1 + q\left(\frac{R_v}{R_a} - 1\right)\right\} + \left(\frac{R_v}{R_a} - 1\right) T q_*$$

z_{bl} is the atmospheric boundary layer height (fixed to 600 meters). β_{gust} is a constant equal to 1.2. R_v and R_a are ideal gas constants for the water vapor and air, respectively.

6. As rainfall contribute to cool the ocean and add a supplementary drag in surface, two corrections τ_p (*Fairall et al.* [1996b]) and H_p (*Gosnell et al.* [1995]) could be added to turbulent fluxes:

$$\tau_p = \frac{\mathcal{R} U}{3600} \tag{2.26}$$

$$H_p = \tilde{\mathcal{R}} c_{p_r} \epsilon (T_s - T_a)\left(1 + \frac{1}{B}\right) \tag{2.27}$$

$\mathcal{R}$ the precipitation rate in mm h^{-1}, and $\tilde{\mathcal{R}}$ in kg s^{-1}; c_{p_r} is the water specific heat (4186 J $kg^{-1}K^{-1}$); $B = \frac{c_p \Delta T}{\mathcal{L} \Delta q}$ is the *Bowen*'s fraction and ϵ is the dew point factor:

$$\epsilon = 1/\left(1 + \frac{R_a}{R_v}\frac{\mathcal{L} d_v}{d_h c_p}\frac{dq_s}{dT}\right)$$

with $\mathcal{L}$ the water latent heat of vaporization, c_p the air specific heat, d_v and d_h are vapor and heat diffusivities.

7. Roughness length z_0 could also be calculated with schemes that take waves effects on roughness into account :

$$Oost\ et\ al.,\ 2002\ \ : \begin{cases} z_0 = \frac{50}{2\pi} L_{wv} \left(\frac{u_*}{C_{wv}}\right)^{4.5} + 0.11 \frac{\nu}{u_*} \\ L_{wv} = \frac{g}{2\pi}(0.729U)^2 \\ C_{wv} = \frac{g}{2\pi}(0.729U) \end{cases} \tag{2.28}$$

$$Taylor\ and\ Yelland,\ 2001\ \ : \begin{cases} z_0 = 1200 H_{wv} \left(\frac{H_{wv}}{L_{wv}}\right)^{4.5} + 0.11 \frac{\nu}{u_*} \\ L_{wv} = \frac{g}{2\pi}(0.729U)^2 \\ H_{wv} = 0.018U^2 \times (1 + 0.015U) \end{cases} \tag{2.29}$$

The ECUME parameterization

The unified parameterization or ECUME (Exchange Coefficients from Unified Multi-campaigns Estimates) is a bulk iterative parameterization developed in order to obtain an optimized parameterization covering a wide range of atmospheric and oceanic conditions (*Weill et al.* [2003]) .
Based on the LKB algorithm, ECUME includes an estimation of neutral transfer coefficients at 10m from a multi-campaign calibration derived from the ALBATROS database that collects data from five flux measurement campaigns:

- POMME “Programme Océanique Multidisciplinaire à Moyenne Echelle”,
- FETCH “Flux, Etat de la mer et Télédetection en Condition de Fetch”,
- SEMAPHORE “Structure des Echanges Mer-Atmosphère, Propriétés des Hétérogénéités Océaniques : Recherche Expérimentale”,
- CATCH “Couplage avec l’ATmosphère en Conditions Hivernales”,
- EQUALANT99.

A more detailed description of each campaign could be found in *Weill et al.* [2003] and *Belamari* [2005] .
A similar post-treatment was applied to the five campaigns data to derive the drag coefficient $C_{D_{10n}}$, the heat coefficient $C_{H_{10n}}$ and the evaporation coefficient $C_{E_{10n}}$ as neutral 10m-wind functions (Figures 2.1, 2.2 and 2.3).

The ECUME parameterization main characteristic are:

1. An important effort was done on the ECUME algorithm in order to assure the convergence in maximum 20 iterations for every kind of conditions (*Belamari* [2005]) . The iterative sequence is stopped when the difference between the scale parameters between two iterations is inferior to prescribed threshold that are 2.10^{-4} m s^{-1} for u_*, 2.10^{-4} K for θ_* and 2.10^{-7} kg/kg for q_*.

   The closure relationship is the multi-campaign calibration of the neutral transfer coefficients at 10 meters.

2. The stability functions are Businger ’s functions with different coefficients than COARE3.0: ψ_m and ψ_h depend on the Monin-Obukhov’s length $\zeta = \frac{z}{L}$ which is computed as described in the following equations:

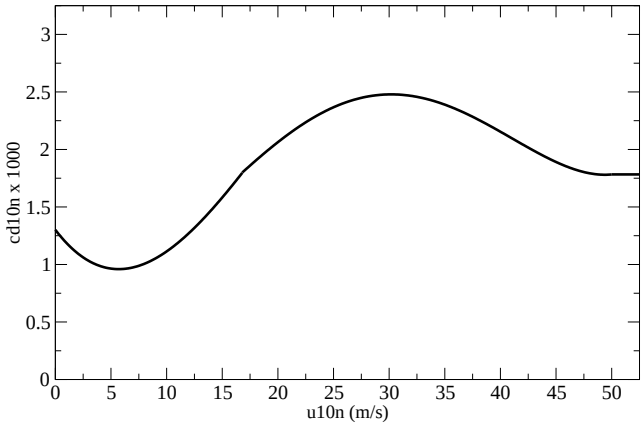

Figure 2.1: Multi-campaign calibration of the neutral drag coefficient at 10 meters $C_{D_{10n}}$.

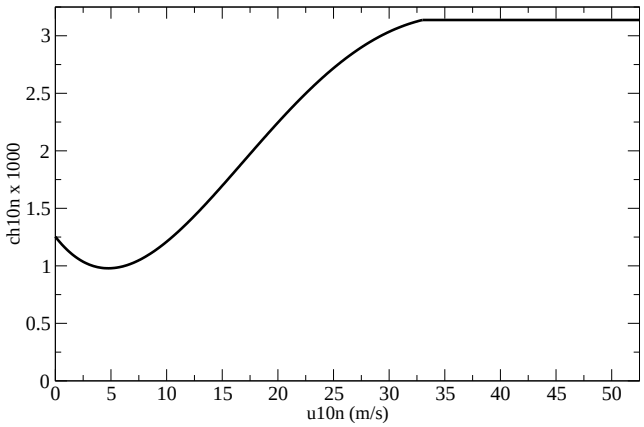

Figure 2.2: Multi-campaign calibration of the neutral heat coefficient at 10 meters $C_{H_{10n}}$.

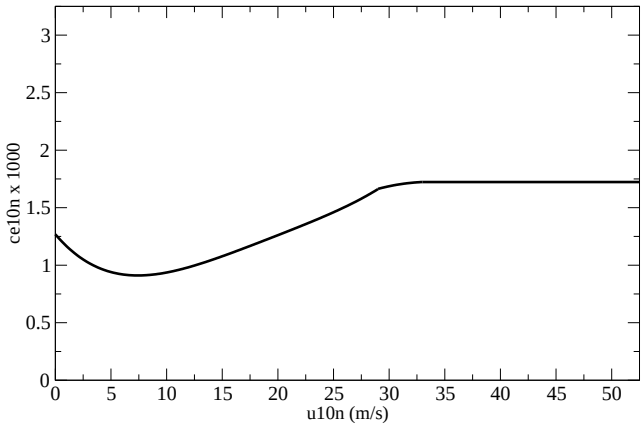

Figure 2.3: Multi-campaign calibration of the neutral evaporation coefficient at 10 meters $C_{E_{10n}}$.

- For wind:

$$ZL = \frac{g\kappa z(T_*(1+r_0 q) + r_0 T q_*)}{T(1+r_0 q) \times [MAX(u_*, 1.10^{-9})]^2}$$

with $r_0 = R_v/R_a - 1$.

$$si \;\; ZL \geq 0 \quad z/L = MIN(ZL, 0.25) \tag{2.30}$$

$$si \;\; ZL < 0 \quad z/L = MAX(ZL, -200) \tag{2.31}$$

- For temperature and humidity:

$$(z/L)_t = z/L \times \frac{z_t}{z}\,; \qquad (z/L)_q = z/L \times \frac{z_q}{z}$$

Finally:

$\zeta = \frac{z}{L}$	$\psi_m(\zeta) =$	$\psi_h(\zeta) =$
stable	$-\Gamma\zeta$	$-\Gamma\zeta$
$(\zeta \geq 0)$	$\Gamma = 7$	
unstable:	$(1-f)\psi_{mK} + f\psi_{mC}$	$(1-f)\psi_{hK} + f\psi_{hC}$
$(\zeta < 0)$	$f = \frac{\zeta^2}{(1.0+\zeta^2)}$	
Kansas	$\psi_{mK} = 2ln(\frac{1+x}{2}) + ln(\frac{1+x^2}{2})$ $-2arctan(x) + \frac{\pi}{2}$ with $x = (1-16\zeta)^{\frac{1}{4}}$	$\psi_{hK} = 2ln(\frac{1+x}{2})$ with $x = (1-16\zeta)^{\frac{1}{2}}$
Convective	$\psi_{mC} = \frac{3}{2}ln(\frac{y^2+y+1}{3})$ $-\sqrt{3}arctan(\frac{2y+1}{\sqrt{3}}) + \frac{\pi}{\sqrt{3}}$ with $y = (1-12.87\zeta)^{\frac{1}{3}}$	$\psi_{hC} = \frac{3}{2}ln(\frac{y^2+y+1}{3})$ $-\sqrt{3}arctan(\frac{2y+1}{\sqrt{3}}) + \frac{\pi}{\sqrt{3}}$ with $y = (1-12.87\zeta)^{\frac{1}{3}}$

3. The roughness length is given by the Smith 's relationship (Eq. 2.10) with $\alpha = 0.011$ and $\beta = 0.11$.

4. The reduction of 2% of the specific humidity at saturation due to seawater salinity is applied (eq. 2.23, *Kraus* [1972]).

5. The gustiness correction could be applied (Eq. 2.25).

6. The corrections due to precipitation τ_p and H_p according to *Fairall et al.* [1996b] and *Gosnell et al.* [1995] could also be computed in the ECUME parameterization (Eq. 2.26 and 2.27).

7. The Webb 's correction (LE_{webb}) is a correction applied to the latent heat flux. It is due to air density variations when the humidity vary under the evaporation action. If $\bar{w}$ is the mean value of the vertical perturbations,

$$\overline{w} = 1.61\overline{w'q'} + (1+1.61q)\frac{\overline{w'T'}}{T} \tag{2.32}$$

the Webb 's correction expression is:

$$LE_{Webb} = \rho_a \mathcal{L} \overline{w} q \tag{2.33}$$

where $\mathcal{L}$ is the latent heat of vaporization for water.

8. No waves effects are taking into account in the ECUME parameterization.

Short summary

LOUIS		
z_0	$z_0 = \frac{\alpha u_*^2}{g}$ (*Charnock* [1955]) if $T > -2$C	or $z_0 = z_{0_{snow}}$ if $T < -2$C
U	$U = \|\vec{v}\|$	
stability functions	Numerical *Louis* [1979]'s functions	
τ_{sea}	$= -\rho_a C_D U^2$	
H_{sea}	$= \rho_a c_{p_a} C_H U(\theta_s - \theta_a)$	
LE_{sea}	$= \rho_a \mathcal{L}_v C_E U(q_s - q_a)$	
COARE3.0		
z_0	$z_0 = \alpha(u)\frac{u_*^2}{g} + \frac{\beta\nu}{u_*}$ *Smith* [1988]	or *Oost et al.* [2002] or *Taylor and Yelland* [2001]
U	$U = \|\vec{v}\|$	or $U = \sqrt{\|\vec{v}\|^2 + w_g^2}$ (gustiness)
stability functions	Modified Businger's functions	
τ_{sea}	$= -\rho_a C_D U^2$	$+\tau_p$ (*Fairall et al.* [1996b])
H_{sea}	$= \rho_a c_{p_a} C_H U(\theta_s - \theta_a)$	$+H_p$ (*Gosnell et al.* [1995])
LE_{sea}	$= \rho_a \mathcal{L}_v C_E U(q_s - q_a)$	
ECUME		
z_0	$z_0 = \frac{\alpha u_*^2}{g} + \frac{\beta\nu}{u_*}$ (*Smith* [1988])	
U	$U = \|\vec{v}\|$	or $U = \sqrt{\|\vec{v}\|^2 + w_g^2}$ (gustiness)
stability functions	Modified Businger's functions	
τ_{sea}	$= -\rho_a C_D U^2$	$+\tau_p$ (*Fairall et al.* [1996b])
H_{sea}	$= \rho_a c_{p_a} C_H U(\theta_s - \theta_a)$	$+H_p$ (*Gosnell et al.* [1995])
LE_{sea}	$= \rho_a \mathcal{L}_v C_E U(q_s - q_a)$	$+LE_{Webb}$ (*Webb et al.* [1980])
C_{D10n}, C_{H10n}	neutral coefficients calibrated at 10m	

2.3 Coupling with a 1D TKE oceanic model

2.3.1 Coupling objectifs and principles

The main objective of the coupling is to improve the fine scale air-sea exchanges modelling in the SURFEX surface scheme. To better represent the fine scale air-sea interactions, it is necessary to take into account the oceanic dynamics and the thermal content evolution (*Lebeaupin Brossier et al.* [2008b,c]) .

The coupled system's principle consists in modelling a seawater column under each grid point containing a fraction of sea and limited by the bottom (Figure 2.4). The ocean model used is the uni-dimensional model described by *Gaspar et al.* [1990] [see section 2.3.2] which allows to represent the oceanic vertical mixing according to a parameterization of turbulence from *Bougeault and Lacarrère* [1989] adapted to ocean. By the turbulent vertical mixing modelling, the 1D ocean model allows to represent the heat, water and momentum exchanges from the superficial oceanic layers in direct interaction with the atmosphere and subjected to radiative effects, to the deepest layers.

2.3.2 Description of the 1D oceanic model in TKE equation

The 1D model includes a prognostic equation for the turbulent kinetic energy (e) with a 1.5 order closure. The other prognostic variables are the temperature (T), the salinity (S), and the current [$\vec{u} = (u, v)$].

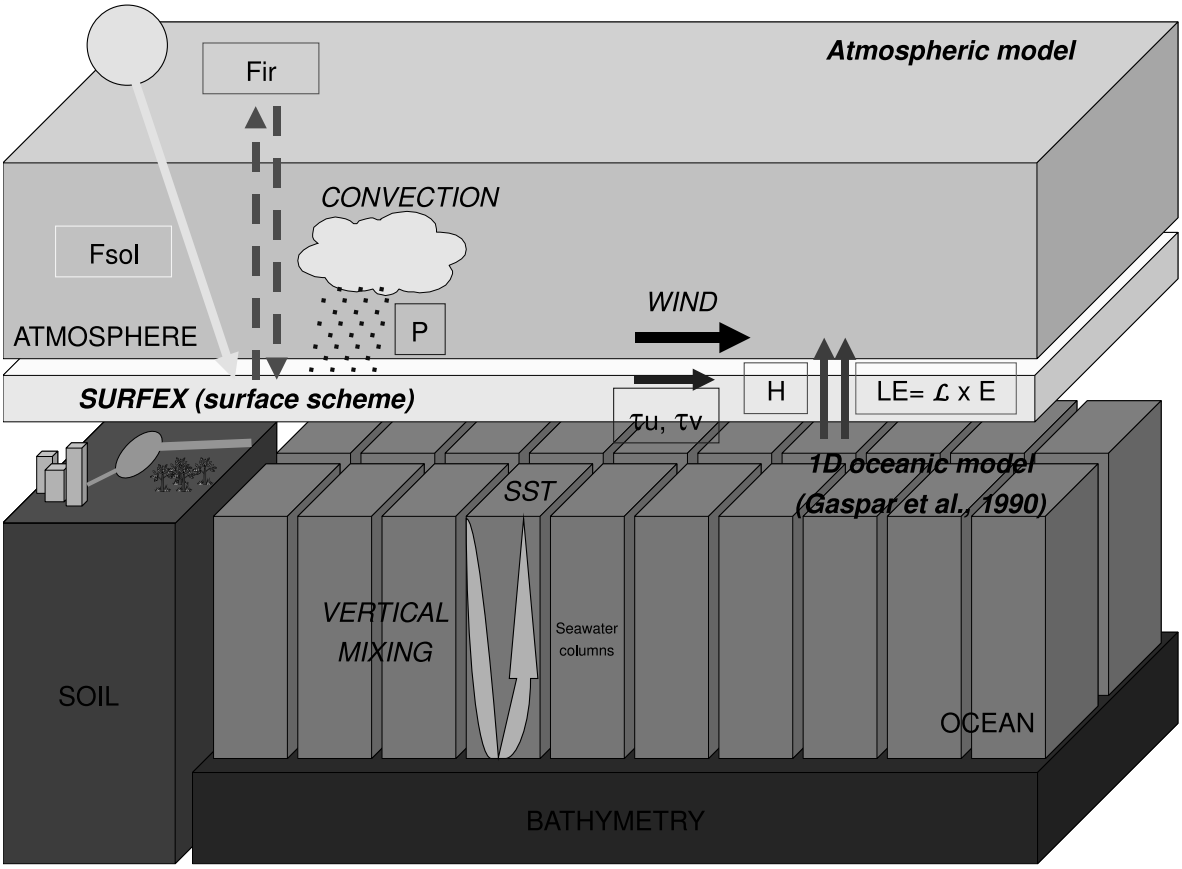

Figure 2.4: The high-resolution ocean-atmosphere coupled system between (MESO-NH) SURFEX and the 1D oceanic model.

Prognostic equations for T, S, u and v

Each of the prognostic variables (α) is decomposed in a mean value ($\overline{\alpha}$) and a perturbation around this mean value (α'), so $\alpha = \overline{\alpha} + \alpha'$. For each seawater column, T, S, u and v evolve under the turbulent vertical mixing effect. This mixing depends of air-sea interface fluxes.
The conservative equations are:

$$\begin{cases} \frac{\partial T}{\partial t} = \frac{F_{sol}}{\rho_0 c_p}\frac{\partial I(z)}{\partial z} - \frac{\partial \overline{T'w'}}{\partial z} \\ \\ \frac{\partial S}{\partial t} = -\frac{\partial \overline{S'w'}}{\partial z} \\ \\ \frac{\partial \vec{u}}{\partial t} = -f\vec{k}\times\vec{u} - \frac{\partial \overline{\vec{u}'w'}}{\partial z} \end{cases} \tag{2.34}$$

where w is the vertical velocity, ρ_0 is a reference density, c_p is the specific heat, f is the Coriolis parameter. $\vec{k}$ is the unit vertical along the vertical, F_{sol} is the solar radiation received by the surface, and $I(z)$ is the solar radiation fraction reaching the depth z ($I(z)$ function decreases exponentially with depth).
The conditions at the top of the model (z=0) are:

$$\begin{cases} -\overline{T'w'}(0) = \frac{F_{nsol}}{\rho_0 c_p} = \frac{H+LE+F_{ir}}{\rho_0 c_p} \\ \\ -\overline{S'w'}(0) = \frac{E-P}{\rho_0 c_p} \\ \\ -\overline{\vec{u}'w'}(0) = \frac{\vec{\tau}}{\rho_0 c_p} \end{cases} \tag{2.35}$$

Fluxes are positive here downwards.

Finally, the forcing variables to give to the oceanic model are:

- the solar radiation F_{sol}
- the infra-red radiation F_{ir}
- the evaporation rate E proportional to the latent heat flux $E = \frac{LE}{\mathcal{L}}$
- the sensible heat flux H
- the zonal and meridional stress components $\vec{\tau} = (\tau_u, \tau_v)$
- the precipitation rate P

F_{nsol} is defined as the sum of the sensible H, the latent heat flux LE and the infra-red radiation F_{ir} and is named non-solar flux.
The closure relationships are given by:

$$\begin{cases} -\overline{T'w'} = K_h \frac{\partial \overline{T}}{\partial z} \\ \\ -\overline{S'w'} = K_s \frac{\partial \overline{S}}{\partial z} \\ \\ -\overline{\vec{u}'w'} = K_m \frac{\partial \overline{\vec{u}}}{\partial z} \end{cases} \tag{2.36}$$

The K_* are diffusivity coefficients linked to the turbulent kinetic energy by:

$$K = c_k l_k \overline{e}^{\frac{1}{2}} = K_h = K_s = \frac{K_m}{Prt} \simeq K_m \tag{2.37}$$

where c_k is a constant to determine; l_k is a mixing length and Prt is the Prandlt's number.

Prognostic equation for turbulent kinetic energy

The equation for TKE $e = \frac{1}{2}(u'^2 + v'^2 + w'^2)$ is given by:

$$\frac{\partial \overline{e}}{\partial t} = -\frac{\partial}{\partial z}\left(\overline{e'w'} + \frac{\overline{p'w'}}{\rho_0}\right) - \overline{\vec{u}'w'} \times \frac{\partial \overline{\vec{u}}}{\partial z} + \overline{b'w'} - \epsilon \tag{2.38}$$

where p is pressure; $\epsilon = c_\epsilon l_\epsilon \overline{e}^{\frac{3}{2}}$ is dissipation; $b = g\frac{\rho - \rho_0}{\rho_0}$ is the buoyancy. The seawater density is diagnosed from temperature and salinity:

$$\rho = \rho_0 + (T - T_{ref}) \times [-0.19494 - 0.49038(T - T_{ref})] + 0.77475(S - S_{ref})$$

where $T_{ref} = 13.5$ C, $S_{ref} = 32.6$ psu and $\rho_0 = 1024.458$ kg/m^3.
The vertical TKE flux is parameterized:

$$-\left(\overline{e'w'} + \frac{\overline{p'w'}}{\rho_0}\right) = K_e \frac{\partial \overline{e}}{\partial z} \tag{2.39}$$

with

$$K_e = c_\epsilon l_\epsilon \overline{e}^{\frac{1}{2}} \tag{2.40}$$

The Bougeault and Lacarrère mixing length are:

$$l_\epsilon = (l_u l_d)^{\frac{1}{2}} \tag{2.41}$$

$$l_k = min(l_u, l_d)\ pour\ k = h, s\ and\ m \tag{2.42}$$

l_u and l_d (for "up" and "down") are estimated as the upwards and downwards distances for which the kinetic energy is transformed in potential energy:

$$\overline{e}(z) = \frac{g}{\rho_0}\int_z^{z+l_u} [\overline{\rho}(z) - \rho(z')]dz' \tag{2.43}$$

$$\overline{e}(z) = \frac{g}{\rho_0}\int_z^{z-l_d} [\overline{\rho}(z) - \rho(z')]dz' \tag{2.44}$$

Discretization

The temporal integration scheme is a semi-implicit scheme for T and S. For the horizontal current $\vec{u} = (u, v)$, the integration scheme is implicit/semi-implicit.
The discretization is here described in detail for the temperature. The same could be done for the salinity, the TKE and the current in complex notation ($\vec{u} \rightarrow u + iv$, $i^2 = -1$).
The equation

$$\frac{\partial T}{\partial t} = \frac{F_{sol}}{\rho_0 c_p}\frac{\partial I(z)}{\partial z} - \frac{\partial}{\partial z}\left(-K\frac{\partial \overline{T}}{\partial z}\right)$$

is decomposed as:

$$\frac{T_k^{t+1} - T_k^t}{\Delta t} = \frac{F_{sol}}{\rho_0 c_p}\frac{\partial I(z)}{\partial z} + \frac{1}{\Delta z_2(k)}[K(k+1)\frac{T_{k+1}^{t+1} - T_k^{t+1}}{\Delta z_1(k)} - K(k)\frac{T_k^{t+1} - T_{k-1}^{t+1}}{\Delta z_1(k)}] \tag{2.45}$$

$$T_{k-1}^{t+1}\left(-\frac{K(k)}{\Delta z_1 \Delta z_2}\right) + T_k^{t+1}\left(\frac{1}{\Delta t} + \frac{K(k+1) - K(k)}{\Delta z_1 \Delta z_2}\right) + T_{k+1}^{t+1}\left(-\frac{K(k+1)}{\Delta z_1 \Delta z_2}\right) = \frac{1}{\Delta t}T_k^t + \frac{F_{sol}}{\rho_0 c_p}\frac{\partial I}{\partial z}$$

In a matricial writing following the vertical levels (k):

$$[\mathcal{M}]\left(T^{t+1}\right) = \frac{1}{\Delta t}\left(T^{t}\right) + [\frac{F_{sol}}{\rho_0 c_p}\frac{\partial I(z)}{\partial z}] \tag{2.46}$$

$$[\mathcal{M}] = \begin{pmatrix} . & . & 0 & & & & \\ . & . & . & 0 & & & \\ 0 & \beta_k & \alpha_k & \gamma_k & 0 & & \\ - & - & - & - & - & - & - \\ & & & 0 & . & . & . \\ & & & & 0 & . & . \end{pmatrix} \tag{2.47}$$

$$\alpha_k = \frac{1}{\Delta t} + \frac{K(k+1) - K(k)}{\Delta z_1 \Delta z_2}$$

$$\beta_k = -\frac{K(k)}{\Delta z_1 \Delta z_2}$$

$$\gamma_k = -\frac{K(k+1)}{\Delta z_1 \Delta z_2}$$

$[\mathcal{M}]$ is a tri-diagonal matrix to invers.

The vertical grid must be a z-coordinates grid as described by Fig. 2.5.

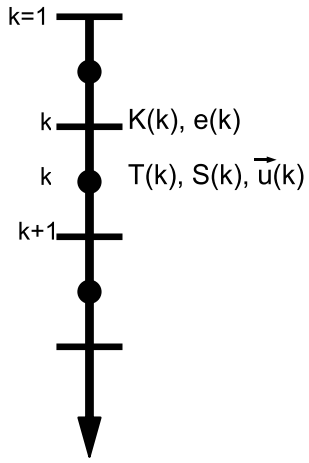

Figure 2.5: Vertical grid description of the 1D oceanic model from Gaspar et al. (1990) .

To take into account the bathymetry effects on the oceanic vertical mixing, we introduced a bathymetry index (as the sea-land mask) which is worth 0 for free sea and 1 for levels under the sea-bed. For the vertical levels which have a bathymetry index equal to 1, we impose the prognostic variables values equal to the last free-sea level values. The 1D model thus does not carry out any energy transfer towards or coming from the bottom. Only the energy contained in the higher free levels is taken into account.
We also introduced a diagnosis of mixed layer depth. The mixed layer base is diagnosed with an arbitrary criterion on the density profile: we assume that the thermocline corresponds to the vertical level for which the seawater density is superior to a 0.02 kg m^{-3} variations compared to the density for a reference level (taken at 5m depth).
Finally, the oceanic model must be initialized in temperature, salinity and current either from an oceanic analysis or from climatologies.

2.4 Inland Water: Lake Model FLake

In this section, a lake model (parameterisation scheme) capable of predicting the temperature structure of lakes of various depth on time scales from a few hours to many years is presented. A detailed description of the model, termed FLake, is given in *Mironov* [2008]. FLake is an integral (bulk) model. It is based on a two-layer parametric representation of the evolving temperature profile within the water column and on the integral energy budget for these layers. The structure of the stratified layer between the upper mixed layer and the basin bottom, the lake thermocline, is described using the concept of self-similarity (assumed shape) of the temperature-depth curve. The same concept is used to describe the temperature structure of the thermally-active upper layer of bottom sediments and of the ice and snow cover. An entrainment equation for the depth of a convectively-mixed layer and a relaxation-type equation for the depth of a wind-mixed layer in stable and neutral stratification are developed on the basis of the turbulence kinetic energy (TKE) equation integrated over the mixed layer. Both mixing regimes are treated with due regard for the volumetric character of solar radiation heating. Simple thermodynamic arguments are invoked to develop the evolution equations for the ice and snow depths. The system of ordinary differential equations for the time-dependent prognostic quantities that characterise the evolving temperature profile, see Figs. 2.6 and 2.7, is closed with algebraic (or transcendental) equations for diagnostic quantities, such as the heat flux through the lake bottom and the equilibrium mixed-layer depth in stable or neutral stratification.

The resulting lake model is computationally very efficient but still incorporates much of the essential physics.

Within FLake, the lake water is treated as a Boussinesq fluid, i.e. the water density is taken to be constant equal to the reference density except when it enters the buoyancy term in the TKE equation and the expression for the buoyancy frequency.

The other thermodynamic parameters are considered constant except for the snow density and the snow heat conductivity.

2.4.1 Equation of State

We utilise the quadratic equation of state of the fresh water,

$$\rho_w = \rho_r \left[1 - \frac{1}{2} a_T \left(\theta - \theta_r\right)^2\right], \tag{2.48}$$

where ρ_w is the water density, $\rho_r = 999.98 \approx 1.0 \cdot 10^3$ kg·m^{-3} is the maximum density of the fresh water at the temperature $\theta_r = 277.13$ K, and $a_T = 1.6509 \cdot 10^{-5}$ K^{-2} is an empirical coefficient (*Farmer and Carmack* [1981]). Equation (2.48) is the simplest equation of state that accounts for the fact that the temperature of maximum density of the fresh water exceeds its freezing point $\theta_f = 273.15$ K. According to Eq. (2.48), the thermal expansion coefficient α_T and the buoyancy parameter β depend on the water temperature,

$$\beta(\theta) = g\alpha_T(\theta) = g a_T(\theta - \theta_r), \tag{2.49}$$

where $g = 9.81$ m·s^{-2} is the acceleration due to gravity.

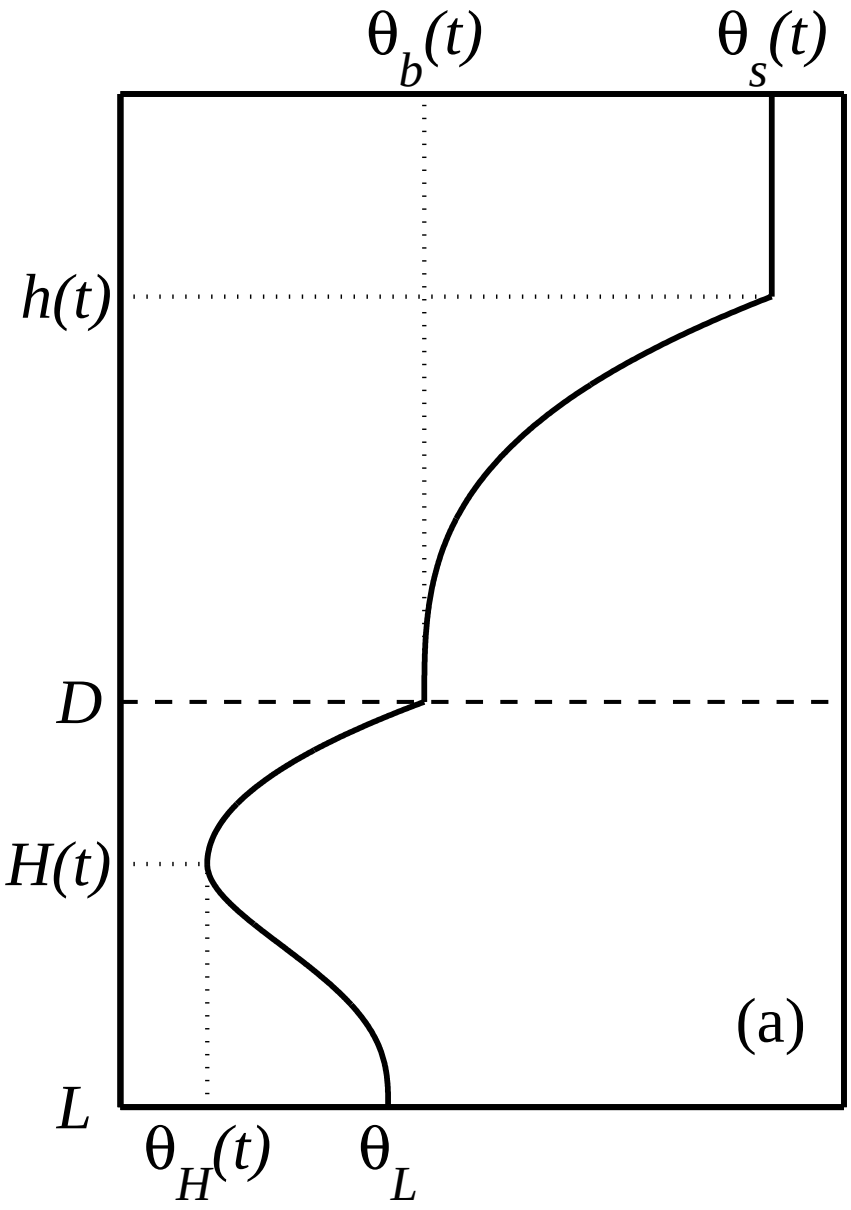

Figure 2.6: Schematic representation of the temperature profile in the mixed layer, in the thermocline, and in the thermally active layer of bottom sediments. The evolving temperature profile is specified by several time-dependent quantities. These are the mixed-layer temperature $\theta_s(t)$ and its depth $h(t)$, the temperature $\theta_b(t)$ at the water-bottom sediment interface, the shape factor $C_\theta(t)$ with respect to the temperature profile in the thermocline, the temperature $\theta_H(t)$ at the lower boundary of the upper layer of bottom sediments penetrated by the thermal wave, and the depth $H(t)$ of that layer. The temperature θ_L at the outer edge $z = L$ of the thermally active layer of bottom sediments is constant.

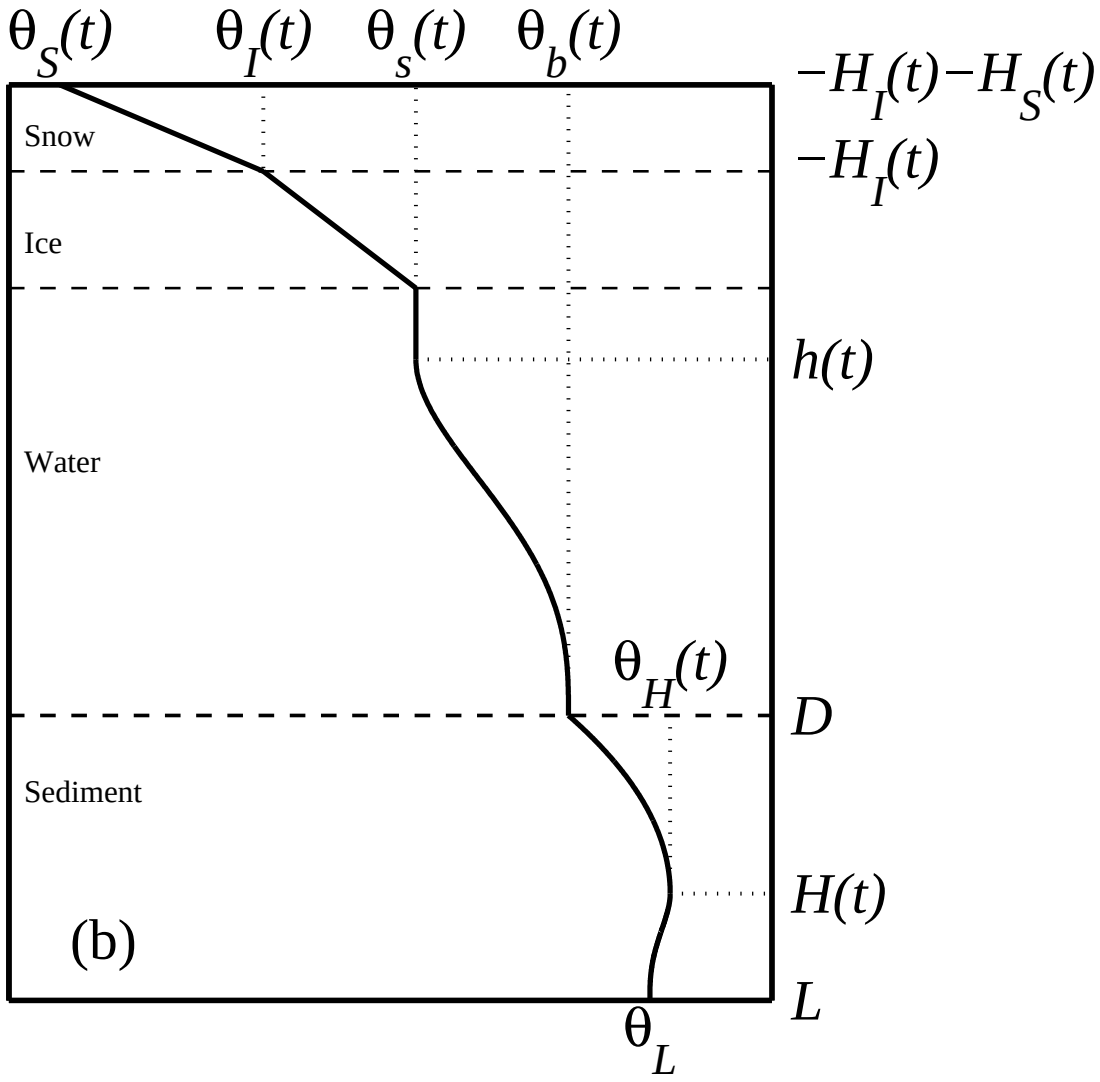

Figure 2.7: Apart from $\theta_s(t)$, $h(t)$, $\theta_b(t)$, $C_\theta(t)$, $\theta_H(t)$, and $H(t)$ (see Fig. 2.6), four additional quantities are computed in case the lake is covered by ice and snow. These are the temperature $\theta_S(t)$ at the air-snow interface, the temperature $\theta_I(t)$ at the snow-ice interface, the snow depth $H_S(t)$, and the ice depth $H_I(t)$.

2.4.2 The Water Temperature

Parameterization of the Temperature Profile and the Heat Budget

We adopt the following two-layer parameterization of the vertical temperature profile:

$$\theta = \begin{cases} \theta_s & \text{at} \quad 0 \le z \le h \\ \theta_s - (\theta_s - \theta_b)\Phi_\theta(\zeta) & \text{at} \quad h \le z \le D, \end{cases} \tag{2.50}$$

where $\Phi_\theta \equiv (\theta_s - \theta) / (\theta_s - \theta_b)$ is a dimensionless function of dimensionless depth $\zeta \equiv (z - h) / (D - h)$. The thermocline extends from the mixed-layer outer edge $z = h$ to the basin bottom $z = D$. Hereinafter the arguments of functions dependent on time and depth are not indicated (cf. Figs. 2.6 and 2.7).

According to Eq. (2.50), h, D, θ_s, θ_b, and the mean temperature of the water column, $\overline{\theta} \equiv D^{-1} \int_0^D \theta dz$, are related through

$$\overline{\theta} = \theta_s - C_\theta(1 - h/D)(\theta_s - \theta_b), \tag{2.51}$$

where

$$C_\theta = \int_0^1 \Phi_\theta(\zeta) d\zeta \tag{2.52}$$

is the shape factor.

The parameterization of the temperature profile (2.50) should satisfy the heat transfer equation

$$\frac{\partial}{\partial t}(\rho c \theta) = -\frac{\partial}{\partial z}(Q + I), \tag{2.53}$$

where Q is the vertical turbulent heat flux, and I is the heat flux due to solar radiation.

Integrating Eq. (2.53) over z from 0 to D yields the equation of the total heat budget,

$$D\frac{d\overline{\theta}}{dt} = \frac{1}{\rho_w c_w}\left[Q_s + I_s - Q_b - I(D)\right], \tag{2.54}$$

where c_w is the specific heat of water, Q_s and I_s are the values of Q and I, respectively, at the lake surface, and Q_b is the heat flux through the lake bottom. The radiation heat flux I_s that penetrates into the water is the surface value of the incident solar radiation flux from the atmosphere multiplied by $1 - \alpha_w$, α_w being the albedo of the water surface with respect to solar radiation. The surface flux Q_s is a sum of the sensible and latent heat fluxes and the net heat flux due to long-wave radiation at the air-water interface.

Integrating Eq. (2.53) over z from 0 to h yields the equation of the heat budget in the mixed layer,

$$h\frac{d\theta_s}{dt} = \frac{1}{\rho_w c_w}\left[Q_s + I_s - Q_h - I(h)\right], \tag{2.55}$$

where Q_h is the heat flux at the bottom of the mixed layer.

Given the surface fluxes Q_s and I_s (these are delivered by the driving atmospheric model or are known from observations), and the decay law for the flux of solar radiation , Eqs. (2.51), (2.54) and (2.55) contain seven unknowns, namely, h, $\overline{\theta}$, θ_s, θ_b, Q_h, Q_b and C_θ. The mixed layer depth, the bottom heat flux and the shape factor are considered in what follows. One more relation is required. Following *Filyushkin and Miropolsky* [1981], *Tamsalu et al.* [1997] and *Tamsalu and Myrberg* [1998], we assume that in case of the mixed layer deepening, $dh/dt > 0$, the profile of the vertical turbulent heat flux in the thermocline can be represented in a self-similar form. That is

$$Q = Q_h - (Q_h - Q_b)\Phi_Q(\zeta) \qquad \text{at} \;\; h \le z \le D, \tag{2.56}$$

where the shape function Φ_Q satisfies the boundary conditions $\Phi_Q(0) = 0$ and $\Phi_Q(1) = 1$. Equation (2.56) is suggested by the travelling wave-type solution to the heat transfer equation. If the mixed layer and the thermocline develop on the background of a deep stably or neutrally stratified quiescent layer (this situation is encountered in the ocean and in the atmosphere), the travelling wave-type solution shows that both the temperature profile and the profile of the turbulent heat flux are described by the same shape function, i.e. $\Phi_\theta(\zeta) = \Phi_Q(\zeta)$. In lakes, the thermocline usually extends from the bottom of the mixed layer down to the basin bottom (except for very deep lakes). In this case, the travelling wave-type solution to the heat transfer equation also suggests self-similar profiles of the temperature and of the heat flux, however the relation between the shape functions $\Phi_\theta(\zeta)$ and $\Phi_Q(\zeta)$ is different. The issue is considered in *Mironov* [2008].
Integrating Eq. (2.53) with due regard for Eqs. (2.50) and (2.56) over z' from h to $z > h$, then integrating the resulting expression over z from h to D, we obtain

$$\frac{1}{2}(D-h)^2\frac{d\theta_s}{dt} - \frac{d}{dt}\left[C_{\theta\theta}(D-h)^2(\theta_s-\theta_b)\right] =$$

$$\frac{1}{\rho_w c_w}\left[C_Q(D-h)(Q_h-Q_b) + (D-h)I(h) - \int_h^D I(z)dz\right], \tag{2.57}$$

where

$$C_Q = \int_0^1 \Phi_Q(\zeta)d\zeta \tag{2.58}$$

is the shape factor with respect to the heat flux, and

$$C_{\theta\theta} = \int_0^1 d\zeta \int_0^{\zeta'} \Phi_\theta(\zeta')d\zeta' \tag{2.59}$$

is the dimensionless parameter. The analysis in *Mironov* [2008] suggests that $C_Q = 2C_{\theta\theta}/C_\theta$.
In case of the mixed-layer stationary state or retreat, $dh/dt \leq 0$, Eq. (2.56) is not justified. Then, the bottom temperature is assumed to be "frozen",

$$\frac{d\theta_b}{dt} = 0. \tag{2.60}$$

If $h = D$, then $\theta_b = \theta_s = \overline{\theta}$ and the mean temperature is computed from Eq. (2.54).

The Mixed-Layer Depth

Convective deepening of the mixed layer is described by the entrainment equation. This equation is conveniently formulated in terms of the dependence of the so-called entrainment ratio A on one or the other stratification parameter. The entrainment ratio is a measure of the entrainment efficiency. It is commonly defined as a negative of the ratio of the heat flux due to entrainment at the bottom of the mixed layer, Q_h, to an appropriate heat flux scale, Q_*. In case of convection driven by the surface flux, where the forcing is confined to the boundary, the surface heat flux Q_s serves as an appropriate flux scale. This leads to the now classical *Deardorff* [1970a, 1970b] convective scaling, where h and $|h\beta Q_s/(\rho_w c_w)|^{1/3}$ serve as the scales of length and velocity, respectively.
The Deardorff scaling is unsuitable for convective flows affected by the solar radiation heating that is not confined to the boundary but is distributed over the water column. If the mixed-layer temperature exceeds the temperature of maximum density, convective motions are driven by surface cooling, whereas radiation heating tends to stabilise the water column, arresting the mixed layer deepening (*Soloviev* [1979], *Mironov and Karlin* [1989]). Such regime of convection is encountered in the oceanic upper layer (e.g. *Kraus and Rooth* [1961], *Soloviev and Vershinskii* [1982], *Price et al.* [1986] and in fresh-water lakes (e.g. *Imberger* [1985]). If the mixed-layer temperature is below that of maximum density, volumetric radiation

heating leads to de-stabilisation of the water column and thereby drives convective motions. Such regime of convection is encountered in fresh-water lakes in spring. Convective mixing often occurs under the ice, when the snow cover overlying the ice vanishes and solar radiation penetrates down through the ice (e.g. *Farmer* [1975], *Mironov and Terzhevik* [2000], *Mironov et al.* [2002], *Jonas et al.* [2003]).
In order to account for the vertically distributed character of the radiation heating, we make use of a generalised convective heat flux scale

$$Q_* = Q_s + I_s + I(h) - 2h^{-1}\int_0^h I(z)dz, \tag{2.61}$$

and define the convective velocity scale and the entrainment ratio as

$$w_* = \left[-h\beta(\theta_s)Q_*/(\rho_w c_w)\right]^{1/3}, \qquad A = -Q_h/Q_*, \tag{2.62}$$

respectively. In order to specify A, we employ the entrainment equation in the form

$$A + \frac{C_{c2}}{w_*}\frac{dh}{dt} = C_{c1}, \tag{2.63}$$

where C_{c1} and C_{c2} are dimensionless constants (the estimates of these and other empirical constants of the model are discussed in Section 2.4.5 and summarised in the Appendix). The second term on the l.h.s. of Eq. (2.63) is the spin-up correction term introduced by *Zilitinkevich* [1975]. This term prevents an unduly fast growth of h when the mixed layer is shallow. If the spin-up term is small, Eq. (2.63) reduces to a simple relation $A = C_{c1}$ that proved to be a sufficiently accurate approximation for a large variety of geophysical and laboratory convective flows *Zilitinkevich* [1991].
Equations (2.61), (2.62) and (2.63) should be used to compute the mixed-layer depth when the buoyancy flux $B_* = \beta(\theta_s)Q_*/(\rho_w c_w)$ is negative. The quantity $-hB_* \equiv w_*^3$ is a measure of the generation rate of the turbulence kinetic energy in a layer of depth h by the buoyancy forces (see a discussion in *Mironov et al.* [2002]. A negative B_* indicates that the TKE is generated through convective instability. Otherwise, the TKE is lost to work against the gravity. This occurs when the density stratification is stable. A different formulation for the mixed-layer depth is then required.

Mironov et al. [1991] used a diagnostic equation to determine the wind-mixed layer depth in stable and neutral stratification. That is, h was assumed to adjust to external forcing on a time scale that does not exceed the model time step. This assumption is fair if seasonal changes of temperature and mixing conditions are considered and the model time step is typically one day. The assumption is likely to be too crude to consider diurnal variations. To this end, We utilise a relaxation-type rate equation for the depth of a stably or neutrally stratified wind-mixed layer. It reads

$$\frac{dh}{dt} = \frac{h_e - h}{t_{rh}}. \tag{2.64}$$

Here, h_e is the equilibrium mixed-layer depth, and t_{rh} is the relaxation time scale given by

$$t_{rh} = \frac{h_e}{C_{rh}u_*}, \tag{2.65}$$

where $u_* = |\tau_s/\rho_w c_w|^{1/2}$ is the surface friction velocity, τ_s being the surface stress, and C_{rh} is a dimensionless constant. A rate equation (2.64) with the relaxation time scale proportional to the reciprocal of the Coriolis parameter [that is a particular case of Eq. (2.65) with h_e specified through Eq. (2.66)] was favourably tested by *Zilitinkevich et al.* [2002] and *Zilitinkevich and Baklanov* [2002] against data from atmospheric measurements and was recommended for practical use.

In order to specify h_e, we make use of a multi-limit formulation for the equilibrium depth of a stably or neutrally stratified boundary layer proposed by *Zilitinkevich and Mironov* [1996]. Based on the analysis of the TKE budget, these authors proposed a generalised equation for the equilibrium boundary-layer depth that accounts for the combined effects of rotation, surface buoyancy flux and static stability at the boundary-layer outer edge [Eq. (30) in op. cit.]. That equation reduces to the equations proposed earlier by *Rossby and Montgomery* [1935], *Kitaigorodskii* [1960] and *Kitaigorodskii and Joffre* [1988] in the limiting cases of a truly neutral rotating boundary layer, the surface-flux-dominated boundary layer, and the imposed-stability-dominated boundary layer, respectively. It also incorporates the *Zilitinkevich* [1972] and the *Pollard, Rhines and Thompson* [1973] equations that describe the intermediate regimes, where the effects of rotations and stratification essentially interfere and are roughly equally important. We adopt a simplified version of the *Zilitinkevich and Mironov* [1996] equation [Eq. (26) in op. cit.] that does not incorporate the *Zilitinkevich* [1972] and the *Pollard et al.* [1973] scales. It reads

$$\left(\frac{fh_e}{C_n u_*}\right)^2 + \frac{h_e}{C_s L} + \frac{N h_e}{C_i u_*} = 1, \tag{2.66}$$

where $f = 2\Omega \sin\phi$ is the Coriolis parameter, $\Omega = 7.29 \cdot 10^{-5}$ s^{-1} is the angular velocity of the earth's rotation, ϕ is the geographical latitude, L is the Obukhov length, N is the buoyancy frequency below the mixed layer, and C_n, C_s and C_i are dimensionless constants. A generalised formulation for the Obukhov length is used, $L = u_*^3/(\beta Q_*/\rho_w c_w)$, that accounts for the vertically distributed character of the solar radiation heating (note that the von Kármán constant is not included into the definition of L). A mean-square buoyancy frequency in the thermocline, $\overline{N} = \left[(D-h)^{-1}\int_h^D N^2 dz\right]^{1/2}$, is used as an estimate of N in Eq. (2.66).

One further comment is in order. *Zilitinkevich et al.* [2002, 2007] reconsidered the problem of the equilibrium stable boundary-layer depth. They concluded that the *Zilitinkevich* [1972] scale, $|u_* L/f|^{1/2}$, and the *Pollard et al.* [1973] scale, $u_*/|Nf|^{1/2}$, are the appropriate depth scales for the boundary layers dominated by the surface buoyancy flux and by the static stability at the boundary-layer outer edge, respectively. In other words, h_e depends on the Coriolis parameter no matter how strong the static stability. This is different from Eq. (2.66) where the limiting scales are L and u_*/N, respectively. The problem was further examined by *Mironov and Fedorovich* [2008]. They showed that the above scales are particular cases of more general power-law formulations, namely, $h/L \propto (|f|L/u_*)^{-p}$ and $hN/u_* \propto (|f|/N)^{-q}$ for the boundary layers dominated by the surface buoyancy flux and by the static stability at the boundary-layer outer edge, respectively. The *Zilitinkevich* [1972] and *Pollard et al.* [1973] scales are recovered with $p = 1/2$ and $q = 1/2$, whereas the *Kitaigorodskii* [1960] and *Kitaigorodskii and Joffre* [1988] are recovered with $p = 0$ and $q = 0$. Scaling arguments are not sufficient to fix the exponents p and q. They should be evaluated on the basis of experimental data. Available data from observations and from large-eddy simulations are uncertain. They do not make it possible to evaluate p and q to sufficient accuracy and to conclusively decide between the alternative formulations for the boundary-layer depth. Leaving the evaluation of p and q for future studies, we utilise Eq. (2.66). This simple interpolation formula is consistent with the complexity of the present lake model and is expected to be a sufficiently accurate approximation for most practical purposes.

One more limitation on the equilibrium mixed-layer depth should be taken into account. Consider the situation where the mixed-layer temperature exceeds the temperature of maximum density, the surface flux Q_s is negative, whereas the heat flux scale Q_* given by Eq. (2.61) is positive (this can take place if $-Q_s/I_s < 1$). A positive Q_* indicates the the mixed layer of depth h is statically stable. A negative Q_s, however, indicates that convective instability should take place, leading to the development of a convectively mixed layer whose deepening is arrested by the solar radiation heating. The equilibrium depth h_c of such mixed

layer is given by (see e.g. *Mironov and Karlin* [1989])

$$Q_*(h_c) = Q_s + I_s + I(h_c) - 2h_c^{-1}\int_0^{h_c} I(z)dz = 0. \tag{2.67}$$

This regime of convection is encountered on calm sunny days. If the wind suddenly ceases, Eq. (2.66) predicts a very shallow stably-stratified equilibrium mixed layer to which the mixed layer of depth $h > h_e$ should relax. In fact, however, the mixed layer would relax towards a convectively mixed layer whose equilibrium depth is given by Eq. (2.67). In order to account for this constraint, we require that $h_e \geq h_c$ if $Q_*(h) > 0$ and $\theta_s > \theta_r$.

2.4.3 The Water–Bottom Sediment Interaction

Parameterization of the Temperature Profile and the Heat Budget We adopt the following two-layer parametric representation, of the evolving temperature profile in the thermally active layer of bottom sediments proposed by *Golosov et al.* [1998]:

$$\theta = \begin{cases} \theta_b - [\theta_b - \theta_H]\,\Phi_{B1}(\zeta_{B1}) & \text{at} \quad D \leq z \leq H \\ \theta_H - [\theta_H - \theta_L]\,\Phi_{B2}(\zeta_{B2}) & \text{at} \quad H \leq z \leq L, \end{cases} \tag{2.68}$$

Where, θ_L is the (constant) temperature at the outer edge $z = L$ of the thermally active layer of the sediments, θ_H is the temperature at the depth H where the vertical temperature gradient is zero, and $\Phi_{B1} \equiv (\theta_b - \theta)/(\theta_b - \theta_H)$ and $\Phi_{B2} \equiv (\theta_H - \theta)/(\theta_H - \theta_L)$ are dimensionless functions of dimensionless depths $\zeta_{B1} \equiv (z - D)/(H - D)$ and $\zeta_{B2} \equiv (z - H)/(L - H)$, respectively.
The parameterization (2.68) should satisfy the heat transfer equation (2.53), where the heat flux Q is due to molecular heat conduction and the bottom sediments are opaque to radiation. Integrating Eq. (2.53) over z from $z = D$ to $z = H$ with due regard for Eq. (2.68), we obtain

$$\frac{d}{dt}\left[(H - D)\theta_b - C_{B1}(H - D)(\theta_b - \theta_H)\right] - \theta_H\frac{dH}{dt} = \frac{1}{\rho_w c_w}\left[Q_b + I(D)\right], \tag{2.69}$$

where the heat flux at $z = H$ is zero by virtue of the zero temperature gradient there.
Integrating Eq. (2.53) over z from $z = H$ to $z = L$, we obtain

$$\frac{d}{dt}\left[(L - H)\theta_H - C_{B2}(L - H)(\theta_H - \theta_L)\right] + \theta_H\frac{dH}{dt} = 0, \tag{2.70}$$

where the heat flux at $z = L$ (the geothermal heat flux) is neglected.
The shape factors C_{B1} and C_{B2} are given by

$$C_{B1} = \int_0^1 \Phi_{B1}(\zeta_{B1})d\zeta_{B1}, \qquad C_{B2} = \int_0^1 \Phi_{B2}(\zeta_{B2})d\zeta_{B2}. \tag{2.71}$$

Heat Flux through the Bottom The bottom heat flux Q_b is due to molecular heat conduction through the uppermost layer of bottom sediments. It can be estimated as the product of the negative of the temperature gradient at $z = D + 0$ and the molecular heat conductivity. The uppermost layer of bottom sediments is saturated with water. Its water content typically exceeds 90% and its physical properties, including the heat conductivity, are very close to the properties of the lake water. Then, the heat flux through the lake bottom is given by

$$Q_b = -\kappa_w\frac{\theta_H - \theta_b}{H - D}\Phi'_{B1}(0), \tag{2.72}$$

where κ_w is the molecular heat conductivity of water. This relation closes the problem.

It should be stressed that Eqs. (2.69), (2.70) and (2.72) do not contain the molecular heat conductivity of bottom sediments, a quantity that is rarely known to a satisfactory degree of precision. It is through the use of the integral (bulk) approach, based on the parameterization (2.68) of the temperature profile, that the molecular heat conductivity of bottom sediments is no longer needed.

2.4.4 Ice and Snow Cover

In this section, a two-layer thermodynamic (no rheology) model of the ice and snow cover is described. It is based on a self-similar parametric representation of the temperature profile within ice and snow and on the integral heat budgets of the ice and snow layers. The approach is, therefore, conceptually similar to the approach used above to describe the temperature structure of the mixed layer, of the lake thermocline, and of the thermally active layer of bottom sediments. Notice that the assumption about the shape of the temperature profile within the ice, the simplest of which is the linear profile, is either explicit or implicit in a number of ice models developed to date. A model of ice growth based on a linear temperature distribution was proposed by Stefan as early as 1891.

Parameterization of the Temperature Profile and the Heat Budget We adopt the following parametric representation of the evolving temperature profile within ice and snow:

$$\theta = \begin{cases} \theta_f - [\theta_f - \theta_I]\Phi_I(\zeta_I) & \text{at} \quad -H_I \le z \le 0 \\ \theta_I - [\theta_I - \theta_S]\Phi_S(\zeta_S) & \text{at} \quad -[H_I + H_S] \le z \le -H_I. \end{cases} \tag{2.73}$$

Here, z is the vertical co-ordinate (positive downward) with the origin at the ice-water interface, H_I is the ice thickness, H_S is the thickness of snow overlaying the ice, θ_f is the fresh-water freezing point, θ_I is the temperature at the snow-ice interface, and θ_S is the temperature at the air-snow interface. Notice that the freezing point of salt water is a decreasing function of salinity. A model that accounts for this dependence and is applicable to the ice over salt lakes or seas is presented by *Mironov and Ritter* [2004]. Dimensionless universal functions $\Phi_I \equiv (\theta_f - \theta)/(\theta_f - \theta_I)$ and $\Phi_S \equiv (\theta_I - \theta)/(\theta_I - \theta_S)$ of dimensionless depths $\zeta_I \equiv -z/H_I$ and $\zeta_S \equiv -(z + H_I)/H_S$, respectively, satisfy the boundary conditions $\Phi_I(0) = 0$, $\Phi_I(1) = 1$, $\Phi_S(0) = 0$, and $\Phi_S(1) = 1$.

According to Eq. (2.73), the heat fluxes through the ice, Q_I, and through the snow, Q_S, due to molecular heat conduction are given by

$$Q_I = -\kappa_i \frac{\theta_f - \theta_I}{H_I} \frac{d\Phi_I}{d\zeta_I}, \qquad Q_S = -\kappa_s \frac{\theta_I - \theta_S}{H_S} \frac{d\Phi_S}{d\zeta_S}, \tag{2.74}$$

where κ_i and κ_s are the heat conductivities of ice and snow, respectively.

The parameterization of the temperature profile (2.73) should satisfy the heat transfer equation (2.53). Integrating Eq. (2.53) over z from the air-snow interface $z = -(H_I + H_S)$ to just above the ice-water interface $z = -0$ with due regard for the parameterization (2.73), we obtain the equation of the heat budget of the snow-ice cover,

$$\frac{d}{dt}\{\rho_i c_i H_I [\theta_f - C_I(\theta_f - \theta_I)] + \rho_s c_s H_S [\theta_I - C_S(\theta_I - \theta_S)]\} - \rho_s c_s \theta_S \frac{d}{dt}(H_I + H_S) =$$

$$Q_s + I_s - I(0) + \kappa_i \frac{\theta_f - \theta_I}{H_I} \Phi_I'(0). \tag{2.75}$$

Here, ρ_i and ρ_s are the densities of ice and of snow, respectively, c_i and c_s are specific heats of these media, and Q_s and I_s are the values of Q and I, respectively, at the air-snow or, if snow is absent, at the air-ice

interface. The radiation heat flux I_s that penetrates into the interior of snow-ice cover is the surface value of the incident solar radiation flux from the atmosphere multiplied by $1-\alpha_i$, α_i being the albedo of the ice or snow surface with respect to solar radiation. The dimensionless parameters C_I and C_S, the shape factors, are given by

$$C_I = \int_0^1 \Phi_I(\zeta_I)d\zeta_I, \qquad C_S = \int_0^1 \Phi_S(\zeta_S)d\zeta_S. \tag{2.76}$$

The heat flux at the snow-ice interface is assumed to be continuous, that is

$$-\kappa_i \frac{\theta_f - \theta_I}{H_I}\Phi_I'(1) = -\kappa_s \frac{\theta_I - \theta_S}{H_S}\Phi_S'(0). \tag{2.77}$$

Equations (2.75) and (2.77) serve to determine temperatures at the air-snow and at the snow-ice interfaces, when these temperatures are below the freezing point, i.e. when no melting at the snow surface (ice surface, when snow is absent) takes place. During the snow (ice) melting from above, the temperatures θ_S and θ_I remain equal to the freezing point θ_f, and the heat fluxes Q_S and Q_I are zero.

Snow and Ice Thickness The equations governing the evolution of the snow thickness and of the ice thickness are derived from the heat transfer equation (2.53) that incorporates an additional term on its right-hand side, namely, the term $f_M(z)L_f dM/dt$ that describes the rate of heat release/consumption due to accretion/melting of snow and ice. Here, M is the mass of snow or ice per unit area, L_f is the latent heat of fusion, and $f_M(z)$ is a function that satisfies the normalization conditions $\int_{H_I}^{H_I+H_S} f_M(z)dz = 1$ and $\int_0^{H_I} f_M(z)dz = 1$ for snow and ice, respectively.

The accumulation of snow is not computed within the ice-snow model. The rate of snow accumulation is assumed to be a known time-dependent quantity that is provided by the atmospheric model or is known from observations. Then, the evolution of the snow thickness during the snow accumulation and no melting is computed from

$$\frac{d\rho_s H_S}{dt} = \left(\frac{dM_S}{dt}\right)_a, \tag{2.78}$$

where $M_S = \rho_s H_S$ is the snow mass per unit area, and $(dM_S/dt)_a$ is the (given) rate of snow accumulation. When the temperature θ_I at the upper surface of the ice is below the freezing point θ_f, the heat conduction through the ice causes the ice growth. This growth is accompanied by a release of heat at the lower surface of the ice that occurs at a rate $L_f dM_I/dt$, where $M_I = \rho_i H_I$ is the ice mass per unit area. The normalization function f_M is equal to zero throughout the snow-ice cover except at the ice-water interface where $f_M = \delta(0)$, $\delta(z)$ being the Dirac delta function. Integrating Eq. (2.53) from $z = -0$ to $z = +0$ with due regard for this heat release yields the equation for the ice thickness. It reads

$$L_f \frac{d\rho_i H_I}{dt} = Q_w + \kappa_i \frac{\theta_f - \theta_I}{H_I}\Phi_I'(0), \tag{2.79}$$

where Q_w is the heat flux in the near-surface water layer just beneath the ice. If the r.h.s. of Eq. (2.79) is negative, i.e. the negative of the heat flux in the water, Q_w, exceeds the negative of the heat flux in the ice, $Q_I|_{z=0}$, ice ablation takes place.

As the atmosphere heats the snow surface, the surface temperature eventually reaches the freezing point and the snow and ice melting sets in. This process is accompanied by a consumption of heat at rates $L_f d\rho_s H_S/dt$ and $L_f d\rho_i H_I/dt$ for snow and ice, respectively. Notice that the exact form of the normalization function f_M is not required by virtue of the normalization conditions considered above. Integrating Eq. (2.53) from $z = -(H_I + H_S) - 0$ to $z = -H_I$ with due regard for the heat loss due to snow melting and adding the (given) rate of snow accumulation yields the equation for the snow thickness,

$$L_f \frac{d\rho_s H_S}{dt} = -(Q_s + I_s) + I(-H_I) + L_f \left(\frac{dM_S}{dt}\right)_a + c_s \theta_f H_S \frac{d\rho_s}{dt}. \tag{2.80}$$

Integrating Eq. (2.53) from $z = -H_I$ to $z = +0$ with due regard for the heat loss due to ice melting yields the equation for the ice thickness,

$$L_f \frac{d\rho_i H_I}{dt} = Q_w + I(0) - I(-H_I). \tag{2.81}$$

If the ice melts out earlier than snow, the snow depth is instantaneously set to zero.

The Temperature Profile beneath the Ice The simplest assumption is to keep the temperature profile unchanged over the entire period of ice cover. This assumption is fair for deep lakes, where the heat flux through the bottom is negligibly small. In shallow lakes, this assumption may lead to an underestimation of the mean temperature. The heat accumulated in the thermally active upper layer of bottom sediments during spring and summer is returned back to the water column during winter, leading to an increase of the water temperature under the ice. The water temperature under the ice can also increase due to heating by solar radiation penetrating down through the ice. The thermodynamic regimes encountered in ice-covered lakes are many and varied. Their detailed description requires a set of sophisticated parameterizations. The use of such parameterizations in the framework of the present lake model is, however, hardly justified. The point is that it is the snow (ice) surface temperature that communicates information to the atmosphere, the water temperature is not directly felt by the atmospheric surface layer. It is, therefore, not vital that the temperature regimes in ice-covered lakes be described in great detail. Only their most salient features should be accounted for, first of all, the heat budget of the water column.

When the lake is ice-covered, the temperature at the ice-water interface is fixed at the freezing point $\theta_s = \theta_f$. In case the bottom temperature is less than the temperature of maximum density, $\theta_b < \theta_r$, the mixed-layer depth and the shape factor are kept unchanged, $dh/dt = 0$ and $dC_\theta/dt = 0$, the mean temperature $\overline{\theta}$ is computed from Eq. (2.54) and the bottom temperature θ_b is computed from Eq. (2.51). If the entire water column appears to be mixed at the moment of freezing, i.e. $h = D$ and $\theta_s = \overline{\theta} = \theta_b$, the mixed layer depth is reset to zero, $h = 0$, and the shape factor is set to its minimum value, $C_\theta = 0.5$ (see Section 2.4.5).

The heat flux from water to ice is estimated from

$$Q_w = -\kappa_w \frac{\theta_b - \theta_s}{D}, \tag{2.82}$$

if $h = 0$, and $Q_w = 0$ otherwise. Notice that the estimate of Q_w given by Eq. (2.82) and the shape factor $C_\theta = 0.5$ correspond to a linear temperature profile over the entire water column. A linear profile is encountered in ice-covered shallow lakes when $\theta_b < \theta_r$ and the heat flux is from the bottom sediments to the lake water.

As the bottom temperature reaches the temperature of maximum density, convection due to bottom heating sets in. To describe this regime of convection in detail, a convectively mixed layer whose temperature is close to θ_r, and a thin layer adjacent to the bottom, where the temperature decreases sharply from $\theta_b > \theta_r$ to θ_r, should be thoroughly considered. We neglect these peculiarities of convection due to bottom heating and adopt a simpler model where the bottom temperature is fixed at the temperature of maximum density, $\theta_b = \theta_r$. The mean temperature $\overline{\theta}$ is computed from Eq. (2.54). If $h > 0$, the shape factor C_θ is kept unchanged, and the mixed-layer depth is computed from Eq. (2.51). As the mixed-layer depth approaches zero, Eq. (2.51) is used to compute the shape factor C_θ that in this regime would increase towards its maximum value C_θ^{max}. The heat flux from water to ice is estimated from

$$Q_w = -\kappa_w \frac{\theta_b - \theta_s}{D} \max\left[1, \Phi'_\theta(0)\right], \tag{2.83}$$

if $h = 0$, and $Q_w = 0$ otherwise.

One more regime of convection is often encountered in ice-covered lakes. In late spring, the snow overlying the ice vanishes and solar radiation penetrates down through the ice. As the mixed-layer temperature is below that of maximum density, the volumetric radiation heating leads to de-stabilisation of the water column and thereby drives convective motions. Such regime of convection was analysed by *Farmer* [1975], *Mironov and Terzhevik* [2000], *Mironov et al.* [2002], and *Jonas et al.* [2003], among others. A parameterization of convection due to solar heating (e.g. a parameterization based on a bulk model developed by *Mironov et al.* [2002]) can, in principle, be incorporated into the present model. We do not do so, however, considering that the major effect of convection beneath the ice is to redistribute heat in the vertical and that it takes place over a limited period of time.

2.4.5 Empirical Relations and Model Constants

The Shape Functions

We adopt the following polynomial approximation of the shape function $\Phi_\theta(\zeta)$ with respect to the temperature profile in the thermocline:

$$\Phi_\theta = \left(\frac{40}{3}C_\theta - \frac{20}{3}\right)\zeta + (18 - 30C_\theta)\,\zeta^2 + (20C_\theta - 12)\,\zeta^3 + \left(\frac{5}{3} - \frac{10}{3}C_\theta\right)\zeta^4. \tag{2.84}$$

The shape factor C_θ is computed from

$$\frac{dC_\theta}{dt} = \text{sign}(dh/dt)\frac{C_\theta^{max} - C_\theta^{min}}{t_{rc}}, \qquad C_\theta^{min} \le C_\theta \le C_\theta^{max}, \tag{2.85}$$

where t_{rc} is the relaxation time scale, and sign is the signum function, sign(x)=-1 if $x \le 0$ and sign(x)=1 if $x > 0$. The minimum and maximum values of the shape factor are set to $C_\theta^{min} = 0.5$ and $C_\theta^{max} = 0.8$. During the mixed-layer deepening, $dh/dt > 0$, the temperature profile evolves towards the limiting curve, characterised by a maximum value of the shape factor, $C_\theta^{max} = 0.8$, and the maximum value of the dimensionless temperature gradient at the upper boundary of the thermocline, $\Phi'_\theta(0) = 4$. During the mixed-layer stationary state or retreat, $dh/dt \le 0$, the temperature profile evolves towards the other limiting curve, characterised by a minimum value of the shape factor, $C_\theta^{min} = 0.5$, and the zero temperature gradient at the upper boundary of the thermocline, $\Phi'_\theta(0) = 0$. Notice that $C_\theta^{min} = 0.5$ is consistent with a linear temperature profile that is assumed to occur under the ice when the bottom temperature is less than the temperature of maximum density (see Section 2.4.4).

According to Eq. (2.84), the dimensionless parameter $C_{\theta\theta}$ defined through Eq. (2.59) is given by

$$C_{\theta\theta} = \frac{11}{18}C_\theta - \frac{7}{45}. \tag{2.86}$$

The relaxation time t_{rc} is estimated from the following arguments. The time t_{rc} is basically the time of the evolution of the temperature profile in the thermocline from one limiting curve to the other, following the change of sign in dh/dt. Then, a reasonable scale for t_{rc} is the thermal diffusion time through the thermocline, that is a square of the thermocline thickness, $(D-h)^2$, over a characteristic eddy temperature conductivity, K_{H*}. Using a mean-square buoyancy frequency in the thermocline, $\overline{N} = \left[(D-h)^{-1}\int_h^D N^2 dz\right]^{1/2}$, as an estimate of N and assuming that the TKE in the thermocline scales either on the convective velocity w_*, Eq. (2.62), or on the surface friction velocity u_*, we propose (see *Mironov* [2008] for details)

$$t_{rc} = \frac{(D-h)^2\overline{N}}{C_{rc}u_T^2}, \qquad u_T = \max(w_*, u_*), \tag{2.87}$$

where C_{rc} is a dimensionless constant estimated at 0.003 (this value may be altered as new information becomes available).

We adopt the following polynomial approximations of the shape functions $\Phi_{B1}(\zeta_{B1})$ and $\Phi_{B2}(\zeta_{B2})$ with respect to the temperature profile in bottom sediments (cf. *Golosov et al.* [1998]):

$$\Phi_{B1} = 2\zeta_{B1} - \zeta_{B1}^2, \qquad \Phi_{B2} = 6\zeta_{B2}^2 - 8\zeta_{B2}^3 + 3\zeta_{B2}^4. \tag{2.88}$$

which are the simplest polynomials that satisfy a minimum set of constraints. The conditions $\Phi_{B1}(0) = \Phi_{B2}(0) = 0$ and $\Phi_{B1}(1) = \Phi_{B2}(1) = 1$ follow from the definition of ζ_{B1}, ζ_{B2}, Φ_{B1}, and Φ_{B2}. The conditions $\Phi'_{B1}(1) = \Phi'_{B2}(0) = \Phi'_{B2}(1) = 0$ provide a zero temperature gradient at the depths $z = H$ and $z = L$, and the condition $\Phi''_{B2}(1) = 0$ follows from the requirement that the temperature θ_L at the outer edge $z = L$ of the thermally active layer of the sediments is constant in time. The shape factors that correspond to Eq. (2.88) are $C_{B1} = 2/3$ and $C_{B2} = 3/5$.

As a zero-order approximation, the simplest linear temperature profile within snow and ice can be assumed, $\Phi_S(\zeta_S) = \zeta_S$ and $\Phi_I(\zeta_I) = \zeta_I$. This gives $C_S = C_I = 1/2$. Although a linear profile is a good approximation for thin ice, it is likely to result in a too thick ice in cold regions, where the ice growth takes place over a long period, and in a too high thermal inertia of thick ice. A slightly more sophisticated approximation was developed by *Mironov and Ritter* [2004] who assumed that the ice thickness is limited by a certain maximum value H_I^{max} and that the rate of ice growth approaches zero as H_I approaches H_I^{max} (the snow layer over the ice was not considered). They proposed

$$\Phi_I = \left[1 - \frac{H_I}{H_I^{max}}\right]\zeta_I + \left[(2 - \Phi_{*I})\frac{H_I}{H_I^{max}}\right]\zeta_I^2 + \left[(\Phi_{*I} - 1)\frac{H_I}{H_I^{max}}\right]\zeta_I^3, \tag{2.89}$$

where Φ_{*I} is a dimensionless constant. The shape factor that corresponds to Eq. (2.89) is

$$C_I = \frac{1}{2} - \frac{1}{12}(1 + \Phi_{*I})\frac{H_I}{H_I^{max}}. \tag{2.90}$$

The physical meaning of the above expressions can be elucidated as follows. The relation $\Phi'_I(0) = 1 - H_I/H_I^{max}$ that follows from Eq. (2.89) ensures that the ice growth is quenched as the ice thickness approaches its maximum value. Equation (2.90) suggests that the shape factor C_I decreases with increasing ice thickness. A smaller C_I means a smaller relative thermal inertia of the ice layer of thickness H_I [the absolute thermal inertia is measured by the term $C_I H_I$ that enters the l.h.s. of Eq. (2.75)]. This is plausible as it is mostly the upper part of thick ice, not the entire ice layer, that effectively responds to external forcing. For use in the global numerical weather prediction model GME of the German Weather Service, *Mironov and Ritter* [2004] proposed an estimate of $H_I^{max} = 3$ m. This value is typical of the central Arctic in winter. The allowable values of Φ_{*I} lie in the range between -1 and 5. $\Phi_{*I} > 5$ yields an unphysical negative value of C_I as the ice thickness approaches H_I^{max}. $\Phi_{*I} < -1$ gives C_I that increases with increasing H_I. There is no formal proof that this may not occur, but it is very unlikely. A reasonable estimate is $\Phi_{*I} = 2$. With this estimate C_I is halved as H_I increases from 0 to H_I^{max}. Notice that the linear temperature profile is recovered as $H_I/H_I^{max} \ll 1$, i.e. when the ice is thin.

It should be stressed that, although the shape functions are useful in that they provide a continuous temperature profile trough the snow, ice, water and bottom sediments, their exact shapes are not required in the present model. It is not $\Phi_\theta(\zeta)$, $\Phi_{B1}(\zeta_{B1})$, $\Phi_{B2}(\zeta_{B2})$, $\Phi_S(\zeta_S)$ and $\Phi_I(\zeta_I)$ per se, but the shape factors C_θ, C_{B1}, C_{B2}, C_S and C_I, and the dimensionless gradients $\Phi'_\theta(0)$, $\Phi'_{B1}(0)$, $\Phi'_S(0)$, $\Phi'_I(0)$ and $\Phi'_I(1)$, that enter the model equations. The estimates of these parameters are summarised in Table 2.2.

Constants in the Equations for the Mixed-Layer Depth The estimates of $C_{c1} = 0.2$ and $C_{c2} = 0.8$ in Eq. (2.63) were recommended by *Zilitinkevich* [1991]. They were obtained using laboratory, atmospheric

and oceanic data. Apart from being commonly used in mixed-layer models of penetrative convection driven by the surface buoyancy flux, these values were successfully used by *Mironov and Karlin* [1989] to simulate day-time convection in the upper ocean that is driven by surface cooling but inhibited by radiation heating, and by *Mironov and Terzhevik* [2000] and *Mironov et al.* [2002] to simulate spring convection in ice-covered lakes where convective motions are driven by volumetric radiation heating of the water at temperature below the temperature of maximum density (*Mironov et al.* [2002] used $C_{c2} = 1.0$). A slightly modified estimate of $C_{c1} = 0.17$ was obtained by *Fedorovich et al.* [2004] from large-eddy simulation data. We adopt the estimates of $C_{c1} = 0.17$ and $C_{c2} = 1.0$ for use in the equation of convective entrainment.

For use in Eq. (2.66) for the equilibrium mixed-layer depth in stable or neutral stratification, we adopt the estimates of $C_n = 0.5$, $C_s = 10$ and $C_i = 20$ obtained by *Zilitinkevich and Mironov* [1996]. The estimates of C_s and C_i are based on a limited amount of data and may need to be slightly altered as new (and better) data become available. The estimate of C_n was corroborated by the results from further studies (*Zilitinkevich and Esau* [2002, 2003]) and is reliable.

The estimates of the dimensionless constant C_{rh} in the relaxation-type rate equation for the depth of a stably or neutrally stratified wind-mixed layer, Eqs. (2.64) and (2.65), are not abundant. *Kim* [1976] and *Deardorff* [1983] recommended that the value of $C_{rh} = 0.28$ be used to describe entrainment into a homogeneous fluid. The same value was used by *Zeman* [1979], and a slightly lower value of $C_{rh} = 0.26$ by *Zilitinkevich et al.* [1979]. The rate equations given by *Khakimov* [1976] and *Zilitinkevich et al.* [2002] use the reciprocal of the Coriolis parameter as the relaxation time scale. Their rate equations suggest the values of $C_{rh} = 0.45$ and $C_{rh} = 0.5$, respectively. A similar form of the rate equation was proposed earlier by *Deardorff* [1971] who used a much lower value of $C_{rh} = 0.025$. We adopt an estimate of $C_{rh} = 0.03$ suggested by the sensitivity experiments with the present lake model (keeping in mind that this value may need to be altered).

The estimates of dimensionless constants in the equations for the mixed-layer depth are summarised in Table 2.2.

Thermodynamic Parameters The exponential approximation of the decay law for the flux of solar radiation is commonly used in applications. It reads

$$I(t,z) = I_s(t) \sum_{k=1}^{n} a_k \exp[-\gamma_k(z + H_S + H_I)], \tag{2.91}$$

where I_s is the surface value of the solar radiation heat flux multiplied by $1 - \alpha$, α being the albedo of the water, ice or snow surface with respect to solar radiation, n is the number of wavelength bands, a_k are fractions of the total radiation flux for different wavelength bands, and $\gamma_k(z)$ are attenuation coefficients for different bands. The attenuation coefficients are piece-wise constant functions of height, i.e. they have different values for water, ice and snow but remain depth-constant within these media. The optical characteristics of water are lake-specific and should be estimated in every particular case. Rough estimates of a_k and γ_k for ice and snow are given by *Launiainen and Cheng* [1998].

The lake model includes a number of thermodynamic parameters. They are summarised in Table 2.3. These thermodynamic parameters can be considered constant except for the snow density and the snow heat conductivity that depend, among other things, on the snow thickness and the snow age. As a first approximation, the following empirical formulations (*Heise et al.* [2003]) can be used that relate ρ_s and κ_s to the snow thickness:

$$\rho_s = \min\left\{\rho_s^{max}, |1 - H_S\Gamma_{\rho_s}/\rho_w|^{-1}\,\rho_s^{min}\right\}, \tag{2.92}$$

where $\rho_s^{min} = 100$ kg·m^{-3} and $\rho_s^{max} = 400$ kg·m^{-3} are minimum and maximum values, respectively, of the snow density, and $\Gamma_{\rho_s} = 200$ kg·m^{-4} is an empirical parameter, and

$$\kappa_s = \min\left\{\kappa_s^{max}, \kappa_s^{min} + H_S \Gamma_{\kappa_s} \rho_s / \rho_w\right\}, \tag{2.93}$$

where $\kappa_s^{min} = 0.2$ J·m^{-1}·s^{-1}·K^{-1} and $\kappa_s^{max} = 1.5$ J·m^{-1}·s^{-1}·K^{-1} are minimum and maximum values, respectively, of the snow heat conductivity, and $\Gamma_{\kappa_s} = 1.3$ J·m^{-2}·s^{-1}·K^{-1} is an empirical parameter.

2.4.6 Conclusions

A lake model suitable to predict the vertical temperature structure in lakes of various depths on time scales from a few hours to many years is developed. The model, termed FLake, is based on a two-layer parametric representation of the evolving temperature profile and on the integral budget of energy for the layers in question. The structure of the stratified layer between the upper mixed layer and the basin bottom, the lake thermocline, is described using the concept of self-similarity (assumed shape) of the temperature-depth curve. The same concept is used to describe the temperature structure of the thermally active upper layer of bottom sediments and of the ice and snow cover. An entrainment equation is used to compute the depth of a convectively-mixed layer. A relaxation-type equation is used to compute the wind-mixed layer depth in stable and neutral stratification, where a multi-limit formulation for the equilibrium mixed-layer depth accounts for the effects of the earth's rotation, of the surface buoyancy flux, and of the static stability in the thermocline. Both mixing regimes are treated with due regard for the volumetric character of solar radiation heating. Simple thermodynamic arguments are invoked to develop the evolution equations for the ice and snow depths. Using the integral (bulk) approach, the problem of solving partial differential equations (in depth and time) for the temperature and turbulence quantities is reduced to solving ordinary differential equations for the time-dependent parameters that specify the evolving temperature profile. The result is a computationally efficient lake model that incorporates much of the essential physics.

It must be emphasised that the empirical constants and parameters of FLake are not application-specific. That is, once they have been estimated using independent empirical and numerical data, they should not be re-evaluated when the model is applied to a particular lake. There are, of course, lake-specific external parameters, such as depth to the bottom and optical characteristics of water, but these are not part of the model physics. In this way FLake does not require "re-tuning", a procedure that may improve an agreement with a limited amount of data and is sometimes justified. This procedure should, however, be considered as a bad practice and must be avoided whenever possible as it greatly reduces the predictive capacity of a physical model (*Randall and Wielicki* [1997]).

Apart from the depth to the bottom and the optical characteristics of lake water, the only lake-specific parameters are the depth L of the thermally active layer of bottom sediments and the temperature θ_L at that depth. These parameters should be estimated only once for each lake, using observational data or empirical recipes (e.g. *Fang and Stefan* [1998]). In a similar way, the temperature at the bottom of the thermally active soil layer and the depth of that layer are estimated once and then used in an NWP model as two-dimensional external-parameter arrays.

The proposed lake model is intended for use, first of all, in NWP and climate models as a module (parameterization scheme) to predict the lake surface temperature. Apart from NWP and climate modelling, practical applications where simple bulk models are favoured over more accurate but more sophisticated models (e.g. second-order turbulence closures) include modelling aquatic ecosystems. For ecosystem modelling, a sophisticated physical module is most often not required because of insufficient knowledge of chemistry and biology.

Appendix. A Summary of Model Parameters

Table 2.2: Empirical Constants and Parameters

Constant/ Parameter	Recommended Value/ Computed from	Comments
C_{c1}	0.17	
C_{c2}	1.0	
C_n	0.5	
C_s	10	
C_i	20	
C_{rh}	0.03	
C_{rc}	0.003	
C_θ	Eq. (2.85)	
C_θ^{min}	0.5	
C_θ^{max}	0.8	
$C_{\theta\theta}$	Eq. (2.86)	
C_Q	$2C_{\theta\theta}/C_\theta$	
C_{B1}	2/3	
C_{B2}	3/5	
C_I	1/2	Optionally Eq. (2.90)
C_S	1/2	
$\Phi'_\theta(0)$	Eqs. (2.84) and (2.85)	
$\Phi'_{B1}(0)$	2	
$\Phi'_I(0)$	1	Optionally Eq. (2.89)
$\Phi'_I(1)$	1	Optionally Eq. (2.89)
$\Phi'_S(0)$	1	
Φ_{*I}	2	
H_I^{max}	3 m	

Table 2.3: Thermodynamic Parameters

Notation	Parameter	Dimensions	Estimate/ Computed from
g	Acceleration due to gravity	$\mathrm{m{\cdot}s^{-2}}$	9.81
θ_r	Temperature of maximum density of fresh water	K	277.13
θ_f	Fresh water freezing point	K	273.15
a_T	Coefficient in the fresh-water equation of state	$\mathrm{K^{-2}}$	$1.6509 \cdot 10^{-5}$
ρ_w	Density of fresh water	$\mathrm{kg{\cdot}m^{-3}}$	Eq. (2.48)
ρ_r	Maximum density of fresh water	$\mathrm{kg{\cdot}m^{-3}}$	$1.0 \cdot 10^3$
ρ_i	Density of ice	$\mathrm{kg{\cdot}m^{-3}}$	$9.1 \cdot 10^2$
ρ_s	Density of snow	$\mathrm{kg{\cdot}m^{-3}}$	Eq. (2.92)
L_f	Latent heat of fusion	$\mathrm{J{\cdot}kg^{-1}}$	$3.3 \cdot 10^5$
c_w	Specific heat of water	$\mathrm{J{\cdot}kg^{-1}{\cdot}K^{-1}}$	$4.2 \cdot 10^3$
c_i	Specific heat of ice	$\mathrm{J{\cdot}kg^{-1}{\cdot}K^{-1}}$	$2.1 \cdot 10^3$
c_s	Specific heat of snow	$\mathrm{J{\cdot}kg^{-1}{\cdot}K^{-1}}$	$2.1 \cdot 10^3$
κ_w	Molecular heat conductivity of water	$\mathrm{J{\cdot}m^{-1}{\cdot}s^{-1}{\cdot}K^{-1}}$	$5.46 \cdot 10^{-1}$
κ_i	Molecular heat conductivity of ice	$\mathrm{J{\cdot}m^{-1}{\cdot}s^{-1}{\cdot}K^{-1}}$	2.29
κ_s	Molecular heat conductivity of snow	$\mathrm{J{\cdot}m^{-1}{\cdot}s^{-1}{\cdot}K^{-1}}$	Eq. (2.93)

Chapter 3

Urban and artificial areas

Contents

3.1 Introduction

Due to the complexity and diversity of towns around the world, conclusions drawn from experimental studies on the interaction between the atmosphere and urbanized areas most of the time are limited either to a particular site or physical processes. To overcome this problem, numerical studies are aimed to simulate the urban climatology or energy budget. However, they still follow some simplified approaches.

Building-resolving models - i.e. models in which individual building shapes are described - allow the detailed examination of some processes (radiative effects see for e.g. *Terjung et al.* [1980], or wind channeling), but because of computational cost, applications are limited to local urbanization and comfort studies. Simpler building-averaged models have also been developed. The most famous is the 'canyon' model, from Oke and colleagues developed during the seventies, dedicated to urban streets: a road is bordered by two facing building walls. Several numerical models are built using the canyon geometry (*Johnson et al.* [1991], *Mills* [1993], *Arnfield et al.* [1998]) to study radiative trapping, surface energy budgets (using multiple facets for each surface) or wind in the canyon.

The two model types presented above are used in urban climatology in order to understand town energetics. The next modelling step is to perform a coupling between the urban surface and the atmosphere in mesoscale atmospheric models. The most common way to do this is to use a vegetation-atmosphere transfer model whose parameters have been modified (*Seaman et al.* [1989], *Menut* [1997]), as opposed to an urban model. Cities are then modeled as bare soil or a concrete plate. The roughness length is often large (one to a few meters, see *Wieringa* [1993] or *Petersen* [1997]). The soil moisture availability (or the soil depth) is reduced, so that the Bowen ratio is shifted towards high values (large sensible heat flux). The most recent works tend to simulate other factors, such as heat storage, by the use of a concrete canopy above the surface. A horizontal plate is in radiative interaction with the surface in *Best* [1998], and the treatment is similar to a forest canopy in *Soux et al.* [1998]. The *Taha* [1999] mesoscale study uses a semi-empirical formulation for the heat storage flux - the Objective Hysteresis Model by *Grimmond et al.* [1991a].

This shows the gap between the state of the art in urban climatology and its parameterization in atmospheric models. The objective of the present paper is to present an urban model which links the climatologists approach of city representation to an atmospheric model.
The Town Energy Budget (TEB) scheme is built following the canyon approach, generalized in order to represent larger horizontal scales. The physics treated by the scheme is relatively complete. Due to the complex shape of the city surface, the urban energy budget is split into different parts: **three** surface energy budgets are considered: one for the roofs, roads, and walls. Orientation effects are averaged for roads and walls. Up to two energy budgets are added for snow when it is present on roofs or roads. Some of the physics were derived from the literature (long wave radiation or thermal conduction through the surfaces), since they are classically assumed to estimate temperatures in conditions without feedback towards the atmosphere (during nights with calm wind). However, most parts of the physics need an original approach (short wave radiation, thermodynamical and anthropogenic flux treatment, rain and snow), since they occur when interaction with the atmosphere is strong.

3.2 Presentation of the Town Energy Budget scheme

3.2.1 Objectives

The TEB model is aimed to simulate the turbulent fluxes into the atmosphere at the surface of a mesoscale atmospheric model which is covered by buildings, roads, or any artificial material. It should parameterize both the urban surface and the roughness sublayer, so that the atmospheric model only 'sees' a constant flux layer as its lower boundary.
It must be considered as a part of the surface parameterization of the atmospheric model. The fluxes should be computed for each land occupation type by the appropriate scheme, and then averaged in the atmospheric

model grid mesh, with respect to the proportion occupied by each type. For example, a partition should be: (1) sea; (2) inland water; (3) natural and cultivated terrestrial surface; (4) towns. The following fluxes are calculated: latent and sensible heat fluxes (W m^{-2}), upward radiative fluxes (W m^{-2}) and momentum fluxes along the axes of the model (m^2 s^{-2}).

3.2.2 Town geometry description

Numerous fine-scale studies on building climatology exist. In those, several individual buildings are usually present in order to study their radiative interaction, the wind channeling effects, or the building insulation. The **canyon** concept, developed by city climatologists (e.g. *Oke* [1987]), uses such a framework: it considers a single road, bordered by facing buildings. In these studies, models are, at best, forced by atmospheric data (radiation, wind above the roofs) but are not in interaction with it.
The TEB model is aimed to parameterize town-atmosphere dynamic and thermodynamic interactions. It is applicable for mesoscale atmospheric models (a grid mesh larger than a few hundred meters). Then, spatial averaging of the town characteristics as well as its effect on the atmosphere, are necessary. The individual shapes of each building are no longer taken into account. The TEB geometry is based on the canyon hypothesis. However, a single canyon would be too restrictive at the considered horizontal scale.
We therefore use the following original city representation:

1. the buildings have the same height and width (in the model mesh). The roof level is at the surface level of the atmospheric model.

2. buildings are located along identical roads, the length of which is considered far greater than their width. The space contained between two facing buildings is defined as a canyon.

3. any road orientation is possible, and they all exist with the same probability. This hypothesis allows the computation of averaged forcing for road and wall surfaces. In other words, when the canyon orientation appears in a formula (with respect to the sun or the wind direction), it is averaged over 360°. In this way, no discretization is performed on the orientation.

These hypotheses, as well as the formulations chosen for the physics (see hereafter), allow the development of a relatively simple scheme. The parameters describing the city are displayed in Table 3.1, and the scheme variables can be found in Table 3.2.
The TEB model does not use one urban surface temperature (representative of the entire urban cover), but **three** surface temperatures, representative of roofs, roads and walls. There are two reasons for that:

- urban climatologists generally consider complex (non-flat) geometry cases, in particular the 'canyon' geometry. In order to be consistent with their findings, the TEB model uses a complex surface consisting of multiple explicit energy budgets.

- one spatially-averaged surface temperature is often used in soil-vegetation schemes, in order to compute the turbulent fluxes towards the atmosphere following the Monin-Obukhov similarity theory. However, over towns, the use of only one surface temperature is debatable, because it has been observed that the Monin-Obukhov similarity theory does not apply for temperature in the urban roughness sublayer.

The second point will be adressed in more detail in section 5.2.5. The parameters of the scheme depend directly on building shapes and construction materials. This makes the TEB scheme easy to initialize,

without the need for any atmospheric data for parameter tuning. Construction material characteristics can be found in the literature (e.g. see *Oke* [1988]).

One must separately treat road and walls, as they react differently to all the physical processes (sky viewing, thermal structure, source of heating inside the buildings, or the presence of water or snow on the road). In contrast, the sunlit and shadowed walls are not treated separately, as the two facing walls are identical for all processes, except one: the direct solar radiation. Note that the two walls behave similarly for the scattered solar radiation (i.e. in cloudy conditions). The problem is that it is not clear how to separate sunlit and shadowed walls. It would be easy if there was only one street direction, but at the town scale, this is not true, and streets parallel or perpendicular to the sun direction are found. To treat separately the walls according to illumination by the sun, would then necessitate a separate treatment for the street directions. A discretization for the streets should be performed at least every 45 or 30°, leading respectively to four or six energy budgets for roads, and twice as many for walls. Furthermore, the effect of the infra-red radiation non-linearities caused by a unique wall temperature is very small: supposing a canyon with a road width equal to the buildings height (leading to a sky-view factor for the walls of $\Psi_w = 0.3$, see section 3.2.6) and a wall emissivity of 0.85, the difference in the canyon top budget between two walls at 290 K or two walls at 280 and 300 K is only 1.5 W m^{-2}. Therefore, for sake of scheme simplicity, only one energy budget is chosen for the walls. Particular attention is still payed to the solar radiation budget, and the validation presented in section 3.2.7 shows it is accurate at canyon scale.

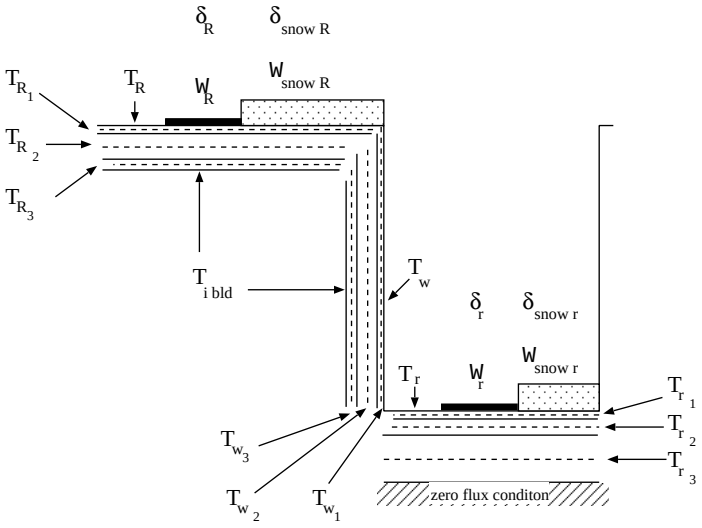

Figure 3.1: Canyon geometry in the TEB scheme ,and its prognostic variables.

3.2.3 Temperature evolution equations

As discussed above, the urban surface is very inhomogeneous with respect to shape and building materials. Urban climatologists need at least four surfaces to describe it: the roof, the road, and two facing walls. The problem considered here (the evaluation of the turbulent and radiative fluxes from the urban cover to the atmosphere) allows the treatment of only three types of surfaces (roof, road, wall), while keeping enough accuracy to correctly represent the different terms of the surface energy budget. This is why the TEB model uses **three** surface temperatures, T_R, T_r and T_w, representative of roofs, roads and walls, respectively.

Furthermore, in order to treat the conduction fluxes to or from the building interiors (roof, wall) or the ground (road), each surface type is discretized into several layers (Figure 3.1). Per convention, the layer with subscript 1 is the one in contact with the air (hereafter 'surface layer').
The equations describing the evolution of the temperatures of the layers (representative of the middle of the layer) are based on energy budget considerations.

The prognostic equations for the surface layers of the roof, wall and road respectively, read:

$$\begin{aligned}
C_{R_1}\frac{\partial T_{R_1}}{\partial t} = &\quad (1-\delta_{snowR}) && \frac{1}{d_{R_1}}\left(S^*_R + L^*_R - H_R - LE_R - G_{R_{1,2}}\right)\\
&\quad +\delta_{snowR} && \frac{1}{d_{R_1}}\left(G_{R_{snow,1}} - G_{R_{1,2}}\right)\\
C_{w_1}\frac{\partial T_{w_1}}{\partial t} = & && \frac{1}{d_{w_1}}\left(S^*_w + L^*_w - H_w - G_{w_{1,2}}\right)\\
C_{r_1}\frac{\partial T_{r_1}}{\partial t} = &\quad (1-\delta_{snowr}) && \frac{1}{d_{r_1}}\left(S^*_r + L^*_r - H_r - LE_r - G_{r_{1,2}}\right)\\
&\quad +\delta_{snowr} && \frac{1}{d_{r_1}}\left(G_{r_{snow,1}} - G_{r_{1,2}}\right)
\end{aligned}$$

These three equations can be written in a generic way:

$$C_{\star_1}\frac{\partial T_{\star_1}}{\partial t} = (1-\delta_{snow\star})\frac{1}{d_{\star_1}}\left(S^*_\star + L^*_\star - H_\star - LE_\star - G_{\star_{1,2}}\right) + \delta_{snow\star}\frac{1}{d_{\star_1}}\left(G_{\star_{snow,1}} - G_{\star_{1,2}}\right) \quad (3.1)$$

Where, the subscript $_\star$ stands either for $_R$, $_r$ or $_w$, describing roof, road and wall variables (only roof and road for water variables) respectively. This convention is used in the rest of this paper.
$T_{\star_k}$ is the temperature of the k^{ith} layer of the considered surface (in the above equations, $k = 1$). $C_{\star_k}$ represents the heat capacity, λ_k the thermal conductivity and $d_{\star_k}$ the layer thickness.
The fluxes $S^*_\star$, $L^*_\star$, $H_\star$, $LE_\star$, $G_{\star_{1,2}}$ and $G_{\star_{snow,1}}$ stand for net solar radiation, net infra-red radiation, sensible heat flux, latent heat flux, and conduction heat flux between surface layer and the underlying layer, conduction heat fluxes between the base of the snow mantel and the surface, respectively. $\delta_{snow\star}$ is the snow fraction on the surface (which is zero on the walls).
It is assumed that the surface layer of each surface is sufficiently thin such that the layer averaged temperature can be used to evaluate the radiative and turbulent surface fluxes. This means that the surface temperatures $T_\star$ are computed as:

$$T_\star = T_{\star_1}$$

For the sake of clarity, the $_1$ subscript will be removed in the next sections.

The other layer temperatures evolve according to a simple heat conduction equation. For the k^{ith} layer:

$$C_{\star_k}\frac{\partial T_{\star_k}}{\partial t} = \frac{1}{d_{\star_k}}\left(G_{\star_{k-1,k}} - G_{\star_{k,k+1}}\right) \quad (3.2)$$

In these equations, the conduction flux between layers k and $k+1$ reads (for $k < n$ where n is the number of layers):

$$G_{\star_{k,k+1}} = \overline{\lambda}_{k,k+1}\frac{T_{\star_k} - T_{\star_{k+1}}}{\frac{1}{2}(d_{\star_k} + d_{\star_{k+1}})} \quad (3.3)$$

with

$$\overline{\lambda}_{k,k+1} = \frac{d_{\star_k} + d_{\star_{k+1}}}{(d_{\star_k}/\lambda_k) + (d_{\star_{k+1}}/\lambda_{k+1})} \tag{3.4}$$

The lower boundary conditions for the roofs and walls are given by the building internal temperature, the road one being represented as a zero flux lower boundary. The fluxes between the n^{th} layer (the inner layer) and the underlying material are then:

$$G_{R_{n,n+1}} = \lambda_n \frac{T_{R_n} - T_{i_{bld}}}{\frac{1}{2}(d_{R_n})} \tag{3.5}$$

$$G_{w_{n,n+1}} = \lambda_n \frac{T_{w_n} - T_{i_{bld}}}{\frac{1}{2}(d_{w_n})} \tag{3.6}$$

$$G_{r_{n,n+1}} = 0 \tag{3.7}$$

Note that the number of layers for roof, wall and road can differ. In this study, three layers for each surface are chosen. Due to large temperature gradients which can exist, and because of the multi-layer structure of the walls or the roofs, it is recommended that at least 3 layers are used to represent each surface.

3.2.4 Water reservoirs evolution

Liquid or solid precipitation intercepted by urban surfaces is rarely addressed in the literature, except for sewer system and hydrological considerations. An exception is *Grimmond et al.* [1991b], however, in which the model used was initially dedicated to forest studies, and is limited to the water budget, computed from the Penman Monteith equation. They added anthropogenic water sources and used the *Grimmond et al.* [1991a] heat storage flux formulation.

Thanks to the presence of the surface temperatures in the TEB scheme, the saturation specific humidity, and then the turbulent latent heat flux can be computed more easily (see section 5.2.5).
The liquid precipitation is intercepted by both roofs and roads. There is runoff from roofs and roads to the sewer system. Roads and roofs can be covered by a certain amount of water, parameterized by the variables W_r and W_R, respectively. These surfaces are impervious. Then, instead of defining a relative humidity, it is more judicious to treat the fraction of surface covered by the water, δ_r and δ_R. This part is saturated (fractional water pools), while the other part is assumed to be dry. Water evaporates when the air humidity is not saturated until all water has disappeared from the impervious surface.
The snow-free fraction of the surface occupied by liquid water is computed as: $\delta_\star = (W_\star/W_{\star_{max}})^{\frac{2}{3}}$, (*Noilhan and Planton* [1989]), where $W_{\star_{max}}$ is the maximum water amount on the surface.

Furthermore, urban dew is taken into account (in case of negative latent heat flux), as its occurrence can have significant effects, as pointed out by *Richards* [1998]. It requires a special treatment: when conditions are present for dew to occur (air humidity larger than the surface saturation humidity), the surface is considered wet ($\delta_* = 1$). This allows then a (negative) latent heat flux, which can fill the interception reservoirs. These treatments are deduced from those for the foliage interception reservoirs in vegetation schemes (*Deardorff* [1978], *Noilhan et al.* [1989]).

Addition of an anthropogenic water source was not retained in TEB, because it does not compute evaporation over gardens or parks. Irrigation water input should be taken into account through the vegetation

scheme dedicated to these natural surfaces. However, anthropogenic fluxes of water vapor directly into the air exist in the scheme (see section 5.2.5), in order to represent factory release for example.

Finally, the water-reservoir evolution equation is (for roof or road):

$$\frac{\partial W_\star}{\partial t} = R - LE_\star/L_v \qquad (W_\star < W_{\star_{max}}) \tag{3.8}$$

where R is the rain rate (kg m^{-2} s^{-1}) and L_v is the latent heat of vaporization.
The reservoirs are of small capacity (the water in excess is lost as runoff). They are set equal to $W_{R_{max}}$=$W_{r_{max}}$=1 kg m^{-2}, which is well in the range of values explored by Grimmond and Oke (1991). The total depletion of the reservoirs by evaporation requires, in general, a few hours for daytime conditions.

3.2.5 Snow effects

Snow is intercepted by roofs and roads. A snow scheme is implemented on each surface type. Snow density, albedo, temperature and thickness of water equivalent depth are parameterized. Radiation, sensible heat flux, sublimation, conduction and melting are taken into account.
The evolution rate of snow albedo is enhanced (and its minimum value lowered) in order to represent car pollution (dirty snow). A time-dependent drainage term is included to take into account snow-plow work (if any).
The snow fraction on roof or road surfaces is set equal to a function of the snow interception reservoir (W_{snow*}): $\delta_{snow*} = (W_{snow*})/(W_{snow*} + W_{snow*max})$. The parameter $W_{snow*max}$ is set equal to 1 kg m^{-2}. The snow has an effect on:

- the energy budget of the surfaces (as part of the downward flux comes from the base of the snow),
- the heat fluxes from the road towards the canyon or from the roof towards the atmosphere,
- the radiative calculations for the canyon surfaces, because of the snow albedo, emissivity and temperature.

3.2.6 Longwave budget

The trapping of long-wave radiation by the canyon surfaces is computed with one re-emission taken into account (from the *Johnson et al.* [1991] formulation).
The sky-view factors are needed. They are computed for the TEB geometry (an infinite canyon) according to *Noilhan* [1981]:

$$\Psi_r = [(h/w)^2 + 1]^{1/2} - h/w \tag{3.9}$$

$$\Psi_w = \frac{1}{2}\{h/w + 1 - [(h/w)^2 + 1]^{1/2}\}/(h/w) \tag{3.10}$$

These factors represent the fraction of sky seen from the road and one wall respectively, compared to the sky fraction that a flat horizontal surface would see without obstruction. The sky-factor for the roof is then equal to 1. If the buildings are very low, Ψ_r tends to 1 and Ψ_w to 0.5 (one wall then sees one half of the sky). In this case, longwave radiative fluxes from the roads will be undisturbed by the walls. On the contrary, if the buildings are very tall, both sky factors tend to zero, and radiative exchanges will mostly occur between the walls, and less energy will escape towards the sky.

The net longwave radiation absorbed by the snow-free road and wall surfaces is given as:

$$\begin{array}{rcccl} L_r^* = & \epsilon_r \Psi_r L^{\downarrow} & - \epsilon_r \sigma T_r^4 & + & \epsilon_r \epsilon_w (1-\Psi_r) \sigma T_w^4 \\ + & \epsilon_r (1-\epsilon_w)(1-\Psi_r)\Psi_w L^{\downarrow} & & + & \epsilon_r \epsilon_w (1-\epsilon_w)(1-\Psi_r)(1-2\Psi_w)\sigma T_w^4 \\ + & \epsilon_r (1-\epsilon_w)(1-\Psi_r)\Psi_w \sigma \overline{\epsilon_r T_r^4} & & & \end{array} \tag{3.11}$$

$$\begin{array}{rcccl} L_w^* = & \epsilon_w \Psi_w L^{\downarrow} & - \epsilon_w \sigma T_w^4 & + & \epsilon_w \Psi_w \sigma \overline{\epsilon_r T_r^4} \\ + & \epsilon_w^2 (1-2\Psi_w)\sigma T_w^4 & & + & \epsilon_w (1-\overline{\epsilon_r})\Psi_w \Psi_r L^{\downarrow} \\ + & \epsilon_w (1-\epsilon_w)\Psi_w (1-2\Psi_w) L^{\downarrow} & & + & \epsilon_w^2 (1-\epsilon_w)(1-2\Psi_w)^2 \sigma T_w^4 \\ + & \epsilon_w^2 (1-\overline{\epsilon_r})\Psi_w (1-\Psi_r)\sigma T_w^4 & & + & \epsilon_w (1-\epsilon_w)\Psi_w (1-2\Psi_w)\sigma \overline{\epsilon_r T_r^4} \end{array} \tag{3.12}$$

Where:

$$\begin{array}{rll} \overline{\epsilon_r} & = (1-\delta_{snowr})\epsilon_r & + \delta_{snowr}\epsilon_{r_{snow}} \\ \overline{\epsilon_r T_r^4} & = (1-\delta_{snowr})\epsilon_r T_r^4 & + \delta_{snowr}\epsilon_{r_{snow}} T_{snow_r}^4 \end{array}$$

By inverting the snow-covered and snow-free road characteristics in Eq. 3.11, the longwave radiative budget on top of snow mantel can be defined. To deduce Eq.s 3.11 and 3.12, we used the fact that if Ψ_r represents the contribution of the sky to the road viewing, then $(1-\Psi_r)$ is the contribution of the two walls. For the budget of one wall, the sky-view factor is Ψ_w, the road view factor is Ψ_w (per symmetry), and the facing wall view factor is $(1-2\Psi_w)$.

3.2.7 Solar radiation

Direct solar radiation

Because of shadow effects, special computations are required to estimate the solar flux received either by the walls or the roads.

Let $S^{\Downarrow}$ be the direct solar radiation received by an **horizontal** surface at the first atmospheric model level. The roof surface receives this amount of radiation.

Let θ be the angle between the sun direction and the canyon axis, and λ be the solar zenith angle (from zenith). Let us first consider a road perpendicular to the sun direction ($\theta = \frac{\pi}{2}$, Figure 3.2). $\lambda_0 = \arctan(w/h)$ is defined as the zenith angle for which the sun begins to illuminate the road. It can be noted that whatever the sun position, one of the two walls is in shadow, the other one is (partially) in light.

The mean direct solar fluxes received by both walls and by the road, for a street direction perpendicular to the sun, are:

$$\begin{array}{rcl} S_w^{\Downarrow}(\theta = \frac{\pi}{2}) & = & \left\{ \begin{array}{ll} \frac{1}{2}\frac{w}{h} S^{\Downarrow} & if\ \lambda > \lambda_0 \\ \frac{1}{2}\tan(\lambda) S^{\Downarrow} & if\ \lambda < \lambda_0 \end{array} \right. \\ S_r^{\Downarrow}(\theta = \frac{\pi}{2}) & = & \left\{ \begin{array}{ll} 0 & if\ \lambda > \lambda_0 \\ \left(1 - \frac{h}{w}\tan(\lambda)\right) S^{\Downarrow} & if\ \lambda < \lambda_0 \end{array} \right. \end{array}$$

In order to take into account the other canyon orientations, one should replace w by $w/\sin(\theta)$ in the above expressions, and then multiply the wall fluxes by $\sin(\theta)$. Then let θ_0 be the critical canyon orientation for which the road is no longer in the light (or for which the radiation is minimum if the sun is high enough), i.e.:

$$\theta_0 = \arcsin\left(\min\left[\frac{w}{h}\frac{1}{\tan(\lambda)}; 1\right]\right)$$

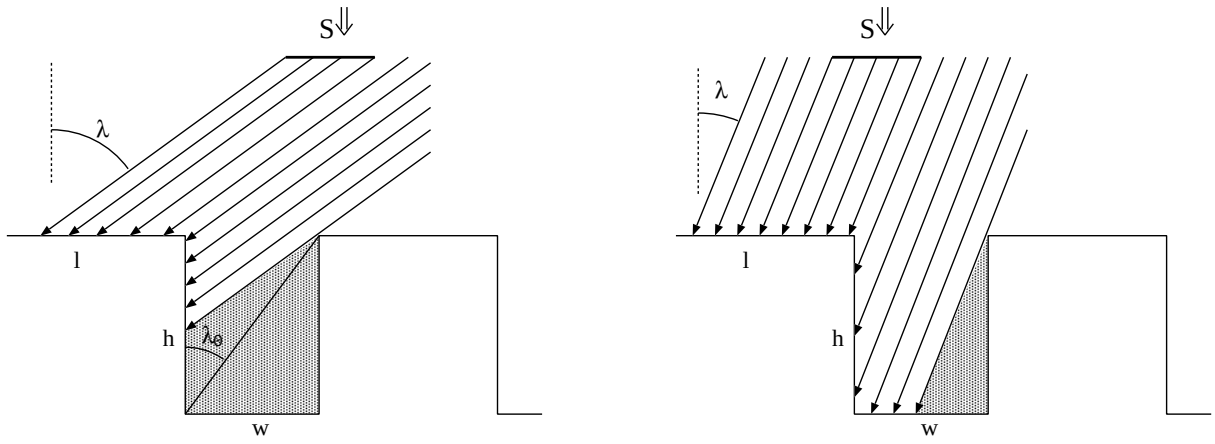

Figure 3.2: Solar radiation input for a road perpendicular to the sun azimuth. In the TEB scheme, the contribution of all the other road directions are averaged with this one.

Averaging a flux with respect to the canyon orientation is performed with two integrations, one between $\theta = 0$ and $\theta = \theta_0$, and the other one between $\theta = \theta_0$ and $\theta = \frac{\pi}{2}$. The direct solar fluxes for walls, roads and roofs then read:

$$S_r^{\Downarrow} = S^{\Downarrow} \left[\frac{2\theta_0}{\pi} - \frac{2}{\pi}\frac{h}{w} tan(\lambda)\left(1 - \cos(\theta_0)\right)\right] \tag{3.13}$$

$$S_w^{\Downarrow} = S^{\Downarrow} \left[\frac{w}{h}\left(\frac{1}{2} - \frac{\theta_0}{\pi}\right) + \frac{1}{\pi} tan(\lambda)\left(1 - \cos(\theta_0)\right)\right] \tag{3.14}$$

$$S_R^{\Downarrow} = S^{\Downarrow} \tag{3.15}$$

Note that from the previous equations, one can check the conservation relation $S_r^{\Downarrow} + 2\frac{h}{w} S_w^{\Downarrow} = S^{\Downarrow}$.

Solar radiation reflections

The scattered solar radiation received by the surfaces ($S_\star^{\downarrow}$) is directly deduced from the sky-view factors. Because of the canyon shape and the possible high albedo of the surfaces (white paint, snow), the shortwave radiative budget is computed by resolving a geometric system for an infinite number of reflections. The reflections are assumed to be isotropic: there is no specular reflection in this model. Details of the following calculations are given in Appendix A.

One defines $M_\star$ as the sum of the reflections against the road and wall:

$$M_r = \frac{R_r(0) + (1-\Psi_r)\overline{\alpha_r}(R_w(0) + \Psi_w \alpha_w R_r(0))}{1-(1-2\Psi_w)\alpha_w + (1-\Psi_r)\Psi_w \overline{\alpha_r}\alpha_w} \tag{3.16}$$

$$M_w = \frac{R_w(0) + \Psi_w \alpha_w R_r(0)}{1-(1-2\Psi_w)\alpha_w + (1-\Psi_r)\Psi_w \overline{\alpha_r}\alpha_w} \tag{3.17}$$

with

$$R_r(0) = \overline{\alpha_r} S_r^{\Downarrow} + \overline{\alpha_r} S_r^{\downarrow}$$

$$\begin{aligned} R_w(0) = &\quad \alpha_w S_w^{\Downarrow} &+\alpha_w S_w^{\downarrow} \\ \overline{\alpha_r} = &\quad (1-\delta_{snowr})\alpha_r &+\delta_{snowr}\alpha_{r_{snow}} \end{aligned}$$

The total solar radiation absorbed by each of the surface types is:

$$S_r^* = \quad (1-\alpha_r)S_r^{\Downarrow} + (1-\alpha_r)S_r^{\downarrow} \quad +(1-\alpha_r)(1-\Psi_r)M_w \tag{3.18}$$

$$S_w^* = \quad (1-\alpha_w)S_w^{\Downarrow} + (1-\alpha_w)S_w^{\downarrow} \quad +(1-\alpha_w)(1-2\Psi_w)M_w + (1-\alpha_w)\Psi_w M_r \tag{3.19}$$

$$S_R^* = \quad (1-\alpha_R)S_R^{\Downarrow} + (1-\alpha_R)S_R^{\downarrow} \tag{3.20}$$

Note that in these equations, a specific albedo of the surfaces (glass, wet surface) for the direct solar radiation, would change only the $\alpha_\star S_\star^{\Downarrow}$ terms.

3.2.8 Anthropogenic fluxes

Due to human activity, heat and moisture are released towards the atmosphere. The two main sources come from domestic heating and from combustion.

Domestic heating is explicitly resolved by assuming a constant internal temperature, whatever the external temperature. The default value is 290.15 K. The heat is then released towards the wall/roof surfaces and then towards the atmosphere through the conduction flux formulation.

The combustion source is split into two contributions in the TEB model: traffic and industry. For each, the heat and moisture fluxes, averaged on the town surface ($H_{traffic}$ and $LE_{traffic}$, $H_{industry}$ and $LE_{industry}$), are specified by the user (from available information on the town activity).
However, these fluxes do **not** directly modify the surface energy budgets since they are released into the air. The traffic related fluxes will modify the canyon air budget (they are incorporated in Equation 3.24, see next section). The industry fluxes are assumed to influence the atmosphere directly.

3.2.9 Turbulent fluxes

Treatment of the urban roughness sublayer, momentum fluxes

In this section, the method to compute the turbulent fluxes between the surfaces and the atmospheric model will be presented. The resolution of the atmospheric model is far too low to be able to represent the urban roughness sublayer motions, as it applies to the mesoscale. The atmospheric models do not usually parameterize the exchange processes in this layer: it is done by the surface scheme. If the first atmospheric level is outside the roughness sublayer, the traditional surface layer formulations can be used to compute the turbulent fluxes. The problem is that the roughness sublayer can have a substantial extension over an urban surface (several tens of meters), and the first level of the atmospheric model (often a couple of tens of meters) is often within it.

It is therefore necessary to have a closer look to the parameterization of the fluxes. *Feigenwinter et al.* [1999] conducted measurements on a 50m height mast in the city of Basel (Switzerland). The authors found that the mechanical properties in the roughness sublayer (such as profiles of velocity variances, non-dimensionalized

velocity variances and spectra of wind components) behave similarly to rural surface layers. Furthermore, they concluded that these quantities are quite well parameterized within the Monin-Obukhov similarity theory, if local Monin-Obukhov length is applied.

Following their results, the TEB scheme computes the **momentum fluxes for the entire urban (or sub-urban) cover**, with a roughness length formulation and the stability coefficients of *Mascart et al.* [1995], whatever the relative positions of the atmospheric level and the roughness sublayer height.

In contrast, *Feigenwinter et al.* [1999] found that the temperature characteristics, and in particular the turbulent heat flux, cannot be satisfactorily reproduced by the Monin-Obukhov similitude framework. They attribute this discrepancy to 'thermal inhomogeneity and/or different source areas'. The use of one unique surface exchanging heat with the atmosphere (the classical surface layer approach) becomes debatable.

The approach of the TEB scheme is to suppose that there are **two** major sources of heat from the artificial cover towards the atmosphere, leading to **two** turbulent heat fluxes. These two different surfaces are the **roofs** on the one hand, and the **canyon systems** on the other hand (see Figure 3.3). The two flux contributions are averaged relative to their horizontal areas: this is a way to represent the mixing in the urban roughness sublayer.

Considerations on the turbulent transfer of moisture

Both for roof and roads, one will also explicitly suppose that the transfer coefficient for turbulent heat and moisture fluxes are identical (but different than for momentum). Very few direct measurements of turbulent moisture fluxes exist in the literature to validate or invalidate this hypothesis.

Roth [1993] and *Roth et al.* [1993] computed statistics from data (including moisture measurements) gathered during 10 days in summer in a suburb of Vancouver. The suburb was composed of 36% artificial cover, and of 64% greenspace. They showed poor correlation between temperature and moisture characteristics, and suggested it was caused by spatial inhomogeneity. They concluded that in their case, the mixing for moisture was less efficient than for heat. However, there was no rain during this period, and the evaporation came from the greenspace. Therefore, it is not possible to draw conclusion about a specific formulation for the moisture flux in the TEB model.

Other latent heat flux data exist, but again during dry periods. *Grimmond et al.* [1999a] gathered data from seven north-American cities, but five of them are suburban cases. The two most purely urban cases (central Mexico city, presented in detail in *Oke et al.* [1999], and an industrial site in Vancouver) show very small evaporative flux: equal to 4% and 10% of the net radiation (during the day) for the two sites, respectively.

Roughness length for momentum fluxes

The momentum fluxes are computed for the entire urban surface. However, one difficulty lies in the determination of the roughness length to use in urban areas. *Wieringa* [1993] reviewed some experimental roughness length estimations for rather homogeneously built-up areas. Dense low building roughness lengths were found between 0.4 and 0.7m, and those for regularly-built towns ranged from 0.7 to 1.5m. In these experiments, they are approximately equal to 1/10 of the houses or building heights. *Bottema* [1997] presents a model computing roughness lengths from building shapes and relative positions (normal or staggered). He found the modeled $z_{0_{town}}$ to be in agreement with the available measurements. Sensitivity experiments of his model show that the ratio $z_{0_{town}}/h$ ranges from 0.05 to 0.1 (except for very sparsely built areas).

Therefore, as a first approximation, the roughness length in the TEB model is set equal to:

$$z_{0_{town}} = h/10$$

(with an arbitrary limit of 5m), but it can be specified independently, either from in-situ measurements or more complicated formulations (see for example the recent review of *Grimmond* [1999b]).

Heat fluxes between roofs and atmosphere

The turbulent heat fluxes for the roofs are also recovered from classical boundary layer laws (because the roof heights are supposed uniform), with a roughness length of 15cm (as observed by *Sturrock et al.* [1977]). Again the stability coefficients of *Mascart et al.* [1995] are used to compute the aerodynamic resistance RES_R.

The effect on temperature and specific humidity of the difference in height between the atmospheric level and the roof level is corrected using the Exner function $\Pi = (p/p0)^{R_d/C_{p_d}}$, where p is the pressure (p_s and p_a are the surface pressure and the first level pressure in the atmospheric model respectively), p_0 is a reference pressure (equal to 100000 Pa), and R_d the gas constant for dry air. One defines:

$$\begin{aligned} \hat{T_a} = & \quad T_a \Pi_s / \Pi_a \\ \hat{q_a} = & \quad q_a \; q_{sat}(\hat{T_a}, p_s)/q_{sat}(T_a, p_a) \end{aligned}$$

The heat and moisture turbulent fluxes between roof and atmosphere read:

$$\begin{aligned} H_R = & \quad C_{p_d}\rho_a \quad (\hat{T_a} - T_{can})/RES_R \\ LE_R = & \quad L_v\rho_a \quad (\hat{q_a} - q_{can})/RES_R \end{aligned}$$

where ρ_a is the air density at first atmospheric level, and C_{p_d} the heat capacity of dry air.

Wind inside the Canyon

The computation of the wind inside the canyon is necessary to estimate the heat fluxes between the surfaces and the canyon. The vertical speed along the walls, W_{can}, as well as the horizontal wind speed in the canyon, U_{can}, must be defined. *Rotach* [1995] presents turbulence measurements in and above a road in the center of Zurich (Switzerland), for which the canyon aspect ratio is $h/w \sim 1$. *Rotach* [1995] observed that fluctuations of the vertical wind speed, σ_w, in the upper part of the canyon, are almost equal to the friction velocity u_*, whatever the stability or wind direction above. *Feigenwinter et al.* [1999] finds that σ_w/u_* is, on the contrary, increasing with height for unstable conditions. However, their value of σ_w/u_* near the roof level (extrapolated using the Monin-Obukhov function) was approximately 1.15, which is of the same order of magnitude as the *Rotach* [1995] results. They also found that for stable to weakly unstable conditions, u_* presents a maximum between the roughness sublayer and the inertial sublayer above. However, u_* does not depart by more than 10% from its value in the inertial sublayer, and is assumed constant with height in the scheme.
Then, (assuming that all this holds true for other canyon aspect ratios), the vertical speed along the walls reads:

$$W_{can} = u_* = \sqrt{C_d}||\vec{U_a}|| \tag{3.21}$$

U_a is the wind velocity at the first atmospheric model level. The drag coefficient, C_d, is computed from the temperatures and humidities in and above the canyon, and from the roughness length, $z_{0_{town}}$, taking into account the stability effects according to *Mascart et al.* [1995].

The horizontal wind speed, U_{can}, is estimated at half the height of the canyon. First, the horizontal wind speed at the top of the canyon is deduced from the logarithmic law above it (Figure 3.3, right side), and the displacement height is equal to two thirds of the building height from road surface (i.e. at $h/3$ under the roof level - which is the zero height of the atmospheric model -, a classical assumption for plant canopies). Furthermore, in order to consider all canyon orientations, and since only the along canyon wind is considered, an integration over 360° is performed. At canyon top, this gives:

$$U_{top} = \frac{2}{\pi} \frac{\ln\left(\frac{h/3}{z_{0_{town}}}\right)}{\ln\left(\frac{\Delta z + h/3}{z_{0_{town}}}\right)} ||\vec{U_a}||$$

where Δz is the height of the first atmospheric model level above the roofs.
To calculate U_{can}, a vertical profile of the wind inside the canyon is assumed. An exponential form is chosen (as is done in vegetation canopies, cf e.g. *Arya* [1988]). Such a profile applied at half-height gives:

$$U_{can} = U_{top} \exp(-N/2)$$

N must be determined. *Rotach* [1995] finds from his case study ($h/w = 1$), that $U_{can} \sim 0.75 U_{top}$. Studies in corn fields ($h/w \sim 4$), which could be assimilated to narrow streets, give $U_{can} \sim 0.4 U_{top}$ (Arya 1988). Therefore, the parameter $N = 0.5 h/w$ should be pertinent.
Then:

$$U_{can} = \frac{2}{\pi} \exp\left(-\frac{1}{4}\frac{h}{w}\right) \frac{\ln\left(\frac{h/3}{z_{0_{town}}}\right)}{\ln\left(\frac{\Delta z + h/3}{z_{0_{town}}}\right)} ||\vec{U_a}|| \tag{3.22}$$

Sensible and latent heat fluxes in the canyon

The turbulent heat fluxes between the canyon air and the atmosphere are computed from the temperature and humidity inside the canyon. The fluxes between surfaces and canyon air follow an empirical formulation. The air characteristics inside the canyon are deduced from the continuity between the fluxes coming from the surfaces and the flux with the atmosphere (inspired by the vegetation canopy scheme of *Deardorff* [1978]). The heat fluxes are used in the energy budget conservation equations involving the surface temperatures. This is why a precise approach has been chosen, specific to each surface. Figure 3.3 displays a summary of the TEB options.

Fluxes between canyon air and atmosphere: Above the canyon, the fluxes are estimated from classical surface boundary layer laws. However in these formulae, the air characteristics in the canyon (T_{can} and q_{can}) are used instead of the surface characteristics. The aerodynamic resistance above the canyon, called RES_{top}, is calculated with $z_{0_{town}}$ using the stability coefficients of *Mascart et al.* [1995] (this formulation leads to different drag coefficients for momentum fluxes and for heat or moisture fluxes).
The heat and moisture turbulent fluxes between canyon and atmosphere then read:

$$\begin{aligned} H_{top} = &\quad C_{p_d}\rho_a \quad (\hat{T_a} - T_{can})/RES_{top} \\ LE_{top} = &\quad L_v\rho_a \quad (\hat{q_a} - q_{can})/RES_{top} \end{aligned}$$

Fluxes between walls, roads and canyon air: Between the canyon surfaces (road and walls) and the canyon air, the *Rowley et al.* [1930] and *Rowley et al.* [1932] aerodynamic formulations are used. They were obtained from in-situ measurements. These formulae are also used in the canyon circulation model of

Mills [1993]. Other formulations of similar form exist in the literature (see e.g. *Sturrock et al.* [1977], either from wind tunnel or in-situ measurements).
For simplicity, the same value is chosen for both road and walls. The resistance is independent of the stability inside or above the canyon. It reads:

$$\begin{aligned} RES_r = RES_w = \quad & C_{p_d}\rho_a \quad \left(11.8 + 4.2\sqrt{U_{can}^2 + (u_* + w_*)^2}\right)^{-1} \\ w_* = & \left(\frac{g}{T_{can}} Q_0 h\right)^{1/3} \end{aligned} \tag{3.23}$$

Where $u_* + w_*$ is the turbulent wind and Q_0 encompasses both road and wall turbulent heat fluxes.
Finally, the heat fluxes between the canyon surfaces and the canyon air read:

$$\begin{aligned} H_r = \quad & C_{p_d}\rho_a \quad (T_r - T_{can})/RES_r \\ H_w = \quad & C_{p_d}\rho_a \quad (T_w - T_{can})/RES_w \\ LE_r = \quad & L_v\rho_a \quad \delta_r(q_{sat}(T_r, p_s) - q_{can})/RES_r \\ LE_w = \quad & 0 \end{aligned}$$

Notice the form of the latent heat flux, where the fraction of wet road, δ_r, is applied outside of the brackets. Therefore, the evaporation from the surface occurs when $q_{sat}(T_r) > q_{can}$, even if very little water remains in the interception reservoir. The same humidity treatment is performed for roofs.

Canyon temperature and humidity

These quantities can be considered as output of a meteorological forecast. They are computed diagnostically: the equilibrium between thermodynamic fluxes for the canyon air is assumed to be valid at each time step. **The anthropogenic flux due to traffic is also taken into account**. Note that in this formula, $H_{traffic}$, representative of the whole urban surface, has been scaled to the road surface.

$$H_{top} = (1 - \delta_{snowr})H_r \quad + \tfrac{2h}{w} H_w \quad + H_{traffic}\frac{1}{1 - a_{bld}} + \delta_{snowr} H_{snowr} \tag{3.24}$$

$$LE_{top} = (1 - \delta_{snowr})LE_r \qquad\qquad + LE_{traffic}\frac{1}{1 - a_{bld}} + \delta_{snowr} LE_{snowr} \tag{3.25}$$

Then

$$T_{can} = \frac{(1 - \delta_{snowr})\frac{T_r}{RES_r} + \frac{2h}{w}\frac{T_w}{RES_w} + \frac{\hat{T_a}}{RES_{top}} + \frac{H_{traffic}}{C_{p_d}\rho_a(1-a_{bld})} + \delta_{snowr}\frac{H_{snowr}}{C_{p_d}\rho_a}}{(1 - \delta_{snowr})\frac{1}{RES_r} + \frac{2h}{w}\frac{1}{RES_w} + \frac{1}{RES_{top}}} \tag{3.26}$$

and

$$q_{can} = \frac{(1 - \delta_{snowr})\frac{\delta_r q_{sat}(T_r, p_s)}{RES_r} + \frac{\hat{q_a}}{RES_{top}} + \frac{LE_{traffic}}{L_v\rho_a(1-a_{bld})} + \delta_{snowr}\frac{LE_{rsnow}}{L_v\rho_a}}{(1 - \delta_{snowr})\frac{\delta_r}{RES_r} + \frac{1}{RES_{top}}} \tag{3.27}$$

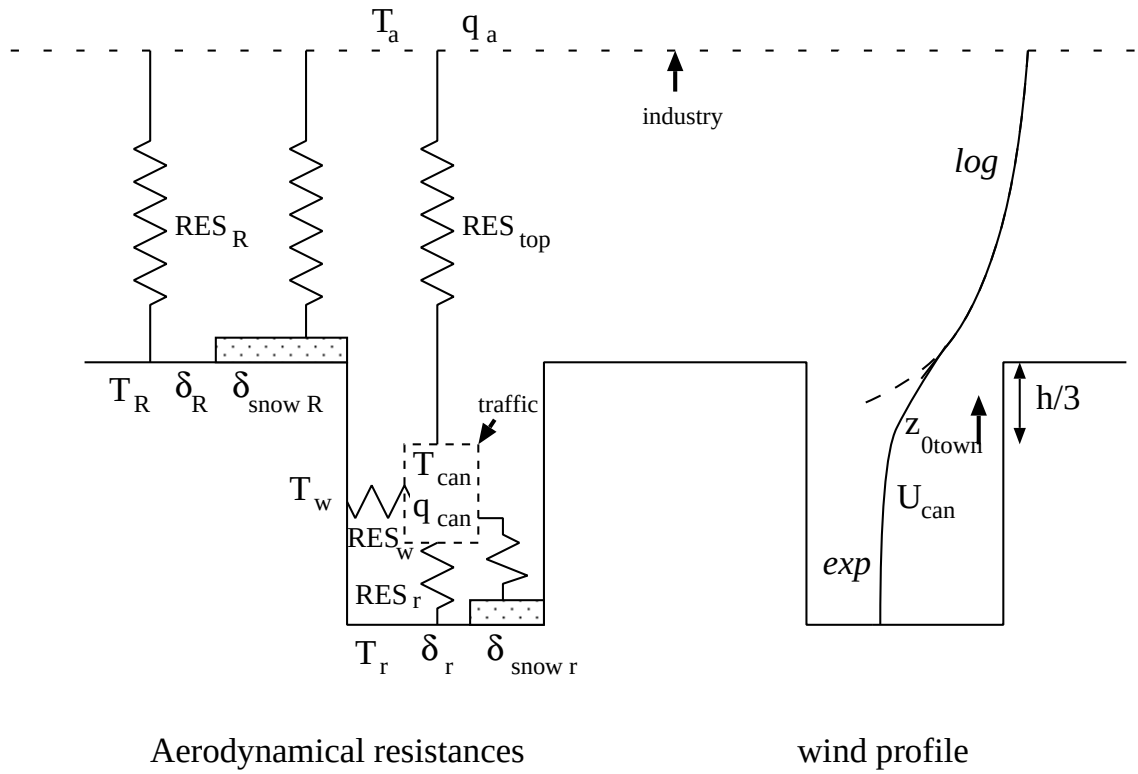

Figure 3.3: Scheme options for: (a) aerodynamic resistances; (b) wind profile within and above the canyon.

Averaged fluxes at town scale

As mentioned above, the averaging operation performed to obtain the turbulent fluxes at town scale is in itself a way to solve the problem of the roughness sublayer: it mimics the mixing of the different sources of turbulent heat fluxes, and then produces **fluxes which are representative of the upper part of the surface layer**, above the roughness sublayer. The energy fluxes released by the industrial activities is also added at this stage.
The total heat fluxes from the artificial material areas towards the atmosphere are then:

$$H_{town} = a_{bld} H_R + (1 - a_{bld}) H_{top} + H_{industry} \tag{3.28}$$

$$LE_{town} = a_{bld} LE_R + (1 - a_{bld}) LE_{top} + LE_{industry} \tag{3.29}$$

In order to have the total turbulent fluxes H, LE from the surface towards the atmospheric model, these fluxes should be averaged with those computed by the vegetation scheme for the other land surfaces (city parks, gardens, fields, forest, bare soil...) and those from water covered surfaces (rivers, lakes, sea...).

Solar radiation reflections

Suppose hereafter that the direct and scattered albedo for each surface are identical. If this is not the case, only the first direct solar reflection would be modified.
When the first reflection occurs, the fluxes stored by the road and wall, A_r and A_w, are respectively:

$$A_r(0) = \quad (1 - \alpha_r)(S_r^{\Downarrow} \quad + S_r^{\downarrow})$$

$$A_w(0) = \quad (1-\alpha_w)(S_w^{\Downarrow} \quad + S_w^{\downarrow})$$

The reflected parts R_r and R_w are:

$$\begin{aligned} R_r(0) = &\quad \alpha_r(S_r^{\Downarrow} \quad + S_r^{\downarrow}) \\ R_w(0) = &\quad \alpha_w(S_w^{\Downarrow} \quad + S_w^{\downarrow}) \end{aligned}$$

After n reflections:

$$\begin{aligned} A_r(n+1) = &\quad A_r(n) \quad + (1-\alpha_r)(1-\Psi_r)R_w(n) \\ A_w(n+1) = &\quad A_w(n) \quad + (1-\alpha_w)\Psi_w R_r(n) + (1-\alpha_w)(1-2\Psi_w)R_w(n) \\ R_r(n+1) = &\quad + \alpha_r(1-\Psi_r)R_w(n) \\ R_w(n+1) = &\quad + \alpha_w\Psi_w R_r(n) + \alpha_w(1-2\Psi_w)R_w(n) \end{aligned}$$

Then

$$\begin{aligned} A_r(n+1) = &\quad A_r(0) \quad + (1-\Psi_r)(1-\alpha_r)\sum_{k=0}^{n} R_w(k) \\ A_w(n+1) = &\quad A_w(0) \quad + \Psi_w(1-\alpha_w)\sum_{k=0}^{n} R_r(k) \\ &\qquad\qquad + (1-2\Psi_w)(1-\alpha_w)\sum_{k=0}^{n} R_w(k) \end{aligned}$$

and

$$\begin{aligned} \sum_{k=0}^{n} R_r(k) = &\quad (1-\Psi_r)\alpha_r \textstyle\sum_{k=0}^{n-1} R_w(k) \quad + R_r(0) \\ \sum_{k=0}^{n} R_w(k) = &\quad \Psi_w\alpha_w \textstyle\sum_{k=0}^{n-1} R_r(k) \\ &\quad + (1-2\Psi_w)\alpha_w \textstyle\sum_{k=0}^{n-1} R_w(k) \quad + R_w(0) \end{aligned}$$

Solving this geometric system yields, in the case of an infinite number of reflections:

$$\begin{aligned} \sum_{k=0}^{\infty} R_r(k) &= R_r(0) + \tfrac{(1-\Psi_r)\alpha_r(R_w(0)+\Psi_w\alpha_w R_r(0))}{1-(1-2\Psi_w)\alpha_w+(1-\Psi_r)\Psi_w\alpha_r\alpha_w} &= M_r \\ \sum_{k=0}^{\infty} R_w(k) &= \tfrac{R_w(0)+\Psi_w\alpha_w R_r(0)}{1-(1-2\Psi_w)\alpha_w+(1-\Psi_r)\Psi_w\alpha_r\alpha_w} &= M_w \end{aligned}$$

The total solar radiation stored by road and wall is then:

$$\begin{aligned} S_r^* = &\quad (1-\alpha_r)S_r^{\Downarrow} + (1-\alpha_r)S_r^{\downarrow} \quad + (1-\alpha_r)(1-\Psi_r)M_w \\ S_w^* = &\quad (1-\alpha_w)S_w^{\Downarrow} + (1-\alpha_w)S_w^{\downarrow} \quad + (1-\alpha_w)(1-2\Psi_w)M_w + (1-\alpha_w)(1-\Psi_w)M_r \end{aligned}$$

The total albedo for the town is:

$$\alpha_{TEB} = 1 - \frac{f_{road}S_{road}^* + f_{wall}S_{wall}^* + f_{roof}S_{roof}^*}{f_{road}(S_{road}^{\Downarrow} + S_{road}^{\downarrow}) + f_{wall}(S_{wall}^{\Downarrow} + S_{wall}^{\downarrow}) + f_{roof}(S_{roof}^{\Downarrow} + S_{roof}^{\downarrow})} \tag{3.30}$$

Where $f_{road} = 1 - a_{bld}$, $f_{roof} = a_{bld}$ and $f_{roof} = 2\frac{h}{w}(1-a_{bld})$

symbol	designation of symbol	unit
geometric parameters		
a_{town}	fractional area occupied by artificial material	-
a_{bld}	fractional artificial area occupied by buildings	-
$1 - a_{bld}$	fractional artificial area occupied by roads	-
h	building height	m
h/l	building aspect ratio	-
h/w	canyon aspect ratio	-
$z_{0_{town}}$	dynamic roughness length for the building/canyon system	m
radiative parameters		
α_R, α_r, α_w	roof, road and wall albedos	-
ϵ_R, ϵ_r, ϵ_w	roof, road and wall emissivities	-
thermal parameters		
d_{R_k}, d_{r_k}, d_{w_k}	thickness of the k^{th} roof, road or wall layer	m
λ_{R_k}, λ_{r_k}, λ_{w_k}	thermal conductivity of the k^{th} roof, road or wall layer	W m^{-1} K^{-1}
C_{R_k}, C_{r_k}, C_{w_k}	heat capacity of the k^{th} roof, road or wall layer	J m^{-1} K^{-1}

Table 3.1: Parameters of the TEB scheme. *Note that a_{town} is not strictly a parameter of the TEB scheme, but is used to average the output TEB fluxes with those computed for the vegetation and water portions of the grid mesh. Note also that some surfaces between the buildings, such as gardens or parks for example, are* **not** *treated by the TEB model, but modify the canyon width, w.*

symbol	designation of symbol	unit
prognostic variables		
$T_{R_k}, T_{r_k}, T_{w_k}$	temperature of the k^{th} roof, road or wall layer	K
W_R, W_r	roof and road water interception reservoir	kg m^{-2}
$W_{snow\,R}, W_{snow\,r}$	roof and road snow interception reservoir	kg m^{-2}
$T_{snow\,R}, T_{snow\,r}$	roof and road snow temperature	K
$\rho_{snow\,R}, \rho_{snow_r}$	roof and road snow density	kg m^{-3}
$\alpha_{snow\,R}, \alpha_{snow\,r}$	roof and road snow albedo	-
diagnostic variables		
T_{can}	canyon air temperature	K
q_{can}	canyon air specific humidity	kg kg^{-1}
U_{can}	along canyon horizontal wind	m s^{-1}
α_{town}	town effective albedo	-
$T_{s_{town}}$	town area averaged radiative surface temperature	K
input energy fluxes		
$L^{\downarrow}$	downward infra-red radiation on an horizontal surface	W m^{-2}
$S^{\downarrow}$	downward **diffuse** solar radiation on an horizontal surface	W m^{-2}
$S^{\Downarrow}$	downward **direct** solar radiation on an horizontal surface	W m^{-2}
$H_{traffic}$	anthropogenic sensible heat flux released in the canyon	W m^{-2}
$LE_{traffic}$	anthropogenic latent heat flux released in the canyon	W m^{-2}
$H_{industry}$	anthropogenic sensible heat flux released by industries	W m^{-2}
$LE_{industry}$	anthropogenic latent heat flux released by industries	W m^{-2}
other energy input		
$T_{i_{bld}}$	building interior temperature	K
output energy fluxes		
S_R^*, S_r^*, S_w^*	net solar radiation budget for roofs, roads and walls	W m^{-2}
L_R^*, L_r^*, L_w^*	net infra-red radiation budget for roofs, roads and walls	W m^{-2}
H_R, H_r, H_w	turbulent sensible heat flux for roofs, roads and walls	W m^{-2}
LE_R, LE_r, LE_w	turbulent latent heat flux for roofs, roads and walls	W m^{-2}
$G_{R_{k,k+1}}, G_{r_{k,k+1}}, G_{w_{k,k+1}}$	conduction heat flux between k^{th} and $k+1^{th}$ roof, road or wall layers	W m^{-2}
H_{town}	town averaged turbulent sensible heat flux	W m^{-2}
LE_{town}	town averaged turbulent latent heat flux	W m^{-2}

Table 3.2: Energy fluxes and variables in the TEB scheme

experiment name → parameter ↓	reference	buildings	suburban	Insulated	Insulated, Ti
a_{town}	100%		70%		
a_{bld}	50%				
h/w	1	3	0.5		
$z_{0_{town}}$	5 m		1 m		
$T_{i_{bld}}$	290.15 K				variable
d_{R_1} (*dense concrete*)	5 cm				
d_{R_2} (*aerated concrete*)	40 cm				
d_{R_3} (*insulation layer*)	5 cm			20 cm	20 cm
d_{w_1} (*dense concrete*)	2 cm				
d_{w_2} (*aerated concrete*)	12.5 cm				
d_{w_3} (*insulation layer*)	2 cm			8 cm	8 cm
d_{r_1} (*asphalt*)	5 cm				
d_{r_2} (*dry soil*)	10 cm				
d_{r_3} (*dry soil*)	100 cm				
α_R	15%				
α_w	25%				
α_r	8%				
ϵ_R	90%				
ϵ_w	85%				
ϵ_r	94%				

Table 3.3: Urban characteristics for the sensitivity experiments. Only the parameters different from the reference experiment are shown. Composition of the layers are displayed with the corresponding layer thickness.

Chapter 4

Soil and vegetation

Contents

4.1 ISBA surface scheme

4.1.1 Force restore approach

Treatment of the soil heat content

The prognostic equations for the surface temperature T_s and its mean value T_2 over one day τ, are obtained from the force-restore method proposed by *Bhumralkar* [1975] and *Blackadar* [1976]:

$$\frac{\partial T_s}{\partial t} = C_T(R_n - H - LE) - \frac{2\pi}{\tau}(T_s - T_2), \tag{4.1}$$

$$\frac{\partial T_2}{\partial t} = \frac{1}{\tau}(T_s - T_2), \tag{4.2}$$

where H and LE are the sensible and latent heat fluxes, and R_n is the net radiation at the surface. The surface temperature T_s evolves due to both the diurnal forcing by the heat flux $G = R_n - H - LE$ and a restoring term towards its mean value T_2. In contrast, the mean temperature T_2 only varies according to a slower relaxation towards T_s.
The coefficient C_T is expressed by

$$C_T = 1/\left(\frac{(1-veg)(1-p_{sng})}{C_g} + \frac{veg(1-p_{snv})}{C_v} + \frac{p_{sn}}{C_s}\right) \tag{4.3}$$

where veg is the fraction of vegetation, C_g is the ground heat capacity, C_s is the snow heat capacity, C_v is the vegetation heat capacity, and

$$p_{sng} = \frac{W_s}{W_s + W_{crn}}; \qquad p_{snv} = \frac{h_s}{h_s + 5000 z_0}; \qquad p_{sn} = (1-veg)p_{sng} + vegp_{snv} \tag{4.4}$$

are respectively the fractions of the bare soil and vegetation covered by snow, and the fraction of the grid covered by snow. Here, $W_{crn} = 10\ mm$, and $h_s = W_s/\rho_s$ is the thickness of the snow pack (ρ_s is the snow density). The partitioning of the grid into bare soil, vegetation, and snow areas, is indicated in Fig.(4.1) .
The heat capacities of the ground and snow canopies are respectively given by

$$C_g = C_{gsat}\left(\frac{w_{sat}}{w_2}\right)^{b/2log10}; C_g \leq 1.5 \times 10^{-5}\ Km^2J^{-1} \tag{4.5}$$

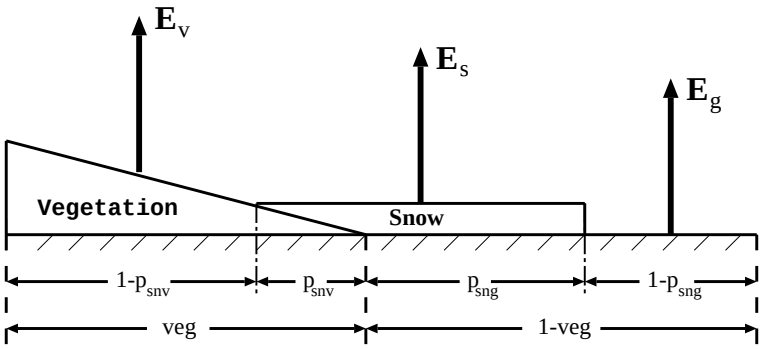

Figure 4.1: Partitioning of the grid

where G_{gsat} is the heat capacity at saturation, and w_{sat} the volumetric moisture content of the soil at saturation; and

$$C_s = 2 \times \left(\frac{\pi}{\lambda_s c_s \tau} \right)^{1/2} \tag{4.6}$$

where $\lambda_s = \lambda_i \times {\rho_s}^{1.88}$; $c_s = c_i(\rho_s/\rho_i)$: λ_i is the ice conductivity; c_i is the heat capacity of ice; and ρ_i is the relative density of ice (*Douville* [1994], *Douville et al.* [1995]).

After an intermediate surface temperature ${T_s}^*$ is evaluated from Eq. (4.1), the cooling due to the melting of snow is considered following

$${T_s}^+ = {T_s}^* - C_T L_f(melt)\Delta t \tag{4.7}$$

where L_f is the latent of fusion, Δt is the timestep, and the melting rate of snow is

$$melt = p_{sn} \left(\frac{T_n - T_0}{C_s L_f \Delta t} \right); \quad melt \geq 0 \tag{4.8}$$

Here,
$T_0 = 273.16\ K$;
$T_n = (1 - veg){T_s}^* + veg T_2$
Similarly, the intermediate mean temperature ${T_2}^*$ obtained from Eq. (2) is also modified due to the melting/freezing of water in the soil layer occurring for temperatures between $-5°C$ and $0°C$ (*Boone et al.* [2000]). The resulting mean temperature is

$${T_2}^+ = {T_2}^* + (\Delta w_2)_{frozen} L_f C_g d \tag{4.9}$$

with

$$(\Delta w_2)_{frozen} = \left[1 - \left(\frac{{T_2}^* - 268.16}{5.} \right) \right] (w_2(t) - w_2(t - \Delta t)) \tag{4.10}$$

$$(\Delta w_2)_{frozen} = 0 \quad if\ T_2 \leq -5°C\ or\ if\ T_2 \geq 0°C \tag{4.11}$$

where $d = 15\ cm$ is an estimated average of the penetration of the diurnal wave into the soil. Only the mean temperature T_2 is modified by this factor. The surface temperature T_s, however, indirectly feels this effect through the relaxation term in Eq. (1).

Treatment of the soil water

Equations for w_g and w_2 are derived from the force-restore method applied by Deardorff (1977) to the ground soil moisture:

$$\frac{\partial w_g}{\partial t} = \frac{C_1}{\rho_w d_1}(P_g - E_g) - \frac{C_2}{\tau}(w_g - w_{geq}) \; ; 0 \leq w_g \leq w_{sat} \tag{4.12}$$

$$\frac{\partial w_2}{\partial t} = \frac{1}{\rho_w d_2}(P_g - E_g - E_{tr}) - \frac{C_3}{d_2 \tau} \, max\left[0., (w_2 - w_{fc})\right] ; 0 \leq w_2 \leq w_{sat} \tag{4.13}$$

where P_g is the flux of liquid water reaching the soil surface (including the melting), E_g is the evaporation at the soil surface, E_{tr} is the transpiration rate, ρ_w is the density of liquid water, and d_1 is an arbitrary normalization depth of 1 centimeter. In the present formulation, all the liquid water from the flux P_g goes into the reservoirs w_g and w_2, even when snow covers fractions of the ground and vegetation. The first term on the right hand side of Eq. (12) represents the influence of surface atmospheric fluxes when the contribution of the water extraction by the roots is neglected. The coefficients C_1 and C_2, and the equilibrium surface volumetric moisture w_{geq}, have been calibrated for different soil textures and moistures (*Noilhan and Planton* [1989]).

The expression for C_1 differs depending on the moisture content of the soil. For wet soils (i.e., $w_g \geq w_{wilt}$), this coefficient is expressed as

$$C_1 = C_{1sat} \left(\frac{w_{sat}}{w_g} \right)^{b/2+1} \tag{4.14}$$

For very dry soils (i.e., $w_g < w_{wilt}$), the vapor phase transfer needs to be considered in order to reproduce the physics of water exchange. These transfers are parameterized as a function of the wilting point w_{wilt}, the soil water content w_g, and the surface temperature T_s, using the Gaussian expression (*Braud et al.* [1993], *Giordani* [1993])

$$C_1 = C_{1max} \exp\left[-\frac{(w_g - w_{max})^2}{2\sigma^2} \right] \tag{4.15}$$

where w_{max}, C_{1max}, and σ are respectively the abscissa of the maximum, the mode, and the standard deviation of the Gaussian functions (see Appendix B). The other coefficient, C_2, and the equilibrium water content, w_{geq}, are given by

$$C_2 = C_{2ref} \left(\frac{w_2}{w_{sat} - w_2 + 0.01} \right) \tag{4.16}$$

$$w_{geq} = w_2 - a w_{sat} \left(\frac{w_2}{w_{sat}} \right)^p \left[1 - \left(\frac{w_2}{w_{sat}} \right)^{8p} \right] \tag{4.17}$$

For the w_2 evolution, Eq. (13) represents the water budget over the soil layer of depth d_2. The drainage, which is proportional to the water amount exceeding the field capacity (i.e., $w_2 - w_{fc}$), is considered in the second term of the equation (see *Mahfouf and Noilhan* [1994]). The coefficient C_3 does not depend on w_2 but simply on the soil texture (see Appendix A). Similarly, run-off occurs when w_g or w_2 exceeds the saturation value w_{sat} or when a sub-grid runoff scheme is used. Coefficients C_{1sat}, C_{1max}, C_{2ref} and p are made dependant on the soil texture (*Noilhan an Mahfouf* [1996])

Root zone soil layer option In the standard two-soil layer version of ISBA, it is not possible to distinguish the root zone and the total soil water reservoirs. With the three-layer version, the deepest soil layer may provide water to the root zone through capillary rises only, and the available water content for transpiration is defined as $(w_{sat} - w_{sat}) \times d_2$.
The bulk soil layer (referred to as w_2 in the previous sections) is divided into a root-zone layer (with a depth d_2) and base-flow layer (with a thickness defined as $d_3 - d_2$). The governing equations for the time evolution of soil moisture for the two sub-surface soil layers are written following *Boone et al.* [1999] as

$$\frac{\partial w_2}{\partial t} = \frac{1}{\rho_w d_2}\left(P_g - E_g - E_{tr}\right) - \frac{C_3}{d_2 \tau}\max\left[0,\ (w_2 - w_{fc})\right] - \frac{C_4}{\tau}\left(w_2 - w_3\right) \tag{4.18}$$

$$\frac{\partial w_3}{\partial t} = \frac{d_2}{(d_3 - d_2)}\left\{\frac{C_3}{d_2 \tau}\max\left[0,\ (w_2 - w_{fc})\right] + \frac{C_4}{\tau}\left(w_2 - w_3\right)\right\} \tag{4.19}$$

$$- \frac{C_3}{(d_3 - d_2)\,\tau}\max\left[0,\ (w_3 - w_{fc})\right];\qquad 0 \le w_3 \le w_{sat} \tag{4.20}$$

where C_4 represents the vertical diffusion coefficient. It is defined as

$$C_4 = C_{4\,ref}\,\overline{w}_{2,3}{}^{C_{4b}} \tag{4.21}$$

$$\tag{4.22}$$

where $\overline{w}_{2,3}$ represents the interpolated volumetric water content representative of the values at the layer interface (d_2). The $C_{4\,ref}$ and C_{4b} coefficients are defined using the soil sand and clay contents, consistent with the other model parameters (see the section on model coefficients). In addition, the $C_{4\,ref}$ coefficient is scaled as a function of grid geometry. The equations are integrated in time using a fully implicit method.

Exponential profile of k_{sat} In this version, the soil column assumes an exponential profile of the saturated hydraulic conductivity, k_{sat}, with soil depth (Decharme et al. 2006). This parameterization depends only on two parameters, which represent the rate of decline of the k_{sat} profile and the depth where k_{sat} reaches its so-called "compacted" value.

$$k_{sat}(z) = k_{sat,c} e^{-f(z - d_c)} \tag{4.23}$$

where $z(m)$ is the depth of the soil profile, $f(m^{-1})$ is the exponential profile decay factor and $d_c(m)$ the compacted depth where k_{sat} reaches its compacted value, $k_{sat,c}$ given by Clapp and Hornberger (1978). In the standard approach, f varies with soil properties (texture and/or rooting depth) but can not exceed $2m^{-1}$ and d_c assumes to be equal to rooting depth d_2. Sensitivity tests to these parameters and a detailed discussion about this parameterization can be found in *Decharme et al.* [2006]. The main hypothesis is that roots and organic matter favor the development of macropores and enhance the water movement near the soil surface, and that soil compaction is an obstacle for vertical water transfer in the deeper soil. This exponential soil profile increases the saturated hydraulic conductivity at the surface by approximately a factor 10, and its mean value increases in the root zone and decreases in the deep layer in comparison with the values given by *Clapp and Horneberger* [1978]. In ISBA, all hydraulic force-restore coefficients ($C1, C2, C3$ and $C4$) are re-formulated to take into account this k_{sat} profile.

Treatment of runoff in th Isba initial version Run-off occurs when w_2 exceeds the saturation value w_{sat}. In its standard version, ISBA simulates surface runoff through the saturation excess mechanism (also known as Dune mechanism), therefore, runoff is only produced when the soil is saturated (i.e. w_2 exceeds the saturation value w_{sat}). Note that if w_3 exceeds the saturation, the excess water is added to the drainage term.

When the scale of variability of runoff production is smaller than the typical scale of the grid scale (which is common in most applications), the soil almost never saturates and the runoff production is very low, even though, in reality, a fraction of the cell is saturated and does produce surface runoff.
In order to account for subgrid scale runoff, three parametrisations are available and are described hereafter.

The variable Infiltration Capacity (VIC) scheme. This subgrid parametrisation was introduced by *Habets et al.* [1999] following the approach of the Variable Infiltration Capacity (VIC) scheme, described in *Wood et al.* [1992] and *Dumenil and Todini* [1992] and inspired from the Nanjing model (*Zhao* [1992]). In this scheme it is considered that the infiltration capacity (the maximum depth of water that can be stored in the soil column) varies non-linearly within the grid cell. The fraction of the grid cell that is saturated is a function of some soil parameters (the soil water content at saturation, the wilting point and the root depth), the soil water content of the root zone (w_2) and a new parameter, called b, which represents the shape of the heterogeneity distribution of effective soil moisture capacity.
This approach is summarized in Fig. 4.2. A grid cell is assumed to be composed of an infinity of elementary reservoirs, whose infiltration capacity continuously varies from 0 and a maximum value i_m. The mean water content (wg_2) is the sum of the water content of all the reservoirs.

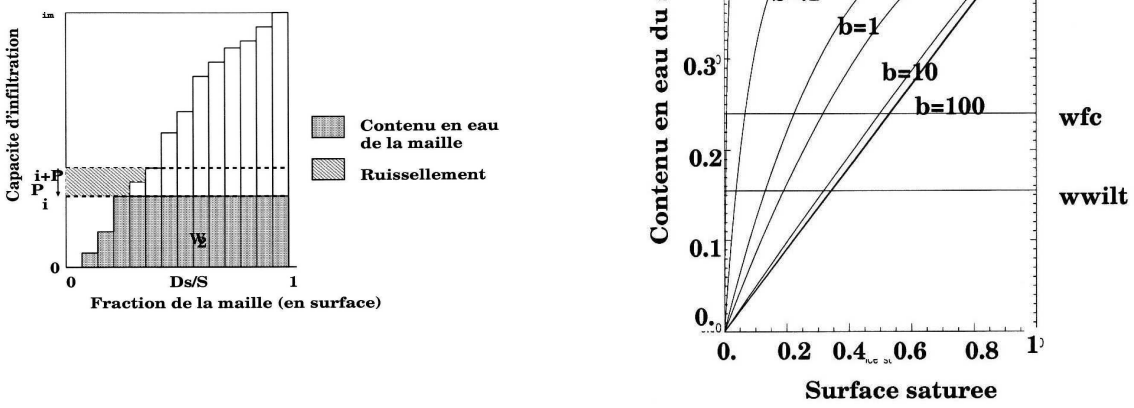

Figure 4.2: Simplified scheme of the VIC subgrid runoff. Left : principles. Right : variation of the saturated proportion of the grid cell for several values of the soil water content and of the parameter b in the VIC model. In Isba, the saturated fraction of the grid is computed between w_{wilt} and w_{sat}

i is the water content of the non satured elementary reservoirs (all reservoirs with a water content below i are saturated). $A(i)$ is the saturated fraction of the cell. In case of precipitation (P), all reservoirs with an infiltration capacity lower than $i + P$ will be filled, and then produce runoff. The runoff is the sum of the contribution of the elementary reservoirs.
In this scheme, the infiltration capacity is given by :

$$i = i_m \left[1 - (1 - A(i))^{\frac{1}{b}}\right] \Longleftrightarrow A(i) = 1 - \left(1 - \frac{i_0}{i_m}\right)^b \tag{4.24}$$

where $A(i)$ is the fraction of the grid cell whose the infiltration capacity is lower than i ($0 \leq A(i) \leq 1$), i_m is the maximum infitration capacity of the grid cell, and b is the curvature parameter, which controls the distribution function A : the runoff is high when b is high, and low when b is small.
In the grid cell, the runoff is given by :

$$Q_r = \int_i^{i+P} A(i)di = P + \frac{i_m}{b+1}\left[\left(1 - \frac{i+P}{i_m}\right)^{b+1} - \left(1 - \frac{i}{i_m}\right)^{b+1}\right] \tag{4.25}$$

For a water content w_2, the saturated fraction of the grid cell ($A(w_2)$) is given by:

$$A(w_2) = 1 - \left(1 - \frac{w_2}{w_{sat}}\right)^{\frac{b}{b+1}} \tag{4.26}$$

After preliminary testing of this parameterization on the Adour watershed, *Habets et al.* [1999] found that the parameterization generated too much runoff in summer for dry soil conditions. To avoid this problem, a threshold was introduced in the soil wetness, under which runoff was not produced. This threshold was set to be the wilting point (w_{wilt}).

TOPMODEL approach TOPMODEL (TOPography based MODEL) attempted to combine the important distributed effects of channel network topology and dynamic contributing areas for runoff generation (*Beven and Kirkby* [1979], *Sivapalan et al.* [1987]). This formalism takes into account topographic heterogeneities explicitly by using the spatial distribution of the topographic indices, $\lambda_i(m)$, in each grid-cell defined as follows:

$$\lambda_i = \ln\left(a_i / \tan\beta_i\right) \tag{4.27}$$

where $a_i(m)$ is the drainage area per unit of contour of a local pixel, i, and $\tan\beta_i$ approximates the local hydraulic gradient where β_i is the local surface slope. If the pixel has a large drainage area and a low local slope, its topographic index will be large and thus, its ability to be saturated will be high. Then, this topographic index can be related to a local water deficit, and using the spatial distribution of the topographic indices over the grid cell, a saturated fraction, fsat, inversely proportional to the grid cell mean deficit, $D_t(m)$, can be defined. The "coupling" between TOPMODEL and ISBA was proposed by *Habets and Saulnier* [2001] and generalized by *Decharme et al.* [2006]. The active layer used for the ISBA-TOPMODEL coupling is the rooting layer, and not the total soil column. TOPMODEL describes generally the evolution of a water storage deficit near the soil surface that reacts quasi-instantaneously following rainy events (*Beven and Kirkby* [1979]). In that case, the root zone appears to be a reasonable compromise in ISBA. So, the relation between the grid cell mean deficit and the soil moisture computed by ISBA is simply expressed as:

$$0 \leq D_t = (w_{sat} - w_2) \times d_2 \leq d_0 \tag{4.28}$$

where $d_2(m)$ is the rooting depth and $d_0(m)$ the maximum deficit computed as the difference between the saturation, w_sat, and the wilting point, w_wilt :

$$d_0 = (w_{sat} - w_{wilt}) \times d_2 \tag{4.29}$$

So for a given rooting soil moisture, w_2, a mean deficit, D_t, is calculated and it is therefore possible to determine the saturated fraction of the grid-cell. The runoff, Q_{top}, is thus simply given by: $Q_{top} = P_g \times f_{sat}$ where P_g is the throughfall rain rate. For w_2 lower than the wilting point, the mean deficit is a maximum, $D_t = d_0$, $f_{sat} = 0$ and no surface runoff occurs. Note that, the spatial distribution of the topographic index in each grid-cell can be computed with the three- parameter gamma distribution introduced by *Silvapalan et al.* [1987]. The three parameters are derived from the mean, standard deviation, and skewness of the actual distribution that can be done by the HYDRO1K dataset at a 1 km resolution or another database. This TOPMODEL approach has been intensively validated both at the regional and global scale (*Decharme et al.* [2006], *Decharme and Douville* [2006 and 2007]).

Horton runoff approach. The Horton runoff occurs for a rainfall intensity that exceeds the effective maximum infiltration capacity. This infiltration excess mechanism tends to dominate the overland flow production in most desert or semiarid regions where short rainfall events can be very intense, but also where the absence of vegetation and other organic matter prevents the development of a porous soil structure through which water can move easily. The development of a thin crust at the soil surface can also inhibit the infiltration (arid or frozen soil). So the Horton runoff, Q_{hort}, is calculated using two infiltration functions following *Decharme and Douville* [2006]:

$$Q_{hort} = (1 - \delta_f) \times \max(0, S_m + P_g - I_{unf}) + \delta_f \max(0, S_m + P_g - I_f) \tag{4.30}$$

where S_m is snowmelt, P_g the throughfall rain rate, I_{unf} and I_f the infiltration functions over unfrozen and frozen soil, and δ_f the fraction of the frozen soil. These functions depend on root zone soil moisture conditions as well as on soil hydraulic properties. When the Horton runoff (being estimated only on the non-saturated fraction of the grid) is activated with the VIC or the TOPMODEL runoff, the surface runoff is given by :

$$Q_s = Q_{top\_or\_vic} + (1 - f_{sat})\, Q_{hort} \tag{4.31}$$

Treatment of drainage The gravitational drainage when $w > w_{fc}$ is given by the following equations (*Mahfouf and Noilhan* [1996], *Boone et al.* [1999]) :

$$K_2 = \frac{C_3}{\tau}\frac{d_3}{d_2}\max[0, (w_2 - w_{fc})] \tag{4.32}$$

$$K_3 = \frac{C_3}{\tau}\frac{d_3}{d_3 - d_2}\max[0, (w_3 - w_{fc})] \tag{4.33}$$

where τ is a characteristic time (one day).

C_3 is the *force-restore* parameter which account for the velocity at which the humidity profile is restored to the field capacity. This parameter depends on the hydraulic properties of the soil (*Noilhan and Mahfouf* [1996]. In ISBA, it can be described by an empirical equation and depends on the proportion of clay in the grid cell.

$$C_3 = 5.327 \cdot X_{clay}^{-1.043} \tag{4.34}$$

Subgrid drainage In the original formulation, the drainage stops below the field capacity w_{fc}. Within the framework of the Safran-Isba-Modcou model (*Habets et al.* [2008]) a subgrid drainage was introduced in order to account for unresolved aquifers in the model. A residual drainage was introduced in ISBA. The equations above are slightly modified :

$$K_2 = \frac{C_3}{\tau}\frac{d_3}{d_2}\max[w_{d2}, (w_2 - w_{fc})] \tag{4.35}$$

$$K_3 = \frac{C_3}{\tau}\frac{d_3}{d_3 - d_2}\max[w_{d3}, (w_3 - w_{fc})] \tag{4.36}$$

In this formulation, w_{di} (for each layer i) is expressed as :

$$w_{di} = w_{drain} max\left(0, \frac{min(w_{fc}, w_i) - w_{g_{min}}}{w_{fc} - w_{g_{min}}}\right) \tag{4.37}$$

where w_{drain} is a parameter to be calibrated, and $w_{g_{min}}$ a small parameter to avoid numerical problems. w_{drain} must be calibrated using discharge measurements during dry periods. See *Caballero et al.* [2007], and *Habets et al.* [2008] for calibration with discharge for the Safran-Isba-Modcou model.

Treatment of soil ice

The inclusion of soil freezing necessitates the addition of so-called phase change to the thermal and hydrologic transfer equations. In addition, a freezing/drying wetting/thawing analogy is used to model changes in the force-restore coefficients so that they must also be modified accordingly. Terms which have been added to the baseline ISBA scheme are underlined in this section, while terms which are modified are denoted using an $*$ superscript. Additional details related to soil freezing scheme can be found in *Boone et al.* [2000] and *Boone* [2000b].
The basic prognostic equations including soil ice are expressed as

$$\frac{\partial T_s}{\partial t} = C_T{}^* \left[R_n - H - LE^* - L_f(M_s - \underline{F_{g\,w}})\right] - \frac{2\pi}{\tau}(T_s - T_2) \ , \tag{4.38}$$

$$\frac{\partial T_2}{\partial t} = \frac{1}{\tau}(T_s - T_2) + C_G{}^* L_f \underline{F_{2\,w}} \ , \tag{4.39}$$

$$\frac{\partial w_g}{\partial t} = \frac{1}{d_1 \rho_w}\left[C_1{}^* (P_g - E_{g\,l} + M_s) - \underline{F_{g\,w}}\right] - \frac{C_2{}^*}{\tau}(w_g - w_{g\,\mathrm{eq}}{}^*) \tag{4.40}$$

$$(w_{\min} \le w_g \le w_{\mathrm{sat}} - w_{g\,f}) \ , \tag{4.41}$$

$$\frac{\partial w_2}{\partial t} = \frac{1}{d_p \rho_w}(P_g - E_{g\,l} - E_{tr}{}^* + M_s - \underline{F_{2\,w}}) - \frac{C_3}{\tau}\max(0\,,\ w_2 - w_{\mathrm{fc}}{}^*) \tag{4.42}$$

$$(w_{\min} \le w_2 \le w_{\mathrm{sat}} - w_{2\,f}) \ , \tag{4.43}$$

$$\frac{\partial w_{g\,f}}{\partial t} = \frac{1}{d_1 \rho_w}(F_{g\,w} - E_{g\,f}) \qquad (0 \le w_{g\,f} \le w_{\mathrm{sat}} - w_{\min}) \ , \tag{4.44}$$

$$\frac{\partial w_{2\,f}}{\partial t} = \frac{1}{(d_2 - d_1)\,\rho_w} F_{2\,w} \qquad (0 \le w_{2\,f} \le w_{\mathrm{sat}} - w_{\min}) \ . \tag{4.45}$$

where $w_{g\,f}$ and $w_{2\,f}$ represent the volumetric soil ice content ($\mathrm{m}^3\ \mathrm{m}^{-3}$) in the surface and deep-soil reservoirs, respectively. The phase change mass and heat sink (source) terms (F; $\mathrm{kg\ m^{-2}\ s^{-1}}$) are expressed as

$$F_{g\,w} = (1 - p_{sng})\,(F_{g\,f} - F_{g\,m}) \ , \tag{4.46}$$

$$F_{2\,w} = (1 - p_{sng})\,(F_{2\,f} - F_{2\,m}) \ , \tag{4.47}$$

where the m and f subscripts represent melting and freezing, respectively. The freezing and melting phase change terms are formulated using simple relationships based on the potential energy available for phase change. They are expressed for the surface soil layer as

$$F_{g\,f} = (1/\tau_i)\ \min\left[K_s\,\epsilon_{s\,f}\max(0,\,T_0 - T_s)/C_I\,L_f,\,\rho_w\,d_1\,(w_g - w_{\min})\right]\ , \tag{4.48}$$

$$F_{g\,m} = (1/\tau_i)\ \min\left[K_s\,\epsilon_{s\,m}\max(0,\,T_s - T_0)/C_I\,L_f,\,\rho_w\,d_1\,w_{g\,f}\right]\ , \tag{4.49}$$

and for the deep soil layer as

$$F_{2\,f} = (\delta_{2\,f}/\tau_i)\ \min\left[\epsilon_{2\,f}\max(0,\,T_0 - T_2)/C_I\,L_f,\,\rho_w\,(d_2 - d_1)\,(w_2 - w_{\min})\right]\ , \tag{4.50}$$

$$F_{2\,m} = (1/\tau_i)\ \min\left[\epsilon_{2\,m}\max(0,\,T_2 - T_0)/C_I\,L_f,\,\rho_w\,(d_2 - d_1)\,w_{2\,f}\right]\ . \tag{4.51}$$

The characteristic time scale for freezing is represented by τ_i (s). The phase change efficiency coefficients, ϵ, introduce a dependence on the water mass available for phase changes which are expressed as the ratio of the liquid volumetric water content to the total soil porosity for freezing, and the ratio of ice content to the porosity for melting. The ice thermal inertia coefficient is defined as $C_I = 2(\pi/\lambda_i\,C_i\rho_i\tau)^{1/2}$ (J m^{-2} K^{-1}). The insulating effect of vegetation is modeled using a coefficient defined as

$$K_s = \left(1 - \frac{veg}{K_2}\right)\left(1 - \frac{LAI}{K_3}\right)\ , \tag{4.52}$$

where the dimensionless coefficients have the values $K_2 = 5.0$ and $K_3 = 30.0$ (*Giard and Bazile* [1999]). The most direct effect of vegetation cover is to slow the rate of phase changes for more dense vegetation cover as energy not used for phase change is assumed to cool/warm the vegetative portion of the lumped soil-vegetation layer.

The deep-soil phase change (freezing) term is multiplied by a factor ($\delta_{2\,f}$) which essentially limits ice production during prolonged cold periods. It is defined as 0 if $z_f \geq z_{f\max}$ where

$$z_{f\max} = 4/\left(C_G{}^*\,c_g\right) \tag{4.53}$$

and the actual depth of ice in the soil is defined as

$$z_f = d_2\left(\frac{w_{2\,f}}{w_{2\,f} + w_2}\right) \qquad (0 \leq z_f < d_2) \tag{4.54}$$

Ice is assumed to become part of the solid soil matrix. This is accomplished by defining the modified porosity (eg. *Johnsson and Lundin* [1991] as

$$w_{sat}{}^* = w_{sat} - w_{j\,f} \tag{4.55}$$

where j corresponds to the surface (g) or sub-surface (2) soil water reservoirs. This, in turn, is used to modify the force-restore coefficients (see *Boone et al.* [2000] for more details).

4.1.2 Diffusive approach

Governing Equations

The governing equations for the heat and mass transfer from the surface down through the soil column for the snow-free case are expressed as (*Boone* [2000], *Boone et al.* [2000], *Habets et al.* [2002]):

$$c_h\frac{\partial T_g}{\partial t} = \frac{\partial G}{\partial z} + \Phi \tag{4.56}$$

$$\frac{\partial w_l}{\partial t} = -\frac{\partial F}{\partial z} - \frac{\Phi}{L_f\rho_w} - \frac{S_l}{\rho_w} \qquad (w_{min} \leq w_l \leq w_{sat} - w_i) \tag{4.57}$$

$$\frac{\partial w_i}{\partial t} = \frac{\Phi}{L_f\rho_w} - \frac{S_i}{\rho_w} \qquad (0 \leq w_i \leq w_{sat} - w_{min}) \tag{4.58}$$

Eq. (4.56) is the vertical component of the heat transfer equation: heat flow is induced along the thermal gradient and due to convection, c_h is the total heat capacity (J m^{-3} K^{-1}): it is represented by a lumped heat capacity in the surface layer, and by the soil heat capacity (c_g) in the sub-surface layers. λ is the thermal conductivity (W m^{-1} K^{-1}), F is the vertical flow rate of water (m s^{-1}), T_g is the composite soil-vegetation temperature (K) at the surface and the soil temperature only for sub-surface layers, Φ (J m^{-3} s^{-1}) is a latent heat source/sink resulting from phase transformation of soil water, and the soil depth, z (m), is increasing downward.

w_l and w_i in Eq.s (4.57) and (4.58) represent the volumetric liquid water and liquid water equivalent ice contents of the soil (m^3 m^{-3}), respectively. They are related to the total volumetric water content (m^3 m^{-3}) through

$$w \;=\; w_l \,+\, w_i \;\; . \tag{4.59}$$

In Eq. (4.57), S_l (evapotranspiration, lateral inflow) and S_i (sublimation) represent external sources/sinks (kg m^{-3} $\mathrm{s}-1$), of the liquid and ice liquid equivalent soil water, respectively, L_f is the latent heat of fusion (3.337 $\times 10^5$ J kg^{-1}), and ρ_w is the density of liquid water (1000 kg m^{-3}). The total soil porosity is w_{sat} (m^3 m^{-3}), and w_{min} is a minimum liquid water threshold (0.001 m^3 m^{-3}).

The phase change terms on the right-hand sides of Eq.s (4.57) and (4.58) represent a mass transfer between the solid and liquid phases of the soil water. The continuity equation for the total soil volumetric water content is obtained by adding Eq.s (4.57) and (4.58) and then substituting Eq. (4.59) into the resulting expression to have

$$\frac{\partial w}{\partial t} \;=\; -\frac{\partial F}{\partial z} \,-\, \frac{1}{\rho_w}\,(S_i \,+\, S_l) \qquad\qquad (w_{min} \,\leq\, w \,\leq\, w_{sat}) \;\; .$$

Surface and soil heat transfer

Heat flow is along the thermal gradient, so that the soil heat flux (W m^{-2}) can be expressed as

$$G = \lambda \frac{\partial T}{\partial z} \;\; .$$

The soil thermal conductivity and heat capacity are expression as functions of soil properties and moisture. The parameterizations are described below.

Calculation of the thermal properties The thermal heat capacity and thermal conductivity are parameterized as functions of the soil moisture and texture by most SVAT schemes. SVAT schemes which participated in PILPS-phase2c predicted, in general, ground heat fluxes poorly, which is most likely related to thermal conductivity parameterization (*Liang et al.* [1998]). ISBA uses the formulations from *McCumber and Pielke* [1981: MP81] together with parameter values from *Clapp and Hornberger* [1978] to evaluate the heat capacity and thermal conductivity (*Noilhan and Planton* [1989: NP89]), but it is known that thermal conductivity estimates using the MP81 model tend to be too large for wet conditions (nearing saturation) while underestimating thermal conductivity for dry soils. Also, there is no consideration of frozen soils in this formulation. There are several alternatives to using the MP81 model for thermal conductivity, and one such method is that discussed in *Peters-Lidard et al.* [1998]. The layer-averaged soil heat capacity can be written as

$$c_{g\,j} \;=\; (1 - w_{sat}) C_{soil} \rho_{soil} \,+\, w_{l\,j} c_w \,+\, w_{i\,j} c_i \tag{4.60}$$

where c_i and c_w are the heat capacities of ice and liquid water, (J K^{-1} m^{-3}). C_{soil} is the specific heat of the soil (J kg^{-1} K^{-1}) and ρ_{soil} represents the soil dry density. The specific heat (C_{soil}) value of 733 J kg^{-1} K^{-1}

for soil minerals/quartz from *Peters-Lidard et al.* [1998] is used. The dry density is sometimes measured, but it can also be estimated from the soil porosity assuming the same solids unit weight (*Peters-Lidard et al.* [1998]):

$$\rho_{soil} \;=\; (1 - w_{sat})\rho_{solids} \;\;,$$

where ρ_{solids} represents the unit weight of the solids (2700 kg m^3). The heat capacity of air in the soil is neglected in Eq. (4.60).

For fine soils or coarse frozen soils, the method of *Johansen* [1975] was shown by *Farouki* [1986] to be the most accurate relative to other commonly used methods for calculating thermal conductivity. Following *Peters-Lidard et al.* [1998], the thermal conductivity is calculated as the weighted sum of the dry and saturated thermal conductivities from (*Johansen* [1975])

$$\lambda \;=\; K_e\,\lambda_{sat} \;+\; (1 - K_e)\,\lambda_{dry} \tag{4.61}$$

where K_e is the non-dimensional Kersten number.

The dry thermal conductivity is defined as

$$\lambda_{dry} \;=\; \frac{0.135\rho_{soil} \;+\; 64.7}{\rho_{solids} \;-\; 0.947\rho_{soil}} \;\;,$$

where λ_{dry} is in W $\mathrm{m}^{-1}\,K^{-1}$. For crushed rock,

$$\lambda_{dry} \;=\; 0.039\,{w_{sat}}^{-2.2} \;\;.$$

The saturated thermal conductivity is written as

$$\lambda_{sat} \;=\; {\lambda_{soil}}^{(1-w_{sat})}\,{\lambda_i}^{(w_{sat}-\chi_u)}\,{\lambda_w}^{\chi_u} \tag{4.62}$$

where χ_u represents the unfrozen volume fraction of the soil. It is defined as

$$\chi_u \;=\; w_{sat}\,(w_l/w) \qquad\qquad (0 \;\leq\; \chi_u \;\leq\; w_{sat}) \;\;.$$

In Eq. (4.62), λ_i represents the thermal conductivity of ice (2.2 W $m^{-1}\,K$), λ_w represents the thermal conductivity of water (0.57 W $m^{-1}\,K$), and the thermal conductivity of solids is written as

$$\lambda_{soil} \;=\; {\lambda_q}^{q}\,{\lambda_o}^{1-q} \;\;.$$

The quartz content ($0 \leq q \leq 1$) is non-dimensional. It is fit as a function of sand (following the method of *Noilhan and Lacarrère* [1995] using the data from PL98:

$$q \;=\; 0.038 \;+\; 0.0095\,X_{\mathrm{sand}} \tag{4.63}$$

where the fraction of the soil comprised by sand is represented by X_{sand} (%). The relation is shown graphically in Fig. (4.3). The thermal conductivity of quartz is represented as λ_q (7.7 W $m^{-1}\,K$), and the thermal conductivity of other minerals is represented as λ_o (W $m^{-1}\,K$) where

$$\lambda_o \;=\; \begin{cases} 2.0 & q > 0.2 \\ \\ 3.0 & q \leq 0.2 \end{cases} \;\;.$$

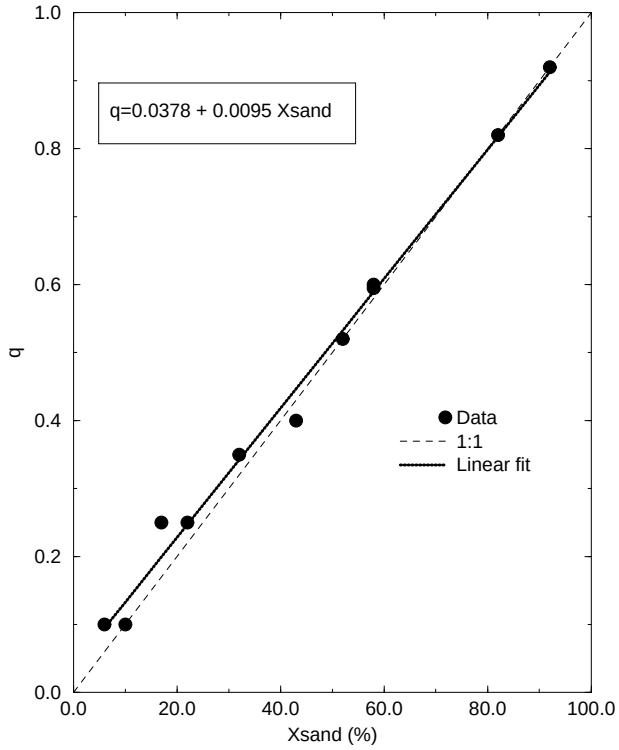

Figure 4.3: The relation between quartz content (q) and sand fraction ($X_{\rm sand}$) of the soil (%). The relationship between quartz and sand content is described by Eq. (4.63). The data are plotted using the values of q from *Peters-Lidard et al.* [1998] and the sand fraction from *Cosby et al.* [1984].

The Kersten number is written as

$$K_e = \begin{cases} 0.7 \log_{10}\theta + 1.0 & \theta > 0.05 \quad \text{coarse} \\ \log_{10}\theta + 1.0 & \theta > 0.1 \quad \text{fine} \end{cases},$$

and for frozen soils it is

$$K_e = \theta \tag{4.64}$$

where θ is the degree of saturation (w/w_{sat}) of the soil layer. Because use of Eq. (4.64) can result in a large jump in K_e as a soil begins to freeze, the following expression is used for partially frozen fine soils:

$$K_e = (w_l/w)\,(\log_{10}\theta + 1.0) + (w_i/w)\theta \tag{4.65}$$

The same weighting scheme in Eq. (4.65) can be used for coarse soils as well.

Integration of the heat equation Integrating the heat transfer equation [Eq. (4.56)] downward into the soil to obtain the average temperature for N soil layers:

$$\int_{-z_j}^{-z_{j-1}} c_h \frac{\partial T_g}{\partial t} dz = \int_{-z_j}^{-z_{j-1}} \frac{\partial G}{\partial z} dz + \int_{-z_j}^{-z_{j-1}} \Phi dz \tag{4.66}$$

where

$$T_{g,j} = \frac{1}{\Delta z_j} \int_{-z_j}^{-z_{j-1}} T_g dz \tag{4.67}$$

$T_{g,\,j}$ is the layer averaged temperature ($j = 1, ..., N$), the vertical index j is increasing downward and Δz_j is defined as $z_j - z_{j-1}$.
Carrying out the integration in Eq. 4.66 using the operator in Eq. 4.67 yields

$$\Delta z_j c_{h\,j} \frac{\partial T_{g,\,j}}{\partial t} \;=\; G_{j-1} \;-\; G_j \;+\; \Delta z_j \Phi_j \tag{4.68}$$

The layer average temperature $T_{g,\,j}$ is assumed to be centered at $(z_j + z_{j-1})/2$. The layer-averaged heat capacity of each layer is represented as

$$c_{h\,j} \;=\; \begin{cases} c_{g\,j} & (j = 2, N) \\ 1/\left(C_T\,\Delta z_1\right) & (j = 1) \end{cases} .$$

where the surface thermal inertia coefficient (C_T: K m^{-2} J^{-1}) is described in the next section. The soil heat flux across each level z_j is defined using the flux defined from *Carslaw and Jaeger* [1959] as

$$G_j = \;\overline{\lambda}_j \frac{\left(T_{g,\,j} - T_{g,\,j+1}\right)}{\left(\Delta z_j + \Delta z_{j+1}\right)/2} \;\;,$$

where $\overline{\lambda}_j$ is the thermal conductivity at the interface between two layers expressed as

$$\overline{\lambda}_j \;=\; \frac{\Delta z_j + \Delta z_{j+1}}{\left(\Delta z_{j+1}/\lambda_{j+1}\right) \,+\, \left(\Delta z_j/\lambda_j\right)} \;\;.$$

In general, the contribution of convective heating to the local soil temperature change is relatively small and can be neglected. Vapor transfer effects have been incorporated and are currently being tested: they are not outlined here. The model grid configuration is shown in Fig. 4.4. The shaded region at the surface represents a vegetation/biomass/litter layer. The prognostic variables ($T_{g,\,j}$, w_l, and w_i) are shown (water store variables will be discussed in subsequent sections).

Boundary conditions

Upper boundary condition The surface temperature of the mixed soil-vegetation medium is expressed as:

$$\frac{1}{C_T}\frac{\partial T_s}{\partial t} \;=\; R_n - H - LE - G_1 + \Delta z_1 \Phi_1 \tag{4.69}$$

where $T_s = T_{g,\,1}$, and the flux between the atmosphere and the surface is expressed as $G_0 = G = R_n - H - LE$. This definition of the prognostic equation for T_s is similar to that presented by *Bhumralkar* [1975] and *Blackadar* [1979]. It is the same as the standard Force-Restore method of *Noilhan and Planton* [1989] if G_1 is expressed as a restore term. The thermal inertia coefficient for the composite surface layer is expressed as

$$C_T = \frac{1}{veg/C_V + (1 - veg)/C_G}$$

where veg represents the vegetation cover fraction. The thermal inertia for the vegetation (C_V) can be case or species dependent. The soil thermal inertia is defined following *Noilhan and Planton* [1989] as

$$C_G = 2\left(\frac{\pi}{\lambda_1 c_{g\,1}\tau}\right)^{1/2}$$

where τ is a time constant corresponding to one day. In ISBA, the vegetation medium and the uppermost soil layer are lumped together and are assumed to have the same temperature (i.e. $T_s = T_v$, where T_v represents

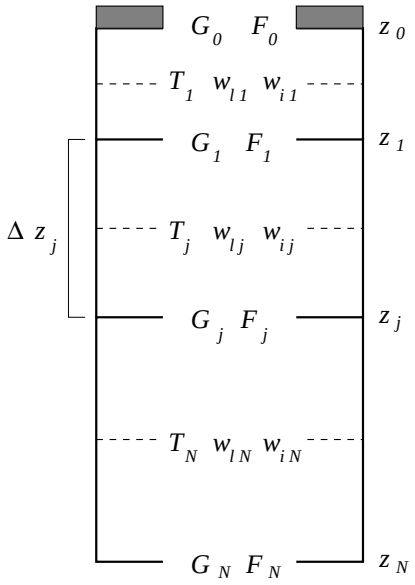

Figure 4.4: The model grid configuration: soil prognostic variables temperature ($T_{g,\,j}$), liquid volumetric water content ($w_{l\,j}$) and volumetric ice content ($w_{i\,j}$) are layer mean quantities. The soil heat (G_j) and liquid water fluxes (F_j) are evaluated at each level, z_j. The surface energy budget is evaluated defining $T_s = T_{g,\,1}$. The shaded region at the surface represents a vegetation/biomass/litter. The soil depth, z, is increasing downward (away from the atmosphere).

the vegetation temperature). The uppermost soil thickness, Δz_1, must be chosen to be sufficiently thin in order to be consistent with the daily surface temperature cycle (i.e., several cm).
The flux between the surface layer and the sub-surface soil layer is expressed as

$$\begin{array}{rcl} G_1 & = & 2\,\overline{\lambda}_1 \frac{(T_s - T_{g,\,2})}{\Delta z_1 + \Delta z_2} \\ \overline{\lambda}_1 & = & \frac{\Delta z_1 + \Delta z_2}{(\Delta z_1/\lambda_s) + (\Delta z_2/\lambda_2)} \end{array} \qquad (4.70)$$

The thermal conductivity of the surface layer is represented by λ_s. There is an option to include the effects of a vegetation/mulch/thin biomass litter layer using:

$$\lambda_s = \left[1 - veg\,(1 - f_v)\right] \lambda_1$$

where f_v is a reduction factor for the surface layer thermal condictivity due to the presence of mulch or organic material. The value of this parameter ranges between $0 < f_v \leq 1$, depending upon the insulating

effect of the material. Following from the ideas of *Gonzalez-Sosa et al.* [1999], it is assumed that the humidity effects dominate the mulch thermal conductivity. Based on the aforementioned work at MUREX, f_v is currently assigned a value of 0.10 (meaning the mulch thermal conductivity is roughly a tenth of that corresponding to the soil). The impact of assuming a lower thermal conductivity for the mulch layer is to increase the insulation of the soil (relative to a baresoil case) thereby increasing the surface energy (which can then increase the surface temperature diurnal wave amplitude, augment the surface fluxes, etc.) and diminishing the thermal wave penetration depth within the soil. In the limit when there is no vegetation (i.e., veg = 0), the thermal inertia coefficient collapses into $1/C_T = \Delta z_1 c_g$ and $\lambda_s = \lambda_1$ so that Eq. (4.69) takes on exactly the same form as the sub-surface soil temperature equations. When the mulch-layer option is inactive, then $\lambda_s = \lambda_1$.

Lower boundary condition The average temperature for the lowest layer is written using Eq.(4.68) as

$$\frac{\partial T_N}{\partial t} \;=\; \frac{(G_{N-1} \,-\, G_N)}{c_{g\,N}\,\Delta z_N} \;\;.$$

where the heat flux from below z_N is assumed to be negligible, resulting in a zero-flux lower boundary condition (i.e. $G_N = 0$). Note that in order for this assumption to be valid, z_N must be sufficiently large (deep). The annual temperature wave penetration depth is, in general, on the order of several meters (eg., Figs 4.5 and 4.6), so that z_N must be at least this deep in oder to accurately model the soil temperature profile at time scales of an annual cycle or more. An alternate method to increasing the soil depth is to specify the lower boundary flux using an annual mean soil temperature and an appropriate scaling depth (*Lynch-Stieglitz* [1994]). This depth can be estimated as the annual wave penetration depth [see Eq. (4.73)]. The only drawback is that the mean annual soil temperature and the annual wave penetration depth must be known *a priori*. The advantages are that less model layers can be used (a lower total model depth) thereby reducing computational expense and memory/storage requirements, and the soil temperature profile is "constrained" to some extent by observational data. Currently in the model, there is an option to apply a prescribed T^* (either as a constant or varying in time) at z_N

$$G_N \;=\; \lambda_N \,\frac{[T_N \,-\, T^*\,(z = z_N)]}{(z_N + z_{N-1})\,/2} \;\;,$$

Vertical grid The soil model grid levels do not necessarily have constant spacing. The assumption that the vertical temperature gradients are largest near the surface and smaller deeper in the soil indicates that the grid spacing can increase with increasing soil depth. It is of interest to specify the first grid level to be thin enough to resolve the diurnal temperature wave. An estimate of this depth is calculated using conductivity calculated by Eq. (4.61) for thawed soils with the relation for wave penetration depth from *Dickinson* [1988]:

$$z_d \;=\; \left(\frac{\lambda_1\,\tau}{c_{g\,1}\,\pi}\right)^{1/2} \tag{4.71}$$

Since the diurnal wave penetration depth (z_d) is a function of soil moisture and texture, an average or maximum value could also be used to a good approximation: this value might represent the z_d depth for the average soil moisture etc. The diurnal wave penetration depths computed using Eq. (4.71) are shown in Fig. (4.6). The depth z_d is plotted as a function of the normalized volumetric water content defined as

$$w_{norm} \;=\; \frac{w \,-\, w_{wilt}}{w_{sat} \,-\, w_{wilt}} \qquad\qquad (0 \,\leq\, w_{norm} \,\leq\, 1) \tag{4.72}$$

The z_d depth usually ranges from 12-18 cm for most soils across their nominal range of soil moisture: values in the range from 12-15 cm could be used for most general cases.

It is of interest to compare the method of Johansen to the method of *McCumber and Pielke* [1981] which is used by many surface vegetation atmosphere transfer (SVAT) schemes including ISBA (*Noilhan and Planton* [1989]). The z_d values computed using the method of *McCumber and Pielke* [1981] together with the soil classification and hydrological parameter values For the force-restore method used by ISBA, this variability in z_d is accounted for as there are no fixed soil depths which effect the diurnal cycle. But when using a fixed grid geometry, as is the case for the diffusion method outlined here, z_d calculated from the method of Johansen is more consistent with a fixed grid geometry.

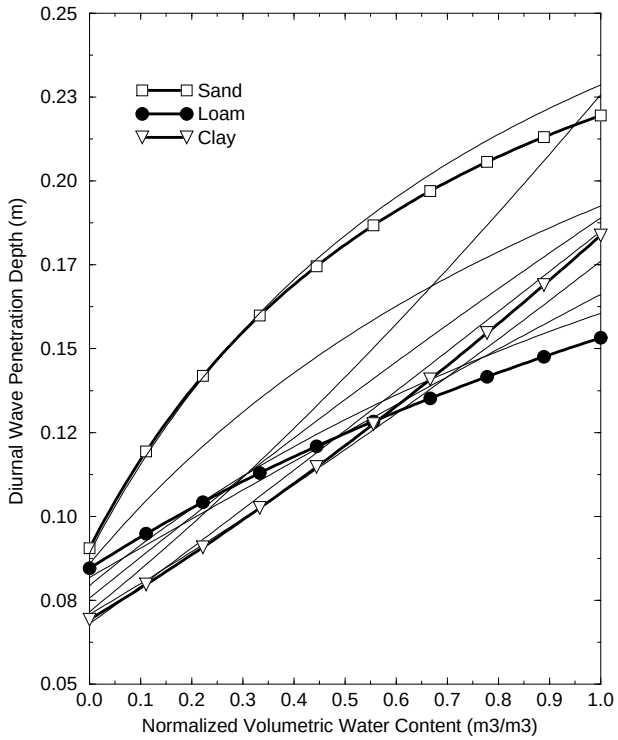

Figure 4.5: The diurnal temperature wave penetration depths (z_d) for the 11 soil classes from *Clapp and Hornberger* [1978]. Depths are plotted as a function of normalized soil water content [Eq. (4.72)]. Thermal conductivity is calculated using the method of *McCumber and Pielke* [1975] together with soil hydraulic parameter values from *Clapp and Hornberger* [1978]. Soil depths are in m.

The depth of the lower limit of the soil-temperature model domain depends upon the time scale: if annual cycles are to be properly handled, the lower boundary depth z_N can be determined using Eq. (4.71) as

$$z_a \;=\; \left(\frac{\lambda \, 365 \, \tau}{c_g \, \pi} \right)^{1/2} \tag{4.73}$$

where z_a denotes the annual wave penetration depth. Note that c_g and λ should be evaluated using an estimate of the total soil column mean water content. The annual wave penetration depths computed using Eq. (4.73) are shown in Fig. (4.6). The depth z_a (labeled on the right side of the figure) is plotted as a function of the normalized volumetric water content.

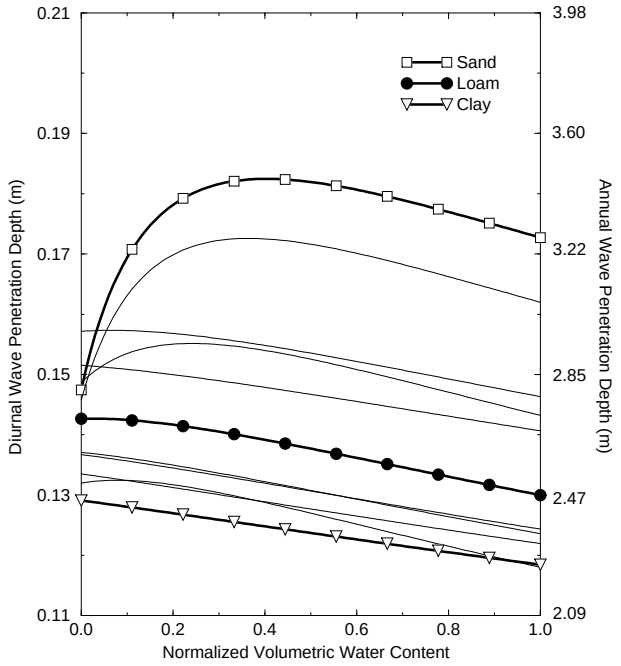

Figure 4.6: The diurnal and annual soil temperature wave penetration depths (z_d) for the 11 soil classes from *Clapp and Hornberger* [1978]. Depths are plotted as a function of normalized soil water content [Eq. (4.72)]. Thermal conductivity is calculated using the method of *Johansen* [1975] as presented by *Peters-Lidard et al.* [1998]. Soil depths are in m: z_d should be used as a guild-line for determining the maximum uppermost soil layer depth, z_1, and the minimum total soil depth, z_N.

Numerical solution of the soil temperature equation Neglecting the phase transformation term, Eq. (4.68) can be written using an implicit time scheme as

$$T_j{}^n \;=\; T_j{}^{n-1} \;+\; \frac{\Delta t}{c_{g\,j}\,\Delta z_j}\left[(1-\varphi)\left({G_{j-1}}^{n-1} \;-\; {G_j}^{n-1}\right) + \varphi\left({G_{j-1}}^{n} \;-\; {G_j}^{n}\right)\right] \tag{4.74}$$

where $\varphi = 1$ (backward difference) is currently used for the soil temperature profile ($\varphi = 1/2$ corresponds to the Crank-Nicolson scheme). Using either scheme, the linear set of diffusion equations can be cast in tridiagonal form and solved with relative ease. Although the Crank-Nicolson scheme is more accurate (second order), the surface energy budget equation is solved in ISBA using the backward difference scheme, so for consistency this scheme is used to evaluate the diffusion term in Eq. (4.68).
The superscripts $n-1$ and n represent the values at the beginning and end of the time step, Δt, respectively. The solution method is shown in Appendix B. Once the new temperature profile has been determined, phase changes are evaluated and the profile is updated. The phase change method is described in section 4.

Liquid Soil Water

The vertical soil water flux from Eq. (4.57) is derived assuming soil water transfer arises due to pressure gradients and a background drainage, and it is expressed as

$$F \;=\; -k\,\frac{\partial}{\partial z}\left(\psi \;+\; z\right) \;-\; \frac{D_{\nu\psi}}{\rho_w}\frac{\partial \psi}{\partial z} - K_d \tag{4.75}$$

where F is the vertical soil water flux ($\mathrm{m\,s^{-1}}$), k is the hydraulic conductivity ($\mathrm{m\,s^{-1}}$), ψ is the soil matric potential (m), K_d is an additonal linear background (low) drainage term (m s-1), and z is the soil depth

(m). The first term on the right hand side of Eq. (4.75) represents Darcy's law for liquid water transfer. The second term represents the water flux due to vapor transfer. The third is used to maintain a minimum streamflow under dry conditions. The isothermal vapor conductivity $D_{\nu\psi}$ (kg m^{-2} s^{-1}) is a function of soil texture, water content and temperature following *Braud et al.* [1993], except for some slight modifications due to the inclusion of soil ice outlined here.
This representation of the fluxes results in the so-called "mixed-form" of the Richard's equation. It permits the use of a heterogenous soil texture profile (by considering the gradient of matric potential as opposed to soil water content).

Flux parameterization The vertical soil water flux term [Eq. (4.75)] can be expressed in more compact form as:

$$F = -\eta \frac{\partial \psi}{\partial z} - \zeta \tag{4.76}$$

where η ($\mathrm{m}^2\,\mathrm{s}^{-1}$) represents the effective diffusion coefficient and ζ is the total drainage flux (m s^{-1}). They are expressed as

$$\begin{aligned} \eta &= \wp\,(k + D_{\nu\psi}) \\ \zeta &= k + K_d \end{aligned} \tag{4.77}$$

The factor $\wp$ is a coefficient which acts to limit vertical diffusion in the presence of a freezing front (see [Eq. (4.80)]). The first term on the RHS of Eq. (4.76) is the diffusion term and usually is positive (directed upward), the exceptions possibly being during precipitation, snowmelt or perhaps soil thaw events. The second term on the RHS of Eq. (4.76) represents total drainage and is always directed (positive) downward. Note that if vapor diffusion is neglected, the soil is not frozen and the linear drainage term (option) is negligible, the vertical flux given by Eq. (4.75) collapses into the standard Darcy flux expression for liquid water movement:

$$F = -k \frac{\partial}{\partial z} (\psi + z) \quad .$$

Soil Freezing As a soil freezes, ice is assumed to become part of the soil matrix thereby reducing the liquid water holding capacity of the soil. The degree of saturation of the soil by liquid water is expressed as

$$\Theta = \frac{w - w_i}{w_{sat} - w_i} = \frac{w_l}{w_{sat\,l}} \qquad (0 \leq \Theta \leq 1) \ ,$$

where $w_{sat\,l}$ represents the soil liquid water holding capacity. The porosity is decreased in the presence of soil ice as it is assumed ice becomes part of the soil matrix (see *Boone et al.* [2000] for more information).
The hydraulic conductivity and soil water potential are related to the liquid volumetric soil water content through the relations (*Clapp and Hornberger* [1978]):

$$k = k_{sat}\,\Theta^{2b+3} \tag{4.78}$$

$$\psi = \psi_{sat}\,\Theta^{-b} \tag{4.79}$$

where b is an empirical parameter, k_{sat} is the hydraulic conductivity at saturation, ψ_{sat} is the water potential at saturation and w_{sat} is the soil porosity. In recent years, several SVATs (eg. VISA: *Yang and Niu* [2002]) have adopted the idea that the saturated hydraulic conducitivity decreases exponentially with increasing soil

depth (*Beven* [1984]). This can be handled by ISBA-DIF since Richard's equation is expressed in mixed-form (i.e. a heterogeneous profile of k_{sat} can be specified).
Soil ice has the effect of decreasing the hydraulic conductivity relative to a thawed soil with the same total soil moisture. The ice impedance coefficient is represented by $\wp$. It is calculated following *Johnsson and Lundin* [1991]:

$$\wp \;=\; 10^{-a_\wp\, w_i/w} \tag{4.80}$$

where the coefficient $a_\wp$ is currently assigned a value of 6 proposed by *Lundin* [1990]. This coefficient prevents an overestimation of the upward liquid water flux to the freezing front. Note that the model is rather sensitive to this parameter, and a calibration might be required to obtain optimal agreement with observations. The dependence of $\wp$ on ice content ratio (w_i/w) is shown in Fig. 4.7. Note that the effect of this coefficient is currently under investigation, and that alternate formulations (such as dependence on soil temperature rather than soil ice) will also be explored.

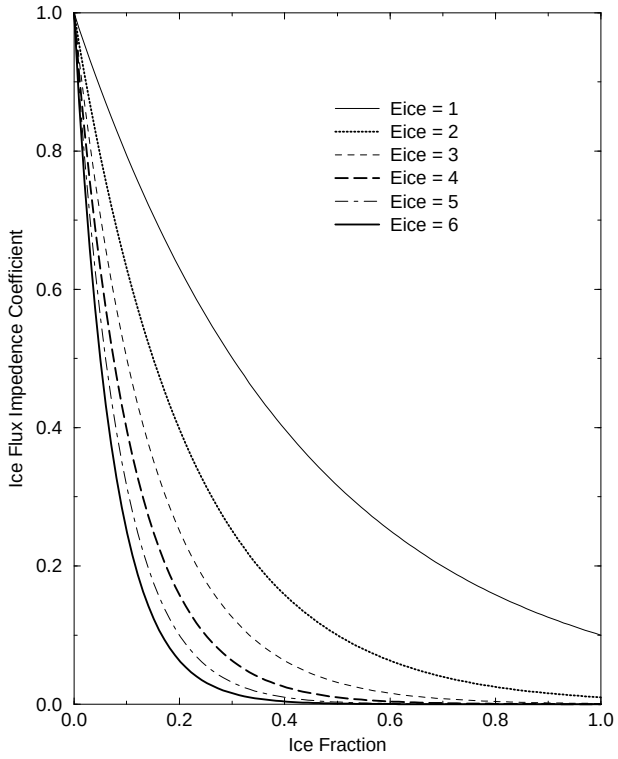

Figure 4.7: The dependence on the water flux impedance factor ($\wp$) on soil ice fraction (w_i/w) for various values of $a_\wp$ (denoted as "Eice" in the figure). This coefficient is multiplied by the vertical soil water flux, and as such can strongly modulate vertical flow of liquid water and subsequent freezing.

Vapor diffusion The isothermal vapor conductivity can be expressed as

$$D_{\nu\psi} \;=\; D_\nu \frac{\partial \rho_\nu}{\partial \psi} \tag{4.81}$$

where ρ_ν represents the water vapor density in the air-filled pore space of the soil, and D_ν represents an effective molecular diffusivity (*Milly* [1982]). It can be written following *Braud et al.* [1993] as

$$D_\nu \;=\; D_{\nu a}\, \alpha_\nu\, f_{\nu a} \frac{p}{(p - p_\nu)} \tag{4.82}$$

where the tortuosity is $\alpha_\nu = 0.66$, and the atmospheric and soil vapor pressures are represented by p and p_ν, respectively. The function $f_{\nu a}$ is defined as

$$f_{\nu a} = \begin{cases} [w_{sat} - (w_l + w_i)]\,[1 + (w_l + w_i)\,/\,(w_{sat} - w_k)] & (w > w_k) \\ \\ w_{sat} & (w \leq w_k) \end{cases} ,$$

where w_k is a parameter which defines the point corresponding to the loss of continuity of the liquid phase in the soil pores (0.05 m^3 m^{-3} for the current study). The function $f_{\nu a}$ is related to the available pore space for vapor, or volumetric air content ($w_{sat} - w_l - w_i$). The molecular diffusivity coefficient for water vapor is given as

$$D_{\nu a} = c_\nu \left(\frac{p_0}{p}\right)\left(\frac{T}{T_f}\right)^{n_\nu} ,$$

where $c_\nu = 2.17 \times 10^{-5}$ m^2 s^{-1}, $n_\nu = 1.88$, and $p_0 = 10^6$ Pa. It is assumed that the soil water vapor is in equilibrium with the liquid, and that the air is saturated with respect to the ice present in the soil so that the vapor density can be expressed as

$$\rho_\nu = \rho_{\nu\,sat}(T)\chi_{sat}\,h_\nu + (1 - \chi_{sat})\,\rho_{\nu\,sat\,i}\min(T, T_f) ,$$

where the humidity is given by

$$h_\nu = \exp\left(\frac{\psi\, g}{R_\nu\, T}\right) .$$

The soil ice factor is defined as

$$\chi_{sat} = (w_{sat} - w_i)/w_{sat} \tag{4.83}$$

Taking the derivative of ρ_ν with respect to ψ and substituting the resulting expression and Eq. (4.82) into Eq. (4.81) using the ideal gas law for water vapor results in

$$D_{\nu\psi} = \frac{\alpha_\nu\, p}{(p - p_\nu)} \frac{D_{\nu a}\, f_{\nu a}\, \chi_{sat}\, g\, p_{\nu\,sat}\, h_\nu}{(R_\nu\, T)^2} .$$

The diffusion coefficient (d_ν) is shown in Fig. (4.8) for four soil textures over the entire range of soil wetness (w_l/w_{sat}) assuming a constant temperature and pressure of 300 K and 101325 Pa, respectively. It is largest, in general, for the most coarse textured soils approximately at or below the soil permanent wilting point value. A comparison between the vapor diffusion and the hydraulic conductivity are shown in Fig. (4.9). This shows that vapor diffusion comprises the most significant contribution to the net diffusion process over a soil water range around the wilting point. In the Isba force-restore method, this vapor phase transfer is parameterized within the coefficient C_1 for dry soil (*Braud et al.* [1993] and *Giordani* [1995]

Linear Drainage ISBA is increasingly used in studies for which river hydrology is simulated. The standard Richard's equation poses a problem for dry conditions in that the observed constant minimum riverflow occuring during dry seasons is poorly simulated. The actual cause of such flows is most likely subterranian lakes, surface lakes, water table interactions, etc., which are all not currently explicitly modeled by ISBA. The most simplistic fix to this problem is to impose a linear drainage term which can be calibrated based on observed minimum riverflows outside of periods of active precipitation or snowmelt.
Etchevers et al. [2001] calibrated such a parameter for the 3-layer ISBA Force-Restore approach and greatly improved discharge statistics for certain sub-basins within the Rhone basin in France. In this method, a drainage is calculated assuming the water content is at some small increment just above field capacity

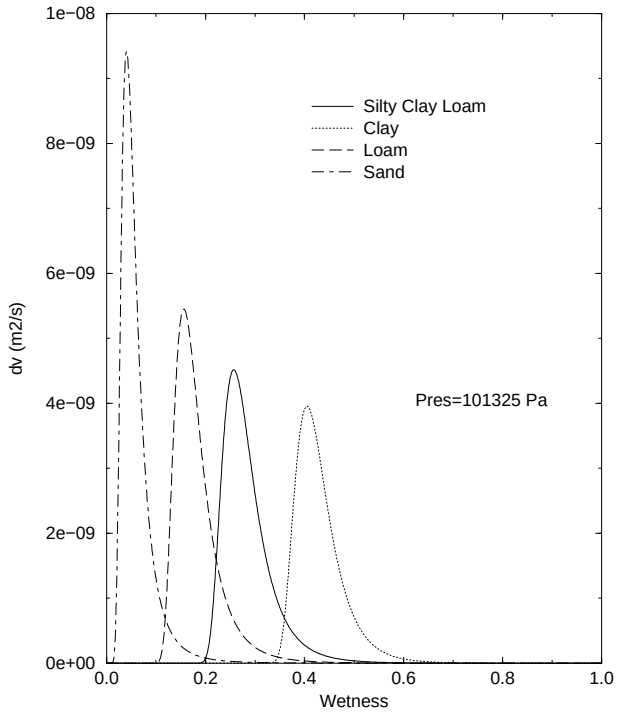

Figure 4.8: Soil vapor diffusion coefficient (d_ν) for four soil textures assuming constant soil temperature and pressure.

(thereby resulting in a steady, but relatively small drainage flux). Adapting this method into the current model results in

$$K_d = k_{sat}[(w_{fc} + w_{drain})/w_{sat}]^{2b+3} \times \left\{ \frac{[\min(w_{fc}, w_l) - w_{min}]}{(w_{fc} - w_{min})} \right\}$$

The term on the left of the multipication sign is constant in time. The rightmost term is a linear scaling term which reduces the constant drainage as the source soil layer dries out. The field capacity water content is given by w_{fc}. The w_{drain} can be calibrated and is generally on the order of 0.001 $\mathrm{m}^3\ \mathrm{m}^{-3}$, although it can vary by an order of magnitude. It is zero (therefore $K_d = 0$) when this option is off (i.e. local scale studies etc.).

Layer averaging Integrating Eq. (4.57) downward into the soil to obtain the prognostic equation for the layer-average volumetric liquid water content for each j layer gives

$$\int_{-z_j}^{-z_{j-1}} \frac{\partial w_l}{\partial t} dz \;=\; -\int_{-z_j}^{-z_{j-1}} \frac{\partial F}{\partial z} dz \;-\; \int_{-z_j}^{-z_{j-1}} \left(S_l - \frac{\Phi}{L_f \rho_w} \right) dz \tag{4.84}$$

where

$$w_{l\,j} \;=\; \frac{1}{\Delta z_j} \int_{-z_j}^{-z_{j-1}} w_l dz \tag{4.85}$$

$w_{l\,j}$ is the layer averaged volumetric liquid water content ($j = 1, ..., N$).
Carrying out the integration in Eq. 4.84 using Eq. 4.85 yields

$$\Delta z_j \frac{\partial w_{l\,j}}{\partial t} \;=\; F\Big|_{-z_j} \;-\; F\Big|_{-z_{j-1}} \;-\; Q_j \;-\; \frac{\Delta z_j\, \Phi_j}{L_f \rho_w} \;\;,$$

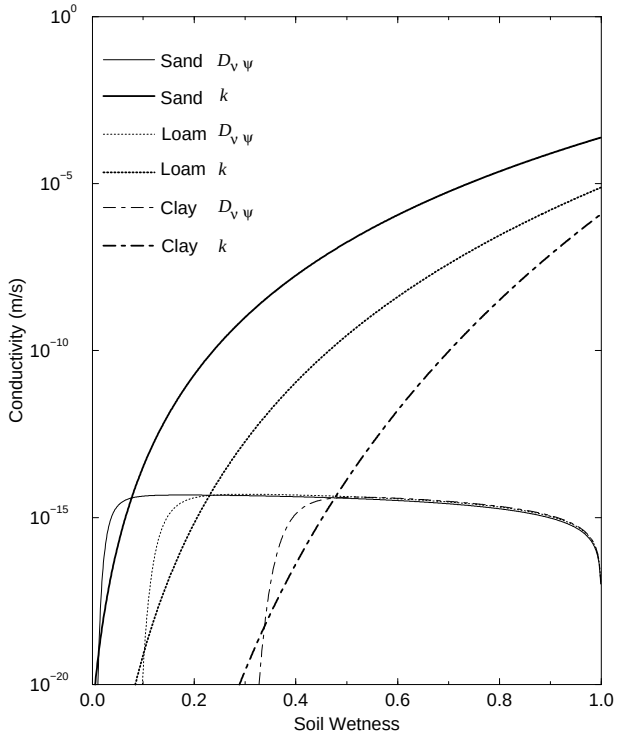

Figure 4.9: The total hydraulic conductivity contributions from liquid water (k) and vapor ($D_{\nu\psi}$) for three soil textures as a function of soil wetness. The soil temperature and surface atmospheric pressure have constant values of 285 K and 10^5 Pa, respectively.

where

$$Q_j \;=\; \Delta z_j \, S_j \tag{4.86}$$

is in kg m^{-2} s-1. The flux across a model level (z_j) is written as

$$F\Big|_{-z_j} \;=\; F_j \;=\; \eta_j(\tilde{\psi}_j) \left[\frac{\psi_{j+1} - \psi_j}{(\Delta z_j + \Delta z_{j+1})/2} \right] - \zeta_j \left(\tilde{\psi}_j \right) \tag{4.87}$$

$\tilde{\psi}$ represents the so-called interfacial matric potential. It is calculated from

$$\tilde{\psi}_j \;=\; \delta_{\psi\,j}\, \psi_j \;+\; (1 - \delta_{\psi\,j}) \psi_{leq\,j} \tag{4.88}$$

where the delta function $\delta_{\psi\,j}$ is defined as

$$\delta_{\psi\,j} \;= \begin{cases} 1 & \psi_j \geq \psi_{leq\,j} \\ \\ 0 & \psi_j < \psi_{leq\,j} \end{cases} .$$

$\psi_{leq\,j}$ is the interfaical matric potential assuming hydrostatic equilibrium. It is calculated assuming that the total matric potential or head is constant from the layer interface (z_j) to the mid-point of the layer below (*Noilhan and Planton* [1989], *Koster and Suarez* [1996]): $\partial\psi/\partial z = -1$:

$$\psi_{leq\,j} \;=\; \psi_{j+1} \;-\; (\Delta z_j + \Delta z_{j+1})/4 \;\; .$$

From Eq. (4.88), diffusivity and conductivity are evaluated using the so-called upstream value of the matric potential, which is similar to the simple model proposed by *Mahrt and Pan* [1984], except that the equilibrium matric potential value is used in place of the lower layer matric potential (equivalently the volumetric water content in their case as they assumed a homogenous soil texture profile). As in *Mahrt and Pan* [1984], the upper layer matric potential (water content in their case) is used in the presence of a wetting front. Such an interpolation is needed due to the coarse nature of the vertical grid mesh typically used in SVATs intended for atmospheric models. A graphic representation of the interpolation method is shown for two contiguous soil layers with different textures (and therefore, different soil hydraulic properties) in Fig. 4.10.

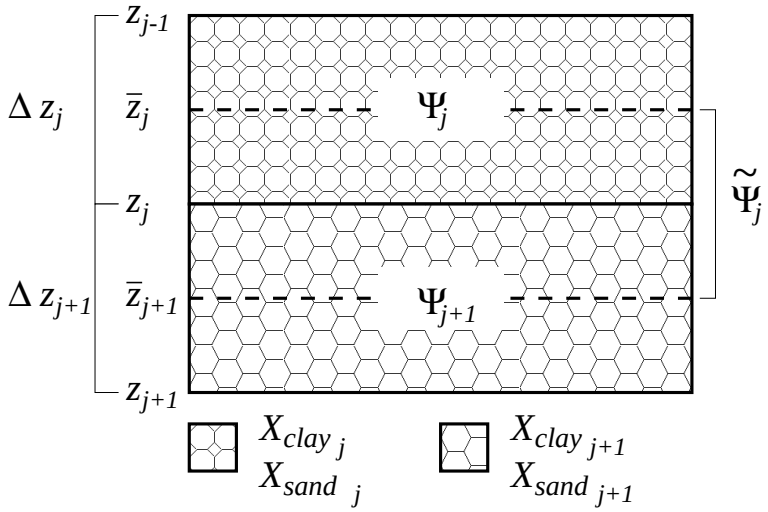

Figure 4.10: The interfacial soil matric potential. $\tilde{\psi}_j$ represents the matric potential centered at z_j, and $\Delta\overline{z}_j = (\Delta z_j + \Delta z_{j+1})/2$.

This method results in a better approximation of the soil water flux than specifying that the flux from the mid-point of layer Δz_j to z_j is equal to that from layer z_j to the mid-point of layer Δz_{j+1} (as is used to derive the soil heat flux), as the diffusivity and conductivity are more consistent with the soil water gradient (*Mahrt and Pan* [1984]).

Boundary Conditions

Lower Boundary The lower boundary condition is modeled as gravitational drainage (vertical diffusion is neglected). The mean water content of the lowest layer is used to evaluate the flux so that from Eq. (4.87) one can write

$$F_N \;=\; -\zeta_N \;=\; -k_N - K_d \;.$$

Under moist conditions, $F_N \approx -k_N$, whereas for very dry conditions, it is possible that K_d dominates the drainage (depending on the value specified for K_d).

The diffusion term (i.e. capillary rise across the lower model boundary) can be significant, however, when the water table is near z_N. An option exists for utilizing this information using a simple expression consistent with the vertical flux formulation used for the other model layers, however it is currently not included in the current model release (as typically water table information is not available in atmospheric models).

Upper Boundary The upper boundary condition represents infiltration. It is written as

$$I \;=\; -F_0 \;=\; \min(R_t - Q_r,\, -F_{max\,0}) \tag{4.89}$$

where I is infiltration (m s^{-1}), R_t (m s^{-1}) is the through-fall rate (sum of canopy drip, precipitation and snow-melt) and $F_{max\,0}$ represents the maximum water flux into the surface soil layer. The sub-grid surface runoff, Q_r, is assumed to be zero for local spatial scales, but it can be significant at larger scales (it is described below). For simplicity, it is assumed that the maximum infiltration rate is simply given by:

$$F_{max\,0} \;=\; k_{sat} \tag{4.90}$$

Note that for small or point scales, $F_{max\,0}$ can be sufficiently small compared to R_t to generate surface runoff from Eq. (4.89). But for climate scale applications (large time steps and spatially averaged precipitation rates), $F_{max\,0}$ from Eq. (4.90) will almost always be larger than R_t (except for the cases of thoroughly frozen soils or large snowmelt rates) because rain rates are averaged over relatively large spatial (and sometimes temporal) scales.

For non-local scale applications, an alternate form of generating surface runoff is needed. A variable-infiltration capacity (VIC: *Dümenil and Todoni* [1992]) sub-grid surface runoff scheme is used in ISBA (*Habets et al.* [1999]). Q_r represents sub-grid surface runoff from saturated regions within the computational unit/cell which is computed as

$$\begin{aligned} Q_{r\,\mathrm{crit}} \;&=\; \left[1 - \frac{(\overline{w}_r - \overline{w}_{wilt})}{(\overline{w}_{sat} - \overline{w}_{wilt})}\right]^{1/(1+B)} \;-\; \frac{R_t \Delta t}{\rho_w z_r}\left[\frac{1}{(1+B)(\overline{w}_{sat} - \overline{w}_{wilt})}\right] \\ Q_r \;&=\; R_t - \frac{\rho_w z_r}{\Delta t}\left\{ (\overline{w}_{sat} - \overline{w}_r) - (\overline{w}_{sat} - \overline{w}_{wilt})\left[\max\left(0,\, Q_{r\,\mathrm{crit}}\right)\right]^{1+B} \right\} \end{aligned} \tag{4.91}$$

with the constraints:

$$Q_r \;=\; 0 \qquad \text{if} \quad (Q_r < 0) \quad \text{or} \quad (\overline{w}_r \le \overline{w}_{wilt}) \;\;,$$

$\overline{w}_r$ represents the average total water content of a soil layer (liquid and solid water: w) integrated from the surface down to the depth z_r. It is defined as

$$\overline{w}_r = \frac{\left(\sum_{j=1}^{N_r} \Delta z_j\, w_j\right) + w_{N_r+1} \max\left(0,\, z_r - z_{N_r}\right)}{\left(\sum_{j=1}^{N_r} \Delta z_j\right) + \max\left(0,\, z_r - z_{N_r}\right)} \qquad (z_r \le z_N)$$

where N_r is the total number of soil layers for which $z_r \ge z_j$ (i.e. the depth is greater than or equal to the lower boundary of the soil layer j). Note that the pososity and wilting point volumetric water contents are also averaged over z_r using the same operator. This depth should be at least several tens of centimeters thick (*Liang et al.* [1996]).

It should also be noted that several authors use a form of Darcy's law assuming the soil right at the surface is saturated as the maximum potential infiltration rate (*Mahrt and Pan* [1984], *Abramopoulos et al.* [1988]). This, however, has a very minimal impact on the infiltration (compared to the above equation) for the time and space scales considered in typical ISBA applications, and the linearization of such a term can pose some numerical problems (the linearized surface flux can actually exceed the amount of water available for infiltration under some rare circumstances). For these two reasons, Eq. (4.90) is used currently in ISBA.

Solution method The equation for liquid water transfer is solved using:

$$\varrho_j({w_l}_j{}^n - {w_l}_j{}^{n-1}) \;=\; (1-\varphi)\left({F_j}^{n-1} \;-\; {F_{j-1}}^{n-1}\right) \;+\; \varphi\,({F_j}^n \;-\; {F_{j-1}}^n) \;-\; {Q_j}^n \;\;.$$

where $\varrho_j = \Delta z_j/\Delta t$, and n indicates the value at the end of the time step, Δt. The Crank-Nicolson time scheme is currently used to integrate the equations in time (i.e., $\varphi = 1/2$). The flux terms can be linearized or an iterative solution method can be used. The linearization method is obviously more attractive for numerical weather prediction applications as it consumes less CPUs, and for this method, an uppermost layer of several cm thickness can safely be used for typical GCM (upper limit for Δt) time steps (*Bonan* [1996]). Note that updates in mass owing to phase changes (Φ) are evaluated in a subsequent computation (see section 4).

Soil moisture sink term The sink term is composed of soil water losses/gains due to evapotranspiration/condensation and gains due to lateral inflow or so-called soil water excess. The production/reduction of soil ice decreases/increases the liquid soil water content while leaving the total soil water content unchanged.

Evapotranspiration Bare soil evaporation, E_g, is extracted from the uppermost soil layer only. Transpiration, E_{tr}, can be extracted from multiple layers. A normalized root-zone fraction is specified for each soil layer, and is zero for layers below the root zone. Normalized transpiration weights are then calculated based on the specified vertical root zone fraction and the thickness of each model soil layer:

$$\xi_j \;=\; \frac{\Upsilon_j\,\Delta z_j}{\sum_{j=1}^{N}\Upsilon_j\,\Delta z_j} \qquad\qquad (0 \;\le\; \xi_j \;\le\; 1) \;\;,$$

where ξ_j represents the transpiration weight. Note that $\sum_{j=1}^{N}\xi_j = 1$ unless there are no roots, in which case $\xi_j = 0$. Υ_j represents the root fraction:

$$\sum_{j}^{N}\Upsilon_j \;=\; 1 \;\;.$$

This parameter is not well known for many regions and transpiration from SVAT models can be highly sensitive to the vertical root zone distribution (*Desborough* [1997]): this study suggests the use of a uniform distribution. A uniform root zone distribution can be specified by setting Υ_j constant within the root zone soil layer(s), or a simple exponential function dependent on plant cover can be specified (*Jackson et al.* [1996]). In ISBA, the effect of water stress on transpiration is modeled using a normalized soil moisture factor (*Noilhan and Planton* [1989], *Calvet et al.* [1998a]):

$$w_{n\,j} \;=\; \frac{{w_l}_j - \chi_{sat\,j}\,w_{wilt\,j}}{\chi_{sat\,j}\,(w_{fc\,j} - w_{wilt\,j})} \qquad\qquad (\epsilon \;\le\; w_{n\,j} \;\le\; 1) \tag{4.92}$$

where w_{wilt} is the wilting point volumetric water content, and ϵ is a small numerical value ($\approx\; 10^{-3}$). The coefficient χ_{sat} is related to the reduction in layer-average porosity due to the inclusion of soil ice [Eq. (4.83)]. From Eq. (4.92), soil ice in the root zone can hinder plant evaporation even if atmospheric conditions are conducive to transpiration and the total soil water content is above field capacity.

The factor in Eq. (4.92) is applied to the stomatal conductance so that transpiration can proceed at an unstressed rate relative the soil water for moisture values above field capacity, and is negligible for soils drier than wilting point. The layer-averaged water stress factor, which is applied to the net transpiration, is calculated as *Pan and Mahrt* [1987]

$$\overline{w}_n \;=\; \sum_{j=1}^{N}\xi_j\,w_{n\,j} \;\;.$$

The above coefficients are simply used to partition the transpiration among the various root-zone soil layers.

Soil moisture excess When the increase over a given time period in observed total soil water content exceeds that of precipitation less evapotranspiration, a laterally induced source (negative sink) is assumed to occur (*Calvet et al.* [1998b]). This can be due to lateral inflow of water (most likely) or capillary rise from below the observation depth. Since vertical diffusion across the base of the model is assumed to be negligible, this source is parameterized as lateral inflow. The vertical distribution is assumed to be linear down to the depth of the soil moisture observations:

$$\upsilon_j \;=\; \frac{\delta_{\upsilon\, j}\Delta z_j}{\sum_{j=1}^{N}\delta_{\upsilon\, j}\Delta z_j} \;\;,$$

where υ_j represents the normalized soil water excess coefficient, and $\delta_{\upsilon\, j}$ is a delta function which is either 1 or 0 depending on whether or not excess inflow is occurring in layer j. For applications where soil moisture excess is not available, this source is set to zero.

Liquid water sink The external soil water source/sink term [Eq. (4.86)] is expressed as

$$Q_j \;=\; \xi_j\left(\frac{w_{n\, j}}{\overline{w}_n}\right) E_{tr} \;+\; \delta_{g\, j}\, E_{g\, L} \;-\; \upsilon_j\, Xs \;\;.$$

Xs represents the soil water excess (lateral inflow). $E_{g\, L}$ is the evaporation from the bare soil surface (uppermost layer), and $\delta_{g\, j}$ is a delta function which is unity only the uppermost soil layer ($\delta_{g\, 1} = 1$), and is zero for all the other soil layers. The uppermost layer is prescribed to be thin in order to capture the daily cycle in bare-soil evaporation. The root zone fraction in this layer, Υ_1, is usually set to zero. The transpiration, bare-soil evaporation and water excess terms are in units of $\mathrm{kg\ m^{-2}\,s^{-1}}$.

Soil ice

Soil ice [Eq. (4.58)] increases when there is energy available for ice production, while decreases are due to melting and sublimation. In order to avoid a more computationally intensive iterative solution procedure [between Eq.s (4.56)-(4.58)], the soil temperature is first calculated using Eq. (4.74), then the phase change term (Φ_j) is evaluated. The temperature for a given layer at time n will then be adjusted at the end of the time step such that ${T_j}^n \;\rightarrow\; T_f$ if melting or freezing occurs (where T_f is the freezing point temperature).
The method presented in *Boone et al.* [2000] and in *Boone* [2000] for ISBA-DIF has been modified owing to research involving PILPS-2e (*Bowling et al.* [2002]) with ISBA (*Habets et al.* [2002]). In original test simulations involving ISBA-DIF using the PILPS-2e experimental design and forcing, it was found that nearly all of the near surface water froze, and this caused some unrealistic conditions (although no observations are available to verify this). *Boone et al.* [2000] treated NWP-time-scale events, and soil freezing was not as extensive as in the PILPS-2e domain. Thus, it was decided to adopt an approach which determines a maximum liquid water content as a function of temperature using the Gibbs free energy method. See for example *Cox et al.* [1999], *Cherkauer and Lettenmaier* [1999] and *Koren et al.* [1999] for examples of this method used in SVATs. Many examples exist in soil-science literature: see *Boone* [2000] for references. The main difference between this method and the one presented in *Boone et al.* [2000] is that not all of the available liquid water is frozen. The method outlined herein represents a near seamless model change in that it does not augment CPU's significantly, and it requires no additional parameters.
The relation between the soil water potential and temperature for sub-freezing conditions is from *Fuchs et al.* [1978]:

$$\psi^* = \frac{L_f\,(T - T_f)}{g\,T}$$

The potential ψ^* can be substituted in the expression for the soil matric potential in order to obtain the maximum unfrozen (liquid) water content at a given soil temperature, T. Currently for ISBA, this is the *Brooks and Corey* [1966] model as modified by *Clapp and Hornberger* [1978], so that

$$w_{l\,\max} = w_{\rm sat}\left(\frac{\psi^*}{\psi_{\rm sat}}\right)^{-1/b}$$

During phase changes, the total soil water content ($w = w_l + w_i$) for each soil layer is conserved, so that, for example, as a soil freezes, the liquid water content will decrease owing to a corresponding increase in soil ice content (w_i). This concept can be used to establish the maximum temperature at which soil ice is present (again using the Gibbs free energy concept) as

$$T_{\max} = \frac{L_f\, T_f}{(L_f - g\,\psi)}$$

where the soil liquid water potential is defined as a function of the liquid water content using the relationship from *Clapp and Hornberger* [1978] [Eq. (4.79)]. The maximum unfrozen fraction ($w_{l\,\max}/w_{\rm sat}$) and $w_{l\,\max}$ as a function of temperature depression are shown in Fig. (4.11). for three soil textures. Note that a larger percentage of liquid water can freeze for more coarse textured soils and that relatively dry soils might have very cold temperatures before any freezing takes place.

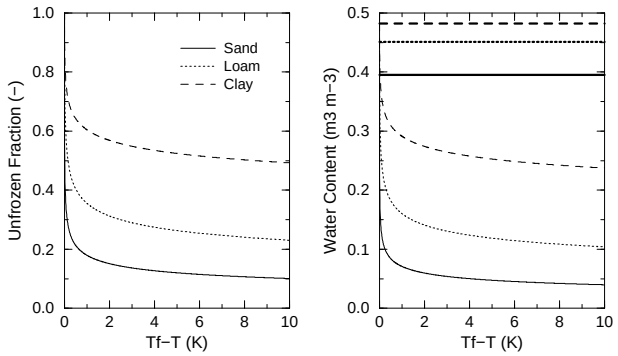

Figure 4.11: The maximum unfrozen fraction ($w_{l\,\max}/w_{\rm sat}$) and $w_{l\,\max}$ as a function of temperature depression for three soil textures. The corresponding porosity values (w_{sat}) are shown in the right panel (thick horizontal lines) as a reference.

The phase change term is parameterized in a manner similar to that presented in *Boone* [2000], *Boone et al.* [2000] and *Giard and Bazile* [2000], but with the available thermal energy evaluated using the difference $T_{\max} - T$ as opposed to $T_f - T$, and the available liquid water for freezing being defined using $w_l - w_{l\,\max}$ as opposed to $w_l - w_{l\,\min}$. The freezing and melting terms are, respectively:

$$\begin{aligned}
\Phi_{f\,j} = &\quad \min\left[K_s \epsilon_f \max\left(0,\, T_{\max\,j} - T_j\right) c_i,\;\; L_f \rho_w \max\left(0,\, w_{l\,j} - w_{l\,\max\,j}\right)\right] / \tau_i \\
\Phi_{m\,j} = &\quad \min\left[K_s \epsilon_m \max\left(0,\, T_j - T_{\max\,j}\right) c_i,\;\; L_f \rho_w w_{i\,j}\right] / \tau_i
\end{aligned} \tag{4.93}$$

where c_i is the heat capacity of ice (1.883×10^6 J K^{-1} m^{-3}). A parameter which represents the characteristic time scale for phase changes is represented by τ_i (*Giard and Bazile* [2000]). It can be determined through calibration, possibly (eventually) be related to soil texture. A constant value of 3300 s^{-1} is currently used. The expressions for the phase change efficiencies (ϵ_f and ϵ_m) are parameterized as functions of liquid soil water for freezing and soil ice for melting (similar to the method used by *Cogley et al.* [1990] and *Pitman et*

al. [1991]:

$$\epsilon_j \;=\; \begin{cases} w_{l\,j}/\left(w_{sat} - w_{i\,j}\right) & (T_j \;\leq\; T_f) \\ \\ w_{i\,j}/\left(w_{sat} - w_{\min}\right) & (T_j \;>\; T_f) \end{cases} .$$

The principle of using such coefficients is that it is assumed that when the grid box average liquid soil moisture is relatively large, more energy is used for freezing the soil compared to a more dry average soil with the same available energy (for freezing). It is also a rudimentary method for modeling sub-grid freezing effects. The same basic idea holds for soil ice melting.

The surface insulation coefficient, K_s, is modelled following *Giard and Bazile* [2000] and is written (here in non-dimensional form) as

$$K_s = \left(1 - \frac{veg}{K_2}\right)\left(1 - \frac{LAI}{K_3}\right) \qquad (0 < K_s \leq 1)$$

where the values from *Giard and Bazile* [2000] are used: $K_2 = 5$ and $K_3 = 30$ m^2 m^{-2}. For relatively dense vegetation covers (i.e., large LAI and veg), more energy is used to heat or cool the vegetation while less is used to freeze/thaw the soil water/ice (compared to a surface with less vegetation).

The total phase change is then simply expressed as the difference between the freezing and melting components, although note that one or the other is always zero:

$$\Phi_j = \Phi_{f\,j} - \Phi_{m\,j}$$

Using the above model, the phase changes tend to follow the so-called soil specific freezing characteristic curve from *Fuchs et al.* [1978], although there can be considerable scatter about this line owing to $\epsilon < 1$ and $K_s < 1$, and ice can be present at significantly above-freezing layer-average temperatures. In the limit as ϵ and K_s become unity, the scatter is greatly reduced, and the presence of ice at above-freezing temperatures is also greatly reduced.

An example of the application of the above model to a cold climate is shown in Fig. (4.12). The forcing and parameters are from Goose Bay, Canada (Ross Brown, personal communication). The relationship between simulated soil temperature and liquid water content for all 5 soil layers using the model as presented herein is shown in the upper panel, and the relationship for which ϵ and K_s have been set to zero is shown in the lower panel. Each point represents at value at a 30-minute time step for which either $T_j \leq T_f$ or $w_{i\,j} \geq 0.001$ m^3 m^{-3}.

Soil ice and the overall soil water content are decreased due to sublimation. This term is expressed as

$$S_i \;=\; \Delta z_1\, E_{g\,I} \quad ,$$

where $E_{g\,I}$ represents the liquid water equivalent loss of soil ice from the bare soil (uppermost) model layer (kg m^{-2} s^{-1}).

The temperature and soil water profiles are updated at the end of the time step, Δt, using the calculated phase change term together with:

$$\begin{aligned} {T_j}^{n\prime} &= {T_j}^n + \tfrac{\Delta t\,\Phi_j}{c_{h\,j}} \\ {w_{L\,j}}^{n\prime} &= {w_{L\,j}}^n - \tfrac{\Delta t\,\Phi_j}{L_f \rho_w} \\ {w_{I\,j}}^{n\prime} &= {w_{I\,j}}^n + \tfrac{\Delta t\,\Phi_j}{L_f \rho_w} \end{aligned} \qquad (4.94)$$

Additional final minor adjustments are made as needed to prevent supersaturation of a layer, etc.

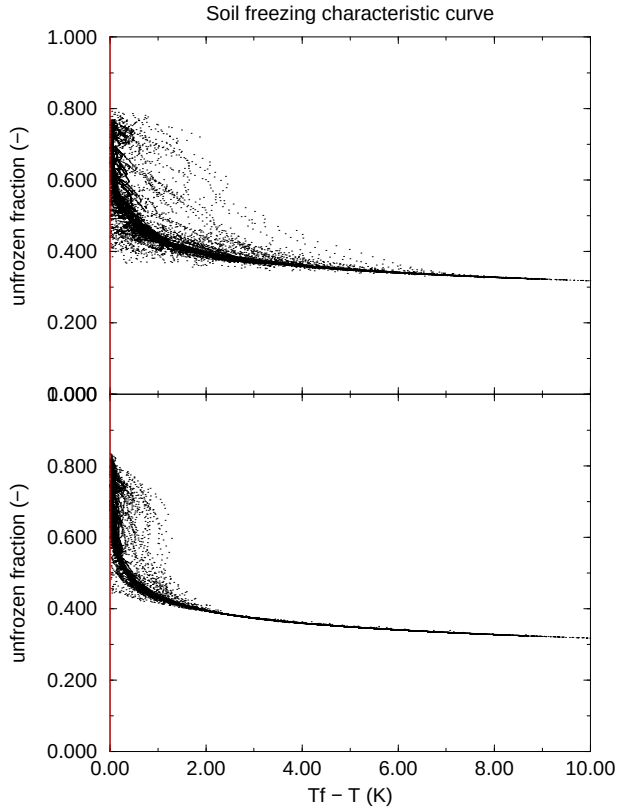

Figure 4.12: The simulated unfrozen liquid water fraction ($w_l/\left(w_i+w_l\right)$) as a function of temperature depression ($T_f - T$) for five soil model layers. The forcing are from Goose Bay, Canada. The parameters ϵ and K_s have been set to one in the lower panel.

4.1.3 Treatment of the intercepted water

Rainfall and dew intercepted by the foliage feed a reservoir of water content W_r. This amount of water evaporates in the air at a potential rate from the fraction δ of the foliage covered with a film of water, as the remaining part $(1-\delta)$ of the leaves transpires.

$$\delta = \left(\frac{W_r}{W_{rmax}}\right)^{2/3} \tag{4.95}$$

Following *Deardorff* [1978], we set

$$\frac{\partial W_r}{\partial t} = vegP - (E_v - E_{tr}) - R_r \; ; \; 0 \leq W_r \leq W_{rmax} \tag{4.96}$$

where P is the precipitation rate at the top of the vegetation, E_v is the evaporation from the vegetation including the transpiration E_{tr} and the direct evaporation E_r when positive, and the dew flux when negative (in this case $E_{tr} = 0$), and R_r is the runoff of the interception reservoir. This runoff occurs when W_r exceeds a maximum value W_{rmax} depending upon the density of the canopy, i.e., roughly proportional to $vegLAI$. According to *Dickinson* [1984], we use the simple equation:

$$W_{rmax} = 0.2 vegLAI \quad [mm] \tag{4.97}$$

4.1.4 Spatial variability of precipitation intensities

With this option, the main assumption is that, generally, the rainfall intensity is not distributed homogeneously over an entire grid cell. As a first-order approximation, the sub- grid variability in liquid precipitation, P_i, can be given by an exponential probability density distribution, $f(P_i)$:

$$f(P_i) = \frac{\mu}{P} e^{-\mu \frac{P_i}{P}} \tag{4.98}$$

where P represent the mean rainfall rate over the grid cell and μ a fraction of the grid cell affected by rainfall. μ is calculated using the results of *Fan et al.* [1996], who showed an exponential relationship between the fractional coverage of precipitation and rainfall rate, based on their analyses of over 2 years radar observations and rain gauge measurements over the Arkansas-Red river basin in the southern plains of the United States. This relationship is:

$$\mu = 1 - e^{-\beta P} \tag{4.99}$$

where β is a parameter which depends on grid resolution, dx :

$$\beta = 0.2 + 0.5 e^{-0.001 dx} \tag{4.100}$$

dx represents represents lengths of square grid cells ranging from 40km to 500km. In consequence, the μ parameter is fixed to 1 at high resolution ($\leq 10km$). This Spatial variability of precipitation intensities induces a new expression for the runoff from the interception reservoir, W_r :

$$W_r = P \times e^{\frac{\mu(W_r - W_{r_{max}})}{P \Delta t}} \tag{4.101}$$

The second consequence is that the Horton runoff, Q_{hort}, is calculated by integrating the difference between the local rainfall and the local maximum infiltration capacity, I_i, as follows:

$$Q_{hort} = \mu \int_{I_i}^{\infty} (P_i - I_i)\, f(P_i) dP_i \tag{4.102}$$

Another assumption is made on the spatial heterogeneity of the local maximum infiltration capacity. Its spatial distribution can also be approximated by an exponential probability density distribution:

$$g(I_i) = \frac{1}{\overline{I}} e^{-\frac{I_i}{\overline{I}}} \tag{4.103}$$

where $\overline{I}$ is the mean maximum infiltration rate over the grid cell. As previously said, $\overline{I}$ is calculated for unfrozen and frozen soil conditions. So Eq.4.102 , without snowmelt, can be noted as :

$$\begin{aligned} Q_{hort} &= \mu(1-\delta_f) \int_0^{\infty} \int_{I_{unf,i}}^{\infty} (P_i - I_{unf,i}) f(P_i) g(I_{unf,i}) dP_i dI_{unf,i} \\ &\quad + \mu \delta_f \int_0^{\infty} \int_{I_{f,i}}^{\infty} (P_i - I_{f,i}) f(P_i) g(I_{f,i}) dP_i dI_{f,i} \end{aligned} \tag{4.104}$$

After some mathematical developments, the Horton runoff in presence of rainfall and snowmelt, S_m, is given following *Decharme and Douville* [2006]:

$$\begin{aligned} Q_{hort} &= (1-\delta_f) \left(\frac{P}{1 + \overline{I_{unf}} \frac{\mu}{P}} + max(0, S_m - \overline{I_{unf}}) \right) \\ &\quad + \delta_f \left(\frac{P}{1 + \overline{I_f} \frac{\mu}{P}} + max(0, S_m - \overline{I_f}) \right) dP_i dI_{f,i} \end{aligned} \tag{4.105}$$

4.1.5 Treatment of the snow

One-layer snow scheme option

The evolution of the equivalent water content of the snow reservoir is given by

$$\frac{\partial W_s}{\partial t} = P_s - E_s - melt \tag{4.106}$$

where P_s is the precipitation of snow, and E_s is the sublimation from the snow surface.
The presence of snow covering the ground and vegetation can greatly influence the energy and mass transfers between the land surface and the atmosphere. Notably, a snow layer modifies the radiative balance at the surface by increasing the albedo. To consider this effect, the albedo of snow α_s is treated as a new prognostic variable. Depending if the snow is melting or not, α_s decreases exponentially or linearly with time.
If there is no melting (i.e., $melt = 0$):

$$\alpha_s(t) = \alpha_s(t - \Delta t) - \tau_a \frac{\Delta t}{\tau} + \frac{P_s \Delta t}{W_{crn}}(\alpha_{smax} - \alpha_{smin}) \tag{4.107}$$

$$\alpha_{smin} \leq \alpha_s \leq \alpha_{smax} \tag{4.108}$$

where $\tau_a = 0.008$ is the linear rate of decrease per day, $\alpha_{smin} = 0.50$ and $\alpha_{smax} = 0.85$ are the minimum and maximum values of the snow albedo.
If there is melting (i.e., $melt > 0$):

$$\alpha_s(t) = [\alpha_s(t - \Delta t) - \alpha_{smin}] \exp\left[-\tau_f \frac{\Delta t}{\tau}\right] + \alpha_{smin} + \frac{P_s \Delta t}{W_{crn}}(\alpha_{smax} - \alpha_{smin}) \tag{4.109}$$

$$\alpha_{smin} \leq \alpha_s \leq \alpha_{smax} \tag{4.110}$$

where $\tau_f = 0.24$ is the exponential decrease rate per day. Of course, the snow albedo increases as snowfalls occur, as shown by the second terms of Eqs. (21) and (23).
The average albedo of a model grid-area is expressed as

$$\alpha_t = (1 - p_{sn})\alpha + p_{sn}\alpha_s \tag{4.111}$$

Similarly, the average emissivity ϵ_t is also influenced by the snow coverage:

$$\epsilon_t = (1 - p_{sn})\epsilon + p_{sn}\epsilon_s \tag{4.112}$$

where $\epsilon_s = 1.0$ is the emissivity of the snow. Thus, the overall albedo and emissivity of the ground for infrared radiation is enhanced by snow.
Because of the significant variability of thermal properties related with the snow compactness, the relative density of snow ρ_s is also considered as a prognostic variable. Based on *Verseghy* [1991], ρ_s decreases exponentially at a rate of τ_f per day:

$$\rho_s(t) = [\rho_s(t - \Delta t) - \rho_{smax}] \exp\left[-\tau_f \frac{\Delta t}{\tau}\right] + \rho_{smax} + \frac{P_s \Delta t}{W_s}\rho_{smin} \tag{4.113}$$

$$\rho_{smin} \leq \rho_s \leq \rho_{smax} \tag{4.114}$$

where $\rho_{smin} = 0.1$ and $\rho_{smax} = 0.3$ are the minimum and maximum relative density of snow.
Finally, the average roughness length z_{0t} is

$$z_{0t} = (1 - p_{snz0})z_0 + p_{snz0}z_{0s} \tag{4.115}$$

where

$$p_{snz0} = \frac{W_s}{W_s + W_{crn} + \beta_s g z_0} \tag{4.116}$$

Here, $\beta_s = 0.408\ s^2 m^{-1}$ and $g = 9.80665\ ms^{-2}$ are physical constants, whereas z_{0s} is the roughness length of the snow.

Multi-layer snow scheme option

An additional snow scheme option has been added to ISBA. It is a so-called intermediate complexity scheme which is representative of a class of snow models which use several layers and have simplified physical parameterization schemes based on those of the highly detailed internal-process models while having computational requirements more closely resembling the relatively simple composite/force-restore or single layer schemes (*Loth et al.* [1993], *Lynch-Steiglitz* [1994], *Sun et al.* [1999]). Compared to the baseline ISBA snow scheme, the explicit multi-layered approach resolves the large thermal and the density gradients which can exist in the snow cover, distinguishes the surface energy budgets of the snow and non-snow covered portions of the surface, includes the effects of liquid water storage in the snow cover, models the absorption of incident radiation within the pack, and calculates explicit heat conduction between the snow and the soil. The conservation equation for the total snow cover mass is expressed as

$$\frac{\partial W_s}{\partial t} = P_s + p_{sn}\ (P - P_s) - E_s - E_{sl} - Q_n\ \ , \tag{4.117}$$

where E_{sl} represents evaporation of liquid water from the snow surface, and the product $p_{sn}\ (P - P_s)$ represents the portion of the total rainfall that is intercepted by the snow surface while the remaining rainfall is assumed to be intercepted by the snow-free soil and vegetation canopy. The snow-runoff rate, Q_n, is the rate at which liquid water leaves the base of the snow cover.

The snow state variables are the heat content (H_s), the layer thickness (D), and the layer average density (ρ_s). The temperature (T_{sn}) and liquid water content (w_{sl}) are defined using the heat content. The total snow depth, D_s (m) is defined as

$$D_s = \sum_{i=1}^{N_s} D_i \tag{4.118}$$

where a three-layer configuration is currently used by default (i.e. $N_s = 3$). The surface snow layer is always less than or equal to 0.05 m, and this temperature is used to calculate the fluxes between the atmosphere and the snow surface. The snow density is compacted using standard empirical relationships (*Anderson* [1976]). Additional changes arise to snowfall which generally reduces the snow density, and densification resulting from ripening. The snow heat content (J m^{-2}) is defined as

$$H_{s\,i} = c_{s\,i}\, D_i\ (T_{sn\,i} - T_0)\ -\ L_f\, \rho_w\, (w_{s\,i} - w_{sl\,i})\ \ , \tag{4.119}$$

where w_s is the total snow layer water equivalent depth (m), w_{sl} is the snow layer liquid water content (m), and c_s is the snow heat capacity (J m^{-3} K^{-1}) (using the same definition as the baseline ISBA snow scheme). The snow heat content is used in order to allow the presence of either cold (dry) snow which has a temperature less than or equal to the freezing point or warm (wet) snow which is characterized by a temperature at the freezing point and contains water in liquid form. The snow temperature and liquid water content can then be defined as

$$T_{sn\,i} = T_f\ +\ (H_{s\,i} + L_f\, \rho_w\, w_{s\,i})\,/\,(c_{s\,i}\, D_i)\ ; \qquad w_{l\,i} = 0 \tag{4.120}$$

$$w_{sl\,i} = w_{s\,i}\ +\ (H_{s\,i}/L_f\, \rho_w)\ ; \qquad T_{sn\,i} = T_f\ \text{ and }\ w_{sl\,i} \leq w_{sl\,\max i} \tag{4.121}$$

where $w_{sl\,\max i}$ is the maximum liquid water holding capacity of a snow layer, which is based on empirical relations. All water exceeding this flows into the layer below where it can do one or all of the following; add to the liquid water content, refreeze, or continue flowing downward.

Snow heat flow is along the thermal gradient as any snow melt or percolated water within the snow cover is assumed to have zero heat content. The layer-averaged snow temperature equation ($T_{s\,i}$) is expressed as

$$c_{s\,i} D_i \frac{\partial T_{sn\,i}}{\partial t} = G_{s\,i-1} - G_{s\,i} + R_{s\,i-1} - R_{s\,i} - S_{s\,i} \ , \tag{4.122}$$

where S_s represents an energy sink/source term associated with phase changes between the liquid and solid phases of water. Incoming short wave radiation (R_s) transmission within the snowpack decreases exponentially with increasing snow depth. At the surface, it is expressed as

$$R_{s\,0} = R_g \ (1 - \alpha_s) \tag{4.123}$$

where the snow albedo is defined using the same relationships as in the baseline version of ISBA (*Douville et al.* [1995]). The sub-surface heat (G_s) flux terms are evaluated using simple diffusion. At the surface, this flux is expressed as

$$G_{s\,0} = \epsilon_s \left(R_A - \sigma_{SB} {T_{sn\,1}}^4 \right) \ - \ H\left(T_{sn\,1}\right) \ - \ LE\left(T_{sn\,1}\right) \ - \ c_w \, p_{sn} \left(P - P_s\right) \left(T_f - T_r\right) \ , \tag{4.124}$$

The last term on the right hand side of the above equation represents a latent heat source when rain with a temperature (T_r) greater than T_0 falls on the snow cover, where c_w represents the heat capacity of water (4187 J kg^{-1} K^{-1}). Rainfall is simply assumed to have a temperature which is the larger of the air temperature (T_a) and the freezing point. The latent heat flux from the snow includes the liquid fraction weighted contributions from the evaporation of liquid water and sublimation.
The ISBA surface soil/vegetation layer temperature is then coupled to the snow scheme using

$$\frac{1}{C_T}\frac{\partial T_s}{\partial t} = (1 - p_n) \left[R_g \left(1 - \alpha\right) + \epsilon_t \left(R_A - \sigma {T_s}^4 \right) - H - LE - \frac{2\pi}{C_T \tau} \left(T_s - T_2\right) \right] \tag{4.125}$$

$$+ p_n \ \left[G_{s\,N} + R_{s\,N} + c_w \, Q_n \ \left(T_f - T_s\right) \right] \ . \tag{4.126}$$

The term on the right hand side of the above equation involving the snow runoff (Q_n) represents an advective term. The net surface fluxes to/from the atmosphere are then calculated as the snow-cover fraction weighted sums over the snow and non-snow covered surfaces. When the 3-layer option is in use, the default ISBA scheme is used when the snow cover is relatively thin (arbitrarily defined as 0.05 m depth). When the snow depth exceeds this threshold, the snow mass and heat is transferred to the multi-layer scheme. This prevents numerical difficulties for vanishingly thin snow packs.

4.1.6 The surface fluxes

Only one energy balance is considered for the whole system ground-vegetation-snow (when the 3-layer snow scheme option is not in use). As a result, heat and mass transfers between the surface and the atmosphere are related to the mean values T_s and w_g.
The net radiation at the surface is the sum of the absorbed fractions of the incoming solar radiation R_G and of the atmospheric infrared radiation R_A, reduced by the emitted infrared radiation:

$$R_n = R_G(1 - \alpha_t) + \epsilon_t \left(R_A - \sigma_{SB} {T_s}^4 \right) \tag{4.127}$$

where σ_{SB} is the Stefan-Boltzmann constant.
The turbulent fluxes are calculated by means of the classical aerodynamic formulas. For the sensible heat flux:

$$H = \rho_a c_p C_H V_a (T_s - T_a) \tag{4.128}$$

where c_p is the specific heat; ρ_a, V_a, and T_a are respectively the air density, the wind speed, and the temperature at the lowest atmospheric level; and C_H, as discussed below, is the drag coefficient depending upon the thermal stability of the atmosphere. The explicit snow scheme sensible heat flux is calculated using the same formulation (but with T_{sn}). The water vapor flux E is the sum of the evaporation of liquid water from the soil surface (i.e., $E_{g\,l}$), from the vegetation (i.e., E_v), and sublimation from the snow and soil ice (i.e, E_s and $E_{g\,f}$):

$$
\begin{aligned}
LE &= LE_{g\,l} + LE_v + L_i\,(E_s + E_{g\,f}) && (4.129)\\
E_{g\,l} &= (1-veg)(1-p_{sng})\,(1-\delta_i)\;\rho_a C_H V_a\,(h_u q_{sat}(T_s) - q_a) && (4.130)\\
E_v &= veg(1-p_{snv})\rho_a C_H V_a h_v\,(q_{sat}(T_s) - q_a) && (4.131)\\
E_s &= p_{sn}\rho_a C_H V_a\,(q_{sat}(T_s) - q_a) && (4.132)\\
E_{g\,f} &= (1-veg)\,(1-p_{sng})\;\delta_i\,\rho_a C_H V_a\,(h_{ui}\,q_{\rm sat}\,(T_s)\;-\;q_a) && (4.133)
\end{aligned}
$$

where L and L_i are the specific heat of evaporation and sublimation, $q_{sat}(T_s)$ is the saturated specific humidity at the temperature T_s, and q_a is the atmospheric specific humidity at the lowest atmospheric level. The water vapor flux E from the explicit snow surface is expressed as

$$
\begin{aligned}
LE\,(T_{sn\,1}) &= LE_{sl} + L_i E_s && (4.134)\\
E_{sl} &= \delta_{sn}\,\rho_a C_{Hs} V_a\,(q_{sat}\,(T_{sn\,1}) - q_a) && (4.135)\\
E_s &= (1-\delta_{sn})\;\rho_a C_{Hs} V_a\,(q_{sat}\,(T_{sn\,1}) - q_a) && (4.136)\\
\delta_{sn} &= w_{sl\,1}/w_{sl\,\max 1}\,; \qquad 0 \le \delta_{sn} \le 1 && (4.137)
\end{aligned}
$$

where evaporation of liquid water is zero when $T_{sn\,1} < T_0$. The transfer coefficient (C_{Hs}) is calculated over the snow covered surface using the same formulation as C_H.

The surface ice fraction is is used to partition the bare soil latent heat flux between evaporation and sublimation, and it is defined as

$$
\delta_i = w_{g\,f}/\,(w_{g\,f} + w_g)\;; \qquad 0 \le \delta_i < 1\;\;. \tag{4.138}
$$

The relative humidity h_u at the ground surface is related to the superficial soil moisture w_g following

$$
\begin{aligned}
h_u &= \frac{1}{2}\left[1 - cos\left(\frac{w_g}{{w_{fc}}^*}\pi\right)\right]\;,\ \text{if } w_g < {w_{fc}}^* && (4.139)\\
h_u &= 1 \qquad\qquad\qquad\qquad ,\ \text{if } w_g \ge {w_{fc}}^* && (4.140)
\end{aligned}
$$

where the field capacity with respect to the liquid water is defined using the modified soil porosity so that ${w_{fc}}^* = w_{fc}\,w^*_{sat}/w_{sat}$. The humidity for the ice covered portion of the grid box is calculated in a similar fashion as

$$
\begin{aligned}
h_{ui} &= \frac{1}{2}\left[1 - cos\left(\frac{w_{g\,f}}{{w_{fc}}^{**}}\pi\right)\right]\;,\ \text{if } w_{g\,f} < {w_{fc}}^{**} && (4.141)\\
h_{ui} &= 1 \qquad\qquad\qquad\qquad ,\ \text{if } w_{g\,f} \ge {w_{fc}}^{**} && (4.142)
\end{aligned}
$$

where ${w_{fc}}^{**} = w_{fc}(w_{sat} - w_g)/w_{sat}$. In case of dew flux when $q_{sat}(T_s) < q_a$, h_u is also set to 1 (see *Mahfouf and Noilhan* [1991] for details). When the flux E_v is positive, the Halstead coefficient h_v takes into account the direct evaporation E_r from the fraction δ of the foliage covered by intercepted water, as well as

the transpiration E_{tr} of the remaining part of the leaves:

$$h_v = (1-\delta)R_a/(R_a+R_s)+\delta \quad (4.143)$$

$$E_r = veg(1-p_{snv})\frac{\delta}{R_a}\left(q_{sat}(T_s)-q_a\right) \quad (4.144)$$

$$E_{tr} = veg(1-p_{snv})\frac{1-\delta}{R_a+R_s}\left(q_{sat}(T_s)-q_a\right) \quad (4.145)$$

When E_v is negative, the dew flux is supposed to occur at the potential rate, and h_v is taken equal to 1. Following *Deardorff* [1978], δ is a power function of the moisture content of the interception reservoir:

$$\delta = (W_r/W_{rmax})^{2/3} \quad (4.146)$$

The aerodynamic resistance is $R_a = (C_H V_a)^{-1}$. The surface resistance, R_s, depends upon both atmospheric factors and available water in the soil; it is given by:

$$R_s = \frac{R_{smin}}{F_1F_2F_3F_4LAI} \quad (4.147)$$

with the limiting factors F_1, F_2, F_3, and F_4:

$$F_1 = \frac{f+R_{smin}/R_{smax}}{1+f} \quad (4.148)$$

$$F_2 = \frac{w_2-w_{wilt}}{w_{fc}-w_{wilt}} \quad and\, 0\le F_2\le 1 \quad (4.149)$$

$$F_3 = 1-\gamma\left(q_{sat}(T_s)-q_a\right) \quad (4.150)$$

$$F_4 = 1-1.6\times10^{-3}(T_a-298.15)^2 \quad (4.151)$$

where the dimensionless term f represents the incoming photosynthetically active radiation on the foliage, normalized by a species-dependent threshold value:

$$f = 0.55\frac{R_G}{R_{Gl}}\frac{2}{LAI} \quad (4.152)$$

Moreover, γ is a species-dependent parameter (see *Jacquemin and Noilhan* [1990]) and R_{smax} is arbitrarily set to $5000\ sm^{-1}$.

The surface fluxes of heat, moisture, and momentum can be expressed as

$$(\overline{w'\theta'})_s = \frac{H}{\rho_a c_p T_a/\theta_a} \quad (4.153)$$

$$(\overline{w'r'_v})_s = \frac{E}{\rho_a(1-q_a)} \quad (4.154)$$

$$|\overline{w'V'}|_s = C_D|V_a|^2 = u_*^2 \quad (4.155)$$

where r_v is the water vapor mixing ratio, w is the vertical motion, θ_a is the potential temperature at the lowest atmospheric level. The primes and overbars denote perturbation and average quantities.

For the drag coefficients C_H and C_D, the formulation of *Louis* [1979] was modified in order to consider different roughness length values for heat z_0 and momentum z_{0h} (*Mascart et al.* [1995]):

$$C_D = C_{DN}F_m\ ;\ C_H = C_{DN}F_h \quad (4.156)$$

with

$$C_{DN} = \frac{k^2}{[ln(z/z_0)]^2} \tag{4.157}$$

(4.158)

where k is the Von Karmann constant. Also

$$F_m = 1 - \frac{10Ri}{1 + C_m\sqrt{|Ri|}} \quad if\ Ri \leq 0 \tag{4.159}$$

$$F_m = \frac{1}{1 + \frac{10Ri}{\sqrt{1+5Ri}}} \quad if\ Ri > 0 \tag{4.160}$$

and

$$F_h = \left[1 - \frac{15Ri}{1 + C_h\sqrt{|Ri|}}\right] \times \left[\frac{ln(z/z_0)}{ln(z/z_{0h})}\right] \quad if\ Ri \leq 0 \tag{4.161}$$

$$F_h = \frac{1}{1 + 15Ri\sqrt{1+5Ri}} \times \left[\frac{ln(z/z_0)}{ln(z/z_{0h})}\right] \quad if\ Ri > 0 \tag{4.162}$$

where Ri is the gradient Richardson number. The coefficients C_m and C_h of the unstable case are given by

$$C_m = 10{C_m}^* C_{DN}(z/z_0)^{p_m} \tag{4.163}$$

$$C_h = 15{C_h}^* C_{DN}(z/z_{0h})^{p_h} \times \left[\frac{ln(z/z_0)}{ln(z/z_{0h})}\right] \tag{4.164}$$

where C_m^*, C_h^*, p_m, and p_h are functions of the ratio $\mu = ln(z_0/z_{0h})$ only:

$$C_h^* = 3.2165 + 4.3431 \times \mu + 0.5360 \times \mu^2 - 0.0781 \times \mu^3 \tag{4.165}$$

$$C_m^* = 6.8741 + 2.6933 \times \mu - 0.3601 \times \mu^2 + 0.0154 \times \mu^3 \tag{4.166}$$

$$p_h = 0.5802 - 0.1571 \times \mu + 0.0327 \times \mu^2 - 0.0026 \times \mu^3 \tag{4.167}$$

$$p_m = 0.5233 - 0.0815 \times \mu + 0.0135 \times \mu^2 - 0.0010 \times \mu^3 \tag{4.168}$$

4.1.7 Summary of Useful Parameters

The parameters have been chosen in order to characterize the main physical processes, while attempting to reduce the number of independant variables. They can be divided into two categories: primary parameters needing to be specified by spatial distribution, and secondary parameters which values can be associated with those of the primary parameters.

In the present state of the method, the primary parameters describe the nature of the land surface and its vegetation coverage by means of only four numerical indices: the percentage of sand and clay in the soil, the dominant vegetation type, and the land-sea mask.

The secondary parameters associated with the soil type are evaluated from the sand and clay composition of the soil, according to the continuous formulation discussed in *Giordani* [1993] and *Noilhan and Lacarrère* [1995] (see Appendix). These parameters are:

- the saturated volumetric moisture content w_{sat};
- the wilting point volumetric water content w_{wilt};

- the field capacity volumetric water content w_{fc};
- the slope b of the retention curve;
- the soil thermal coefficient at saturation C_{Gsat};
- the value of C_1 at saturation (i.e., C_{1sat});
- the reference value of C_2 for $w_2 = 0.5 w_{sat}$ (i.e., C_{2ref});
- the drainage coefficient C_3 ;
- the diffusion coefficients $C_{4\,ref}$ and C_{4b} ;
- and the coefficients a, p for the w_{geq} formulation.

On the other hand, the parameters associated with the vegetation can either be derived from the dominant vegetation type, or be specified from existing classification or observations. They are

- the fraction of vegetation veg;
- the depth of the soil column d_2 (or the root zone depth);
- the depth of the soil column d_3 (if third soil layer option in use);
- the minimum surface resistance R_{smin};
- the leaf area index LAI;
- the heat capacity C_v of the vegetation;
- the R_{Gl} and γ coefficients found in the formulation of the surface resistance R_s;
- and the roughness length for momentum z_0 and for heat z_{0h}.

Other necessary parameters are

- the albedo α
- the emissivity ϵ.
- and characteristic time scale for phase changes (currently constant) τ_i.

4.1.8 Appendix A: Continuous formulation of the soil secondary parameters

Following *Giordani* [1993], *Noilhan and Lacarrère* [1995], the sand and clay composition (i.e., $SAND$ and $CLAY$) are expressed in percentage.

The saturated volumetric water content ($m^3 m^{-3}$):

$$w_{sat} = (-1.08 SAND + 494.305) \times 10^{-3} \tag{4.169}$$

The wilting point volumetric water content ($m^3 m^{-3}$):

$$w_{wilt} = 37.1342 \times 10^{-3} (CLAY)^{0.5} \tag{4.170}$$

The field capacity volumetric water content ($m^3 m^{-3}$):

$$w_{fc} = 89.0467 \times 10^{-3} (CLAY)^{0.3496} \tag{4.171}$$

The slope of the retention curve:

$$b = 0.137 CLAY + 3.501 \tag{4.172}$$

The soil thermal coefficient at saturation ($Km^2 J^{-1}$):

$$C_{Gsat} = -1.557 \times 10^{-2} SAND - 1.441 \times 10^{-2} CLAY + 4.7021 \tag{4.173}$$

The value of C_1 at saturation:

$$C_{1sat} = (5.58 CLAY + 84.88) \times 10^{-2} \tag{4.174}$$

The value of C_2 for $w_2 = 0.5 w_{sat}$:

$$C_{2ref} = 13.815 CLAY^{-0.954} \tag{4.175}$$

The coefficient C_3:

$$C_3 = 5.327 CLAY^{-1.043} \tag{4.176}$$

The coefficient C_{4b}:

$$C_{4b} = 5.14 + 0.115\, CLAY \tag{4.177}$$

The coefficient $C_{4\,ref}$:

$$C_{4\,ref} = \frac{2(d_3 - d_2)}{(d_2\, {d_3}^2)} \log_{10}{}^{-1} \left[\beta_0 + \sum_{j=1}^{3} \left(\beta_j\, SAND^{\,j} + \alpha_j\, CLAY^{\,j} \right) \right] \tag{4.178}$$

where the β_j $(j = 0, 3)$ coefficients are 4.42×10^{-0}, 4.88×10^{-3}, 5.93×10^{-4} and -6.09×10^{-6}. The α_j $(j = 1, 3)$ coefficients are defined as -2.57×10^{-1}, 8.86×10^{-3} and -8.13×10^{-5}.
The coefficients for the w_{geq} formulation:

$$a = 732.42 \times 10^{-3} CLAY^{-0.539} \tag{4.179}$$

$$p = 0.134 CLAY + 3.4 \tag{4.180}$$

4.1.9 Appendix B: Gaussian formulation for the C_1 coefficient

Following *Giordani* [1993] and *Braud et al.* [1993], for dry soils (i.e., $w_g < W_{wilt}$), the C_1 coefficient in Eq. (13) is approximated by the Gaussian distribution:

$$C_1(w) = C_{1max} \exp \left[-\frac{(w_g - w_{max})^2}{2\sigma^2} \right] \tag{4.181}$$

In this expression,

$$C_{1max} = (1.19 w_{wilt} - 5.09) \times 10^{-2} T_s + (-1.464 w_{wilt} + 17.86) \tag{4.182}$$

$$w_{max} = \eta w_{wilt} \tag{4.183}$$

with

$$\eta = (-1.815 \times 10^{-2} T_s + 6.41) w_{wilt} + (6.5 \times 10^{-3} T_s - 1.4) \tag{4.184}$$

and

$$\sigma^2 = -\frac{W_{max}^2}{2ln\left(\frac{0.01}{C_{1max}}\right)} \tag{4.185}$$

4.2 ISBA-A-gs surface scheme

4.2.1 The Model

Introduction

Météo-France is developing SURFEX (SURFace EXternalisée) to be used in operational NWP models, and offline for applications in hydrology and vegetation monitoring (*Martin et al.* [2007]). SURFEX serves the merging of a number of land and ocean surface models. Over land, SURFEX includes ISBA-A-gs, a CO_2 responsive land surface model able to simulate the diurnal cycle of carbon and water vapour fluxes (*Calvet et al.* [1998], *Calvet et al.* [2004], *Gibelin et al.* [2006], *Calvet et al.* [2007]). This latter model accounts for different feedbacks in response to changes in $[CO_2]$, photosynthesis enhancement and transpiration reduction (fertilization and antitranspirant effects, respectively). Daily values of Leaf Area Index (LAI) and biomass can be produced by ISBA-A-gs.

ISBA-A-gs uses a CO_2 responsive parameterization of photosynthesis based on the model of *Goudriaan et al.* [1985] modified by *Jacobs* [1994] and *Jacobs et al.* [1996]. This parameterization is less detailed than that commonly used in most land surface models (*Farquar et al.* [1980] for C_3 plants and *Collatz et al.* [1992] for C_4 plants), but it has the same formulation for C_4 plants as for C_3 plants differing only by the input parameters. The model also includes an original representation of the soil moisture stress. Two different types of drought responses are distinguished for both herbaceous vegetation (*Calvet* [2000]) and forests (*Calvet et al.* [2004]), depending on the evolution of the water use efficiency (WUE) under moderate stress: WUE increases in the early soil water stress stages in the case of the drought-avoiding response, whereas WUE decreases or remains stable in the case of the drought-tolerant response.

ISBA-A-gs calculates interactively the leaf biomass and the LAI (defined as the leaf area per unit ground area), using a simple growth model (*Calvet et al.* [1998]). The leaf biomass is supplied with the carbon assimilated by photosynthesis, and decreased by a turnover and a respiration terms. LAI is inferred from the leaf biomass multiplied by the Specific Leaf Area ratio, which depends on the leaf nitrogen concentration (*Calvet and Soussana* [2001], *Gibelin et al.* [2006]). *Gibelin et al.* [2006] showed that ISBA-A-gs simulates realistic LAI at the global scale under various environmental conditions. The physics of ISBA-A-gs has been implemented in SURFEX by CNRM. Meanwhile, the physics of ISBA-A-gs has been implemented in the ECMWF land surface scheme TESSEL (*Van den Hurk et al.* [2000]) by KNMI. The A-gs extension of TESSEL is called CTESSEL (*Voogt et al.* [2006], *Lafont et al.* [2006]).

Background information

Vegetation patches SURFEX contains the ISBA-A-gs photosynthesis model, for which particular vegetation types need to be distinguished. In each grid box several vegetation types are present, with their own water and energy budget, and their own roughness length. ISBA-A-gs has a reduced number of parameters but is able to represent contrasting vegetation types. The model includes 7 vegetation types: 3 of them are high vegetation types: deciduous broadleaf forest, coniferous forest and evergreen broadleaf forest. The other 4 are low-vegetation types: C_3 grass, C_4 grass, C_3 crops and C_4 crops. The C_3 and C_4 carbon fixation mechanisms correspond to contrasting photosynthetic biochemical pathways. C_3 plants represent the vast majority of the Earths plant biomass. C_4 plants consist mainly of tropical grasses and some of them are cultivated (maize, sorghum, millet, sugar cane).

The canopy resistance in ISBA-A-gs is calculated in the routine COTWORES (or COTWORESTRESS for the most recent version able to differentiate drought-avoiding from drought-tolerant biomes). The photosynthesis model is called from COTWORES (or COTWORESTRESS).

Table 4.1: Options of ISBA-A-gs

Option	Drought response	Leaf Area Index and leaf biomass	Above-ground biomass (non-woody)
AGS	*Calvet et al.* [1998]	Not calculated (prescribed value is used)	Not calculated
LAI	*Calvet et al.* [1998]	Calculated (from photosynthesis)	Not calculated
AST	Avoiding or Tolerant *Calvet* [2000], *Calvet et al.* [2004]	Not calculated (prescribed value is used)	Not calculated
LST	Avoiding or Tolerant *Calvet* [2000], *Calvet et al.* [2004]	Calculated (from photosynthesis)	Not calculated
NIT	Avoiding or Tolerant *Calvet* [2000], *Calvet et al.* [2004]	Calculated (from photosynthesis)	Calculated (nitrogen dilution)

! The parameters of ISBA-A-gs cannot be aggregated/averaged. Spatial heterogeneity within a grid cell has to be represented by running the model several times (as many times as the number of patches found within the grid cell).

Options of ISBA-A-gs Five options of ISBA-A-gs (Table 4.1) can be activated by using the NAM_ISBA namelist

! The use of the most recent drought response formulation (present in options AST, LST, NIT) is recommended as it is based on meta-analyses of leaf-level observations and was validated successfully at the field and at the global scale (see *Rivalland et al.* [2006], *Gibelin et al.* [2006, 2008] and *Calvet et al.* [2008]).
This option is used in CTESSEL (*Voogt et al.* [2006]).

Photosynthesis Model (no water stress)

The canopy resistance is calculated from the photosynthesis, which is the net CO_2 assimilation (A_n) of the canopy. An is calculated as a function of different environmental factors based on the approach by *Goudriaan et al.* [1985].
First, CO_2 assimilation limited by the air CO_2 concentration is determined via a saturation equation:

$$A_m = A_{m,max}\left[1 - \exp\left\{-g_m^*(C_i - \Gamma)/A_{m,max}\right\}\right] \tag{4.186}$$

where $A_{m,max}$ is the maximum net CO_2 assimilation, g_m^* is the mesophyll conductance (with no soil water stress), C_i is the CO_2 concentration in the leaf and Γ is the CO_2 concentration at which assimilation compensates respiration, called CO_2 compensation concentration. $A_{m,max}$ depends on temperature via a Q_{10} function:

$$A_{m,max}(T_s) = \frac{A_{m,max}(25) \times Q_{10}^{(T_s-25)/10}}{\left[1 + \exp\left\{0.3(T_1 - T_s)\right\}\right]\left[1 + \exp\left\{0.3(T_s - T_2)\right\}\right]} \tag{4.187}$$

where $A_{m,max}(25)$ is $A_{m,max}$ at 25°C, Q_{10} is fixed at 2.0, T_s is the skin temperature in °C and T_1 and T_2 are reference temperature values (see Table 4.2). g_m in unstressed soil moisture conditions, g_m^*, depends on temperature via the same Q_{10} function as $A_{m,max}$. The dependence on temperature of Γ is described by:

$$\Gamma(T_s) = \Gamma(25) \times Q_{10}^{(T_s-25)/10} \tag{4.188}$$

where Q_{10} is fixed at 1.5.

Table 4.2: Values of model parameters at 25°C and of parameters in the temperature response functions (T in °C)

Mechanism	Parameter (X)	X(@25)	Q_{10}	T_1 [°]	T_2 [°]
C_3	ϵ_0 $[mg\ J^{-1}]$	0.017	-	-	-
	f_0^*	0.85	-	-	-
	Γ $[ppm]$	45	1.5	-	-
	g_m^* $[mm\ s^{-1}]$	7.0	2.0	5	36[1]
	$A_{m,max}$ $[mg\ m^{-2}\ s^{-1}]$	2.2	2.0	8	38
C_4	ϵ_0 $[mg\ J^{-1}]$	0.014	-	-	-
	f_0^*	0.50	-	-	-
	Γ $[ppm]$	2.8	1.5	-	-
	g_m^* $[mm\ s^{-1}]$	17.5	2.0	13	36
	$A_{m,max}$ $[mg\ m^{-2}\ s^{-1}]$	1.7	2.0	13	38

As can be seen from Table 4.2, some parameters depend only on the photosynthesis mechanism (C_3/C_4). Others, like g_m^*, depend on the vegetation type (Table 4.5). The internal CO_2 concentration C_i, is directly derived from the CO_2 concentration in the air C_s. It is controlled by the air humidity via:

$$C_i = fC_s + (1-f)\Gamma \tag{4.189}$$

and

$$f = f_0^* \left(1 - \frac{D_s}{D_{max}^*}\right) + f_{min} \left(\frac{D_s}{D_{max}^*}\right) \tag{4.190}$$

where D_{max}^* is the maximum specific humidity deficit of the air tolerated by the vegetation (with no soil water stress) and D_s is the actual deficit. If the deficit exceeds D_{max}^*, the plant closes its stomata. f_0^* is the value of f if there is no saturation deficit (with no soil water stress). Both the unstressed D_{max}^* and unstressed f_0^* are parameters that are vegetation type specific (Table 4.5). Depending on vegetation type and stress strategy, soil moisture stress influences these values (see Section 4.2.1). f_{min} is given by:

$$f_{min} = \frac{g_c}{g_c + g_m^*} \tag{4.191}$$

where g_c is the cuticular conductance, its value depending on vegetation type (Table 4.5). The CO_2 assimilation limited by CO_2 concentration is further limited by radiation by:

$$A_n = (A_m + R_d)\left[1 - \exp\left\{-\epsilon I_a/(A_m + R_d)\right\}\right] - R_d \tag{4.192}$$

where I_a is the photosynthetically active radiation (PAR), ϵ is the initial quantum use efficiency and R_d is the dark respiration. ϵ is given by:

$$\epsilon = \epsilon_0 \frac{C_i - \Gamma}{C_i + 2\Gamma} \tag{4.193}$$

[1] see section 4.2.3

where ϵ_0 is the maximum quantum use efficiency (Table 4.2). R_d is parameterized simply as:

$$R_d = A_m/9 \tag{4.194}$$

The stomatal conductance to CO_2, g_{sc}, is estimated using a flux-gradient relationship, modified to account for the effect of a specific humidity deficit on stomatal aperture. The first guess g^*_{sc} is given by:

$$g^*_{sc} = \frac{A_n - A_{min}\left(\frac{D_s}{D^*_{max}}\frac{A_n+R_d}{A_m+R_d}\right) + R_d\left(1 - \frac{A_n+R_d}{A_m+R_d}\right)}{C_s - C_i} \tag{4.195}$$

where A_{min} represents the residual photosynthesis rate (at full light intensity) associated with cuticular transfers when the stomata are closed because of a high specific humidity deficit. It is parameterized as:

$$A_{min} = g^*_m(C_{min} - \Gamma) \tag{4.196}$$

where C_{min} is the value of C_i at maximum specific humidity deficit ($D_s = D^*_{max}$):

$$C_{min} = \frac{g_c C_s + g^*_m \Gamma}{g_c + g^*_m} \tag{4.197}$$

Taking into account the ratio of diffusivity of water vapour and CO_2 (=1.6), the first guess of the stomatal conductance to water vapour is:

$$g_s^{first} = 1.6 g_{sc}^{first} \tag{4.198}$$

The diffusion of CO_2 interacts with that of water vapour. The first guess of the stomatal conductance to CO_2, must be corrected for this interaction by:

$$g_{sc} = g_{sc}^{first} + E\frac{M_a}{\rho_a M_v}\frac{C_s + C_i}{2(C_s - C_i)} \tag{4.199}$$

where M_a and M_v are molecular masses of air and water vapour respectively, ρ_a is the air density and E is leaf transpiration based on the first guess of the stomatal conductance to water vapour:

$$E = \rho_a g_s^{first} D_s \tag{4.200}$$

In order to refine the estimation of the stomatal conductances to CO_2 and water vapour, a single iteration over Eqs. 4.198, 4.200 and 4.199 is applied. Finally, the stomatal conductance to water vapour is given by:

$$g_s = 1.6 g_{sc} + g_c \tag{4.201}$$

Soil moisture stress parameterization

Initial version In the initial version of ISBA-A-gs (*Calvet et al.* [1998]), the effect of soil moisture stress was applied to the mesophyll conductance, by multiplying g^*_m by the normalized soil moisture. This quantity is referred to by the function f_2:

$$f_2 = \frac{\bar{\theta} - \theta_{wilt}}{\theta_{fc} - \theta_{wilt}} \tag{4.202}$$

In this version D^*_{max} was fixed at 45 $g\ kg^{-1}$. The value of f_0 for C_3 plants was 0.85 and for C_4 plants 0.5. The routine corresponding to the initial version is called COTWORES.

Table 4.3: Differences between figure 4.13 and the model

	f_{2c}	D_{maxX}	D_{maxN}
Figure	0.5	403	55
Model	0.3	300	30

Improved representation of plant response to drought The initial parameterization is replaced by a more complex one, based on a meta-analysis of several herbaceous and woody vegetation types (*Calvet* [2000], *Calvet et al.* [2004]). The meta-analysis shows relationships between g_m and D_{max} for low vegetation and between g_m and f_0 for high vegetation. Furthermore, it seems that plants react in two different ways to soil moisture stress. There are plants that try to avoid stress, by reducing the evaporation via stomatal regulation, and/or growing during well-watered conditions. This stress strategy is typified as drought-avoiding (or defensive). Others apply another strategy in order to resist stress, by a more efficient root water-uptake or a more rapid growing cycle. This stress strategy is typified as drought-tolerant (or offensive). Among species within the 7 vegetation classes of ISBA-A-gs both strategies may occur. Therefore, it is not easy to generalize the strategy for each class. It seems most likely that coniferous forests and C_3 crops have a drought-avoiding strategy, whereas an drought-tolerant strategy is assigned to the other classes. In both stress strategies, 2 regimes are distinguished. One with moderate stress, in which the normalized soil moisture f_2 exceeds the critical value f_{2c}. The other with severe stress, where f_2 is less than f_{2c}. The critical value is fixed at 0.3 for global modelling. For local modelling this value may be adapted to available data.

Low vegetation *Calvet* [2000] discusses the soil moisture stress response by low vegetation types. In unstressed conditions, the following relationship holds for low vegetation types:

$$C_3\ plants: \ \ln(g_m^*) = 2.381 - 0.6103 \ln(D_{max}^*) \tag{4.203}$$

$$C_4\ plants: \ \ln(g_m^*) = 5.323 - 0.8923 \ln(D_{max}^*) \tag{4.204}$$

with g_m^* in mms^{-1} and D_{max}^* in gkg^{-1}.
The negative correlation between g_m and D_{max} indicates that plants that are sensitive to the air humidity (low D_{max} value), compensate the early closing of the stomata by a high mesophyll conductance. On the other hand, plants that are less sensitive to the air humidity have a lower mesophyll conductance. Figure 4.13 shows the stress response for low vegetation types schematically. The symbol θ is equal to f_2. The figure represents an example of a C_3 plant with specific parameter values. Table 4.3 presents differences between the example in the figure and the model values.
The starting point is the unstressed condition (θ=100%). First we follow the drought-avoiding strategy. When stress sets in, D_{max} decreases while g_m increases until the critical soil moisture is reached. This is described by:

$$D_{max} = D_{max}^N + (D_{max}^* - D_{max}^N)\frac{f_2 - f_{2c}}{1 - f_{2c}} \tag{4.205}$$

This strategy leads to less evaporation, but keeps up the CO_2 assimilation, thereby increasing the water use efficiency. Under moderate stress Eq. 4.203 is still valid. Via this equation, the maximum value of g_m, g_m^X,

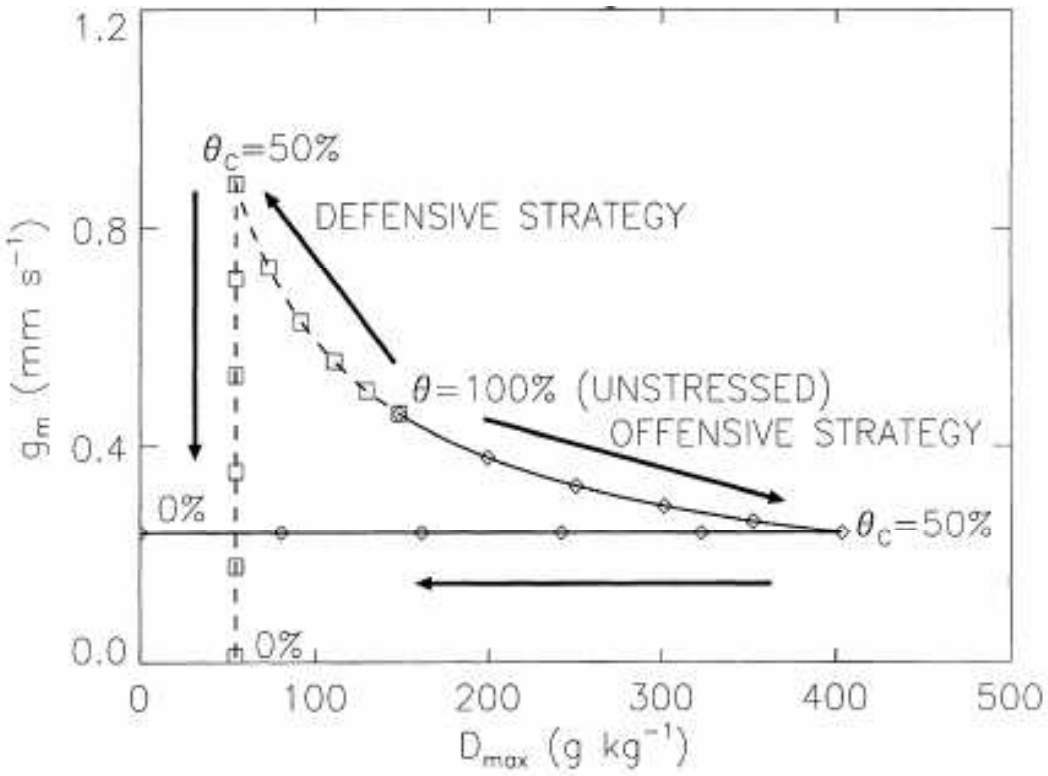

Figure 4.13: Stress responses for C_3 low vegetation. Defensive and offensive strategies represent drought-avoiding and drought-tolerant responses, respectively. Reproduced from *Calvet* [2000]

follows from the value of D_{maxN}. If the stress goes below the critical value (severe stress), D_{max} does not change anymore, but g_m drops with ongoing severity of stress:

$$g_m = g_m^X \frac{f_2}{f_{2c}} \tag{4.206}$$

Now we follow the drought-tolerant strategy. When stress sets in, D_{max} increases while g_m decreases until the critical soil moisture is reached. This is described by:

$$D_{max} = D_{max}^X + (D_{max}^* - D_{max}^X)\frac{f_2 - f_{2c}}{1 - f_{2c}} \tag{4.207}$$

This strategy leads to more evaporation, thereby possibly decreasing the water use efficiency. If the stress goes below the critical value (severe stress), g_m does not change anymore, but D_{max} drops with ongoing severity of stress:

$$D_{max} = D_{max}^X \frac{f_2}{f_{2c}} \tag{4.208}$$

For low vegetation types in the new parameterization, D_{max}^* follows from g_m^* via Eq. 4.203. f_0^* for C_3 plants is fixed at 0.95 and for C_4 plants at 0.6. The routine corresponding to the new version is called COTWORESTRESS.

High vegetation *Calvet et al.* [2004] discuss the soil moisture stress response by high vegetation types. In unstressed conditions, the following relationship holds for low vegetation types:

$$\ln(g_m^*) = 4.7 - 7f_0^* \tag{4.209}$$

with g_m^* in $mm\ s^{-1}$. The product $g_m f_0$ controls A_m, since C_i is influenced by f_0. Therefore the negative correlation between the two parameters makes that CO_2 assimilation flux does not drop too much. Figure 4.14 shows the stress response for high vegetation types schematically. The starting point is the unstressed condition (θ=100%). First we follow the drought-avoiding strategy. When stress sets in, f_0 decreases while g_m keeps its unstressed value until the critical soil moisture is reached. This is described by:

$$f_0 = f_0^* + (f_0^* - f_0^N)\frac{1 - f_2}{1 - f_{2c}} \tag{4.210}$$

where f_0^N is the value of f_0 given by the relationship between g_m and f_0 under severe stress conditions, with $g_m = g_m^*$:

$$\ln(g_m^*) = 2.8 - 7f_0 \tag{4.211}$$

This strategy leads to an increase of the water use efficiency. If the stress goes below the critical value (severe stress), f_0 increases and g_m decreases via:

$$g_m = g_m^* \frac{f_2}{f_{2c}} \tag{4.212}$$

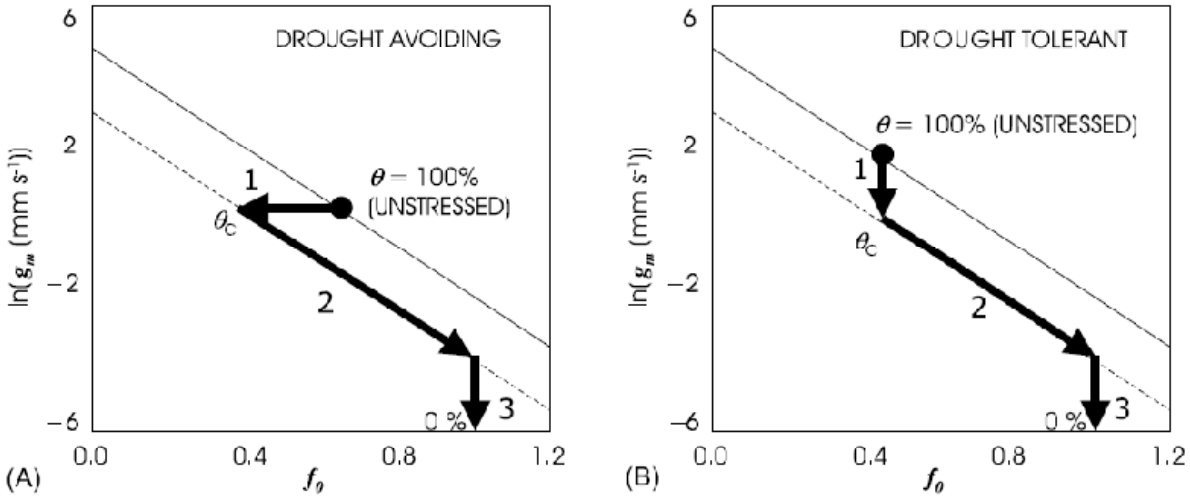

Figure 4.14: Stress responses for high vegetation. Reproduced from *Calvet et al.* [2004]

Now we follow the drought-tolerant strategy. When stress sets in, f_0 keeps its unstressed value while g_m decreases until the critical soil moisture is reached. This is described by:

$$g_m = g_m^* - (g_m^* - g_m^N)\frac{1 - f_2}{1 - f_{2c}} \tag{4.213}$$

where g_m^N is the value of g_m given by Eq. 4.211 with $f_0 = f_0^*$. This strategy leads to a decrease of the water use efficiency. If the stress goes below the critical value (severe stress), f_0 increases and g_m decreases via:

$$g_m = g_m^N \frac{f_2}{f_{2c}} \tag{4.214}$$

For high vegetation types in the new parameterization, f_0^* follows from g_m^* via Eq. 4.209. For D_{max}^* a relationship with g_m^* was developed based on results from *Calvet et al.* [2004]:

$$D_{max}^* = -37.97 \ln(g_m^*) + 150.4 \tag{4.215}$$

This equation was used in Table 4.5 to determine D_{max}^* in the case of forests.

From leaf to canopy

The photosynthesis model calculates the net CO_2 assimilation at the leaf scale. For the upscaling to the canopy, integration over the canopy is needed. It is assumed that variables T_s, D_s and C_s do not vary within the canopy together with the model parameters. In SURFEX, wet leaves from the interception of rain or leaves covered by snow do not assimilate CO_2. The tile-specific skin temperature T_s is calculated by solving the surface energy balance for each tile. In COTWORES (and COTWORESTRESS), D_s at canopy level is calculated from D_s at the reference atmospheric level from a simple flux-gradient relationship by using the aerodynamic resistance ra and the water vapour flux of the previous time step. For C_s, this is done too, with the net CO_2 flux. The incoming shortwave radiation is attenuated in the canopy. At the top of the canopy, the incoming PAR is assumed to be 48% of the incoming shortwave radiation. The PAR extinction is described by *Roujean* [1996]. The PAR at height z in the canopy is given by:

$$I_a(z) = (1 - K(z)) \times I_a(h) \tag{4.216}$$

where h is the height of the top of the canopy and K is the extinction coefficient given by:

$$K(z) = f(\theta_s) \times K_{df}(z) + (1 - f(\theta_s)) \times K_{dr}(z) \tag{4.217}$$

Where $K_{df}(z)$ and $K_{dr}(z)$ are the extinction coefficients of diffuse and direct light, respectively:

$$K_{df}(z) = 1 - \exp(-0.8bLAI(h - z)/h) \tag{4.218}$$

$$K_{dr}(z) = 1 - \exp\left(-\frac{G}{\cos\theta_s} bLAI(h - z)/h\right) \tag{4.219}$$

where θ_s is the solar zenith angle and G is a parameter that describes the distribution of leaves (a spherical angular distribution is assumed: G=0.5). f is the ratio of diffuse to total downward shortwave radiation at the top of the canopy given by:

$$f(\theta_s) = \frac{0.25}{0.25 + \cos\theta_s} \tag{4.220}$$

b is the foliage scattering coefficient:

$$b = 1 - \frac{1 - \sqrt{1 - \omega}}{1 + \sqrt{1 - \omega}} \tag{4.221}$$

where ω (=0.2) is the leaf single scattering albedo in the part of the solar spectrum corresponding to the PAR.

Assuming an homogeneous leaf vertical distribution, the integrated canopy net CO_2 assimilation and conductance can be written as:

$$A_{nI} = \frac{LAI}{h} \int_0^h A_n dz \tag{4.222}$$

$$g_{sI} = \frac{1}{r_s} = \frac{LAI}{h} \int_0^h g_s dz \tag{4.223}$$

where r_s is the canopy resistance. The integrations are parameterized with a three-point Gauss quadrature method:

$$A_{nI} = LAI \times \sum_{i=1}^{3} W_i A_n(z_i) \tag{4.224}$$

$$g_{sI} = LAI \times \sum_{i=1}^{3} W_i g_s(z_i) \tag{4.225}$$

where z_i and W_i are the Gauss levels and weights respectively. r_s is used in the calculation of the exchange of water vapour between the vegetation and the atmosphere.

Biomass evolution

The user may define whether the vegetation must be calculated interactively, or must follow from surface climatology fields of LAI. This can be done via a flag (Table 4.1) in the namelist NAM_ISBA (CPHOTO). This section presents the calculations belonging to interactive vegetation.
With a dynamic representation of LAI, the model is able to account for interannual variability, droughts in particular. The interactive LAI is based on biomass evolution due to photosynthetic activity. The biomass module simulates growth and mortality of the vegetation.

Initial version In the initial version a single biomass reservoir B is considered (*Calvet et al.* [1998]). It represents the photosynthetic active biomass, including the leaves and also a proportion of the stem and roots, which provide water for transpiration. Once a day (Δt = 1 day), at midnight, both growth and mortality is calculated:

$$B(t + \Delta t) = B(t) + \Delta B^+ - \Delta B^- \tag{4.226}$$

The growth is based on the accumulated net CO_2 assimilation over the previous day:

$$\Delta B^+ = \frac{M_C}{P_C M_{CO_2}} A_{nI,day} \Delta t \tag{4.227}$$

where P_c is the proportion of carbon in the dry plant biomass, for which a constant value of 0.4 is chosen, and M_C and M_{CO_2} are the molecular weights of carbon and CO_2 (12 and 44 $gmol^{-1}$). $A_{nI,day}$ is the daily accumulated A_{nI} . Mortality can be due to soil moisture stress, diseases and senescence but also to the transportation of organic molecules from the active biomass to stocking and structural organs. It is given by an exponential extinction of B characterized by a time-dependent effective life expectancy:

$$\Delta B^- = B \left(1 - \exp\left(-\frac{\Delta t}{\tau}\right)\right) \tag{4.228}$$

and

$$\tau(t) = \tau_M \frac{A_{nfm}(t)}{A_{n,max}} \tag{4.229}$$

where τ_M is the maximum effective life expectancy, depending on vegetation type (Table 4.5), A_{nfm} is the maximum leaf A_n reached on the previous day and $A_{n,max}$ is the optimum leaf A_n obtained when:
$D_s = 0\ g\ kg^{-1}$
$I_a(h) = 500\ W\ m^{-2}$
$T_s = 25$°C for C_3 plants and $T_s = 35$ °C for C_4 plants.

In order to avoid extreme loss of biomass in periods when A_n is low, the following constraint on leaf span time is imposed:

$$\tau \geq 5\ days \tag{4.230}$$

The LAI is obtained from the biomass assuming a constant ratio, depending on vegetation type (Table 4.5):

$$\alpha_B = \frac{B}{LAI} \tag{4.231}$$

One other vegetation parameter is needed, in order to enable vegetation to start assimilating CO_2 after a period of unfavourable conditions: a LAI minimum value LAI_{min} (Table 4.5). The routine of biomass loss is called LAILOSS. The routine of biomass growth is called LAIGAIN.

Version with nitrogen dilution

Theory In reality, α_B depends on climate (temperature and CO_2 concentration) and nitrogen fertilisation. In order to account for plant morphology, the nitrogen dilution concept by *Lemaire and Gastal* [1997] is applied in the new version of biomass evolution. The plant N decline model is a well-established agronomical law relating the plant N in non-limiting N-supply conditions to the accumulated aboveground dry matter. The critical plant N is the value of N maximizing growth, and this value decreases for increasing biomass accumulation following a negative power law. The basis of the model is that the metabolic component of the plant biomass is related to total biomass through an allometric logarithmic law (*Calvet and Soussana* [2001]). In ISBA-A-gs, the metabolic biomass component is identified as the active biomass, or leaf biomass. The relationship between active biomass B and total, non-woody aboveground biomass B_T is:

$$B_T = \left(\frac{B}{c}\right)^{1/(1-a)} \tag{4.232}$$

where a and c are constant parameters: $c = 0.754$, and a may vary with CO_2 concentration, but for the sake of simplicity a constant value $a = 0.38$ is used (XCA_1x_CO2_NIT). The total aboveground biomass consists of the active biomass reservoir and the structural aboveground reservoir (B_s), which can be considered as the "living" structural biomass, like the stem. For forests, wood is a dead reservoir and does not contribute to B_s. Within the nitrogen dilution model a relationship between the leaf area ratio LAR and the aboveground nitrogen concentration N_T is applied:

$$LAR = \frac{LAI}{B_T} = eN_T + f \tag{4.233}$$

where e and f are called plasticity parameters and are derived per vegetation type (Table 4.5). Eq. 4.233 can be used as a closure equation to estimate α_B:

$$\alpha_B = \frac{1}{eN_a + f/(cB_T^{-a})} \tag{4.234}$$

where N_a is the nitrogen concentration in the active biomass. It depends on vegetation type and on the nitrogen fertilisation. For further details and derivations see *Calvet and Soussana* [2001]. In this way, α_B has become a model variable depending on B_T . However, for global simulations, it is desirable to keep α_B as a constant parameter in order to let α_B represent rather intrinsic plant characteristics denoting a biological adaptation to average climate and growing conditions (*Calvet and Soussana* [2001]). For that purpose, Eq. 4.234 can only be solved by iteration. Moreover, LAR and N_T data to derive the plasticity parameters by regression is lacking. However, data is available for leaves in the form of the specific leaf area SLA and the nitrogen content in leaves N_L:

$$SLA = \frac{LAI}{B_L} = eN_L + f \tag{4.235}$$

Both the iteration issue and the availability of data to derive e and f give rise to modify the nitrogen dilution module. Eq. 4.234 is simplified by considering α_B as the ratio of the biomass of green leaves to LAI:

$$\alpha_B = \frac{1}{SLA} = \frac{1}{eN_L + f} \tag{4.236}$$

It must be noted that N_L may decrease for increasing CO_2 concentration (*Calvet et al.* [2008] and section 4.2.3).

Biomass reservoirs The different biomass reservoirs are calculated using a simplified allocation scheme (*Calvet and Soussana* [2001]). Figure 4.15 presents the allocation scheme schematically. Next to B and B_s, there is a belowground structural biomass reservoir B_{s2}. The active biomass is calculated in the same way as in the initial version (Eq. 40). The B-decline term (Eq. 4.228) is split into a mortality and storage term:

$$\Delta B^- = M_B + S_B \tag{4.237}$$

In the growing phase ($\Delta B^+ \geq \Delta B^-$) the N decline equations can be applied. When the vegetation becomes senescent ($\Delta B^+ < \Delta B^-$), the equations are no longer valid. Therefore a distinction between the two phases is made.

In the growing phase, following the N decline equations, B_T is derived from B using Eq. 4.232 and B_s is the difference between the two terms. The mortality of B_s is assumed to be independent of photosynthesis and is given by:

$$M_{Bs} = B_s \left(1 - \exp\left(-\frac{\Delta t}{\tau_M}\right)\right) \tag{4.238}$$

The structural biomass also looses carbon through respiration. This term is estimated using the common observation that maintenance respiration of non-active biomass is proportional to the biomass value, with a Q_{10} temperature dependence:

$$R_{Bs} = \eta_R B_s Q_{10}^{(T_s - 25)/10} \Delta t \tag{4.239}$$

where T_s is the skin temperature in °C, η_R is a respiration rate fixed at $1\% day^{-1}$ and $Q_{10} = 2.0$. Finally, the storage term S_B is calculated as the residual of the structural biomass budget:

$$S_B = \Delta B_s - M_{Bs} - R_{Bs} \tag{4.240}$$

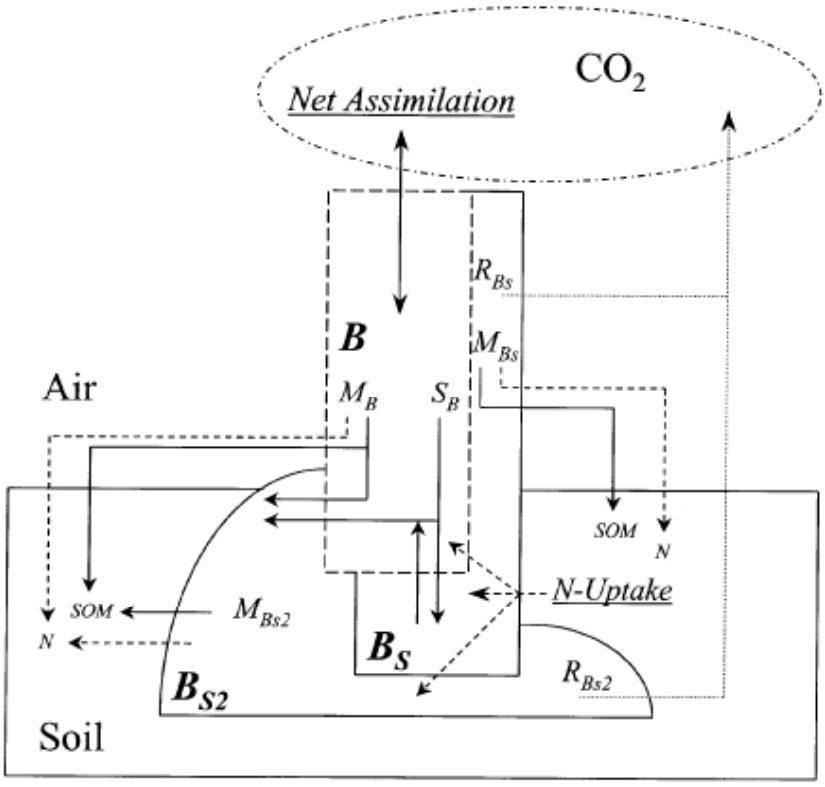

Figure 4.15: Schematic representation of the simple biomass model. Nitrogen (N) and carbon fluxes are represented by dashed and solid lines, respectively. The three biomass (B) compartments are indicated together with storage and mortality terms (S and M, respectively). Heterotrophic respiration (R) is represented by dotted lines. The mortality terms may be used as an input of a model of wood production and SOM. From: *Calvet and Soussana* [2001]

The mortality M_B in Eq. 4.237 is obtained by difference. In situations where S_B exceeds ΔB^- (implying that $M_B < 0$), an alternative formulation of B-decline is employed. It is assumed that there is no loss of active biomass outside the plant system during the considered time step, so $M_B = 0$ and that the difference in total aboveground biomass is the difference between the biomass gain due to daily net assimilation and the mortality and respiration losses of structural biomass:

$$\Delta B_T = \Delta B^+ - M_{Bs} - R_{Bs} \tag{4.241}$$

B_T is derived from this difference and the value at the previous time step. B follows from B_T via Eq. 4.232 and B_s is the difference between the two terms. A new value of the storage term S_B is given by Eq. 4.240. In the senescent phase, B_s evolves independently from B. S_B is set to zero and the mortality and respiration losses are directly applied to B_s:

$$B_s = B_s^{t-1} - M_{Bs} - R_{Bs} \tag{4.242}$$

The belowground structural biomass B_{s2} is not treated by the plant N decline model. The mortality and respiration losses of B_{s2} are calculated using equations similar to Eqs. 4.238 and 4.239:

$$M_{Bs2} = B_{s2}\left(1 - \exp\left(-\frac{\Delta t}{\tau_M}\right)\right) \tag{4.243}$$

$$R_{Bs2} = \eta_R B_{s2} Q_{10}^{(T_{soil}-25)/10} \Delta t \tag{4.244}$$

where T_{soil} is the temperature in °C of the soil layer in the force-restore version of ISBA. Note that both R_{Bs} and R_{Bs2} are calculated every time step and accumulated over one day. B_{s2} is fed by two mechanisms. First, when the storage term S_B is negative (this may happen, e.g., when a cut is prescribed in the model), this quantity is redirected to B_{s2}. Second, when the total aboveground plant biomass B_T is lower than $c^{1/a}$, it is assumed that the mortality term M_B becomes a storage term that increases B_{s2}.
The routine corresponding to the nitro dilution version is called NITRO_DECLINE.

The module can be coupled to a soil organic matter (SOM) model. The SOM is fed by the mortality terms (*Calvet and Soussana* [2001]). Besides, the model still lacks a wood (dead biomass) reservoir. Those extensions have been developed by *Gibelin et al.* [2008] (ISBA-CC).

Note: In the model, the biomass loss is calculated before the biomass gain. When NITRO_DECLINE is called and values from the previous day are needed, those are the values of the previous day calculated in NITRO_DECLINE, so before the biomass growth due to photosynthesis (calculated in LAIGAIN) is added to the biomass reservoir. In that case, LAILOSS is not called (in VEGETATION_EVOL).

Respiration

Since the biomass model is not coupled to a soil model, soil respiration needs to be parameterized in another way. In ISBA-A-gs, a simple Q_{10} equation is used to represent the ecosystem respiration, but this method lacks a representation of the effect of soil moisture on the soil respiration. The representation of all the respiration terms (including the heterotrophic respiration and its dependence on soil moisture) was developed by *Gibelin et al.* [2008] in ISBA-CC.
The CO_2 ecosystem respiration is parameterised by a Q_{10} function:

$$R_{ECO} = R_{E25} Q_{10}^{(T_{soil}-25)/10} \tag{4.245}$$

where R_{E25} is the reference respiration at 25 °C , T_{soil} is the temperature in °C of the soil layer in the force-restore version of ISBA and Q_{10} is fixed at 2.0. R_{E25} has to be determined per vegetation type in each grid box, assuming equilibrium between multi-annual CO_2 assimilation by photosynthesis (or gross primary production, GPP, i.e. raw carbon uptake by photosynthesis), harvest and ecosystem respiration:

$$GPP_{acc} - Harvest_{acc} = R_{ECOacc} = R_{E25} \left\{ Q_{10}^{(T_{soil}-25)/10} \right\}_{acc} \tag{4.246}$$

where acc stands for accumulated over the multi-year period. For harvest, examples of yearly harvest estimates per vegetation type are given in Table 4.4. Numbers are based on a 40% carbon content of dry biomass.
Once R_{E25} is calibrated for each vegetation type within each grid box, it may be treated as a surface climatology field, which is input to the model.

! Ecosystem respiration is to a large extent driven by soil respiration. Soil respiration depends on soil temperature and on soil moisture. In the present version of the model, the soil moisture effect is not accounted for. A simple, proportional dependence of R_{E25} to surface soil moisture (e.g. ratio of surface soil moisture to field capacity) is being tested.

Table 4.4: Example of harvest estimates ($t\ C\ ha^{-1}\ y^{-1}$)

Vegetation type	Harvest
Deciduous	3.2
Coniferous	2.3
Evergreen	3.2
C_3 grass	2.3
C_4 grass	3.2
C_3 crops	2.3
C_4 crops	3.2

CO_2 fluxes

The photosynthesis model is called from COTWORES (or COTWORESTRESS) for all present vegetation tiles (Section 4.2.1).

The net ecosystem CO_2 exchange (NEE) per vegetation type is given by:

$$NEE = GPP - R_{ECO} \tag{4.247}$$

Throughout SURFEX, the unit of the kinematic CO_2 flux is $kgCO_2\ kgAir^{-1}\ m\ s^{-1}$ (as opposed to dynamic CO_2 flux units of $kgCO_2\ m^{-2}\ s^{-1}$).

4.2.2 Vegetation parameters

Gibelin et al. [2006] have proposed default values for the parameters of the new version of ISBA-A-gs (NIT option). They are listed in Table 4.5 for 7 vegetation types.

! In the code, g_m^*, τ_M, LAI_{min}, D_{max}^*, f_0^*, g_c, θ_C, e, f, N_l are named GMES, SEFOLD, LAIMIN, DMAX, FZERO, GC, F2I, CE_NITRO, CF_NITRO, CNA_NITRO, respectively.
GMES and GC are in units of $m\ s^{-1}$, SEFOLD in s, DMAX in $kg\ kg^{-1}$

For herbaceous vegetation: f_0^* is prescribed in MODD_CO2V_PAR, D_{max}^* is derived from the inversion of 4.203.

In the case of trees: f_0^* and D_{max}^* are not prescribed in the code, they are derived from the inversion of Eqs 4.209 and 4.215, respectively.

4.2.3 Discussion

In this final chapter, some issues are discussed that deserve attention for future code development.

Table 4.5: Values of ISBA-A-gs parameters for the ECOCLIMAP vegetation types (g_m^* in $mm\ s^{-1}$, τ_M in days, LAI_{min} in $m^2\ m^{-2}$, D_{max}^* in $g\ kg^{-1}$, f_0^* dimensionless, g_c in $mm\ s^{-1}$, strategy of response to soil moisture stress (drought-tolerant or drought-avoiding), θ_C dimensionless, e in $m^2\ kg^{-1}\ \%^{-1}$, f in $m^2\ kg^{-1}$, and N_l in %

Vegetation type	g_m^*	τ_M	LAI_{min}	D_{max}^*	f_0^*	g_c	Strategy	θ_C	e	f	N_l
Deciduous broadleaf trees	3	230	0.3	109	0.51	0.15	tolerant	0.3	4.83	2.53	2
Evergreen broadleaf trees	2	365	1	124	0.57	0.15	tolerant	0.3	4.83	2.53	2.5
Needle leaf trees	2	365	1	124	0.57	0	avoiding	0.3	4.85	-0.24	2.8
C_3 crops	1	150	0.3	50	0.95	0.25	avoiding	0.3	3.79	9.84	1.3
C_4 crops	9	150	0.3	33	0.6	0.15	tolerant	0.3	7.68	-4.33	1.9
C_3 natural herbaceous	1	150	0.3	50	0.95	0.25	tolerant	0.3	5.56	6.73	1.3
C_4 natural herbaceous	6	150	0.3	52	0.6	0.15	tolerant	0.3	7.68	-4.33	1.3

Respiration

Ecosystem respiration is a major component of the net CO_2 flux. ISBA-A-gs lacks a soil carbon reservoir and a wood (dead biomass) reservoir. Moreover, roots are not explicitly represented. Those extensions (and the associated respiration fluxes) are present in the ISBA-CC version, which is being coded into SURFEX. This provides possibilities for respiration calculations for each of the carbon reservoirs, that might replace the present respiration calibration. There is a strong need for direct respiration measurements to validate the parameterization.

With respect to the present Q_{10} calibration of ecosystem respiration, soil moisture effects are not accounted for. This hypothesis is not correct and a simple representation of the surface soil moisture effect on ecosystem respiration has to be introduced in SURFEX. Furthermore, the value of Q_{10} is fixed at 2, because it is generally used in literature about respiration. However, climate conditions may ask for a differentiation in the Q_{10} value.

Soil moisture stress parameterization

The soil moisture stress parameterization may depend on the way soil hydrology is represented. Since the soil moisture content depends on the soil parameterization, which is different for ISBA-FR and ISBA-DF, this may lead to divergent behaviour. The use of ISBA-A-gs with the ISBA-DF option has still to be tested.

Temperature response of g_m for C_3 plants

Table 4.2 presents for C_3 plants a T_2 of 36 °C for g_m. However, in the beginning of the ISBA-A-gs development, this value was 28 °C (*Calvet et al.* [1998]). This was changed during the development of new versions (e.g. *Calvet* [2000]). This implies that the temperature response of g_m, which is a sensitive parameter for photosynthesis, for C_3 plants approaches the response for C_4 plants, i.e. an optimal temperature for photosynthesis of 32 °C. This is certainly too high for boreal forests and grasslands adapted to cold climates (high

latitudes or mountainous areas). The T_2 parameter will have to be adapted as a function of a climatology of air temperature.

Radiative transfer within the vegetation

The radiative transfer equations and the quadrature method described in section 4.2.1 are based on many approximations (*Calvet et al.* [1998]). In particular, the representation of (1) scattering of the photosynthetically active radiation (PAR), (2) the interception of the diffuse radiation, within the canopy, may be oversimplified for regions/seasons with a lot of diffuse PAR (clouds, high solar zenith angles), especially for dense canopies.

The radiative transfer influences (1) photosynthesis and the canopy conductance, (2) mortality. Moreover, *Calvet et al.* [2008] have shown that the way light interception within the canopy is modelled may impact the simulated plant response to climate change.

Tropical evergreen forests Simulations with ISBA-A-gs showed that A_n is underestimated in tropical evergreen forest. This may cause an underestimation of net primary production (NPP) and an overestimation of the mortality of leaves. A solution must be found to improve photosynthesis and mortality. Mortality depends on the optimum net CO_2 assimilation (with 500 $W\ m^{-2}$ PAR). For evergreen forests that have a high radiation extinction in the canopy, 500 $W\ m^{-2}$ PAR may not be realistic under optimal conditions. Therefore, mortality might be overestimated. This could be dealt with by either reducing the optimum PAR or by considering a different mortality parameterization. Radiative transfer equations may also be improved for dense canopies in order to account better for diffuse radiation.

For the photosynthesis and canopy resistance, the vegetation parameter values in the photosynthesis model may be reconsidered. Therefore, data sets of tropical evergreen forests are needed to calibrate parameters like g_m and N_a.

Representation of mortality In NITRO_DECLINE, a correction of mortality is introduced for dense canopies. The effective life expectancy of the leaves (governing the exponential decline of B) is increased. Indeed, Eq. 4.229 relates mortality to the factors acting on photosynthesis at the leaf level. The factors accounted for by Eq. 4.229 include self shading since A_{nfm} is the maximum average leaf net assimilation: this quantity depends on LAI, which is employed to compute the extinction of solar radiation (see section 4.2.1). Preliminary tests of the nitrogen dilution option (NIT) showed that at very high values of LAI, the self shading effect in Eq. 4.229 may trigger exaggerated values of mortality and, finally, underestimated values of biomass. Therefore, Eq. 4.229 was modified such as, for dense canopies, the leaf-level $A_{nfm}/A_{n,max}$ ratio is replaced by a value representative of the canopy:

$LAI\ A_{nfm}/(X\ A_{n,max})$, where X represents the maximum value of the ratio between canopy- and leaf-level optimum net assimilation. The value of X denotes the relative advantage of a well-developed canopy over a single horizontal leaf in terms of net assimilation of CO_2, in optimal conditions. This value was searched for various models parameters such as LAI, and g_m, by performing simulations over one annual cycle at several latitudes. In each configuration, a value of LAI (always higher than 5 $m^2\ m^{-2}$) maximising the ratio between canopy- and leaf-level optimum net assimilation could be found. A logarithmic relationship between the optimal value of X and gm was obtained (X tends to decrease for increasing values of g_m). This relationship depends on latitude because of the influence of maximum solar elevation on X (X is lower at high latitudes). Finally, Eq. 4.229 was rewritten as:

$$\tau(t) = \tau_M \frac{A_{nfm}(t)}{A_{n,max}} Max\left\{1, g_m^{0.321} LAI/LAI_B\right\} \tag{4.248}$$

where g_m is expressed in units of $mm\ s^{-1}$, and LAI_B represents a limit value of LAI depending on latitude (L_a) as:

$$LAI_B = 5.76 - 0.64 \tan\left(Min\left\{\|L_a\|, 73^\circ\right\}\right) \tag{4.249}$$

The LAI_B parameter ranges from 5.6 to 3.6, from equator to latitudes higher than 73°. For values of g_m close to 1 $mm\ s^{-1}$, it represents the maximum LAI value for which the leaf-level net assimilation may be employed to represent mortality. Those equations were derived with the radiative transfer parameterisation described in section 4.2.1 and may be different for another radiative transfer model.

Representation of crops

In ISBA-A-gs, crops are represented like natural vegetation. There is no particular description of the harvested elements like fruits and e.g. grain yield (cereals) is not directly simulated. Nevertheless, *Calvet et al.* [2008] show that the maximum above-ground biomass simulated by the model correlates with the crop yield and that the model is able to simulate realistic time series of LAI values over one annual cycle, and to represent the interannual variability.
Moreover, a simple representation of irrigation was implemented in SURFEX, and the possibility to simulate crops sown at springtime.

Irrigation An irrigation amount of 30mm is added to the precipitation forcing each time the simulated extractable soil moisture content (dimensionless) reaches a predefined threshold. This threshold decreases from 0.70 for the first irrigation, to 0.55 for the second, 0.40 for the third, and 0.25 for the following ones (*Calvet et al.* [2008]). The threshold values are declared in MODD_AGRI.

Emergence Whereas the LAI annual cycle of natural vegetation (leaf onset, senescence, regrowth) is driven by climate conditions, crops are sown at dates chosen by the farmers. In ISBA-A-gs, crops sown at wintertime (i.e. emerging at springtime like natural vegetation) like wheat, are simulated in the same way as natural vegetation. The advantage of this is that no ancillary information is needed and that possible regrowths after a drought period are simulated interactively with the climate.
On the other hand, crops developing at summertime cannot be simulated like natural vegetation. An emergence date has to be prescribed and before this date (MODD_AGRI_n), LAI is limited to a minimum value (e.g. 0.3 $m^2\ m^{-2}$). An harvest date is not prescribed. It is considered that climatic conditions (drought, cold) permit to drive the senescence.
In order to prescribe emergence dates, future developments should couple SURFEX to existing crop calendars, at the global scale.

Representation of nitrogen dilution

The CO_2 fertilization effect tends to increase the vegetation biomass but this effect is limited by nitrogen dilution. In Calvet et al. 2008, nitrogen dilution is accounted for by parameterizing the change in leaf nitrogen mass-based concentration N_L in response to [CO_2] rise. The sensitivity of leaf nitrogen concentration versus [CO_2] is accounted for by using the meta-analysis of the literature carried out by Yin 2002 (Yi02). The meta-analysis of Yi02 indicates that, on average, a CO_2-doubling causes a 18% decrease in N_L, but

that the N_L response to CO_2 is influenced by a number of factors. A change in [CO_2], from [CO_2] = C_1 to [CO_2] = C_2, produces a change in N_L from N_{L1} to N_{L2} following:

$$\ln\left(\frac{N_{L2}}{N_{L1}}\right) = -a\exp\left[b - \frac{N_{L1}}{N_{Lmax}}\right]\ln\left(\frac{C_2}{C_1}\right) \tag{4.250}$$

with a=0.048 and N_{Lmax}=6.3 %. In the Yi02 study, C_2/C_1 ranges from 0.53 to 3.2. The b parameter may vary significantly from one vegetation type to another. For example, in median radiation and air temperature (Ta) conditions, b = 1.48 for a fertilised crop, b = 2.56 for a deciduous forest, b = 1.81 for a coniferous forest or natural grasslands. The values of b are given by:

$$b = 0.75DF - 0.33FERT + 1.1PPFD + \frac{T_a}{23} \tag{4.251}$$

with DF=1 for deciduous forests (0 for other biomes), and FERT=1 for fertilized ecosystems like crops (0 for other biomes). PPFD is the average photosynthetically active solar radiation reaching the leaf within the vegetation canopy (median value of 0.74 $mmol\ m^2\ s^1$, equivalent to a total solar radiation of 335 $W\ m^2$). In this study, no solar radiation or temperature effect is associated with a change in [CO_2] and the median PPFD and Ta values of Yi02 are used in Eq. 4.251.

Annex 1: Description of the Fortran routine used to calculate the CO_2 flux

SUBROUTINE COTWORESTRESS
This routine is used at the time step of SURFEX (e.g. 300 s).
1. The photosynthetically active radiation (PAR) is derived from the incident shortwave radiation. A constant factor of 0.48 is used.

2. Drought-avoiding and drought-tolerant responses to soil moisture stress are simulated for herbaceous and for woody plants (depending on the vegetation type of the considered patch). Namely, the photosynthesis parameters are refreshed to be consistent with the root-zone soil moisture.

3. The CO_2 compensation concentration of photosynthesis (ZGAMMT), the maximum photosynthesis (ZANMAX), and the mesophyll conductance (ZGMEST) are refreshed to be consistent with the leaf temperature (i.e. surface temperature in a single-source configuration).

4. The leaf-to-air saturation deficit within the canopy (depends on leaf temperature and air humidity) is refreshed (ZDSP).

5. The CO_2 concentration within the canopy is refreshed (ZCSP).

6. Ecosystem respiration is refreshed (ZRSOIL).

7. The solar zenith angle is prescribed (PZENITH).

8. Integrated canopy values of photosynthesis (ZTPST), net assimilation (ZTAN), and leaf conductance (ZTGS) are obtained by a 3-point Gauss quadrature method (SIZE(PABC) is equal to 3 ; can be modified).

9. The PAR at each Gauss level is calculated by radiative transfer equations in SUBROUTINE CCETR. In CCETR, the interception of direct and diffuse light is represented. The fraction of diffuse radiation (ZXFD)

depends on the solar zenith angle, only.

10. At each Gauss level within the canopy, the photosynthesis model (SUBROUTINE COTWO) is run.

11. The canopy resistance (PRS) is calculated, as well as the net ecosystem exchange of CO_2 (PCO2FLUX).

Chapter 5

Surface boundary layer scheme

Contents

5.1 Introduction

Surface atmosphere exchanges, mainly momentum, water and heat surface fluxes, drive the boundary layer evolution, and influence the formation of low level clouds and more generally the synoptic flows and climate system. The modelling of these fluxes is performed by specific surface schemes: Soil-Vegetation-Atmosphere Transfer (SVATs) schemes for vegetation (*Chen et al.* [1997] review the vegetation schemes used in the intercomparison exercice on Cabauw grass site), urban schemes for cities (see a review in *Masson* [2006]), or schemes dedicated to sea or ice surfaces. The degree of complexity of these schemes is wide. The simplest models are bucket models (e.g. *Manabe* [1969], *Robock et al.* [1995]), with only one water reservoir in the soil. Next are the so-called big leaf models (*Deardorff* [1978], *Noilhan and Planton* [1989]) with only one surface energy balance and no canopy. The more detailed schemes have several layers in the soil, several energy budgets (low vegetations, snow and tree canopy) and photosynthesis production to simulate the carbon cycle (see *Simon et al.* [2007]). The same degree of variability exists in the complexity of the physical processes described in urban schemes (see *Masson* [2006]).

However, the present paper will not discuss on the complexity of the physical and physiological processes of the soil or plants in these schemes. The topic of this paper is to discuss the coupling of surface schemes

to atmospheric models. Independantly of the complexity of the processes, two coupling methods are usually used (fig 10.1):

- single-layer coupled schemes: these surface schemes are forced by only one atmospheric layer (i.e. the lowest atmospheric layer of an atmospheric model, as in fig 10.1b). The surface schemes respond to atmospheric variables at this level (temperature, wind, humidity, incoming radiation, etc...) and they produce averaged upwards turbulent fluxes and radiative quantities (albedo, emissivity, surface temperature). Note that this level is physically supposed to be high enough above the surface to be in the inertial sublayer (or constant flux layer), most schemes using Monin-Obukhov theory to parameterize turbulent fluxes. These exchanges have been normalized in the Assistance for Land-surface Modelling activities (ALMA) norm (see *Best et al.* [2004] and *Polcher et al.* [1998]).
  Because of the simplicity of this type of coupling, these surface schemes can be used off-line (e.g. forced directly by observations), so that they can be used for a wide range of applications (e.g. hydrology). All schemes presented in the offline intercomparison by *Chen et al.* [1997] are single-layer schemes. These schemes can have a separate modelling of the soil and of the canopy, but the coupling with the atmosphere is always done at a forcing level above the canopy. The link between the forcing level and the soil/canopy to compute energy fluxes is usually done using systems of aerodynamical/stomatal resistances (as in *Deardorff* [1978]), that may depend on many factors, such as plant stress or atmospheric stability.

- multi-layer coupled schemes: these schemes are coupled with several atmospheric levels (fig 10.1c). They interact not by surface fluxes (except for the lowest level), but directly throughout the prognostic variables equations of the atmospheric model at each level. For example, drag forces by the obstacles (trees or buildings) will slow the wind and increase the turbulence, heat (water) fluxes by these obstacles will produce differential heating (moistening) between the levels. *Xinmin et al.* [1999] use such a scheme coupled inline to a planetary boundary layer model to study the influence of the tree density in a forest on the air characteristic within the canopy at day and at night. Recently *Simon et al.* [2007] built a multilayer scheme to describe precisely the water and carbon dioxyde fluxes inside the Amazonian forest. For building canopies, *Martilli et al.* [2002], *Coceal and Belcher* [2005] and *Kondo et al.* [2005] are example of multi-layer schemes. The drawback of this high resolution description of the atmospheric processes is an intimate coupling of the surface scheme and the atmospheric model. Furthermore, because atmospheric layers are thin near the surface (depth of the order of 1m) to finely describe the air profile in the Surface Boundary Layer (SBL), the time step of the atmospheric model must usually be much smaller in order to insure numerical stability.
  Such schemes are used when one wants to describe very finely the interaction between the atmosphere and the surface features. For example, low vegetation and soil will interact with air temperature near the surface (say 1m), while tree leaves exchange temperature and humidity with higher level air (with other temperature, humidity). This therefore allows a priori a better simulation of the physical and physiological processes. Another interest of these schemes is the direct simulation of air characteristics down to the surface itself, allowing several specific applications (wind stress in forest ridges, air temperature profile between buildings, etc...).

The objective of this paper is to implement into single-layer schemes the fine description of air profiles near the ground of the multi-layer schemes. That way, the single-layer schemes will gain the explicit physical representation of the surface boundary layer thanks to additionnal air layers, and still be coupled to atmospheric models through only one layer.

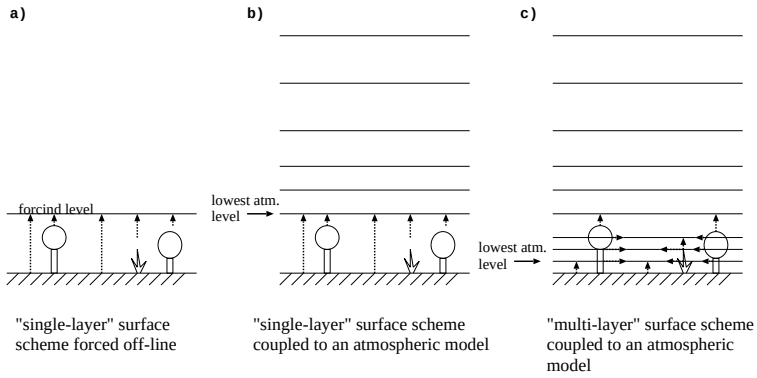

Figure 5.1: Schematic view of surface scheme coupling: a) single-layer surface scheme forced offline. b) single-layer surface scheme forced by an atmospheric model. c) multi-layer scheme forced by an atmospheric model. Dotted arrows show the interactions between surface and coupling/atm. forcing: (a) with the forcing level, (b) the lowest atm level and (c) with all levels intersecting the canopy.

5.2 Theory

5.2.1 Atmospheric equations

The atmosphere can be described by dynamical (3 wind components) and thermodynamical variables (heat content or temperature, water vapor, possibly other water phases quantities). In this study, only the Planetary Boundary Layer was considered, neglecting mean vertical velocity and horizontal turbulent fluxes. The Boussinesq hypothesis is applied for the sake of simplicity. However, the following derivation can be generalized to more complex equation systems. Only the theory is described in the main part of the paper. The numerics for implementation and coupling in models are discussed in the last section.

Using mean horizontal wind components (U, V), potential temperature (θ) and water vapor specific humidity (q), without water phase changes, the equations describing the atmosphere evolution can be written as:

$$\left\{\begin{array}{rcl@{\quad}l@{\quad}l@{\quad}l}
\frac{\partial U}{\partial t} & = & \underbrace{-U\frac{\partial U}{\partial x}-V\frac{\partial U}{\partial y}}_{Adv} & \underbrace{-fV}_{Cor} & \underbrace{+fV_g}_{Pres.} & \underbrace{-\frac{\partial \overline{u'w'}}{\partial z}}_{Turb} \\
\frac{\partial V}{\partial t} & = & \underbrace{-U\frac{\partial V}{\partial x}-V\frac{\partial V}{\partial y}}_{Adv} & \underbrace{+fU}_{Cor} & \underbrace{-fU_g}_{Pres.} & \underbrace{-\frac{\partial \overline{v'w'}}{\partial z}}_{Turb} \\
\frac{\partial \theta}{\partial t} & = & \underbrace{-U\frac{\partial \theta}{\partial x}-V\frac{\partial \theta}{\partial y}}_{Adv} & +\underbrace{\dot{Q}}_{Diab.} & & \underbrace{-\frac{\partial \overline{w'\theta'}}{\partial z}}_{Turb} \\
\frac{\partial q}{\partial t} & = & \underbrace{-U\frac{\partial q}{\partial x}-V\frac{\partial q}{\partial y}}_{Adv} & & & \underbrace{-\frac{\partial \overline{w'q'}}{\partial z}}_{Turb}
\end{array}\right. \tag{5.1}$$

where $U_g = -\frac{1}{f\rho}\frac{\partial p}{\partial x}$ and $V_g = -\frac{1}{f\rho}\frac{\partial p}{\partial y}$ are the geostrophic wind components, $\overline{u'w'}$, $\overline{v'w'}$, $\overline{w'\theta'}$ and $\overline{w'q'}$ are the turbulent fluxes, and $\dot{Q}$ represents the diabatic sources of heat (e.g. radiative tendency).

In addition, a Turbulent Kinetic Energy (TKE, noted $e = \frac{1}{2}(\overline{u'^2} + \overline{v'^2} + \overline{w'^2})$) equation can be used to

describe the turbulence in some atmospheric models:

$$\frac{\partial e}{\partial t} = \underbrace{-U\frac{\partial e}{\partial x} - V\frac{\partial e}{\partial y}}_{Adv} \underbrace{-\overline{u'w'}\frac{\partial U}{\partial z} - \overline{v'w'}\frac{\partial V}{\partial z}}_{Dyn.Prod.} + \underbrace{\frac{g}{\theta}\overline{w'\theta'_v}}_{Therm.Prod.} - \underbrace{\frac{\partial \overline{w'e}}{\partial z}}_{Turb} - \underbrace{\epsilon}_{Diss.} \tag{5.2}$$

where Right Hand Side terms stand for advection of TKE, dynamical production, thermal production, turbulent transport of TKE and dissipation respectively.

5.2.2 Atmospheric equations modified by canopy obstacles

The above equations refer to air parcels that do not interact with any obstacles. Near the surface, when one wants to take into account the influence of obstacles on the flow, these equations must be modified. In atmospheric models, this is done by adding additional terms for each variable, representing the average effect of these obstacles on the air contained in the grid mesh. One should note here that ideally, the volume of the obstacles (trees, buildings) contained into the grid mesh should be removed from the volume of air of the grid mesh. However, this significantly complexifies a lot the atmospheric model, and the approximation to keep the air volume constant even in the presence of obstacles is normally done. This simplification is also chosen here. Then, obstacles impact on the flow is parameterized as:

$$\left\{ \begin{array}{rcllllll} \frac{\partial U}{\partial t} & = & Adv & +Cor & +Pres. & +Turb(U) & +\mathrm{Drag_u} \\ \frac{\partial V}{\partial t} & = & Adv & +Cor & +Pres. & +Turb(V) & +\mathrm{Drag_v} \\ \frac{\partial \theta}{\partial t} & = & Adv & +Diab. & & +Turb(\theta) & +\frac{\partial \theta}{\partial t}_{canopy} \\ \frac{\partial q}{\partial t} & = & Adv & & & +Turb(q) & +\frac{\partial q}{\partial t}_{canopy} \end{array} \right. \tag{5.3}$$

and

$$\frac{\partial e}{\partial t} = Adv + Dyn.Prod. + Therm.Prod. + Turb + Diss. + \frac{\partial e}{\partial t}_{canopy} \tag{5.4}$$

where,

- $\mathrm{Drag_u}$ and $\mathrm{Drag_v}$ are the drag forces (due to pressure forces against the obstacles) that slow the flow,
- $\frac{\partial \theta}{\partial t}_{canopy}$ is the heating/cooling rate due to the heat release/uptake by the surfaces of the canopy obstacles in the grid mesh,
- $\frac{\partial q}{\partial t}_{canopy}$ is the moistening/drying impact of these obstacles,
- and $\frac{\partial e}{\partial t}_{canopy}$ represents the TKE production due to wake around and behind obstacles as well as the additionnal dissipation due to leaves-induced small-scale turbulence.

The prescription of these terms due to the obstacle impact on the flow are parameterized differently for each multi-level surface scheme, and this is not described in detail here. Parameterizations for dynamical variables are often similar for forest canopies. Wind drag is usually parameterized as the opposite of the square of the wind, as in *Shaw and Schumann* [1992] or *Patton et al.* [2001]: $\mathrm{Drag_u} = -C_d a(z) U \sqrt{U^2 + V^2}$ and $\mathrm{Drag_v} = -C_d a(z) V \sqrt{U^2 + V^2}$, where C_d is a drag coefficient and $a(z)$ is the leaf area density at height z (this parameter can be derived from Leaf Area Index and vegetation height, assuming a normalized vertical profile of leaves distribution in the canopy). The TKE production/destruction term can be parameterized as the sum of two effects: wake production by the leaves (parameterized as proportionnal to the cubic

power of wind: $\frac{\partial e}{\partial t}_{canopy} \propto C_d(U^2+V^2)^{\frac{3}{2}}$ as in *Kanda and Hino* [1994]) and the energy loss due to fast dissipation of small scale motions (leaves are of a much smaller scale than the grid mesh). The latter term is often parameterized as proportionnal to the product of wind by TKE ($\frac{\partial e}{\partial t}_{canopy} \propto -C_d e\sqrt{U^2+V^2}$ as in *Kanda and Hino* [1994], *Shen and Leclerc* [1997], *Patton et al.* [2003]). Because of the high degree of complexity of the processes involved (and hence of possibles simplifications), parameterizations for temperature and humidity exchanges are much more variables. For example, *Sun et al.* [2006] parameterize heating effects simply as a function of radiation vertical divergence, while more complex vegetation models, as in *Park and Hattori* [2004], solve leaves temperature and use it to estimate at each atmospheric layer the heat and water vapor exchanges between the forest canopy and the air: $\frac{\partial \theta}{\partial t}_{canopy} \propto a(z)(\theta_l - \theta)$ and $\frac{\partial q}{\partial t}_{canopy} \propto a(z)(q_{sat}(\theta_l) - q)$, where θ_l is the leaves potential temperature and q_{sat} is humidity at saturation (proportionnality coefficients depend on physiological processes of the plant).

For urban canopies, the same drag approach is chosen in general for the effect on wind, and only the wake production term is kept for TKE (because turbulent eddies are large behind buildings, so their dissipation is not as fast as those produced by leaves). Heat exchanges are however more complex and detailled (see *Masson* [2006] for a review), as radiative trapping and shadows, different building heights, and sometimes even road trees are taken into account in state-of-the-art urban models. An exemple of urban canopy parameterization is given in *Hamdi and Masson* [2008].

As stated above, these additional terms allow a fine description of the mean variable profiles in the atmospheric model in the SBL (e.g. wind and temperature profile as a function of stability, wind speed in forest canopy, etc...) and of the flow statistics (non constant flux layer inside the canopy for example).

5.2.3 Implementation of the SBL equations into a surface scheme

The objective of this paper is to provide a way to implement such a description of the SBL with a lot of atmospheric layers directly into the surface scheme. Such a scheme could be used offline (figure 10.2a) or coupled to an atmospheric model (figure 10.2b). As seen by comparing with figure 10.2c, the vertical resolution is the same as with a multi-layer model. The problem is that the computation of most of the terms of the equations (advection, pressure forces, diabatic heating) requires the atmospheric model dynamics and physical parameterizations.

The set of equation (5.3) is rewritten by separating the processes as (i) 'large scale forcing' (LS, that are solved by the atmospheric model), (ii) the turbulence and (iii) the canopy effects:

$$\left\{\begin{array}{lcll} \frac{\partial U}{\partial t} & = & LS(U) & +Turb(U) \quad +\mathrm{Drag_u} \\ \frac{\partial V}{\partial t} & = & LS(V) & +Turb(V) \quad +\mathrm{Drag_v} \\ \frac{\partial \theta}{\partial t} & = & LS(\theta) & +Turb(\theta) \quad +\frac{\partial \theta}{\partial t}_{canopy} \\ \frac{\partial q}{\partial t} & = & LS(q) & +Turb(q) \quad +\frac{\partial q}{\partial t}_{canopy} \end{array}\right. \tag{5.5}$$

The TKE equation remains the same:

$$\frac{\partial e}{\partial t} = Adv(e) + Dyn.Prod. + Therm.Prod. + Turb + Diss. + \frac{\partial e}{\partial t}_{canopy} \tag{5.6}$$

To represent the SBL into the single-layer surface scheme, one considers prognostic atmospheric layers, between the surface and the forcing level of the surface scheme (that is the level that is coupled to the

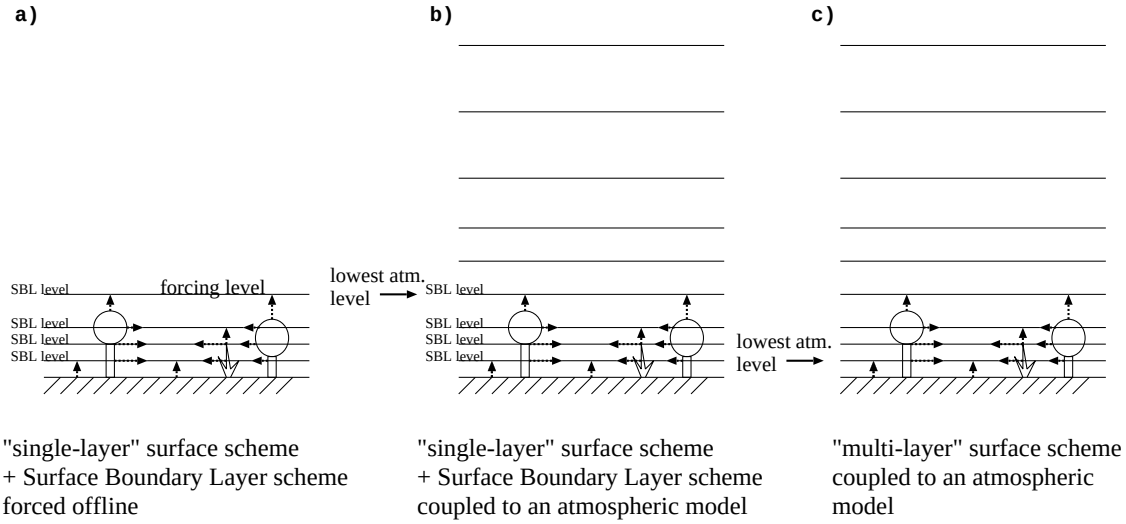

Figure 5.2: Schematic view of the coupling between surface scheme and SBL scheme : a) single-layer surface scheme with SBL scheme forced offline. b) single-layer surface scheme with SBL scheme forced by an atmospheric model. c) multi-layer scheme coupling (as c) in figure 10.1). Dotted arrows show the interactions between surface and SBL scheme (a and b). Upper SBL level is at same height as atmospheric forcing level.

atmosphere). Each of these layers is represented by the wind speed, the potential temperature, the humidity and the Turbulent kinetic energy (all these variables being prognostically computed). They satisfy the set of equations (5.5). In order to solve them, the following assumptions are made:

- The mean wind direction does not vary in the SBL (Rotation due to Coriolis inside the SBL is neglected).
- The advection of TKE is negligible. This assumption is not valid for horizontal scales (and grid meshes) of the order of a few times the canopy height, as equilibrium with forcing condition above is not reached (*Belcher et al.* [2003], *Coceal and Belcher* [2005]), but it is valid for larger scales.
- The turbulent transport of TKE ($\overline{w'e}$) is negligible near the ground and in the SBL. This assumption is fairly valid, this term being generally important only higher in the BL .
- Above the canopy, the turbulent fluxes are uniform with height (constant flux layer).
- The Large Scale forcing terms ($LS(U), LS(V), LS(\theta), LS(q)$) are supposed to be uniform with height in the SBL. It is assumed, for example, that advection and pressure forces are driven by synoptic flow or by the mesoscale BL flow (e.g. sea breeze). Diabatic effects on temperature are also supposed to be uniform.

Then, the equations can be solved if the turbulent terms in the SBL (see subsection (5.2.5)), the canopy terms (depending on each surface scheme physics), and the (uniform with height) large scale forcing are known or parameterized.

Writing the equations at the forcing level ($z = z_a$), which is supposed to be above the canopy (all canopy terms are set to zero) and therefore in the constant flux layer (the turbulent fluxes are supposed to be uniform,

so that the divergences of turbulent fluxes are small), large scale terms can be estimated from the temporal evolution of the variables at the forcing level:

$$\left\{ \begin{array}{lcl} \frac{\partial U}{\partial t}(z=z_a) & = & LS(U) \\ \frac{\partial V}{\partial t}(z=z_a) & = & LS(V) \\ \frac{\partial \theta}{\partial t}(z=z_a) & = & LS(\theta) \\ \frac{\partial q}{\partial t}(z=z_a) & = & LS(q) \end{array} \right. \tag{5.7}$$

In reality, the constant flux layer hypothesis supposes not a constant turbulent flux but a small variation of the turbulent flux compared to its value. The small decrease/increase of the turbulent flux can lead to tendencies of the mean variables. However, this small variation is generally relatively uniform in the whole boundary layer (e.g. uniform heating of the convective boundary layer). This impact of the fluxes at the scale of the whole BL is included in the LS terms.

5.2.4 Boundary conditions

Finally, one obtains (using only one wind component, as the wind does not veer with height in the SBL):

$$\left\{ \begin{array}{lcllll} \frac{\partial U}{\partial t} & = & \frac{\partial U}{\partial t}(z=z_a) & +Turb(U) & +\mathrm{Drag_u} \\ \frac{\partial \theta}{\partial t} & = & \frac{\partial \theta}{\partial t}(z=z_a) & +Turb(\theta) & +\frac{\partial \theta}{\partial t}_{canopy} \\ \frac{\partial q}{\partial t} & = & \frac{\partial q}{\partial t}(z=z_a) & +Turb(q) & +\frac{\partial q}{\partial t}_{canopy} \end{array} \right. \tag{5.8}$$

And

$$\frac{\partial e}{\partial t} = Dyn.Prod. + Therm.Prod. + Diss. + \frac{\partial e}{\partial t}_{canopy} \tag{5.9}$$

The surface condition for the wind equation is given by the turbulent flux at the surface $\overline{u'w'}(z=0)$. The value at the top of the SBL scheme is given by wind at forcing level: $U = U(z=z_a)$.
The surface condition for the potential temperature equation is given by the turbulent flux at the surface $\overline{w'\theta'}(z=0)$. The value at the top is given by the temperature at forcing level: $\theta = \theta(z=z_a)$.
The surface condition for the humidity equation is given by the turbulent flux at the surface $\overline{w'q'}(z=0)$. The value at the top is given by humidity at forcing level: $q = q(z=z_a)$.

The turbulent fluxes at the surface are computed by the surface scheme, using the atmospheric variables of the lowest level of the SBL (and not at the usual forcing level at z_a). The exact formulation depends on the surface scheme used. For example, a lot of (1 layer) surface schemes use to compute the surface heat (vapor) flux a formulation with exchange coefficients C_h (including a dependancy with stability), surface and air temperatures (humidity) ($\overline{w'\theta'}(z=0) = C_h(\theta_s - \theta_a)$). With the SBL scheme, θ_a is the temperature at first SBL level, and the stability in the lowest layer in near neutral (because of the proximity to the ground -we used 50cm as first layer-).

There is no need of boundary condition for the TKE at the surface or at the forcing level, as no vertical gradient of TKE is used. The only term that needs special computation near the surface is the Dynamical production term, as it uses a vertical gradient of mean wind.

5.2.5 Turbulence scheme

One turbulence scheme is of course needed in the SBL. A TKE turbulence scheme, developed by *Cuxart et al.* [2000], is chosen here. The mixing length is computed as in *Redelsperger et al.* [2001]. Mixing and dissipative length scales are not equal, in order to represent accurately the dissipation modification due to the -1 power law of the turbulence in the SBL. Other turbulence schemes may be used.

A summary of the turbulence scheme is given below:

$$\left\{ \begin{array}{lcl} \overline{u'w'} & = & -C_u l \sqrt{e} \frac{\partial U}{\partial z} \\ \overline{w'\theta'} & = & -C_\theta l \sqrt{e} \frac{\partial \theta}{\partial z} \\ \overline{w'q'} & = & -C_q l \sqrt{e} \frac{\partial q}{\partial z} \\ \frac{\partial e}{\partial t} & = & \underbrace{-\overline{u'w'} \frac{\partial U}{\partial z}}_{Dyn.Prod.} + \underbrace{\frac{g}{\theta} \overline{w'\theta'_v}}_{Therm.Prod.} - \underbrace{C_\epsilon \frac{e^{\frac{3}{2}}}{l_\epsilon}}_{Diss.} + \frac{\partial e}{\partial t}_{canopy} \end{array} \right. \tag{5.10}$$

with $C_u = 0.126$, $C_\theta = C_q = 0.143$, $C_\epsilon = 0.845$ (from *Cheng et al.* [2002] constants values for pressure correlations terms and using *Cuxart et al.* [2000] derivation). The mixing and dissipative lengths, l and l_ϵ respectively, are equal to (from *Redelsperger et al.* [2001], $\alpha = 2.42$) :

$$\left\{ \begin{array}{lcll} l & = & \kappa z / [\sqrt{\alpha} C_u \phi_m^2 (z/L_{MO}) \phi_e (z/L_{MO})]^{-1} & \\ l_\epsilon & = & l \alpha^2 C_\epsilon / C_u / (1 - 1.9 z/L_{MO}) & \text{if} \quad \mathrm{z/L_{MO} < 0} \\ l_\epsilon & = & l \alpha^2 C_\epsilon / C_u / (1 - 0.3 \sqrt{z/L_{MO}}) & \text{if} \quad \mathrm{z/L_{MO} > 0} \end{array} \right. \tag{5.11}$$

Where L_{MO} is the Monin-Obukhov length, ϕ_u and ϕ_e the Monin-Obukhov stability functions for momentum and TKE.

5.3 conclusion

A formulation allowing to include prognostic atmospheric layers in offline surface schemes is derived from atmospheric equations. The interest of this approach is to use the advanced physical description of the SBL-canopy interactions that was available only in complex coupled multi-layer surface schemes. The coupling only occurs at the bottom level of the atmospheric model that should be coupled above the surface+SBL scheme. Variables that must be exchanged are: incoming radiation and forcing level air characteristics towards the surface scheme, upward radiative and turbulent fluxes from it. The air layers prognostically simulated with the SBL scheme take into account:

- The term that is related to large-scale forcing (e.g. advection). The detail of this term is not known by the SBL scheme. The evolution of the air characteristics at the forcing level is supposed to take into account all these large-scale forcing terms.
- The turbulent exchanges in the SBL (including in the canopy, if any). They will modify vertical profiles in the SBL. For example, the logarithmic profile of wind is directly induced by these turbulent fluxes, and is well reproduced by the SBL scheme.
- The drag and canopy forcing terms. These are computed for each layer, due to the interaction between air and the canopy. These exchanges have to be modeled by the surface scheme to which the SBL scheme is coupled. In the present paper, for forests, it takes into account the dynamical terms: drag and impact on Tke.

The possible applications of a SBL scheme included in surface schemes can be:

- a more physical determination of standard 2m variables and 10m wind. It can be seen as a drastic increase of the vertical resolution of the atmospheric models near the ground, without the drawback of a smaller time step (that would be necessary to resolve the advection on a very fine grid). Furthermore, because the additional air layers are not handled by the atmospheric model, the SBL scheme (associated to a surface single-layer scheme) is easy to couple with Numerial Weather Prediction or research atmospheric models.
- a better description of the turbulent exchanges and the stability in the SBL, including over complex terrain, for low-level flow and dispersion studies near the surface. As future applications, the dispersion processes in presence of canopy (e.g. chemistry vertical diffusion in urban areas) could then be more accurately simulated.
- the inclusion of the detailed physics of the multi-layer schemes (e.g. the interactions of forest or urban canopy with atmospheric layers in the SBL) into single-layer schemes.

5.4 Appendix: Vertical and temporal discretization

5.4.1 Vertical discretization

The vertical grid for the SBL scheme is a staggered grid (figure 5.3). Historical variables (U, θ, q, e) are defined on 'full' levels. The temporal evolution terms due to canopy obstacles ($\mathrm{Drag_u}$, $\frac{\partial\theta}{\partial t}_{canopy}$, $\frac{\partial q}{\partial t}_{canopy}$, $\frac{\partial e}{\partial t}_{canopy}$) are also located on these full levels. The turbulent fluxes computed by the SBL scheme are computed on the 'flux' levels, staggered between the full levels. The height of full levels is exactly at middle height between half levels. Note that the grid can be (and is most of the time) stretched, with a higher resolution near the ground. The ground is the first flux level (to be consistent with the boundary condition provided: the surface turbulent fluxes). The atmospheric forcing level is the upper full level (to be consistent with the upper boundary condition).

5.4.2 Temporal discretization

For any variable X (U, θ, q or e), the evolution equation can be written as:

$$\frac{\partial X}{\partial t} = \frac{\partial X}{\partial t}(z = z_a) - \frac{\partial F(\frac{\partial X}{\partial z})}{\partial z} + For(X) \tag{5.12}$$

where F is the turbulent flux for $X = [U, \theta, q]$, and For contains canopy forcing terms ($\frac{\partial X}{\partial t}_{canopy}$ for $X = [U, \theta, q, e]$) and other RHS forces for $X = [e]$. Note that the turbulent flux terms F depend formally on the vertical derivative of the variable ($\frac{\partial X}{\partial z}$) while canopy forces and RHS TKE forces depend on the variable itself (X).

In order to satisfy the stability of the SBL scheme at large time-steps, an implicit solving is performed. If the coupling at the atmospheric level is explicit, the atmospheric forcing is not modified in the current time-step by the SBL and surface schemes (i.e. $\frac{\partial X}{\partial t}(z = z_a)$ does not change during the SBL solving). Of course, the atmosphere will further evolve in response to the turbulent SBL fluxes (through the atmospheric model turbulence parameterization). In these conditons, the SBL implicit solving writes:

$$\frac{X^+ - X^-}{\Delta t} = \frac{\partial X^-}{\partial t}(z = z_a) - \frac{\partial F^-}{\partial z} - \frac{\partial \frac{\partial F}{\partial z}^-}{\partial \frac{\partial X}{\partial z}} \times \left(\frac{\partial X^+}{\partial z} - \frac{\partial X^-}{\partial z} \right) + For^- + \frac{\partial For^-}{\partial X} \times (X^+ - X^-) \tag{5.13}$$

Where Δt is the time step, $^-$ subscript stands for previous time-step variable (known), and $^+$ subscript for the future time-step variable (which one seeks to calculate). Such an implicit scheme leads to a linear system linking all variables at each level to those from the levels below and above (due to the vertical gradient at instant $^+$). This system is tridiagonal, and easy to solve numerically.

5.4.3 Implicit coupling with the atmospheric model

It may be necessary in some atmospheric models (essentially due to very long time steps - half an hour- and the turbulence scheme used in the atmospheric model) to couple implicitly the surface (including the SBL scheme here) and the atmosphere. First RHS term in Equation 5.13 is now equal to $[X^+_{(z=z_a)} - X^-_{(z=z_a)}]/\Delta t$. The atmospheric variable at time $^+$ is modified by the surface flux at the forcing level. It is formalized by

Best et al. [2004] : $X^+_{(z=z_a)} = A \times F^+_{(z=z_a)} + B$ (where A and B are known). Therefore, Equation 5.13, in case of implicit coupling with the atmosphere, writes:

$$\begin{aligned}\frac{X^+ - X^-}{\Delta t} = \quad & \frac{B - X(z=z_a)^-}{\Delta t} + \frac{A}{\Delta t} \times \left\{ F^-_{(z=z_a)} + \frac{\partial F}{\partial(\frac{\partial X}{\partial z})}^-(z=z_a) \times \left(\frac{\partial X}{\partial z}^+(z=z_a) - \frac{\partial X}{\partial z}^-(z=z_a) \right) \right\} \\ & - \frac{\partial F}{\partial z}^- - \frac{\partial \frac{\partial F}{\partial z}}{\partial \frac{\partial X}{\partial z}}^- \times \left(\frac{\partial X}{\partial z}^+ - \frac{\partial X}{\partial z}^- \right) + For(X)^- + \frac{\partial For}{\partial X}^- \times (X^+ - X^-)\end{aligned} \tag{5.14}$$

This is still a linear system involving variables at future time step at all levels of the SBL scheme, but this system is no longer tridiagonal, because the term $\frac{\partial X}{\partial z}(z=z_a)^+$ (i.e. at upper SBL level) influences directly the variable X^+ at each level. However, such a system is still resolvable, showing the generality of the SBL scheme method proposed here.

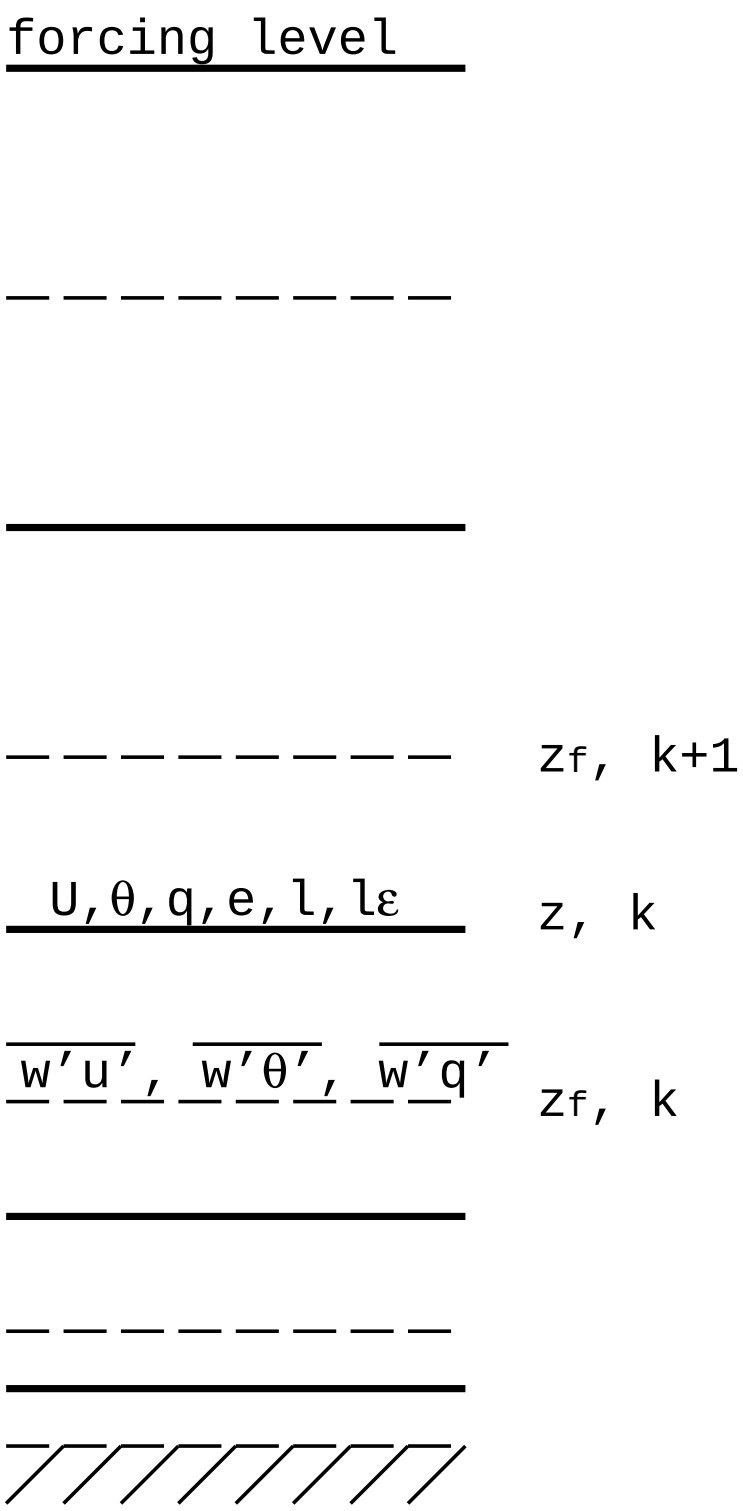

Figure 5.3: Schematic view of the vertical discretization for the SBL scheme. Plain lines are full levels. Dotted lines are flux levels.

Chapter 6

Chemistry and aerosols

Contents

6.1 Dust aerosols

Dust is mobilized from dry desert surfaces when the wind friction speed reaches a threshold wind friction speed of approximately 0.2 m/s. Dust is an important aerosol with annual global emissions ranging from 1000 to 3000 $Tg\ yr^{-1}$ and average global load around 10-30 Tg (*Zender et al.* [2004]).
Dust is mobilized by two related processes called saltation and sandblasting. Saltation is the horizonal movement of soil grains in a turbulent near surface layer. Sandblasting is the release of fine dust when the saltating grains hit the surface. Several papers document these two processes. *Marticorena and Bergametti* [1995] and references therein describe the physics of saltations, and *Shao et al.* [1993] describe the physics of sandblasting.

6.1.1 Implementation in the Externalized surface

The dust fluxes are calculated using the Dust Entrainment And Deposition (DEAD) model (*Zender et al.* [2003]). This model is based on *Marticorena and Bergametti* [1995]. The dust fluxes are calculated consistently with the ISBA soil surface scheme. Table 6.1 gives an overview of the main input to the dust production model.

Table 6.1: ISBA variables used by the dust module

PARAMETER	EFFECT ON DUST EMISSION	REFERENCE
wind friction speed	Increase emissions	*Marticorena and Bergametti* [1995]
Soil moisture	Inhibit emissions	*Fecan et al.* [1999]
Vegetation fraction	Inhibit emissions	*Marticorena and Bergametti* [1995]
Surface roughness	Inhibit emissions	*Laurent et al.* [2005]
Surface texture	Soil sizes $> 50\mu m$ increase saltation flux	*Iversen and White* [1982]

6.1.2 Features of the model

Emission process

The production of desert aerosols follows in fact the sandblasting process following the bombing of the aggregates present at the surface by particles in saltation (Figure 6.1). These processes depend on both weather conditions and surface states. Indeed, the kinetic energy of the grains caused by saltation is used in shocks induced by these particles, when they fall to the ground to release and eject fine particles constituting aggregates (*Gillette and Goodwin* [1974], *Gomes et al.* [1990]). The resistance to wrenching, concerns soil properties like the gravity force and the inter-particle forces. Moreover, emission of aerosols is a threshold phenomenon: it occurs only when the wind friction force exerted on soil grains becomes greater than the forces that maintain them to the ground. When this threshold is exceeded, the soil grains start moving horizontally. The smallest particles can be suspended in the atmosphere and constitute the desert aerosol. The production intensity of fine particles thus depends on the ratio between the transfered kinetic energy flow and the cohesion forces of the particles forming the aggregates.

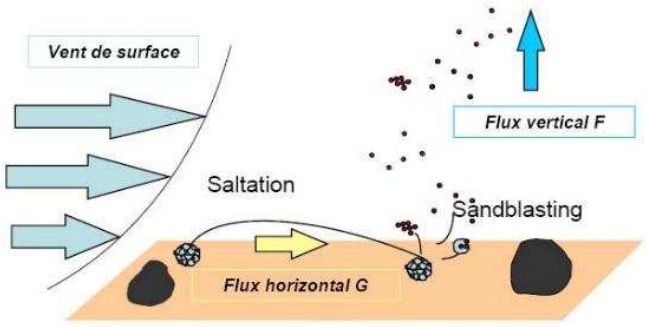

Figure 6.1: illustration of the two main processes involved in the emission of aerosols desert (saltation and sandblasting) when the erosion threshold is exceeded.

Once the particle is injected into the atmosphere, the forces to which it is subjected will control its suspension. It is generally accepted, given the balance of forces, that only particles with a diameter less than about 20 µm can be transported (*Nickling* [1994]). Those fine particles, named aerosols, constitute the main part of the vertical flow of desert aerosol (F). This vertical flow is defined as the mass of particles crossing per unit of time a unitary surface parallel to the surface.

Parameterization of the friction velocity

Wind is the driving force in the aerosols desert generating process. The ground surface opposes the air flow and slows the air mass at its base. The surface wind is very sensitive to changes in surface characteristics at small scale. These changes may be due, for example, to the presence of vegetation or rocks. In the first few meters of the atmosphere, a surface boundary layer (CLS) develops, in which the horizontal component of the wind speed has a vertical gradient whose intensity depends on the ability of the soil surface to slow the flow (Figure 6.2). For a laminar flow over a horizontal surface, the shear constraint (τ) exerted by the wind on the surface is connected to the vertical gradient of the wind speed (U) by:

$$\tau = \mu \frac{\partial U}{\partial Z} \tag{6.1}$$

Where is the air dynamic viscosity coefficient and Z the height above the ground.

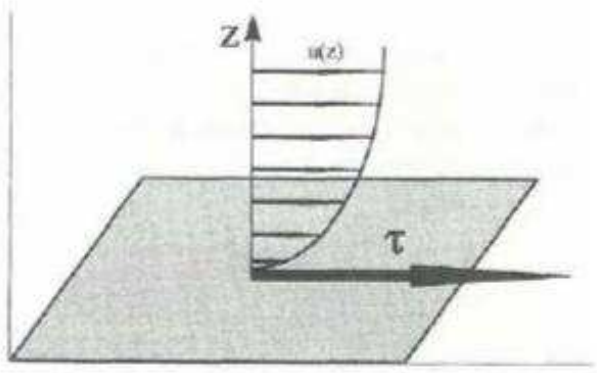

Figure 6.2: Representation of the effect of soil on the airflow and of the shear stress τ exerted by the flow on the ground.

The shear constraint can also be expressed in terms of friction wind speed U_*, which is usually the physical quantity used to quantify friction forces exerted by wind on a surface:

$$\tau = \rho_a U_* \tag{6.2}$$

Where ρ_a is the air density. Under conditions of thermal neutrality, U_* can be determined from the wind speed U at a height z from the ground and the height of aerodynamic roughness (Z_0) using a wind speed logarithmic profile (*Priestley* [1959]):

$$U(Z) = \frac{U_*}{\kappa} \ln(\frac{z}{Z_0}) \tag{6.3}$$

Where $\kappa = 0.4$ is the Von Karman constant.
Physically, Z_0 reflects the length scale of the sink of air momentum induced by the surface roughness. More specifically, Z_0 represents quantitatively the effect of erodible elements (soil grains) or non-erodible ones (rocks or vegetation) on the transfer of wind energy to the surface.

Friction velocity threshold

The resistance of the surface on the motion is represented by the friction velocity threshold U_{*_t}. Indeed, the friction velocity threshold U_{*t} controls both the frequency and the intensity of emissions of aerosols desert, so it is important to parameterize carefully U_{*_t} and give special attention to obtain the quantities it depends on. The erosion threshold is mainly computed from the soil grains diameter D_p, the surface roughness (Rug) and the soil moisture (w). The friction velocity threshold is expressed as:

$$U_{*_t} = U_{*_t}(D_p) \cdot F(Rug) \cdot F(w) \tag{6.4}$$

$U_{*_t}(D_p)$: depends on the friction speed with the diameter of soil grains. $F(Rug)$ and $F(w)$: weighting functions of the influence of roughness and soil moisture. Under idealized conditions, ie for a smooth surface and a loose and dry soil, the friction velocity threshold $U_{*_t}(D_p)$ can be determined using the formulation of *Marticorena and Bergametti* [1995], which consists in adjusting an empirical expression as a function of the particle diameter. Under standard atmospheric conditions ($\rho_a = 0.00123g \cdot cm^{-3}$, $\rho_p = 2.65g \cdot cm^{-3}$), the friction velocity threshold $U_{*_t}(D_p)$ is given by:

$$U_{*_t}(D_p) = \frac{0.129K}{\left(1.928{Re_{*_t}}^{0.092}\right)^{0.5}} \qquad , 0.03 \leq Re_{*_t} \leq 10 \tag{6.5}$$

$$U_{*_t}(D_p) = 0.129K\left[1 - 0.0858\exp\left(-0.0617\left(Re_{*_t} - 10\right)\right)\right] \, , Re_{*_t} > 10 \tag{6.6}$$

Where $Re_{*_t} = U_{*_t}D_p/\nu$ is the Reynolds number threshold ($\nu = 0.157\ cm^2s^{-1}$: kinematic viscosity)

and: $K = \left(\frac{\rho_p g D_p}{\rho_a}\right)^{0.5}\left(1 + \frac{0.006}{\rho_p g {D_p}^{2.5}}\right)^{0.5}$

The optimal diameter of the particle is equal to 75 µm.

Influence of soil moisture on friction velocity threshold

The presence of interstitial water between soil grains has the effect of increasing the cohesion of the soil, thus increasing the friction velocity threshold. This increase is integrated in the module DEAD from the parameterization developed by *Fecan et al.* [1999]. The proposed equation, expresses the threshlod increase, under wet conditions $U_{*_{tw}}$ compared to that in dry conditions.

$$U_{*_{tw}} = U_{*_t} \qquad for\ w\ <\ w^{'} \tag{6.7}$$

$$U_{*_{tw}} = U_{*_t}\left[1 + 1.21(w - w^{'})^{0.68}\right]^{0.5} \quad for\ w\ >\ w^{'} \tag{6.8}$$

With: w: mass soil moisture (% mass water / mass dry soil). And soil moisture threshold is given by:

$$w^{'} = 0.17(\%clay) + 0.14(\%clay)^2 \tag{6.9}$$

Aerodynamical roughness height

The effects of the internal boundary layer (IBL) on friction velocity threshold, due to the presence of stones, is set in DEAD scheme by *Marticorena and Bergametti* [1995]. The energy distribution is defined in this parameterization as the ratio between the IBL shear friction and the total shear friction of the surface boundary layer (SBL). This ration is given by:

$$f_{eff}(Z_0, Z_{0s}) = 1 - \left[\ln(Z_0/Z_{0s})/\ln(0.35(10/Z_{0s})^{0.8})\right] \tag{6.10}$$

$Z_{0s} = 33.3 \times 10^{-6}\ m$: roughness length of the smooth surface
$Z_0 = 100.0 \times 10^{-6}\ m$: roughness length of the erodible surface
The friction velocity threshold is expressed as:

$$U_{*_t}(D_p, Z_0, Z_{0s}) = \frac{U_{*_t}(D_p)}{f_{eff}(Z_0, Z_{0s})} \tag{6.11}$$

Surface flux

The horizontal saltation flux (G) is calculated in module DEAD through the *White* [1979] relationship :

$$G = c \cdot \frac{\rho}{g} {U_*}^3 \left(1 - \frac{U_{*_t}}{U_*}\right)\left(1 + \frac{U_{*_t}}{U_*}\right) \tag{6.12}$$

With $c = 2.61$. The ratio between the vertical flux and the horizontal flux is a function of clay content. For contents between 0 and 20%, this ratio is :

$$\alpha = \frac{F}{G} = 100 \exp\left[(13.4(\%clay) - 6) \times \ln(10)\right] \tag{6.13}$$

In the DEAD module, the fraction of clay is considered constant and is equal to 20%. The final vertical flux is averaged by a pre-determined factor equals to 0.0021 and by the sand fraction.

Mass flux repartition

Upon *Alfaro and Gomes* [2001] the mass flux is partitioning on the different modes upon the surface friction velocity. More the collision energy is strong more the dust aggregates can be separates into small particles. In surfex, two possibilities are offered. Users can fix the partitioning or the mass flux on the differents modes considered, or compute automatically this partitioning upon the ISBA friction velocity. In this latter case, *Alfaro and Gomes* [2001] gives the following partitionning:

- u* less than 0.32 $m.s^{-1}$, all particles are emitted in the coarse mode.
- u* at 0.42 $m.s^{-1}$, 63 % of the mass flux is in the bigger coarse mode (D=14.2 μm) , 36 % in the lower coarse mode (D=6.7 μm), and 1 % in the accumulation mode (D=1.5 μ m)
- u* at 0.50 $m.s^{-1}$, 49 % of the mass flux is in the bigger coarse mode (D=14.2 μm) , 43 % in the lower coarse mode (D=6.7 μm), and 8 % in the accumulation mode (D=1.5 μ m)
- u* at 0.66 $m.s^{-1}$, 9 % of the mass flux is in the bigger coarse mode (D=14.2 μm) , 76 % in the lower coarse mode (D=6.7 μm), and 15 % in the accumulation mode (D=1.5 μ m)

Between these friction velocities values, the mass flux partitioning is linearly interpolated.

6.2 Sea Salt emission

Sea salt aerosols are produced as film and jet droplets when bubbles, entrained in the water by breaking waves, disrupt the sea surface (Blanchard, 1983), and at winds speeds exceeding about 9 $m.s^{-1}$, by direct disruption of the wave tops (spume droplets) (*Monahan et al.* [1983]).
Sea Salt emission are parameterized upon the formulation of *Vignati et al.* [2001] (effective source function) or upon a lookup table defined by *Schulz et al.* [2004]. *Vignati et al.* [2001] gives a formulation of particles emission upon the wind at 10 meters as:

- $F(R = 0.2\mu m) = 10^{0.09U_{10m}+0.283} particles.cm^{-2}.s^{-1}$
- $F(R = 2\mu m) = 10^{0.0422U_{10m}+0.288} particles.cm^{-2}.s^{-1}$
- $F(R = 12\mu m) = 10^{0.069U_{10m}-3.5} particles.cm^{-2}.s^{-1}$

6.3 Dry deposition of gaseous species

The removal of gases from the atmosphere by turbulent transfer and uptake at the surface is defined as dry deposition. This process enables some chemically reactive gases to be efficiently removed from the atmosphere. Dry deposition is usually parametrized through a deposition velocity v_d, defined by $v_d = -\frac{F_c}{c(z)}$, where F_c is the flux of the considered compound (F_c is assumed constant over the considered range of heights) and $c(z)$ is the concentration at height z (molecules/cm^3). v_d depends on many variables such as wind speed, temperature, radiation, the considered species and the surface conditions. It is commonly described through a resistance analogy often called "Big-Leaf" Model (e.g. *Wesely and Hicks* [1977]).

$$v_d(z) = \frac{1}{R_a + R_b + R_c}$$

where R_a is the aerodynamic resistance, which is a function of the turbulence in the boundary layer, R_b the quasi-laminar resistance partially controlled by molecular diffusion, and R_c the surface resistance, which combines all the transfer pathways playing a role in the uptake of trace gases by the surface.

Meso-NH surface for dry deposition

As shown fig. 6.3, earth surface is divided into four major parts. On those surfaces calculation of specific parameters are done (friction velocities, surface resistances, ...). The earth splitting is done as follows : town horizontal fraction (*Masson* [2000]), inland water and sea surfaces (differents because of their surface temperature) and nature fractions. Nature surface is cut into 9 cover type, which can be reorganized by 'patches' (1 to 9). One 'patch' contains one or several cover types (user choice). These cover types are connected with the Wesely classes of vegetation for the surface resistance data parameters (see table 6.2).

6.3.1 Resistances for dry deposition

Aerodynamic resistance R_a

R_a determines the rate of transport of gases between a given level in the atmosphere and the height of the effective surface sink. It is usually calculated as the bulk aerodynamic resistance to the transfer of momentum : $R_a(z_R) = \frac{1}{\mathbf{C_D V_A}}$, where $\mathbf{C_D}$ is the drag coefficient for momentum (see for example *Wesely and Hicks* [1977]; *Sheih et al.* [1979]; *Walcek et al.* [1996]) and $\mathbf{V_A}$ the wind speed (in the following,

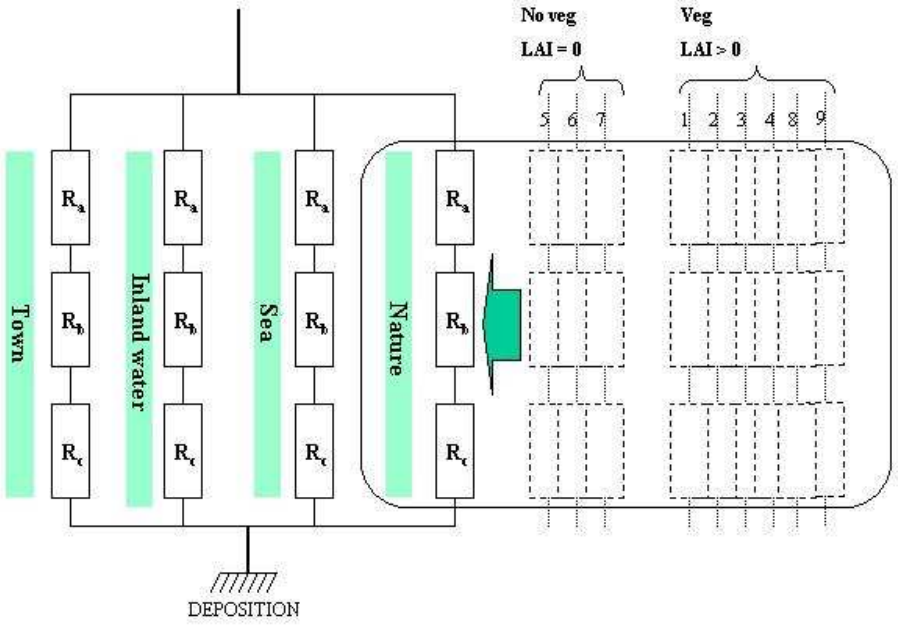

Figure 6.3: *Schematic resistances for dry deposition module in accordance with the surface state. Ra represents the aerodynamic resistance, Rb the quasi-laminar resistance and Rc the surface resistance.*

the parameters which are already used or calculated in the MESO-NH subroutines will be noted in bold characters). The reference height z_R is taken as the lowest atmospheric level in the ISBA scheme.

An alternate way is to use the ISBA calculation of $\mathbf{R_a}$, $\mathbf{R_a(z_R)} = \frac{\mathbf{1}}{\mathbf{C_H V_A}}$ which determines the transfer of water vapor. $\mathbf{C_H}$ is then the drag coefficient depending upon the thermal stability of the atmosphere.
Heat drag coefficients are calculated in WATER_FLUX for inland water and sea, in URBAN for artificial land (town) and in ISBA for the other nature cover types or patch. So there is one $\mathbf{R_a}$ different for each different coefficient.
This formulation of $\mathbf{R_a}$ requires an additional term to the quasi-laminar resistance described below.

Quasi-laminar resistance R_b

The component R_b is associated with transfer through the quasi-laminar layer in contact with the surface. R_b quantifies the way in which pollutant or heat transfer differ from momentum transfer in the immediate vicinity of the surface (this is due to the effects of molecular diffusion and the difference of roughness lengths found for momentum and mass transfer). R_b depends on both turbulence characteristics and the molecular diffusion of the considered gas. Transport of a gas through the quasi-laminar layer by molecular diffusion depends on the thickness of the layer, the concentration gradient over the layer and on a diffusion constant, which in turn depends on the radius of the gas molecule and on the temperature. The complexity of vegetation generally limits the accuracy with which the magnitude of this mechanism can be estimated in

Meso-NH nature cover type	Wesely correspondence class
C3 cultures types(low)	(2) Agricultural land
C4 cultures types(hight)	(2) Agricultural land
forest and trees	(4) Deciduous and (5) coniferous forest
grassland	(3) Range land
no vegetation (smooth)	(8) Baren land, mostly desert
no vegetation (rocks)	(11) Rocky open areas with low-growing shrubs
permanent snow and ice	No correspondence
irrigated crops	(9) None forested wetland
irrigated parks gardens or peat bogs	(6) Mixed forest including weet land and (9) none forest wetland

Table 6.2: *Meso-NH vegetative cover type and Wesely connected class for dry deposition calculation*

the field. This resistance can be conveniently written as:

$$R_b = \frac{1}{ku^*} \log(\frac{z_0}{z_c})$$

k is the Von Karman constant and u^* the friction velocity. z_c is the roughness length for the pollutant under investigation (Baldocchi et al. (1987)).
According to *Hicks et al.* [1987], *Garrat and Hicks* [1973] R_b can be approximated for vegetation and fibrous roughness elements by :

$$R_b = \frac{2}{\mathbf{ku}^*}(\frac{Sc}{Pr})^{2/3}$$

Sc and Pr are the Schmidt and Prandtl numbers respectively. $Pr = 0.72$ and $Sc = \frac{\nu}{D_i}$, with ν the kinematic viscosity of air (0.15 cm^2s^{-1}, 20^o C, p = 1 atm) and D_i the molecular diffusivity of gas i (see table 6.3 for some of these constants). For snow, ice, water and bare soil, R_b can be calculated by (*Ganzeveld and Lelieveld* [1995]):

$$R_b = \frac{1}{\mathbf{ku}^*}(\frac{Sc}{Pr})^{2/3}$$

This formulation is used for all Meso-NH grid fraction cover with no vegetation (Leaf Area Index = 0), that include artificial land, water and sea.
Definition of friction velocity in MNH is given by : $u^* = \sqrt[4]{< \mathbf{u'w'} >_{\mathbf{xx}}{}^2 + < \mathbf{v'w'} >_{\mathbf{xx}}{}^2}$. Where $< u'w' >_{xx}$ and $< v'w' >_{xx}$ represents surface fluxes of horizontal momentum in x and y directions (xx for sea, water, town and nature patch). Molecular diffusivity species/air can be obtain by the knowledge of H_2O/air diffusivity. The coefficient of diffusivity is given by the general formula as:
$D = vl/3 = \frac{0.376kT}{N(MCste)^{0.5}}$
with l mean free path, v mean molecular velocity, k Boltzmann constant, T temperature, N concentration, M molecular mass. So we use for computing molecular diffusivity:

$$D(gaz) = D(H_2O) \left(\frac{M(H_2O)}{M(gaz)}\right)^{0.5}$$

with

$$D(H_2O) = 2.22e-5 + 1.2510^{-7}(T+273) for 193K < T < 0K$$

$$D(H_2O) = 2.22e-5 + 1.4610^{-7}(T+273) for 273K < T < 323K$$

However, these formulations of R_b remain still controversial. Recent results from fields studies indicate that they are not in agreement with experimentally derived results, at least for the transfer of HNO_3 over wheat (*Muller et al.* [1993]). At last, velocity dry deposition is not very sensitive of the choosen definition of R_b (*Ganzeveld and Lelieveld* [1995]).

Surface Resistance R_c

The surface resistance is the most difficult of the three resistances to describe. R_c values can be obtained from theoretical considerations based for instance on solubility and equilibrium; calculations in combination with simulation of vegetation specific processes, such as accumulation, transfer process through stomata, mesophyll, cuticles, etc ... (*Baldocchi et al.* [1987], *Wesely* [1989]). The values of R_c are based on measurements of V_d. By determining R_a and R_b from the meteorological measurements, R_c is calculated as the residual resistance. The calculated R_c are then related to surface conditions, time of day, etc ... in order to obtain parametrizations of R_c.

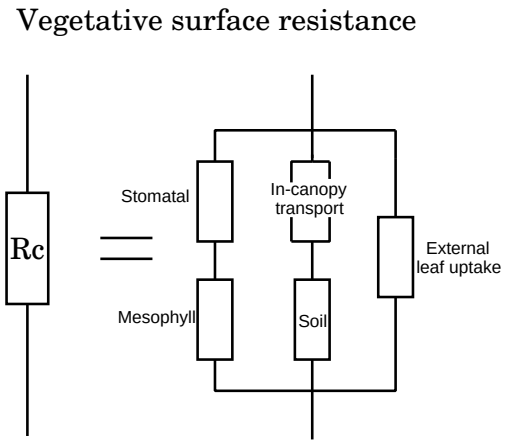

Figure 6.4: *Surface resistance schematic for vegetation.*

R_c is a function of the canopy stomatal resistance R_{stom} and mesophyll resistance R_m, the canopy cuticle or external leaf resistance R_{ext}, the soil resistance R_{soil} and in-canopy resistance R_{inc}, and the resistance to surface waters or moorland pools, R_{wat}, R_{sea} (*Erisman and Baldocchi* [1994]). In turn, these resistances are affected by leaf area index, stomatal physiology, soil and external leaf surface, pH presence and chemistry of liquid drops and films. In summary, R_c should be calculated as *Erisman and Baldocchi* [1994] :

- Vegetative surfaces : $R_c = \left(\frac{1}{R_{stom}+R_m} + \frac{1}{R_{inc}+R_{soil}} + \frac{1}{R_{ext}} \right)^{-1}$
- Water surfaces : $R_c = R_{wat}$
- Sea surfaces : $R_c = R_{sea}$
- Bare soil (no vegetation) : $R_c = R_{no}$
- Rock surfaces : $R_c = R_{rock}$
- Snow/ice cover : $R_c = R_{snow}$
- Artificial land : $R_c = R_{town}$

Stomatal and mesophyll resistance R_{stom} and R_m

The stomatal resistance for water vapor is calculated in the ISBA subroutines as

$$\mathbf{R_{stom}} = \frac{\mathbf{R_{smin}}}{\mathbf{F_1 F_2 F_3 F_4 \, LAI}},$$

where $\mathbf{LAI}$ is the leaf area index computed by patch, and F_1, F_2, F_3, F_4 are limiting factors depending on radiation, wetness of soil and temperature. In order to describe the stomatal resistance for another gas, the ISBA $\mathbf{R_{stom}}$ for water vapor should be corrected as followed :

$$R_{stom,x} = \mathbf{R_{stom}} \times \frac{D_{H_2O}}{D_x},$$

D_{H_2O} and D_x are the diffusion coefficients of H_2O and x respectively (*Wesely* [1989]).

There is not much knowledge on the mesophyll resistance for different gases and the conditions which determine its value. For some gases, such as SO_2 O_3 and NH_3, R_m is experimentally found near zero values (*Erisman and Baldocchi* [1994]). This is in agreement with the parametrization suggested by *Wesely* [1989] for the calculation of the mesophyll resistance :

$$R_{mx} = (\frac{H^*}{3000} + 100 f_0)^{-1}$$

In this expression, H^* is the Henry's law constant for the considered gas, f_0 a reactivity factor which determines the rate of reduction of the substance. Two parallel pathways are thus assumed, one for highly reactive gases, the other one for soluble substances. Table 6.3 lists H^* and f_0 for some species (*Baer and Nester* [1992]).

External leaf uptake R_{ext}

The external leaf uptake can act as an effective sink, especially for soluble gases at wet surfaces. The resistance of the outer surfaces in the upper canopy (leaf cuticular resistance in healthy vegetation) is computed by *Wesely* [1989], for a dry surface to any gas (x), as :

$$R_{ext.x.dry} = R_{ext}(10^{-5} H^* + f_0)^{-1}$$

In this expression, R_{ext} is given by land category and season in table 6.4, the constants (H^*, f_0) can be found in table 6.3.
The following equation is supposed to give an analytic expression of $\mathbf{R_{ext}}$ in accordance with Wesely table 6.4, and including seasonal variations through the leaf area index $\mathbf{LAI}$:

$$R_{ext} = 6000 - 4000 \tanh(1.6(\mathbf{LAI} - 1.6))$$

These results had been compared with Wesely table in accordance with Méso-NH (ISBA) data of LAI (see fig. 6.3.1).
In case of dew or rain, and according to the same author and *Walmsley and Wesely* [1996], the equation should be replaced by :

$$R_{ext.x.wet} = [1/(3R_{ext.x.dry}) + (10^{-7} H^* + f_0/R_{extOzone}]^{-1}$$

with

Species	Reactivity factor	Henry's law (M/atm)
Sulfur dioxide	0	$1.6(1 + 2.1\ 10^{-2}/H+)$
Nitric oxide	0	$1.9\ 10^{-3}$
Nitrogen dioxide	0.1	10^{-2}
Nitric acid	0	$5.8\ 10^{6}/H+$
Ozone	1.	$1.5\ 10^{-2}$
Hydrogen peroxide	0	$1.8\ 10^{5}$
Formaldehyde	0	$3.26\ 10^{-4}$
Aldehydes	0	76
Organic acids	0	$1.45\ 10^{-4}$
Organic peroxide	0.25	665
Peroxyacetic acid	0.5	1635
Peroxyacetyl nitrate	0.1	3.6
Other alkanes	0	$1.\ 10^{-3}$
Ethane	0	$1.9\ 10^{-3}$
Ethene	0	$4.9\ 10^{-3}$
Propene	0	$4.7\ 10^{-3}$
Butene and other olefins	0	$1.3\ 10^{-3}$
Toluene	0	0.15
Xylene	0	0.1

Table 6.3: *Reactivity factor and Henry's law constants for different chemical species*

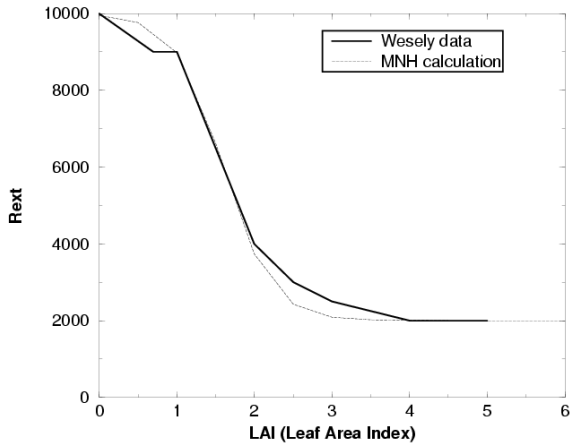

Figure 6.5: $\mathbf{R_{ext}}$ *fonction of* $\mathbf{LAI}$ *(from Wesely table)*

1	2	3	4	5	6	7	8	9	10	11
Midsummer with lush vegetation										
9999	2000	2000	2000	2000	2000	9999	9999	2500	2000	4000
Autumn with unharvested cropland										
9999	9000	9000	9000	4000	8000	9999	9999	9000	9000	9000
Late autumn after frost, no snow										
9999	9999	9000	9000	4000	8000	9999	9999	9000	9000	9000
Winter										
9999	9999	9999	9999	6000	9000	9999	9999	9000	9000	9000
Spring										
9999	4000	4000	4000	2000	3000	9999	9999	4000	4000	8000

Table 6.4: *Input resistances for calculation of external leaf resistance (Wesely,1989) : (1)urban land, (2)agricultural land, (3)range land, (4)deciduous forest, (5)coniferous forest, (6)mixed forest including wetland, (7)water, (8)barren land, mostly desert, (9)nonforested wetland, (10)mixed agricultural and range land, (11)rocky-open areas with low-growing shrubs*

- Rain :

$$R_{extOzone} = (1/(3R_{ext}) + 1/1000)^{-1}$$

- Dew :

$$R_{extOzone} = (1/(3R_{ext}) + 1/3000)^{-1}$$

To apply the same comput for each species we approximate in case of wet soil these formulas by using $R_{extOzone}$ as 3000 s/m .
These formulas should be corrected when surface temperature decreases below -2^{o}C by adding the value $1000\exp(-T-4)$, in order to take into acccount the lesser uptake by surfaces when cold.

In-canopy transport R_{inc}

Deposition to soils under vegetation can be relatively important. *Meyers and Baldocchi* [1988] found that 20% - 30% of SO_2 was deposited in summer to the soil under a deciduous forest. This transport is due to large-scale intermittent eddies through the vegetation. The corresponding resistance has been parametrized by *Erisman and Baldocchi* [1994] using data of *VanPul and Jacobs* [1994] as :

$$R_{inc} = \frac{b\,\mathbf{LAI}\,h}{\mathbf{u}^*}$$

b is an empirical constant estimated at 14 m^{-1}. $\mathbf{LAI} = \mathbf{LAI\_patch}$ is the leaf area index given by patches computed in the GROUND_PARAMn files and $\mathbf{h}$ is the vegetation height which can be calculated as four times the vegetation roughness length (formula of *Kondo and Yamazawa* [1986], assuming a dense vegetation canopy with similar height).

Soil resitances for surfaces with no vegetation and those under vegetation

Table 6.5 presents a review of soil resistances for SO_2 and O_3 for clay, sand, snow and it is completed with table 6.6, Wesely value for all other vegetation types, town and rock.
For other gases, the resistance can be computed following *Wesely* [1989] :

$$R_{soilx} = (\frac{H^*}{10^5 R_{soilSO_2}} + \frac{f_0}{R_{soilO_3}})^{-1}$$

According to the same author, this formula should be corrected when surface temperature decreases below -2^{o}C by adding the value :

$$R_{soilx} = R_{soilx} + 1000\exp(-T-4)$$

For no vegetation cover soil surface composition (sand, clay) is considered. If it is covered by snow, this formlation will be update by using table 6.5.

$$R_{sandx} = (\frac{H^*}{10^5 R_{sandSO_2}} + \frac{f_0}{R_{sandO_3}})^{-1}$$

$$R_{clayx} = (\frac{H^*}{10^5 R_{claySO_2}} + \frac{f_0}{R_{clayO_3}})^{-1}$$

$$R_{snowx} = (\frac{H^*}{10^5 R_{snowSO_2}} + \frac{f_0}{R_{snowO_3}})^{-1}$$

In this context $R_{no.x}$ for bare ground (no veg.) without snow is the weighted average of R_{sandx} and R_{clayx} as:

$$R_{no.x} = (\frac{\alpha_{sand}}{R_{sandx}} + \frac{\alpha_{clay}}{R_{clayx}})^{-1}$$

with
α_{sand} : percentage of sand in the ground
α_{clay} : percentage of clay in the ground
For all the other type of soil, resistance is calculated with table 6.6 as :

$$\begin{aligned}
R_{rockx} &= (\frac{H^*}{10^5 R_{rockSO_2}} + \frac{f_0}{R_{rockO_3}})^{-1} \\
R_{townx} &= (\frac{H^*}{10^5 R_{townSO_2}} + \frac{f_0}{R_{townO_3}})^{-1} \\
R_{c3x} &= (\frac{H^*}{10^5 R_{c3SO_2}} + \frac{f_0}{R_{c3O_3}})^{-1} \\
R_{c4x} &= (\frac{H^*}{10^5 R_{c4SO_2}} + \frac{f_0}{R_{c4O_3}})^{-1} \\
R_{treex} &= (\frac{H^*}{10^5 R_{treeSO_2}} + \frac{f_0}{R_{treeO_3}})^{-1} \\
R_{grassx} &= (\frac{H^*}{10^5 R_{grassSO_2}} + \frac{f_0}{R_{grassO_3}})^{-1} \\
R_{irrx} &= (\frac{H^*}{10^5 R_{irrSO_2}} + \frac{f_0}{R_{irrO_3}})^{-1} \\
R_{parkx} &= (\frac{H^*}{10^5 R_{parkSO_2}} + \frac{f_0}{R_{parkO_3}})^{-1}
\end{aligned}$$

Type of soil	SO_2	O_3
snow	540 at T $<$-1^{o}C	2000
	70(2-T) at -1 $<$ T $<$ 1	
sand	1000	200
clay	1000	100

Table 6.5: *Soil resistance*

MNH cover type									
c3	c4	tree	grass	no	rock	snow/ice	irr	park	town
Soil resistance for SO_2									
150	150	500	350	1000	400	no data	0	100	400
Soil resistance for O_3									
150	150	200	200	400	200	no data	1000	700	300

Table 6.6: *Soil resistance for MNH-C decomposition from Wesely table (quasi constant during the year). Values for "snow/ice" and "no" (no veg.) are not used see table 6.5.*

Surfaces resistances for sea and water

For deposition over water surface bodies, the surface resistance can be calculated from the expression recommended by Sehmel (1980) that incorporates wind speed and and air/water partitioning coefficient, rather than from Wesely's tabulated values for water bodies. The surface resistance over water is:

$$R_{waterx} = \frac{2,54.10^{-4}}{H^{*}\mathbf{T_{water}}\mathbf{u}_{*}} = Rc_{waterx}$$

$$R_{seax} = \frac{2,54.10^{-4}}{H^{*}\mathbf{T_{sea}}\mathbf{u}_{*}} = Rc_{seax}$$

6.3.2 Dry deposition velocity formulation

Artificial land resistance

$$Rglobal^{town} = Ra^{town} + Rb^{town} + Rc^{town}$$

Sea and water resistance

$$Rglobal^{water} = Ra^{water} + Rb^{water} + Rc^{water}$$

$$Rglobal^{sea} = Ra^{sea} + Rb^{sea} + Rc^{sea}$$

Nature final resistance

$$Rglobal^{nature} = \sum_{i=1}^{nvegtype} \left(\frac{\alpha_i}{Ra^{j_{patch}} + Rb^{j_{patch}} + Rc^{i}} \right)^{-1}$$

with
$i \overset{f}{\longmapsto} f(i) = j_{patch}$ like $i \in [1, nvegtype]$, $f(i) = j_{patch} \in [1, npatch \leq nvegtype]$
and α_i fraction of cover type (9 types)

Dry deposition velocity

Final dry deposition formulation:

$$v_{drydeposition} = \frac{\alpha_{water}}{Rglobal^{water}} + \frac{\alpha_{sea}}{Rglobal^{sea}} + \frac{\alpha_{townmax}}{Rglobal^{town}} + \frac{\alpha_{nature}}{Rglobal^{nature}}$$

where

α_{water} : fraction of water
α_{sea} : fraction of sea
$\alpha_{townmax}$: fraction of town increased
α_{sea} : fraction of nature

Fraction of town has to be increased in order to take account of the non negligible dry deposition on vertical surfaces in artificial area. The increase is done as follows :
$\alpha_{townmax} = \alpha_{town}(1 + 2\frac{H}{L}\,\alpha_{bld})$ with :
α_{town} horizontal fraction of town
H building height
L building caracteristic width
α_{bld} fraction of buildings in artificial areas (only)

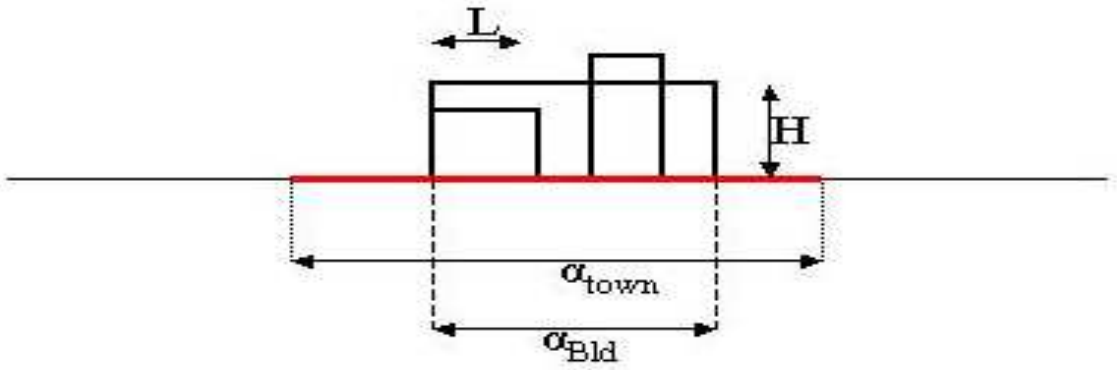

Figure 6.6: *town parameters in MNH (modd_gr_field) to increase fraction of town*

6.4 Dry deposition of aerosols

Brownian diffusivity and sedimentation velocity

Dry deposition and sedimentation of aerosols are driven by the Brownian diffusivity:

$$D_p = \left(\frac{kT}{6\pi\nu\rho_{air}r_p}\right) C_c \tag{6.14}$$

and by the gravitational velocity:

$$V_g = \left(\frac{2g}{9\nu}\left(\frac{\rho_{p,i}}{\rho_{air}}\right) r_p^2\right) C_c \tag{6.15}$$

where k is the Bolzmann constant, T the ambient temperature, ν the air kinematic velocity, ρ_{air} the air density, g the gravitational acceleration, $\rho_{p,i}$ the aerosol density of mode i, and $C_c = 1 + 1.246\frac{\lambda_{air}}{r_p}$ the gliding coefficient. These expressions need to be averaged on the k^{th} moment and mode i as:

$$\hat{X} = \frac{1}{M_{k,i}} \int_{-\infty}^{\infty} X r_p^k n_i(\ln r_p) d(\ln r_p) \tag{6.16}$$

where X represents either D_p or v_g. After integration, we obtain for Brownian diffusivity:

$$\hat{D}_{p_{k,i}} = \tilde{D}_{p_{g,i}} \left[\exp\left(\frac{-2k+1}{2}\ln^2\sigma_{g,i}\right) + 1.246 K n_g \exp\left(\frac{-4k+4}{2}\ln^2\sigma_{g,i}\right)\right] \tag{6.17}$$

with $\tilde{D}_{p_{g,i}} = \left(\frac{kT}{6\pi\nu\rho_{air}R_{g,i}}\right)$
and for gravitational velocity:

$$\hat{Vg}_{p_{k,i}} = \tilde{Vg}_{p_{g,i}} \left[\exp\left(\frac{4k+4}{2}\ln^2\sigma_{g,i}\right) + 1.246 K n_g \exp\left(\frac{2k+4}{2}\ln^2\sigma_{g,i}\right)\right] \tag{6.18}$$

with $\tilde{Vg}_{p_{g,i}} = \left(\frac{2g\rho_{p,i}}{9\nu\rho_{air}} R_{g,i}^2\right)$

Dry deposition

According to *Seinfeld and Pandis* [1997] and using the resistance concept of *Wesely* [1989], aerosol dry deposition velocity for the k^{th} moment and mode i is:

$$\hat{v}_{d_{k,i}} = (r_a + \hat{r}_{d_{k,i}} + r_a \hat{r}_{d_{k,i}} \hat{Vg}_{p_{k,i}})^{-1} + \hat{Vg}_{p_{k,i}} \tag{6.19}$$

where surface resistance $\hat{r}_{d_{k,i}}$ is given by

$$\hat{r}_{d_{k,i}} = \left[(\hat{Sc}_{k,i}^{-2/3} + 10^{-3/\hat{St}_{k,i}})\left(1 + 0.24\frac{w_*^2}{u_*^2}\right) u_*\right]^{-1} \tag{6.20}$$

Schmidt and Stokes number are respectively equal to $\hat{Sc}_{k,i} = \nu/\hat{D}_{p_{k,i}}$ and $\hat{St}_{k,i} = (u_*^2/g\nu)\hat{v}_{d_{k,i}}$. One can observe that the friction velocity u_* and the convective velocity w_* depend on meteorological and surface conditions.

6.5 Biogenic VOC fluxes

Biogenic fluxes are parameterize on-line in the surfex code. For a model grid-cell, biogenic fluxes of isoprene and monoterpenes are calculated according to the classical Guenthers approach (*Guenther et al.* [1994, 1995]), using the general formulation :

$$F_x^{cell} = \sum_N \nu_n X.EP_{x,n} X.ECF_{x,n} \tag{6.21}$$

Where Fxcell (in g.m-2.h-1) is the grid-cell averaged biogenic fluxes in which x refers either to isoprene or monoterpenes. ν_n represents the surface fractions occupied by N sub-grid emitting ecosystems (forests,

shrublands, crops, etc). The related emission potential, $EP_{x,n}$, (in $\mu g.m^{-2}.h^{-1}$), accounts for the emission capacity of the underlying nth ecosystem under fixed climatic conditions. According to Guenthers approach, EPiso is standardized to a surface vegetation temperature Ts of 303 K and a photosynthetically active radiation (par) of 1000 $\mu E.m^{-2}.s^{-1}$, whereas EPmono is generally standardized only for Ts =303 K. The temporal evolution of fluxes is given by environmental correction factors ECFx,n calculated from the canopy micro-climates of the N underlying ecosystems. This formulation assumes a simple homogeneous vertical leaf distribution in ecosystem canopies. Over France, emission potential have been pre calculated by GIS treatment of land use data base (Corine Land Cover), forest composition data for the main tree species (Inventaire forestier national) and species emission factors collected in the literature. The resulting emission potential maps are given at a resolution of 2km and are then interpolated on the MNH grid (during the prepPGD). The environmental correction factor, which accounts for radiation and vegetation temperature variation effects on emissions is calculated using the surface energy budget (calculated by ISBA) and a simple in canopy radiation transfer scheme (similar as ISBA-Ags) for each of the ecosystem (Forest, shrublands, etc) contained in the model grid cells (cf PATCH approach). More details on the method can be found in *Solmon et al.* [2004].

Chapter 7

References

Contents

7.1 Isba

Anderson, E. A., 1976: A point energy and mass balance model of a snow cover. *NOAA Tech. Rep. NWS 19*, 150 pp. U.S. Dept. of Commer., Washington, D.C.

Beven KJ, Kirkby MJ (1979) A physically-based variable contributing area model of basin hydrology. Hydrol. Sci. Bull. 24: 43-69.

Best, M.J., A. Beljaars, J. Polcher, P. Viterbo, 2004: A proposed structure for coupling tiled surfaces with the planetary boundary layer. *Journal of Hydrometeorology*, **5**, 1271-1278.

Bhumralkar, C.M., 1975: Numerical experiment on the computation of ground surface temperature in an atmospheric general circulation model. *J. Appl. Meteor.*, **14**, 1246-1258.

Blackadar, A.K., 1976: Modeling the nocturnal boundary layer. *Proc. Third Symp. on Atmospheric Turbulence, Diffusion and Air Quality* , Boston, Amer. Meteor. Soc., 46-49.

Boone, A., Modelisation des processus hydrologiques dans le schema de surface ISBA: Inclusion d'un reservoir hydrologique, du gel et modelisation de la neige. PhD thesis, University Paul Sabatier, TOULOUSE, France, 2000. 252pp.

Boone, A., and P. Etchevers, 2000: An intercomparison of three snow schemes of varying complexity coupled to the same land-surface and macroscale hydrologic models. *J. Hydrometeor.*,

Boone, A., J.-C. Calvet and J. Noilhan, 1999: Inclusion of a third soil layer in a land-surface scheme using the force-restore method, *J. Appl. Meteor.*, **38**, 1611-1630.

Boone, A., V. Masson, T. Meyers, and J. Noilhan, 2000: The influence of the inclusion of soil freezing on simulations by a soil-atmosphere-transfer scheme. *J. Appl. Meteor.*, (in press).

Braud, I., J. Noilhan, P. Bessemoulin, P. Mascart, R. Haverkamp, and M. Vauclin, 1993: Bare-ground surface heat and water exchanges under dry conditions: Observations and parameterization. *Bound.-Layer Meteror.*, **66**, 173-200.

Caballero, Y., Voirin-Morel, S., Habets, F., Noilhan, J., LeMoigne, P., Lehenaff, A., and Boone, A.: Hydrological sensitivity of the Adour-Garonne river basin to climate change, Water. Resour. Res., 43, W07448, doi:10.1029/2005WR004192, 2007

Clapp R, Hornberger G (1978) Empirical equations for some soil hydraulic properties. Wat. Resour. Res. 14: 601-604.

Deardorff, J.W., 1978: Efficient prediction of ground surface temperature and moisture with inclusion of a layer of vegetation. *J. Geophys. Res.*, **20**, 1889-1903.

Deardorff, J.W., 1977: A parameterization of ground surface moisture content for use in atmospheric prediction models. *J. Appl. Meteor.*, **16**, 1182-1185.

Decharme B., H. Douville, A. Boone, F. Habets, and J. Noilhan, 2006: Impact of an exponential profile of saturated hydraulic conductivity within the ISBA LSM: simulations over the Rhne basin. J. Hydrometeor, 7, 61-80.

Decharme B. and H. Douville, 2006: Introduction of a sub-grid hydrology in the ISBA land surface model. Climate Dyn., 26, 65 - 78.

Decharme B. and H. Douville, 2007: Global validation of the ISBA Sub-Grid Hydrology. Climate Dyn., 29, 21-37.

Dickinson, R.E., 1984: Modeling evapotranspiration for three dimensional global climate models. *Climate Processes and Climate Sensitivity. Geophys. Monogr.*, **29**, 58-72.

Douville, H., 1994: Développement et validation locale d'une nouvelle paramétrisation du manteau neigeux. Note 36 GMME/Météo-France.

Douville, H., J.-F. Royer, and J.-F. Mahfouf,1995: A new snow parameterization for the French community climate model. Part I: Validation in stand-alone experiments. *Climate Dyn.*, submitted.

Fan Y, Wood EF, Baeck ML, Smith JA (1996) The fractional coverage of rainfall over a grid: Analyses of NEXRAD data over the southern plains. Water Resour. Res. 32: 2787-2802. Habets F, Saulnier GM (2001) Sub-grid runoff parameterization. Phys. Chem. Earth 26: 455- 459.

Giard, D., and E. Bazile, 1999: Implementation of a new assimilation scheme for soil and surface variables in a global NWP model. *Mon. Wea. Rev.*, (in press).

Giordani, H., 1993: Expériences de validation unidimensionnelles du schéma de surface NP89 aux normes Arpège sur trois sites de la campagne EFEDA 91. Note de travail 24 GMME/Météo-France.

Giordani, H., J. Noilhan, P. Lacarrere, P. Bessemoulin, and P. Mascart, 1996 : Modelling the surface processes and the atmospheric boundary layer for semi-arid conditions. Agricultural and Forest Meteorology, 80, 263287.

HABETS F., NOILHAN J., GOLAZ C., GOUTORBE J.P., LACARRERE P., LEBLOIS E., LEDOUX E., MARTIN E., OTTLE C., VIDAL-MADJAR D., 1999. The ISBA surface scheme in a macroscale hydrological model applied to the Hapex-Mobilhy area. Part I : model and data base, Journal of Hydrology, 217, p.75-96.

Habets F. and Saulnier G.-M.,Subgrid runoff parameterization. Physics and Chemistry of the Earth, Part B: Hydrology, Oceans and Atmosphere Volume 26, Issues 5-6, 2001, Pages 455-459

Jacquemin, B., and J. Noilhan, 1990: Validation of a land surface parameterization using the HAPEX-MOBILHY data set. *Bound.-Layer Meteor.*, **52**, 93-134.

Johnsson, H., and L.-C. Lundin, 1991: Surface runoff and soil water percolation as affected by snow and soil frost. *J. Hydro.*, **122**, 141-158.

Loth, B., H.-F. Graf, and J. M. Oberhuber, 1993: Snow cover model for global climate simulations. *J. of Geophys. Res.*, **98**, 10451-10464.

Louis, J.F., 1979: A parametric model of vertical eddy fluxes in the atmosphere. *Bound.-Layer Meteor.*, **17**, 187-202.

Lynch-Stieglitz, M., 1994: The development and validation of a simple snow model for the GISS GCM. *J. Clim.*, **7**, 1842-1855.

Mahfouf, J.-F., J. Noilhan, and P. Péris, 1994: Simulations du bilan hydrique avec ISBA: Application au cycle annuel dans le cadre de PILPS. Atelier de modélisation de l'atmosphère, CNRM/Météo-France, December 1994, Toulouse, France, 83-92.

Mahfouf, J.-F., and J. Noilhan, 1991: Comparative study of various formulations of evaporation from bare soil using in situ data. *J. Appl. Meteor.*, **9**, 1354-1365.

Mahfouf, J.-F. and Noilhan J., 1996: Inclusion of gravitational drainage in a land surface scheme based on the force restore method. Journal of Applied Meteorology, 35, 987-992.

Mascart, P., J. Noilhan, and H. Giordani, 1995: A modified parameterization of flux-profile relationships in the surface layer using different roughness length values for heat and momentum. *Bound.-Layer Meteor.*,**72**, 331-344.

Masson, 2000: A physically-based scheme for the urban energy budget in atmospheric models. *Boundary Layer Meteorology*, in press.

Masson V., J.-L. Champeaux, F. Chauvin, C. Meriguet and R. Lacaze, 2003 : A global database of land surface parameters at 1km resolution in meteorological and climate models. *J. Climate*,**16**, 1261-1282.

Noilhan, J., and P. Lacarrère, 1995: GCM grid-scale evaporation from mesoscale modeling. *J. Climate*, in press.

Noilhan, J., and S. Planton, 1989: A simple parameterization of land surface processes for meteorological models. *Mon. Wea. Rev.*, **117**, 536-549.

Noilhan J. and Mahfouf J.-F., 1996: The ISBA land surface parameterisation scheme Global and Planetary Change, 13, 145-159.

Polcher, J., B. McAveney, P. Viterbo, M.-A. Gaertner, A. Hahmann, J.-F. Mahfouf, J. Noilhan, T. Phillips, A. Pitman, C.A., Schlosser, J.-P. Schulz, B. Timbal, D. Verseghy and Y. Xue, 1998: A proposal for a general interface between land-surface schemes and general circulation models. *Global and Planetary Change*, **19**, 261-276.

Silvapalan M, Beven KJ, Wood EF (1987) On hydrologic similarity: 2. A scaled model of storm runoff production, Water Resour. Res. 23: 2266-2278.

Sun, S., J. Jin, and Y. Xue, 1999: A simple snow-atmosphere-soil transfer (SAST) model. *J. of Geophys. Res.*, **104**, 19587-19579.

Verseghy, D., 1991: CLASS - A Canadian land surface scheme for GCMs. I: Soil model. *Int. J. Climatol.*, **11**, 111-133.

7.2 Isba-A-gs

Calvet, J.-C., J. Noilhan, J.-L. Roujean, P. Bessemoulin, M. Cabelguenne, A. Olioso, and J.-P. Wigneron (1998), An interactive vegetation SVAT model tested against data from six contrasting sites, Agric. For. Meteorol., 92, 73-95.

Calvet, J.-C. (2000), Investigating soil and atmospheric plant water stress using physiological and micrometeorological data, Agric. For. Meteorol., 103, 229-247.

Calvet, J.-C., and J.-F. Soussana (2001), Modeling CO2-enrichment effects using an interactive vegetation SVAT scheme, Agric. For. Meteorol., 108, 129-152.

Calvet, J.-C., V. Rivalland, C. Picon-Cochard, and J.-M. Guehl (2004), Modelling forest transpiration and CO2 fluxes - response to soil moisture stress, Agric. For. Meteorol., 124, 143-156.

Calvet, J.-C., A.-L. Gibelin, E. Martin, P. Le Moigne, H. Douville, J. Noilhan (2008), Past and future scenarios of the effect of carbon dioxide on plant growth and transpiration for three vegetation types of south-western France, Atmos. Chem. Phys., 8, 397406.

Collatz, G. J., M., Ribas-Carbo, J. A., Berry (1992), Coupled photosynthesis-stomatal conductance model for leaves of C4 plants. Aust. J. Plant Physiol. 19, 519538. GSWP2 (2002) Science and implementation plan gswp2, IGPO Publication Series, 37.

Farquhar, G. D., S., von Caemmerer, J. A., Berry (1980), A biochemical model of photosynthetic CO2 assimilation in leaves of C3 species. Planta, 149, 7890.

Gibelin, A.-L., J.-C. Calvet, J.-L. Roujean, L. Jarlan, S. O. Los (2006), Ability of the land surface model ISBA-A-gs to simulate leaf area index at the global scale: comparison with satellites products. J. Geophys. Res. 111, D18102.

Gibelin, A.-L., J.-C. Calvet, and N. Viovy (2008), Modelling energy and CO2 fluxes with an interactive vegetation land surface model Evaluation at high and middle latitudes, Agric. For. Meteorol., 148, 1611-1628, doi: 10.1016/j.agrformet.2008.05.013.

Goudriaan, J., H.H. van Laar, H. Van Keulen, and W. Louwerse (1985), Photosynthesis, CO2 and plant production. In: W. Day and R.K. Atkin (Eds.), Wheat growth and modelling. NATO ASI Series, Plenum Press, New York, Series A, 86, 107-122.

Jacobs, C. M. J. (1994), Direct impact of CO2 enrichment on regional transpiration. Ph. D. Thesis, Agricultural University, Wageningen

Jacobs, C. M. J., B. J. J. M. Van den Hurk, and H. A. R. De Bruin (1996), Stomatal behaviour and photosynthetic rate of unstressed grapevines in semi-arid conditions, Agric. For. Meteorol., 80, 111-134.

Lafont S., A. Beljaars, M. Voogt, L. Jarlan, P. Viterbo, B. van den Hurk, J.-C. Calvet (2006), Comparison of C-TESSEL CO2 fluxes with TransCom CO2 fluxes. Proc. Second Recent Advances in Quantitative Remote Sensing II, Torrent (Valencia), Spain, 26-29 September 2006, 474-477.

Lemaire, G. and F. Gastal (1997), N uptake and distribution in plant canopies. In: Lemaire, G. (Ed.), Diagnosis of the Nitrogen Status in Crops. Springer, Berlin, pp. 343.

Martin, E., Le Moigne, P., Masson, V., et al. (2007), Le code de surface externalisée SURFEX de Météo-France, Ateliers de Modélisation de lAtmosphère (http://www.cnrm.meteo.fr/ama2007/), Toulouse, 1618 January, 2007.

Masson, V., J.-L. Champeaux, F. Chauvin, C. Meriguet and R. Lacaze (2003), A global database of land surface parameters at 1-km resolution in meteorological and climate models, J. Climate, 16, 1261-1282.

Norman, J.M., R. Garcia, S.B. Verma (1992), Soil surface CO2 fluxes and the carbon budget of a grassland, J. Geophys. Res., 97(D17), 18845-18853.

Rivalland, V., J.-C. Calvet, P. Berbigier, Y. Brunet, A. Granier (2005), Transpiration and CO2 fluxes of a pine forest: modelling the undergrowth effect, Ann. Geophys., 23, pp 291-304.

Roujean, J.-L. (1996), A tractable physical model of shortwave radiation interception by vegetative canopies. J. Geophys. Res., 101D5, 9523-9532.

Van den Hurk, B. J. J. M., P. Viterbo, A. C. M. Beljaars, and A. K. Betts (2000), Offine validation of the ERA40 surface scheme, ECMWF TechMemo. 295, 42 pp., ECMWF, Reading.

Voogt, M., B.J.J.M. van den Hurk and C. Jacobs (2006), The ECMWF land surface scheme extended with a photosynthesis and LAI module tested for a coniferous site, KNMI publication: WR-06-02, 3/1/2006, 22 pp, De Bilt, The Netherlands, http://www.knmi.nl/publications/fulltexts/agrformetd0600207.pdf .

Yin, X. (2002), Responses of leaf nitrogen concentration and specific leaf area to atmospheric CO2 enrichment: a retrospective synthesis across 62 species, Global Change Biol., 8(7), 631642.

7.3 Teb

Arnfield A.J. and Grimmond C.S.B.. An urban energy budget Model and its application to Urban Storage Heat Flux modeling. Energy and buildings, 27:6168, 1998.

Arya S.P. Introduction to Micrometeorology. Academic Press, Inc., 1988.

Best M.J. A model to predict surface temperatures. Boundary-Layer Meteorol., 88:279306, 1998.

Bottema M. Urban Roughness modelling in relation to Pollutant Dispersion. Atmos. Environ., 31(18):30593075, 1997.

Deardorff J.W. Efficient prediction of ground temperature and moisture with inclusion of a layer of vegetation. J. Geophys. Res., 83:18891903, 1978.

Feigenwinter C., Vogt R., and Parlow E. Vertical structure of selected turbulence characteristics above an urban canopy. Theor. Appl. Climatol., 62:5163, 1999.

Grimmond C.S.B. and Oke T.R. Aerodynamic Properties of urban areas derived from Analysis of Surface form. J. Appl. Meteorol., 38:12621292, 1999b.

Grimmond C.S.B. and Oke T.R. An evapotranspiration-interception Model for Urban areas. Water Resour. Res., 27:17391755, 1991.

Grimmond C.S.B. and Oke T.R. Heat storage in urban areas : Local-scale observations and evaluation of a simple model. J. Appl. Meteorol., 38:922940, 1999a.

Grimmond C.S.B., Cleugh H.A. and Oke T.R. An objective Urban Heat Storage model and its comparison with other Schemes. Atmos. Environ., 25B:311326, 1991.

Johnson G.T., Oke T.R., Lyons T.J., Steyn D.G., Watson I.D., and Voogt J.A. Simulation of surface urban heat islands under ideal conditions at night. part i: theory and tests against field data. Boundary-Layer Meteorol., 56:275294, 1991.

Lemonsu, A.; Grimmond, C. S. B. and Masson, V. Modeling the surface energy balance of the core of an old mediterranean city: Marseille. J. Appl. Meteorol., 2004 , 43 , 312-327

Lemonsu, A. and Masson, V. Simulation of a summer urban breeze over Paris Boundary-Layer Meteorol., 2002 , 104 , 463-490

Lemonsu, A.; Pigeon, G.; Masson, V. and Moppert, C. Sea-town interactions over Marseille: 3D urban boundary layer and thermodynamic fields near the surface Theor. and Appl. Climatol., 2006 , 84 , 171-178

Mascart P., Noilhan J., and Giordani H. A modified parameterization of flux-profile relationship in the surface layer using different roughness length values for heat and momentum. Boundary-Layer Meteorol., 72:331344, 1995.

Menut L. Etude experimentale et theorique de la couche limite Atmospherique en agglomeration parisienne (experimental and theoretical study of the ABL in Paris area). PhD thesis, University Pierre et Marie Curie, PARIS, France, 1997. 200pp.

Mills G.M. Simulation of the energy budget of an urban canyon-i. model structure and sensitivity test. Atmos. Environ., 27B(2):157170, 1993.

Noilhan J. A Model for the Net Total Radiation flux at the Surfaces of a Building. Building and Environment, 16(4):259266, 1981.

Noilhan J. and Planton S. A simple parameterization of land surface processes for meteorological models. Mon. Wea. Rev., 117:536549, 1989.

Offerle, B.; Grimmond, C. S. B. and Fortuniak, K. Heat storage and anthropogenic heat flux in relation to the energy balance of a central European city centre Int. J. Climatol., 2005 , 25 , 1405-1419

Oke, T.R. Boundary layer climates. 2nd edition. Methuen, London, 1987. 435pp.

Oke, T.R. The urban energy balance. Prog. Phys. Geogr., 12:471508, 1988.

Oke, T.R., R.A. Spronken-Smith, E. Jauregui, and C.S.B. Grimmond. The energy balance of central Mexico City during the dry season. Atmos. Environ., 33:39193930, 1999.

Peterseni R.L. A wind tunnel evaluation of methods for estimating surface roughness length at industrial facilities. Atmos. Environ., 31(1):4557, 1997.

Pigeon, G.; Lemonsu, A.; Long, N.; Barri, J.; Durand, P. and Masson, V. Urban thermodynamic island in a coastal city analyzed from an optimized surface network Boundary-Layer Meteorol., 2006 , 120 , 315-351

Pigeon, G.; Lemonsu, A.; Grimmond, C.; Durand, P.; Thouron, O. and Masson, V. Divergence of turbulent fluxes in the surface layer: case of a coastal city Boundary-Layer Meteorol., 2007 , 124 , 269-290

Pigeon, G.; Moscicki, M. A.; Voogt, J. A. and Masson, V. Simulation of fall and winter surface energy balance over a dense urban area using the TEB scheme Meteorology and Atmospheric Physics, 2008, vol 102, 159-172

Richards K. and Oke T.R. Dew in urban environments. Procedings of IInd AMS Urban Environment Symposium, 1998.

Roberts, S. M.; Oke, T. R.; Grimmond, C. S. B. and Voogt, J. A. Comparison of four methods to estimate urban heat storage JAMC, 2006 , 45 , 1766-1781

Rotach M.W. Profiles of turbulence statistics in and above an urban street canyon. Atmos. Environ., 29(13):14731486, 1995.

Roth M. Turbulent transfert: relationships over an urban surface. ii: Integral statistics. Quart. J. Roy. Meteor. Soc., 119:11051120, 1993.

Roth M. and Oke T.R. Turbulent transfert: relationships over an urban surface. ii: spectral characteristics. Quart. J. Roy. Meteor. Soc., 119:10711104, 1993.

Rowley F.B., Algren A.B., and Blackshaw J.L. Surface conductances as affected by air velocity, temperature and character of surface. ASHRAE Trans., 36:429446, 1930.

Rowley F.B. and Eckley W.A. Surface coefficients as affected by wind direction. ASHRAE Trans., 38:3346, 1932.

Sarrat, C.; Lemonsu, A.; Masson, V. and Guedalia, D. Impact of urban heat island on regional atmospheric pollution Atmospheric Environment, 2006 , 40 , 1743-1758

Seaman N.L., Ludwig F., Donall E.G., Warner T.T., and Bhumralkar C.M. Numerical studies of urban planetary boundary-layer structure under realistic synoptic conditions. J. Appl. Meteorol., 28:760781, 1989.

Soux A., Oke T.R., and Voogt J.A. Modelling and remote sensing of the urban surface. Procedings of IInd AMS Urban Environment Symposium, 1998.

Sturrock N.S. and Cole R.J. The convective heat exchange at the external surface of buildings. Building and environment, 12:207214, 1977.

Taha H. Modifying a Mesoscale Meteorological Model to better incorporate Urban Heat Storage : A bulk parametrerization approach. J. Appl. Meteorol., 38:466473, 1999.

Terjung W.H. and ORourke P.A. Influences of physical structures on urban energy budgets. Boundary-Layer Meteorol., 19:421439, 1980.

Wieringa J. Representative roughness parameters for homogeneous terrain. Boundary-Layer Meteorol., 63:323363, 1993.

7.4 Surface Boundary Layer scheme

Belcher, S. E., N. Jerram, and J. C. R. Hunt, 2003: Adjustment of a turbulent boundary layer to a canopy of roughness elements. Journal of Fluid Mechanics, 488, 369398.

Beljaars, A. C. M. and A. A. M. Holtslag, 1991: Flux parameterization over land surfaces for atmospheric models. J. Appl. Meteorol., 30, 327341.

Best, M. J., A. Beljaars, J. Polcher, and P. Viterbo, 2004: A proposed structure for coupling tiled surfaces with the planetary boundary layer. Journal of hydrometeorology, 5, 12711278.

Bougeault, P., B. Bret, P. Lacarr‘ere, and J.Noilhan, 1988: Design and implementation of a land surface processes parameterization in a mesoscale model. Parameterization of fluxes over land surface, European Center of Medium-Range Weather Forecasting, Shinfield Park, Reading RG2 9AX, U.K., 95120.

Bubnova, R., G. Hello, P. Benard, and J.-F. Geleyn, 1995: Integration of the fully elastic equations cast in the hydrostatic pressure terrain-following coordinate in the framework of the ARPEGE/ALADIN NWP system. Mon. Wea. Rev., 123, 515535.

Chen, T. H. and coauthors, 1997: Cabauw experimental results from the project for intercomparison of land-surface parameterization schemes. Journal of Climate, 10, 11941215.

Cheng, Y., V. Canuto, and A. Howard, 2002: An improved model for the turbulent pbl. J. Atmos. Sci., 59, 15501565.

Coceal, O. and S. E. Belcher, 2005: A canopy model of mean winds through urban areas. Quart. J. Roy. Meteor. Soc., 130, 13491372.

Cuxart, J., P. Bougeault, and J.-L. Redelsperger, 2000: A turbulence scheme allowing for mesoscale and large-eddy simulations. Quart. J. Roy. Meteor. Soc., 116, 130.

Deardorff, J., 1978: Efficient prediction of ground temperature and moisture with inclusion of a layer of vegetation. J. Geophys. Res., 83, 18891903.

Geleyn, J.-F., 1988: Interpolation of wind, temperature and humidity values from model levels to the height of measurement. Tellus, 40A, 347351.

Grini, A., P. Tulet, and L. Gomes, 2006: Dusty weather forecast using the mesonh atmospheric model. J. Geophys. Res., 111, D19 205, doi:10.1029/2005JD007007.

Hamdi, R. and V. Masson, 2008: Inclusion of a drag approach in the town energy balance (teb) scheme: offline 1-d validation in a street canyon. Journal of Applied Meteorology and Climatology, in press.

Hogstrom, U., 1988: Non-dimensional wind and temperature profiles in the atmospheric surface layer: A re-evaluation. Boundary-Layer Meteorol., 42, 680687. Kanda, M. and M. Hino, 1994: Organized structures in developing turbulent flow within and above a plant canopy, using a large eddy simulation. Boundary-Layer Meteorol., 68, 237 257.

Kondo, H., Y. Genchi, Y. Kikegawa, Y. Ohashi, H. Yoshikado, and H. Komiyama, 2005: Development of a multi-layer urban canopy model for the analysis of energy consumption in a big city: Structure of the urban canopy model and its basic performance. Boundary-Layer Meteorology, 116, 395421, doi:doi:10.1007/s10546-005-0905-5.

Lafore, J.P., J. Stein, N. Asencio, P. Bougeault, V. Ducrocq, J. Duron, C. Fischer, P. Hreil, P. Mascart, V. Masson, J.P. Pinty, J.L. Redelsperger, E. Richard, and J. Vila-Guerau de Arellano, 1998: The Mso-NH atmospheric simulation system. Part I : Adiabatic formulation and control simulation. Ann. Geophys., 16, 90109.

Lee, H. N., 1997: Improvement of surface flux calculations in the atmospheric surface layer. J. Appl. Meteorol., 36, 14161423.

Manabe, S., 1965: Climate and the ocean circulation 1. the atmospheric circulation and the hydrology of the earths surface. Mon. Wea. Rev., 97, 739774.

Martilli, A., A. Clappier, and M. Rotach, 2002: An urban Surface exchange Parameterization for mesoscale Models. Boundary-Layer Meteorol., 104, 261304.

Masson, V., 2006: Urban surface modeling and the meso-scale impact of cities. Theoretical and Appl. Climatology, 84, 3545.

Masson, V., J.L. Champeaux, F. Chauvin, C. Meriguet, and R. Lacaze, 2003: A global data base of land surface parameters at 1 km resolution in meteorological and climate models. J. of Climate, 16 (9), 12611282.

Noilhan, J. and S. Planton, 1989: A simple parameterization of land surface processes for meteorological models. Mon. Wea. Rev., 117, 536549.

Park, H. and S. Hattori, 2004: Modeling scalar and heat sources, sinks, and fluxes within a forest canopy during and after rainfall events. J. Geophys. Res., 109, D14 301, dOI:10.1029/2003JD004360.

Patton, E. G., K. J. Davis, M. C. Barth, and P. P. Sullivan, 2001: Decaying scalars emitted by a forest canopy - a numerical study. Boundary-Layer Meteorol., 100, 91129.

Patton, E. G., P. P. Sullivan, and C.-H. Moeng, 2003: The influence of a forest canopy on topdown and bottom-up diffusion in the planetary boundary layer. Quart. J. Roy. Meteor. Soc., 129, 14151434.

Paulson, C. A., 1970: The mathematical representation of wind and temperature profiles in the unstable atmospheric surface layer. J. Appl. Meteorol., 9, 857861.

Pinty, J.-P. and P. Jabouille, 1998: A mixed-phase cloud parameterization for use in a mesoscale non-hydrostatic model: Simulations of a squall line and of orographic precipitation. Conf. on Cloud Physics, Everett, WA, AMS, 217220.

Pleim, J. E., 2006: A simple, efficient solution of flux-profile relationships in the atmospheric surface layer. J. Appl. Meteorol. Clim., 45, 341347.

Polcher, J. and coauthors, 1998: A proposal for a general interface between land-surface schemes and general circulation models. Global Planet. change, 19, 263278.

Redelsperger, J.-L., F. Mahe, and P. Carlotti, December 2001: A simple and general subgrid model suitable both for surface layer and free-stream turbulence. Boundary-Layer Meteorology, 101, 375408.

Robock, A., K. Y. Vinikov, C. A. Schlosser, N. A. Speranskaya, and Y. Xue, 1995: Use of midlatitude soil moisture and meteorological observations to validate soil moisture simulations with biosphere and bucket models. Journal of Climate, 8, 1535.

Rotach, M. W., V. R., B. D., B. E., C. A., C. A., F. B., G. S.-E., M. G., M. H., M. V., O. T. R., P. E., R. H., R. M., R. Y.-A., R. D., S. J.-A., S. M., and V. J. A., 2005: Bubble - an urban boundary layer meteorology project. Theoretical and Applied Climatology, 81, 231261, dOI 10,1007/s00704-004-0117-9.

Shaw, R. and U. Schumann, 1992: Large-eddy simulation of turbulent flow above and within a forest. Boundary-Layer Meteorol., 61, 119131.

Shen, S. and M. Y. Leclerc, 1997: Modelling the turbulence structure in the canopy layer. Agricultural and Forest Meteorology, 87, 184.

Simon, E., F. X. Meixmer, L. Ganzeveld, and J. Kesselmeier, 2005: Coupled carbon-water exchange of the amazon rain forest, 1. model description, parameterization and sensitivity analysis. Biogeosciences Discussions, 2, 333397.

Stull, R. B., 1988: An introduction to Boundary Layer Meteorology. Kluwer, 666pp.

Suna, H., T. L. Clarka, R. B. Stulla, and T. A. Black, 2006: Two-dimensional simulation of airflow and carbon dioxide transport over a forested mountain part i: Interactions between thermally-forced circulations. Agricultural and Forest Meteorology, 140, 338351, doi:10.1016/j.agrformet.2006.03.023.

Tulet, P., V. Crassier, F. Solmon, D. Guedalia, and R. Rosset, 2003: Description of the mesoscale non-hydrostatic chemistry model and application to a transboundary pollution episode between northern france and southern england. J. Geophys. Res., 108, D1, 4021.

Xinmin, Z., Z. Ming, S. Bingkai, and W. Hanjie, 1999: Study on a boundary-layer numerical model with inclusion of heterogeneous multi-layer vegetation. Advances in Atmospheric Sciences, 16, 431442, doi:10.1007/s00376-999-0021-4.

7.5 1D TKE Oceanic model

Belamari, S., 2005 : Report on uncertainty estimates of an optimal bulk formulation for surface turbulent fluxes. MERSEA IP Deliverable, D.4.1.2, 29.

Bougeault, P. and P. Lacarrère, 1989 : Parameterization of orography-induced turbulence in a mesobeta scale model. Mon. Wea. Rev., 117, 18721890.

Brunke, M. A., C. W. Fairall, X. Zeng, L. Eymard, and J. A. Curry, 2003 : Which bulk aerodynamic algorithms are least problematic in computing ocean surface turbulent fluxes ? J. Climate, 16, 619 635.

Businger, J. A., J. C. Wyngaard, Y. Izumi, and E. Bradley, 1971 : Flux profile relationship in the atmospheric surface layer. J. Atmos. Sci., 28, 181189.

Charnock, H., 1955 : Wind stress on a water surface. Quart. J. Roy. Meteor. Soc., 81, 639640.

Fairall, C.W., E. F. Bradley, J. S. Godfrey, G. A.Wick, J. B. Edson, and G. S. Young, 1996a : Cool-skin and warm-layer effects on sea surface temperature. J. Geophys. Res., 101, 12951308.

Fairall, C. W., E. F. Bradley, J. E. Hare, A. A. Grachev, and J. B. Edson, 2003 : Bulk parameterization of air-sea fluxes : Updates and verification for the COARE algorithm. J. Climate, 16, 571591.

Fairall, C.W., E. F. Bradley, D. P. Rogers, J. B. Edson, and G. S. Young, 1996b : Bulk parameterization of air-sea fluxes for Tropical Ocean-Global Atmosphere Coupled-Ocean Atmosphere Response Experiment. J. Geophys. Res., 101, 37473764.

Gaspar, P., Y. Grégoris, and J.-M. Lefevre, 1990 : A simple Eddy Kinetic Energy model for simulations of the oceanic vertical mixing : Tests at station Papa and Long-Term Upper Ocean Study site. J. Geophys. Res., 95, 1617916193.

Gosnell, R., C. Fairall, and P. J. Webster, 1995 : The sensible heat of rainfall in the tropical ocean. J. Geophys. Res., 100, 1843718442.

Grachev, A. A. and C. W. Fairall, 1997 : Dependence of the Monin-Obukhov stability parameter on the bulk richardson number over the ocean. J. Appl. Meteor., 36, 406414. Hare, J. E., P. O. G. Persson, C.W. Fairall, and J. B. Edson, 1999 : Behavior of Charnocks relationship for high wind conditions. 13th Symp. on Boundary Layers and Turbulence, Amer. Meteor. Soc., Dallas, TX, 252255.

Kraus, E. B., 1972 : Atmosphere-ocean interactions. London Oxford University press.

Lebeaupin Brossier, C., 2007 : étude du couplage océan-atmosphère associé aux épisodes de pluie intenses en région Méditerranéenne. Ph.D. thesis, Univ. P. Sabatier, Toulouse III, 228 pp.

Lebeaupin Brossier, C., V. Ducrocq, and H. Giordani, 2008a : Sensitivity of threeMediterranean heavy rain events to two different sea surface fluxes parameterization in high-resolution numerical modelling. J. Geophys. Res., in revision.

7.6 Flake

Beyrich, F., J.-P. Leps, M. Mauder, J. Bange, T. Foken, S. Huneke, H. Lohse, A. Luedi, W. M. L. Meijninger, D. Mironov, U. Weisensee, and P. Zittel, 2006: Area-averaged surface fluxes over the LITFASS region based on eddy-covariance measurements. Boundary-Layer Meteorol., 121, 33-65. doi:10.1007/s10546-006-9052-x

Braslavski, D., 2004: Experiments with Zero-Dimensional Lake Model. M.Sc. Thesis, Russian State Hydrometeorological University, St. Petersburg, Russia, 51 pp. (in Russian)

Dutra, E., V. Stepanenko, P. A. Miranda, P. Viterbo, D. Mironov, and V. N. Lykosov, 2006: Evaporation and seasonal temperature changes in lakes of the Iberian Peninsula. Proc. of the 5th Portuguese-Spanish Assembly of Geophysics and Geodesy, 30 January - 3 February 2006, Sevilha, Spain, 4 pp. (PDF)

Ganbat, G. O., 2006: External-Parameter Fields for Hydrodynamic Models of the Atmosphere. B.Sc. Thesis, Russian State Hydrometeorological University, St. Petersburg, Russia, 36 pp. (in Russian) (PDF)

Golosov, S., O. Maher, E. Schipunova, A. Terzhevik, G. Zdorovennova, and G. Kirillin, 2006: Physical background of the development of oxygen depletion in ice-covered lakes. Oecologia, 151, 331-340. doi: 10.1007/s00442-006-0543-8

Golosov, S. G., A. Terzhevik, O. A. Maher, E. Shipunova, and G. Zdorovennova, 2004: Modelling seasonal dynamics of dissolved oxygen in a shallow stratified lake. Proc. of the 8th Workshop on Physical Processes in Natural Waters, L. Bengtsson and O. A. Maher, Eds., University of Lund, Lund, Sweden, 153-164.

Kirillin, G., 2003: Modelling of the shallow lake response to climate variability. Proc. of the 7th Workshop on Physical Processes in Natural Waters, A. Yu. Terzhevik, Ed., Northern Water Problems Institute, Russian Academy of Sciences, Petrozavodsk, Karelia, Russia, 144-148. (PDF)

Kourzeneva K., and D. Braslavsky, 2005: Lake model FLake, coupling with atmospheric model: first steps. Proc. of the 4th SRNWP/HIRLAM Workshop on Surface Processes and Assimilation of Surface Variables jointly with HIRLAM Workshop on Turbulence, S. Gollvik, Ed., 15-17 September 2004, SMHI, Norrkoping, Sweden, 43-54. (PDF)

Maher, O. A., S. Golosov, A. Mitrokhov, N. Palshin, M. Petrov, E. Shipunova, A. Terzhevik, R. Zdorovennov, and G. Zdorovennova, 2004: Dynamics of Dissolved Oxygen in a Shallow Lake: Measurements and Modelling. Department of Water Resources Engineering, Institute of Technology, University of Lund, Report 3247, Lund, 51 pp.

Martynov, A., R. Laprise, and L. Sushama, 2008: Off-line lake water and ice simulations: a step towards the interactive lake coupling with the Canadian Regional Climate Model. Geophysical Research Abstracts, Vol. 10, EGU2008-A-02898. (PDF)

Mironov, D. V., 1991: Air-water interaction parameters over lakes. Modeling Air-Lake interaction. Physical Background, S. S. Zilitinkevich, Ed., Springer-Verlag, Berlin, etc., 50-62.

Mironov, D. V., 2008: Parameterization of lakes in numerical weather prediction. Description of a lake model. COSMO Technical Report, No. 11, Deutscher Wetterdienst, Offenbach am Main, Germany, 41 pp. (PDF)

Mironov, D., S. Golosov, E. Heise, E. Kourzeneva, B. Ritter, N. Scheider, and A. Terzhevik, 2005a: FLake - A Lake Model for Environmental Applications. Proc. of the 9th Workshop on Physical Processes in Natural Waters, 4 - 6 September 2005, A. Folkard and I. Jones, Eds., Lancaster University, UK, 73. (PDF)

Mironov, D. V., S. D. Golosov, S. S. Zilitinkevich, K. D. Kreiman, and A. Yu. Terzhevik, 1991: Seasonal changes of temperature and mixing conditions in a lake. Modeling Air-Lake interaction. Physical Background, S. S. Zilitinkevich, Ed., Springer-Verlag, Berlin, etc., 74-90.

Mironov, D. V., S. D. Golosov, and I. S. Zverev, 2003a: Temperature profile in lake bottom sediments: an analytical self-similar solution. Proc. of the 7th Workshop on Physical Processes in Natural Waters, A. Yu. Terzhevik, Ed., Northern Water Problems Institute, Russian Academy of Sciences, Petrozavodsk, Karelia, Russia, 90-97. (PDF)

Mironov, D., E. Heise, E. Kourzeneva, B. Ritter, and N. Schneider, 2007: Parameterisation of lakes in numerical weather prediction and climate models. Proc. of the 11th Workshop on Physical Processes in Natural Waters, L. Umlauf and G. Kirillin, Eds., Berichte des IGB, Vol. 25, Berlin, Germany, 101-108. (PDF, download the entire volume)

Mironov, D., G. Kirillin, E. Heise, S. Golosov, A. Terzhevik, and I. Zverev, 2003b: Parameterization of lakes in numerical models for environmental applications. Proc. of the 7th Workshop on Physical Processes in Natural Waters, A. Yu. Terzhevik, Ed., Northern Water Problems Institute, Russian Academy of Sciences, Petrozavodsk, Karelia, Russia, 135-143. (PDF)

Mironov, D., and B. Ritter, 2003: A first version of the ice model for the global NWP system GME of the German Weather Service. Research Activities in Atmospheric and Oceanic Modelling, J. Cote, Ed., Report No. 33, April 2003, WMO/TD, 4.13-4.14. (PDF)

Mironov, D., and B. Ritter, 2004a: A New Sea Ice Model for GME. Technical Note, Deutscher Wetterdienst, Offenbach am Main, Germany, 12 pp. (PS)

Mironov, D., and B. Ritter, 2004b: Testing the new ice model for the global NWP system GME of the German Weather Service. Research Activities in Atmospheric and Oceanic Modelling, J. Cote, Ed., Report No. 34, April 2004, WMO/TD-No. 1220, 4.21-4.22. (PDF)

Mironov, D., and B. Ritter, 2007: A thermodynamic sea ice model for the global numerical weather prediction system GME of the German Weather Service. Submitted to Mon. Weather. Rev.

Mironov, D., N. Schneider, B. Ritter, and E. Heise, 2005b: Implementation of a Lake Model FLake into the Limited-Area NWP System LM of the German Weather Service: Preliminary Results. Research Activities in Atmospheric and Oceanic Modelling, J. Cote, Ed., Report No. 35, Month 2005, WMO/TD-No. 1220, 4.15-4.16. (PDF, username science, password science)

Mironov, D., A. Terzhevik, F. Beyrich, and E. Heise, 2004: A Lake Model for Use in Numerical Weather Prediction Systems. Research Activities in Atmospheric and Oceanic Modelling, J. Cote, Ed., Report No. 34, April 2004, WMO/TD-No. 1220, 4.23-4.24. (PDF, username science, password science)

Mironov, D., A. Terzhevik, F. Beyrich, E. Heise, and H. Lohse, 2003c: A two-layer lake model for use in numerical weather prediction. Proc. of the Baltic HIRLAM Workshop, 17-20 November 2003, St. Petersburg, Russia, 83-85. (PDF)

Mironov, D., A. Terzhevik, E. Heise, and F. Beyrich, 2003d: Parameterization of lakes in NWP: description of a lake model and single-column tests. Fifth International SRNWP-Workshop on Nonhydrostatic Modelling. Abstracts, Deutscher Wetterdienst, Geschaeftsbereich Forschung und Entwicklung, Arbeitsergebnisse Nr. 78, E. Heise and J. Steppeler, Eds., October 2003, Offenbach am Main, Germany.

Petrov, M., A. Terzhevik, N. Palshin, R. Zdorovennov, and G. Zdorovennova, 2005: Absorption of solar radiation by snow-and-ice cover of lakes. Vodnye Resursy, 32, 546-554. (in Russian; English translation: Water Resources, p. 496-504)

Petrov, M., A. Terzhevik, R. Zdorovennov, and G. Zdorovennova, 2006: The thermal structure of a shallow lake in early winter. Vodnye Resursy (Water Resources), 33, 154-162. (in Russian; English translation: Water Resources, p. 135-143)

Petrov, M., A. Terzhevik, R. Zdorovennov, and G. Zdorovennova, 2007: Water motions in a shallow ice-covered lake. Vodnye Resursy (Water Resources), 34, 113-122.

Stepanenko, V. M., 2007: Numerical Modelling of the Interaction of the Atmosphere with Inland Water Bodies. Ph.D. Thesis, Moscow State University, Scientific Research Computing Center, Moscow, Russia, 159 pp. (in Russian) (PDF, DJVU) (Abstract of thesis, 32 pp., in Russian, PDF)

Wilberforce, K., 2006: Lake Parameterisation in NWP and Climate Models. B.Sc. Thesis, Russian State Hydrometeorological University, St. Petersburg, Russia, 23 pp.

7.7 Chemistry

Alfaro, S., and L. Gomes, Modeling mineral aerosol production by wind erosion: Emission intensities and aerosol size distributions in source areas, J. Geophys. Res., 106(D16), 18,07518,084, 2001.

Baer, M., and K. Nester, Parametrization of trace gas dry deposition velocities for a regional mesoscale diffusion model, Ann. Geophys., 10, 1992.

Baldocchi, D., B. Hicks, and P. Camara, A canopy stomatal resistance model for gaseous deposition to vegetated surfaces, Atmos. Environ., 21, 1987.

Blanchard, D. C., The production, distribution, and bacterial enrichment of the sea-salt aerosol. air-sea exchange of gases and particles, p. s. liss andw. g. n. slinn, eds., d. reidel, Norwell, Mass., pp. 407454, 1983.

Erisman, J., and D. Baldocchi, Modelling dry deposition of so2 , Tellus, 46B, 159171, 1994.

Fecan, F., B. Marticorena, and G. Bergametti, Parameterization due to the increase of the aeolian erosion threshold wind friction velocity due to soil moisture for arid and semi-arid areas, Annales Geophysicae, 17, 149157, 1999.

Ganzeveld, L., and J. Lelieveld, Dry deposition parametrization in a chemistry general circulation model and its influence on the distribution of reactive trace gases., J. Geophys. Res., 100, 20,99921,012, 1995.

Garrat, J., and B. B. Hicks, Momentum, heat and water vapor transfer to and from natural and artificial surfaces., Quart. J. Roy. Meteor. Soc., 99, 680687, 1973.

Grini, A., G. Myhre, C. Zender, and I. Isaksen, Model simulation of dust sources and transport in the global atmosphere. effects of soil erodibility and wind speed variability, J. Geophys. Res., doi:10.1029/DOO4JD005037, 2005.

Hicks, B., D. Badolcchi, T. Meyers, R. Hoskers, and D. Matt, A preliminary multiple resistance routine for deriving dry deposition velocities from measured quantities, Water Air Soil Pollu., 36, 311330, 1987. Iversen, J., and B. White, Saltation threshold on earth, mars and venus, Sedimentology, 29, 111119, 1982. Kondo, J., and H. Yamazawa, Measurement of snow surface emissivity., Bound. Layer. Meteor., 34, 415 416, 1986.

Laurent, B., B. Marticorena, G. Bergametti, P. Chazette, F. Maignan, and C. Schmechtig, Simulation of the mineral dust emission frequencies from desert areas of china and mongolia using an aerodynamic roughness length map derived from polder/adeos 1 surface products, J. Geophys. Res., 110, D18S04, doi:10.1029/2004JD005013, 2005.

Marticorena, B., and G. Bergametti, Modeling of the atmospheric dust cycle: 1. design of a soil derived dust emission scheme, J. Geophys. Res., 100, 16,41516,429, 1995.

Masson, V., A physically-based scheme for the urban energy balance in atmospheric models, Boundary-Layer Meteorology, 94, 357397, 2000.

Meyers, T. P., and D. D. Baldocchi, A comparison of models for deriving dry deposition fluxes of o3 and so2 to a forest canopy., Tellus, 40B, 270284, 1988.

Monahan, E. C., C. W. Fairall, K. L. Davidson, and P. J. Boyle, Observed inter-relations between 10 m winds, ocean whitecaps and marine aerosols., Quart. J. Roy. Meteor. Soc., 109, 379392, 1983.

Muller, H., F. Meixner, G. Kramm, D. Fowler, G. J. Dollard, and M. Possanzini, Determination of hno3 deposition by modified bowen ratio and aerodynamic profile techniques., Tellus, 45B, 346367, 1993.

Schulz, M., G. deLeeuw, and Y. Balkanski, Sea-salt aerosol source functions and emissions. emissions of atmospheric trace compounds, P.A.C. Granier and C.E. Reeves, Eds., Kluwer, pp. 333359, 2004.

Sehmel, G., Particle and gas dry deposition: a review., Atmos. Environ., 14, 9811011, 1980.

Seinfeld, J., and S. Pandis, Atmospheric Chemistry and Physics, Wiley interscience pub, 1997.

Shao, Y., A model for mineral dust erosion, J. Geophys. Res., 106(D17), 20,23920,254, 2001.

Shao, Y., M. Raupach, and P.A.Findlater, The effect of saltation bombardment on the entrainment of dust by wind., J. Geophys. Res., 98, 12,71912,726, 1993.

Sheih, C., M. Wesely, and B. Hicks, Estimated dry deposition velocities of sulfur over the eastern united states and surrounding regions, Atmos. Environ., 13, 1979.

Solmon, F., C. Sarrat, D. Serca, P. Tulet, and R. Rosset, Isoprene and monoterpenes biogenic emissions in france: modeling and impact during a regional pollution episode, Atmos. Environ., 38, 38533865, 2004.

VanPul, W. A. J., and A. F. G. Jacobs, The conductance of a maize crop and the underlying soil to ozone under various environmental conditions., Bound. Layer. Meteor., 63, 8399, 1994.

Vignati, E., G. DeLeeuw, and R. Berkowicz, Modeling coastal aerosol transport and effects of surf-produced aerosols on processes in the marine atmospheric boundary layer., J. Geophys. Res., 106(D17), 20,225 20,238, 2001.

Walcek, C., R. Brost, J. Chang, and M. Wesely, So2 , sulfate and hno3 deposition velocities computed using regional landuse and meteorological data, Atmos. Environ., 20, 949964, 1996.

Walmsley., J., and M. Wesely, Modification of coded parametrizations of surface resistances to gaseous dry deposition, Atmos. Environ., 30, 11811188, 1996.

Wesely, M., Parametrizations of surface resistance to gaseous dry deposition in regional scale, numerical models, Atmos. Environ., 23, 12931304, 1989.

Wesely, M., and B. Hicks, Some factors that affect the deposition rates of sulfur dioxide and similar gases on vegetation, J. Air. Control. Assoc., 27, 11101116, 1977.

Zender, C., H. Bian, and D. Newman, The mineral dust entrainment and deposition (dead) model: Description and global dust distribution, J. Geophys. Res., 108(D14), 4416, http://dust.ess.uci.edu/dead/, 2003.

Zender, C., R. Miller, and I. Tegen, Quantifying mineral dust mass budgets: Terminology, constraints, and current estimate, Eos Trans, 85(48), 509512, 2004.

Part II

LAND USE: ECOCLIMAP

Chapter 8

Introduction

Ecoclimap is a global database of land surface parameters at 1-km resolution. It is intented to be used to initialize the soil-vegetation-atmosphere transfer schemes (SVATs) in meteorological and climate models. A first version was developed in 2003 (*Masson et al.* [2003]). A second version was developed in 2008 on Europe and is implemented into Surfex. Ecoclimap is designed to satisfy both the Surfex ”tile” approach: each grid box is made of four adjacent surfaces for nature (NAT), urban areas (TWN), sea or ocean (SEA) and lake (WAT), and the Isba ”vegetation types” structure (see tab. 8.1).

ISBA vegetation type (vegtype)	**abbreviation**
bare soil	NO
bare rock	ROCK
permanent snow	SNOW
deciduous broadleaved	TREE
needleleaved	CONI
evergreen broadleaved	EVER
C3 crops	C3
C4 crops	C4
irrigated crops	IRR
temperate grassland	GRAS
tropical grassland	TROG
wetlands, parks and gardens	PARK

Table 8.1: The 12 ISBA vegetation types

It consists first of a global land cover map at 1/120°resolution that is directly read by Surfex. This map proposes a set of classes (or covers) which represent homogeneous ecosystems. Secondly, Surfex interprets these covers in terms of tiles and vegetation types. Land surface parameters (see tab. 8.2 and tab. 8.3 for the list of parameters) depend on tiles, vegetation types and on covers for some of them. A mechanism of aggregation is used to compute the surface parameters for each grid point, according to the horizontal resolution, by combining land covers defined over the 4 tiles and represented by a fraction of the 12 vegetation types (table 8.1) obtained from the 1km resolution land cover map.

In the first version of Ecoclimap, two hundred and fifteen ecosystems were obtained by combining existing

land cover and climate maps, in addition to using Advanced Very High Resolution Radiometer (AVHRR) satellite data. Then, all surface parameters were derived for each of these ecosystems using lookup tables with the annual cycle of the leaf area index (LAI) being constrained by the AVHRR information. The second version uses more recent existing land cover maps. Moreover, ecosystems are now built through an automatic classification process applied on normalized difference vegetation index (NDVI) seven-years time series from SPOT/VEGETATION satellite data, more precise than AVHRR. Existing land cover maps give starting classes which are split in clusters by the classification process. Then, surface parameters are still derived using lookup tables but the annual cycle of the LAI stems from MODIS satellite data. It's possible to run Surfex with LAI values averaged on available years or to choose one particular year.

surface parameter	**abbreviation**	associated tile
leaf area index	LAI	nature (monthly)
height of trees	HT	nature
first soil depth	DG1	nature
root depth	ROOT_DEPTH / DG2	nature
total soil depth	GROUND_DEPTH / DG3	nature
town roughness length	Z0_TOWN	town
albedo of roofs, roads, walls	ALB_ROOF, ALB_ROAD, ALB_WALL	town
emissivity of roofs, roads, walls	EMIS_ROOF, EMIS_ROAD, EMIS_WALL	town
heat capacity of roofs, roads, walls (*3 layers)	HC_ROOF*3, HC_ROAD*3, HC_WALL*3	town
thermal conductivity of roofs, roads, walls (*3 layers)	TC_ROOF*3, TC_ROAD*3, TC_WALL*3	town
width of roofs, roads, walls (*3 layers)	D_ROOF*3, D_ROAD*3, D_WALL*3	town
buildings height	BLD_HEIGHT	town
building shape	WALL_O_HOR	town
building fraction	BLD	town
canyons shape	CAN_HW_RATIO	town
anthropogenic sensible heat fluxes due to traffic, due to factory	 H_TRAFIC, H_INDUSTRY	town
anthropogenic latent heat fluxes due to traffic, due to factory	 LE_TRAFIC, LE_INDUSTRY	town
seeding date	SEED	nature
reaping date	REAP	nature
water supply quantity	WATSUP	nature
flag for irrigation	IRRIG	nature
vegetation fraction	VEG	nature (monthly)
dynamical vegetation roughness length	Z0	nature (monthly)
emissivity	EMIS	nature (monthly)
ratio of z0 for momentum and heat	Z0_O_Z0H	nature

Table 8.2: Surface parameters given by Ecoclimap (1/2)

surface parameter	abbreviation	associated tile
near infrared albedo	ALBNIR_VEG	nature
visible albedo	ALBVIS_VEG	nature
UV albedo	ALBUV_VEG	nature
minimum stomatal resistance	RSMIN	nature
coefficient for the calculation of the surface stomatal resistance	GAMMA	nature
coefficient for maximum water interception storage on capacity on the vegetation	WRMAX_CF	nature
maximum solar radiation usable in photosynthesis	RGL	nature
vegetation thermal intertia coefficient	CV	nature
mesophyll conductance	GMES, GMES_ST	nature (AGS)
ecosystem respiration parameter	RE25	nature (AGS)
cuticular conductance	GC, GC_ST	nature (AGS)
critical normalized soil water content for stress parameterisation	F2I	nature (AGS)
ratio d(biomass)/d(LAI)	BSLAI, BSLAI_ST	nature (AGS)
maximum air saturation deficit tolerated by vegetation	DMAX, DMAX_ST	nature (AGS)
vegetation response type to water stress (true: defensive false: offensive)	STRESS	nature (AGS)
e-folding time for senescence	SEFOLD, SEFOLD_ST	nature (AGS)
minimum LAI	LAIMIN	nature (AGS)
leaf area ratio sensitivity to nitrogen concentration	CE_NITRO	nature (AGS)
lethal minimum value of leaf area ratio	CF_NITRO	nature (AGS)
nitrogen concentration of active biomass	CNA_NITRO	nature (AGS)
root extinction	ROOT_EXTINCTION	nature
ponderation coefficient between root fractions formulations	ROOT_LIN	nature
coefficient for SO2 deposition	SOILRC_SO2	nature
coefficient for O3 deposition	SOILRC_O3	nature
cumulative root fraction	CUM_ROOT_FRAC	nature
biomass/LAI ratio from nitrogen declin theory	BSL_INIT_NITRO	nature

Table 8.3: Surface parameters given by Ecoclimap (2/2)

Chapter 9

Ecoclimap characteristics

9.1 Surface parameters definition

Parameters listed in tab. 8.2 and 8.3 are initialized:

- by cover and vegetation types for LAI, HT, DG (3 layers), SEED, REAP, WATSUP, IRRIG. Indeed, these parameters are not only a feature of a given vegetation type but also of regional considerations;
- by vegetation type for other natural parameters. They are thus viewed as depending on the vegetation type only and not on the location;
- by cover for town parameters: the ”town” tile is not subdivided in types like the ”nature” tile.

Some of the natural parameters receive immediate values whereas others are calculated from some of the former. Tab. 9.1 and tab. 9.2 give modes of obtaining of the natural parameters (lines), by vegetation type (columns). Report to tab. 8.1 to get the meaning of abbreviations of parameters names.
Tab 9.3 delivers values for urban parameters, by type of class. Types of Ecoclimap urban classes come from the Corine Land Cover (CLC) classification that is considered in the two versions of Ecoclimap (see tab. 9.4 for the correspondence).
All these values and formulas date from Ecoclimap-I and come from previous studies. Part of them are mentionned and detailed in *Masson et al.* [2003], other can be found in literature.

9.2 Aggregation method

The aggregation of parameters assumes two aspects:

- the aggregation in ”patchs” of several vegetation types;
- the geographic aggregation linked to the spatial resolution.

Indeed, the Surfex user can choose to work with a number of 1 to 12 patchs of vegetation types. Tab. 9.5 gives the combinations of vegetation types according to the retained number of patches: numbers associated to vegetation types (columns) correspond to patchs to which they are attached, depending on the total number of patches (lines and left column). The Surfex user also chooses his own spatial resolution whose maximum is this of Ecoclimap: 1/120°. When the chosen resolution is coarser, parameters by grid point take aggregated values from the 1-km ones.

The common method for these two kinds of aggregation is nearly linear, apart from the fact that some particular averages are applied to several parameters (see tab. 9.6 for more details) : contributions of every vegetation type to each gridpoint and each patch are weighted and added, next the total value in one point and one patch is brought back to the total number of contributions, that is the total weight, providing the wanted average value of the parameter. As seen in tab. 10.1, weights vary with parameters, depending on the surface on which they make sense.

9.3 Writing of parameters in a latex file

Distribution of classes among tiles and vegetation types, also values of surface parameters are described in a tex file called *class_cover_data.tex*. It can be compiled to get a ps or pdf file that recapitulates all these values in different arrays.

parameter	NO	ROCK	SNOW	TREE	CONI	EVER
LAI	from satellite data by cover and vegetation type					
HT	by cover and vegetation type					
DG1	by cover and vegetation type					
DG2	by cover and vegetation type					
DG3	by cover and vegetation type					
SEED	by cover and vegetation type					
REAP	by cover and vegetation type					
WATSUP	by cover and vegetation type					
IRRIG	by cover and vegetation type					
VEG	0.			0.95	0.95	0.99
GREEN	0.			$MIN(1-e^{-0.5*LAI}, 0.95)$		0.99
Z0	0.1	1.	0.01	HT	HT	HT
EMIS	$VEG*0.97+(1-VEG)*0.94$		1.	$VEG*0.97+(1-VEG)*0.94$		
Z0_O_Z0H	10.					
ALBNIR_VEG	0.3	0.3	0.3	0.25	0.15	0.21
ALBVIS_VEG	0.1	0.1	0.1	0.05	0.05	0.05
ALBUV_VEG	0.06	0.06	0.06	0.525	0.0425	0.038
RSMIN	40.	40.	40.	150.	150.	250.
GAMMA	0.	0.	0.	0.04	0.04	0.04
WRMAXCF	0.2	0.2	0.2	0.1	0.1	0.1
RGL	100.	100.	100.	30.	30.	30.
CV	$2E^{-5}$	$2E^{-5}$	$2E^{-5}$	$1E^{-5}$	$1E^{-5}$	$1E^{-5}$
GMES	0.02	0.02	0.02	0.001	0.001	0.001
GMES_ST	0.003	0.003	0.003	0.003	0.002	0.002
RE25	$3E^{-7}$	$3E^{-7}$	$3E^{-7}$	$3E^{-7}$	$1E^{-7}$	$3E^{-7}$
GC	0.00025	0.00025	0.00025	0.00015	0.	0.00015
GC_ST	0.00015	0.00015	0.00015	0.00015	0.	0.00015
F2I	0.3	0.3	0.3	0.3	0.3	0.3
BSLAI	0.36	0.36	0.36	0.25	0.25	0.25
BSLAI_ST	0.08	0.08	0.08	0.125	0.50	0.25
DMAX	0.1	0.1	0.1	0.1	0.1	0.1
DMAX_ST	0.05	0.05	0.05	0.109	0.124	0.124
STRESS	1.	1.	1.	0.	1.	0.
SEFOLD	90.*XDAY			365.*XDAY		
SEFOLD_ST	150.*XDAY			230*XDAY	365.*XDAY	
LAIMIN	0.3	0.3	0.3	0.3	1.	1.
CE_NITRO	7.68	7.68	7.68	4.83	4.85	4.83
CF_NITRO	-4.33	-4.33	-4.33	2.53	-0.24	2.53
CNA_NITRO	1.3	1.3	1.3	2.	2.8	2.5
ROOT_EXTINCTION	0.961	0.961	0.961	0.966	0.943	0.962
ROOT_LIN	0.05	0.05	0.05	0.05	0.05	0.05
SOILRC_SO2	1000.	400.	100.	500.	500.	200.
SOILRC_O3	400.	200.	3500.	200.	200.	500.
CUM_ROOT_FRAC	$ROOT\_LIN*MIN(\frac{DG}{DG2}, 1.)+(1-ROOT\_LIN)*\frac{(1-ROOT\_EXT.)^{DG*100.}}{(1-ROOT\_EXT.)^{DG2*100.}}$					
BSL_INIT_NITRO	$1./(CE\_NITRO+CNA\_NITRO+CF\_NITRO)$					

Table 9.1: Lookup tables for Ecoclimap natural parameters, by vegetation type (1/2)

parameter	C3	C4	IRR	GRAS	TROG	PARK
LAI	from satellite data by cover and vegetation type					
HT	by cover and vegetation type					
DG1	by cover and vegetation type					
DG2	by cover and vegetation type					
DG3	by cover and vegetation type					
SEED	by cover and vegetation type					
REAP	by cover and vegetation type					
WATSUP	by cover and vegetation type					
IRRIG	by cover and vegetation type					
VEG	$1-e^{-0.6*LAI}$			0.95	0.95	0.95
GREEN	$1-e^{-0.6*LAI}$			$MIN(1-e^{-0.6*LAI}, 0.95)$		
Z0	$MIN(1., e^{(LAI-3.5)/1.3})$	$MIN(2.5, e^{(LAI-3.5)/1.3})$		$LAI/6$		
EMIS	$VEG*0.97+(1-VEG)*0.94$					
Z0_O_Z0H	10.					
ALBNIR_VEG	0.3	0.3	0.3	0.3	0.3	0.3
ALBVIS_VEG	0.1	0.1	0.1	0.1	0.1	0.1
ALBUV_VEG	0.06	0.06	0.045	0.08	0.125	0.045
RSMIN	40.	120.	40.	40.	120.	40.
GAMMA	0.	0.	0.	0.	0.	0.
WRMAXCF	0.2	0.2	0.2	0.2	0.2	0.2
RGL	100.	100.	100.	100.	100.	100.
CV	$2E^{-5}$	$2E^{-5}$	$2E^{-5}$	$2E^{-5}$	$2E^{-5}$	$2E^{-5}$
GMES	0.003	0.003	0.003	0.02	0.02	0.02
GMES_ST	0.001	0.009	0.009	0.001	0.006	0.006
RE25	$3E^{-7}$	$2.5E^{-7}$	$3E^{-7}$	$3E^{-7}$	$3E^{-7}$	$3E^{-7}$
GC	0.00025	0.00025	0.00025	0.00025	0.00025	0.00025
GC_ST	0.00025	0.00015	0.00015	0.00025	0.00015	0.00025
F2I	0.3	0.3	0.3	0.3	0.3	0.3
BSLAI	0.06	0.06	0.06	0.36	0.36	0.36
BSLAI_ST	0.06	0.06	0.06	0.08	0.08	0.08
DMAX	0.1	0.1	0.1	0.1	0.1	0.1
DMAX_ST	0.05	0.033	0.033	0.05	0.052	0.05
STRESS	1.	0.	1.	0.	0.	0.
SEFOLD	60.*XDAY			90.*XDAY		
SEFOLD_ST	150.*XDAY					
LAIMIN	0.3	0.3	0.3	0.3	0.3	0.3
CE_NITRO	3.79	7.68	7.68	5.56	7.68	5.56
CF_NITRO	9.84	-4.33	-4.33	6.73	-4.33	6.73
CNA_NITRO	1.3	1.9	1.9	1.3	1.3	1.3
ROOT_EXTINCTION	0.961	0.972	0.961	0.943	0.972	0.943
ROOT_LIN	0.05	0.05	0.05	0.05	0.5	0.5
SOILRC_SO2	150.	150.	0.001	350.	350.	100.
SOILRC_O3	150.	150.	1000.	200.	200.	700.
CUM_ROOT_FRAC	$ROOT\_LIN*MIN(\frac{DG}{DG2}, 1.)+(1-ROOT\_LIN)*\frac{(1-ROOT\_EXT.)^{DG*100.}}{(1-ROOT\_EXT.)^{DG2*100.}}$					
BSL_INIT_NITRO	$1./(CE\_NITRO+CNA\_NITRO+CF\_NITRO)$					

Table 9.2: Lookup tables for Ecoclimap natural parameters, by vegetation type (2/2)

parameter	**151**	**152**	**155**	**156**	**157**	**158**	**159**	**160**	**161**
ALB_ROOF	0.15								
ALB_ROAD	0.25								
ALB_WALL	0.08								
EMIS_ROOF	0.90								
EMIS_ROAD	0.94								
EMIS_WALL	0.85								
HC_ROOF(1)	$2.11E^6$								
HC_ROOF(2)	$0.28E^6$								
HC_ROOF(3)	$0.29E^6$								
HC_ROAD(1)	$1.94E^6$								
HC_ROAD(2)	$1.28E^6$								
HC_ROAD(3)	$1.28E^6$								
HC_WALL(1)	$1.55E^6$								
HC_WALL(2)	$1.55E^6$								
HC_WALL(3)	$0.29E^6$								
TC_ROOF(1)	1.51								
TC_ROOF(2)	0.08								
TC_ROOF(3)	0.05								
TC_ROAD(1)	0.7454								
TC_ROAD(2)	0.2513								
TC_ROAD(3)	0.2513								
TC_WALL(1)	0.9338								
TC_WALL(2)	0.9338								
TC_WALL(3)	0.05								
D_ROOF(1)	0.05								
D_ROOF(2)	0.4								
D_ROOF(3)	0.1								
D_ROAD(1)	0.05								
D_ROAD(2)	0.1								
D_ROAD(3)	1.								
D_WALL(1)	0.02								
D_WALL(2)	0.125								
D_WALL(3)	0.05								
Z0_TOWN	3.	1.	2.	0.5	2.	0.01	0.1	0.5	1.
BLD_HEIGHT	30.	10.	20.	5.	20.	10.	5.	5.	10.
WALL_O_HOR	1.	0.5	0.5	0.5	1.	0.5	0.5	0.5	1.
BLD	0.5	0.5	0.5	0.1	0.5	0.1	0.1	0.1	0.5
CAN_HW_RATIO	$0.5 * \frac{WALL\_O\_HOR}{1-BLD}$								
H_TRAFIC	20	10.	10.	30.	10.	10.	0.	0.	0.
H_INDUSTRY	10.	5.	20.	0.	20.	0.	0.	0.	0.
LE_TRAFIC	0.	0.	0.	0.	0.	0.	0.	0.	0.
LE_INDUSTRY	0.	0.	0.	0.	0.	0.	0.	0.	0.

Table 9.3: Lookup tables for Ecoclimap urban parameters, by cover

cover name	cover(s) number(s)
dense urban	151
suburban	152,153,154,7
industries and commercial areas	155
road and rail networks	156
port facilities	157
airport	158
mineral extraction and construction sites	159
urban parks	160
sport facilities	161

Table 9.4: Ecoclimap covers numbers for urban classes

patchs	NO	ROCK	SNOW	TREE	CONI	EVER	C3	C4	IRR	GRAS	TROG	PARK
1	1	1	1	1	1	1	1	1	1	1	1	1
2	1	1	1	2	2	2	1	1	1	1	1	1
3	1	1	1	2	2	2	3	3	3	3	3	3
4	1	1	1	2	2	2	3	3	3	4	4	4
5	1	1	1	2	2	2	3	3	4	5	5	4
6	1	1	1	2	2	2	3	3	4	5	5	6
7	1	1	2	3	3	3	4	4	5	6	6	7
8	1	1	2	3	3	3	4	5	6	7	7	8
9	1	1	2	3	4	3	5	6	7	8	8	9
10	1	1	2	3	4	5	6	7	8	9	9	10
11	1	2	3	4	5	6	7	8	9	10	10	11
12	1	2	3	4	5	6	7	8	9	10	11	12

Table 9.5: Combinations of vegetation types according to the retained number of patchs in Surfex

averaging type	name	added element	averaging	affected parameters
ARI	arithmetic	X	Σ/Γ	every but...
INV	inverse	$1./X$	Γ/Σ	RSMIN, CV, HC_ROOF, HC_ROAD, HC_WALL
CDN	inverse of square logarithm	$1./LN(DZ/X)^2$ with DZ height of the first model mass level if available and 20m otherwise	$DZ * e^{-\sqrt{\Gamma/\Sigma}}$	Z0, Z0_TOWN
MAJ	dominant date	no addition: the most frequently occurrent date is selected	none	SEED, REAP

Table 9.6: Averaging types and associated parameters in Ecoclimap. X is a single value of the parameter to average; Σ represents the total of the added weighted elements; Γ represents the total weight of the added weighted elements.

type of weight	**name**	**value**	**associated parameters**
ALL	all	1.	fractions of tiles NAT,TWN,SEA,WAT
NAT	nature	fraction of tile ”nature” (* fraction of added vegtype)	fractions of vegtypes, VEG, Z0, Z0_O_Z0H, EMIS, DG, CUM_ROOT_FRAC, RE25
TRE	tree	fraction of tile ”nature” * (either) fraction of vegtype TREE *(or) fraction of vegtype CONI *(or) fraction of vegtype EVER (non-zero only for trees vegtypes)	HT, DMAX_ST, DMAX
LAI	LAI	fraction of tile ”nature” * fraction of added vegtype * associated LAI value	RSMIN
VEG	fraction of vegetation	fraction of tile ”nature” * fraction of added vegtype * associated VEG value	all remaining natural parameters
TWN	town	fraction of tile ”town”	every town parameter but...
BLD	building	fraction of tile ”town” * fraction of building BLD	ALB_ROOF, EMIS_ROOF, HC_ROOF, TC_ROOF, D_ROOF, ALB_WALL, EMIS_WALL, HC_WALL, TC_WALL, D_WALL, WALL_O_HOR
STR	street	fraction of tile ”town” * (1.-fraction of building BLD)	ALB_ROAD, EMIS_ROAD, HC_ROAD, TC_ROAD, D_ROAD

Table 9.7: Weighting functions and associated parameters in Ecoclimap. Parenthesis indications in the ”value” column refer to what happens in case of calculation defined by patch, ie for all natural parameters but neither for the fractions of tiles and vegetation types nor for the town parameters.

Chapter 10

Ecoclimap-II realization

Ecoclimap-II has been developed on a European field. Its limits are 11W and 62E in longitude and 25N and 75N in latitude.

10.1 The Ecoclimap-II map

10.1.1 The initial map

Existing land cover maps taken into account in this development are:

- Global Land Cover 2000 (GLC2000)[1];
- Corine Land Cover 2000 (CLC2000)[2];

GLC2000 was built from daily SPOT/VEGETATION satellite data for year 2000 (dataset VEGA2000). The spatial resolution is 1/112° (corresponding to $\sim$1.1km) and the projection is latlon. Several regional maps and a global map of 23 classes exist. The latter global map is taken as a basis and classes from available regional maps are added when relevant.
Then, CLC2000 covers only a part of the domain (political Europe) and includes 44 classes. It was realized by photo-interpretation of SPOT and LANDSAT satellite images. The projection is Lambert's azimuthal equivalent and the resolution is 100m. In order to fit Ecoclimap, Corine data are reprojected and brought back to the same resolution. In these conditions, the Corine class number attributed to the pixel at 1-km resolution is this of the most numerous class into the pixel. It's decided to introduce majority classes at more than 70% in the map under construction. It happens that 55% of Corine pixels are kept by this way. So-obtained Corine pixels have priority on GLC information because their contents is better known and supposed to characterize more homogeneous ecosystems.
The resulting map comprises classes from several origins and potentially complementary: their headings and geographic distribution give indications to melt some of them. After a couple of such combinations, a 76-covers map (called **C76** from now on) is finally obtained on the considered area. This map is the reference used for the further classification process. It's thus a mix of GLC2000 and CLC2000.

[1] http://www-gvm.jrc.it/glc2000
[2] http://www.ifen.fr, http://www.eea.eu.int

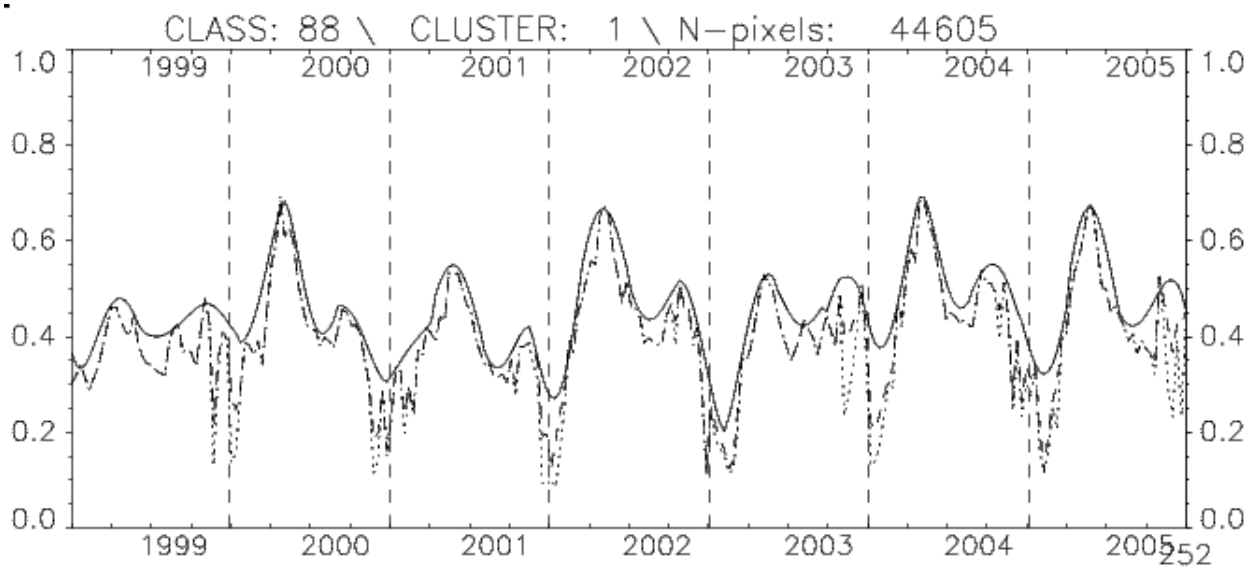

Figure 10.1: Example of NDVI profiles: rough (dotted), masked (dashed), smoothed (solid). (A technical error led to NDVI values overestimated of 0.09 but it has no impact on classification which is relative).

10.1.2 NDVI satellite data

NDVI is deduced from B2 (red) and B3 (near infrared) satellite normalized reflectances (ratios of the reflected over the incoming radiation in each spectral band) according to the formula:

$$NDVI = \frac{B3 - B2}{B3 + B2} \qquad (1)$$

This rate usually ranges from 0 to 1. Negative values indicate the presence of snow. Works have shown a correlation between NDVI values and the vegetation photosynthesis activity. The LAI and NDVI annual cycles are supposed to be correlated. In Ecoclimap-I, LAI profiles by cover were obtained from NDVI through the formula:

$$LAI(t) = LAI_{min} + (LAI_{max} - LAI_{min}) * \frac{NDVI(t) - NDVI_{min}}{NDVI_{max} - NDVI_{min}} \qquad (2)$$

LAI_{min} and LAI_{max} being set from in-situ measurements or empirically following ISBA simulations. Then, LAI profiles by vegetation types (inside covers) are deduced from these LAI by cover thanks to simple rules, mostly by changing extreme values of the cycle (LAI_{min} and LAI_{max}) depending on the vegetation height in the formula (2), sometimes looking for ”pure” near ”mixte” covers and giving ”pure” LAI to vegetation types in mixte covers. Note that for the NO, ROCK and SNOW vegetation types LAI profiles are equal to zero.

In Ecoclimap-II, NDVI satellite data come from SPOT/VEGETATION[3]. They are decadal, at true 1-km resolution, that is to say that, contrary to AVHRR, one pixel signal is theorically not contaminated by pixels around. Data range from 1999, january to 2005, december.
They are delivered with a mask encoded on 8 bits: 2 bits represent the situations: clear sky, shadow, uncertain, cloud; 1 bit for snow and ice, 1 bit for the land sea mask, and the 4 last bits for the quality of the 4

[3]http://free.vgt.vito.be/, http://www.spot.vegetation.com

satellite radiometric bands. This mask is applied in order to keep clear sky pixels for which the quality of bands B2 (red) and B3 (near infrared) is good. The land/sea/snow distinction is set by to the classification.
The plots of NDVI mean profiles for the covers of the C76 map show that data, even if cleared from aberrant values by the mask, remain noisy. That's why a smoothing is realized at the upper envelope of the rough curve because highest values are supposed better because atmospheric parameters (clouds, water vapor, aerosols) are likely to attenuate the signal reflected to the satellite. Anyway the work on NDVI time series is relative and the exact NDVI values don't matter. The smoothing is based on a 4-degree polynomial. The figure 10.1 shows effects of the mask and smoothing on the mean NDVI signal for a given class. The distance between the rough and the smoothed curves is relative to this mean: the smoothing is done pixel by pixel, filtering out low values entering the mean in the rough case.

10.1.3 The automatic classification process

The classification algorithm is **k-means**. It consists in reading the NDVI profiles of all pixels of one class, then of gathering closest profiles according to the Euclidian distance. Initial center-profiles of clusters are randomly defined and successive iterations are performed: each pixel is linked to the most like-looking center-profile; centers of clusters are recalculated; pixels are linked to the most like-looking center-profile again, and so on. It's thus necessary to fix from the beginning the number of wished clusters by class.
A first map is realized by setting high numbers of clusters by classes, then looking at NDVI profiles and geographic positions of the clusters, and setting new lower numbers of clusters, until a satisfying classification is obtained. This first map comprises 464 classes and is called **C464**.
However, for practical purposes, this method poses several problems:

- When each class of C76 is split into several clusters, the total number of classes increases very fast, rendering reading, interpretation and processing hard;
- it boils down to consider initial classes as frozen and separated each from one another, what can prove false, notably with various initial maps;
- the continuity of analysis is compromised and the quality of NDVI as classification criterion is hard to evaluate. Moreover, numbers of clusters have no option but being arbitrarily posed.

Owing to all these reasons, NDVI is no longer used as a secondary classification criterion: it's admitted that it can rival the initial C76 classes boundaries. Moreover, three quantities are now taken into account during the NDVI classification:

- the Euclidian distance between profiles (still);
- the correlation between profiles, focusing on the shapes of profiles;
- a criterion mixing the two precedents: $\frac{euclidian\ distance}{correlation^2}$, outlining the shapes of profiles without neglecting the distance between them.

The principle is to gather profiles using a threshold for one or the other of the latter criterions. Other conditions come then into the picture:

- the size of classes: for example, the threshold is looser for smaller classes, in order not to encourage the formation of low pixels number classes;
- the NDVI maximum: as NDVI is the expression of vegetation activity, it's not relevant with low-vegetated areas, also low NDVI maximum areas;

- the cover type: water, town and bare soil pixels can't be distinguished through the NDVI, they have to conform the initial nomenclature.

Lastly, comparisons are conducted:

- between profiles of clusters and classes they come from: if the cluster is closer to another class than the one it comes from, it can be linked to the former class;

- families of classes are formed, then splited in a number of clusters equal to the number of classes constituing them, through the automatic classification. Clusters obtained by this totally automatic means are compared to initial classes, in order to verify the robustness of the first method through it consistency with the second one.

At each step, the geographic position, the contents of classes according to the initial nomenclature, NDVI profiles and standard deviations are observed. These operations allow a better approach of the NDVI time series, adapting to the different types of covers and ensuring more mixing and flexibility than if initial boudaries between classes were perfectly respected and if the strict k-means method was applied. At this point, the map under construction comprises 257 classes and is called **C257**.

10.1.4 To the resulting map

Several means are added to complete the new map realization:

- C257 is compared with the map realized by purely respecting the classes boundaries, C464. Every class of each map is splited into 5 clusters through the automatic classification. The distance, the correlation and the standard deviation between each cluster and its mother-class are calculated. Maximum, minimum and median of these quantities are compared for C257 and C464. Results are equivalent whereas the total numbers of classes clearly vary between the two maps.

- C257 is compared to C76. C76 covers are grouped into 14 general types, close to ISBA vegetation types. Then, each C257 class is divided in its contributions to the latter 14 types. Associated NDVI profiles are plotted; geographic distribution of so-obtained clusters is also examined. These operations aim at verifying that mixing of initial classes produce consistent and acceptable results.
  First, given the high resemblance of NDVI profiles of some classes, pixels from a class corresponding to a type (among the 14) that is neither its first nor its second prevailing are moved to a class where the considered type prevails, provided that the resemblance between the two classes is sufficient (on NDVI profiles). The $\frac{distance}{correlation^2}$ criterion is used with a threshold: the moving occurs if the criterion is lower than 1., provided that the correlation is positive and higher than 0.9. This operation allows to considerably reduce the distance between C76 and C257 in terms of nomenclature. It's also verified that geographically gathered parts of land are not contradictory. Results are satisfying. Lastly, on a case by case basis, couple of last reshapings are done. The C257 map becomes at this point **C271** (with 271 classes).

- NDVI profiles are plotted for only part of the pixels of classes. They are plotted for french pixels and on several specialized classes coming from CLC2000: vineyards, orchards, rice fields, olive groves. The goal is to check that those pixels, often melted in larger classes, haven't a very particular behaviour that would have been flooded during the classification. This process leads to add still 2 classes of vineyards. The final resulting map comprises 273 classes and is called **C273**.

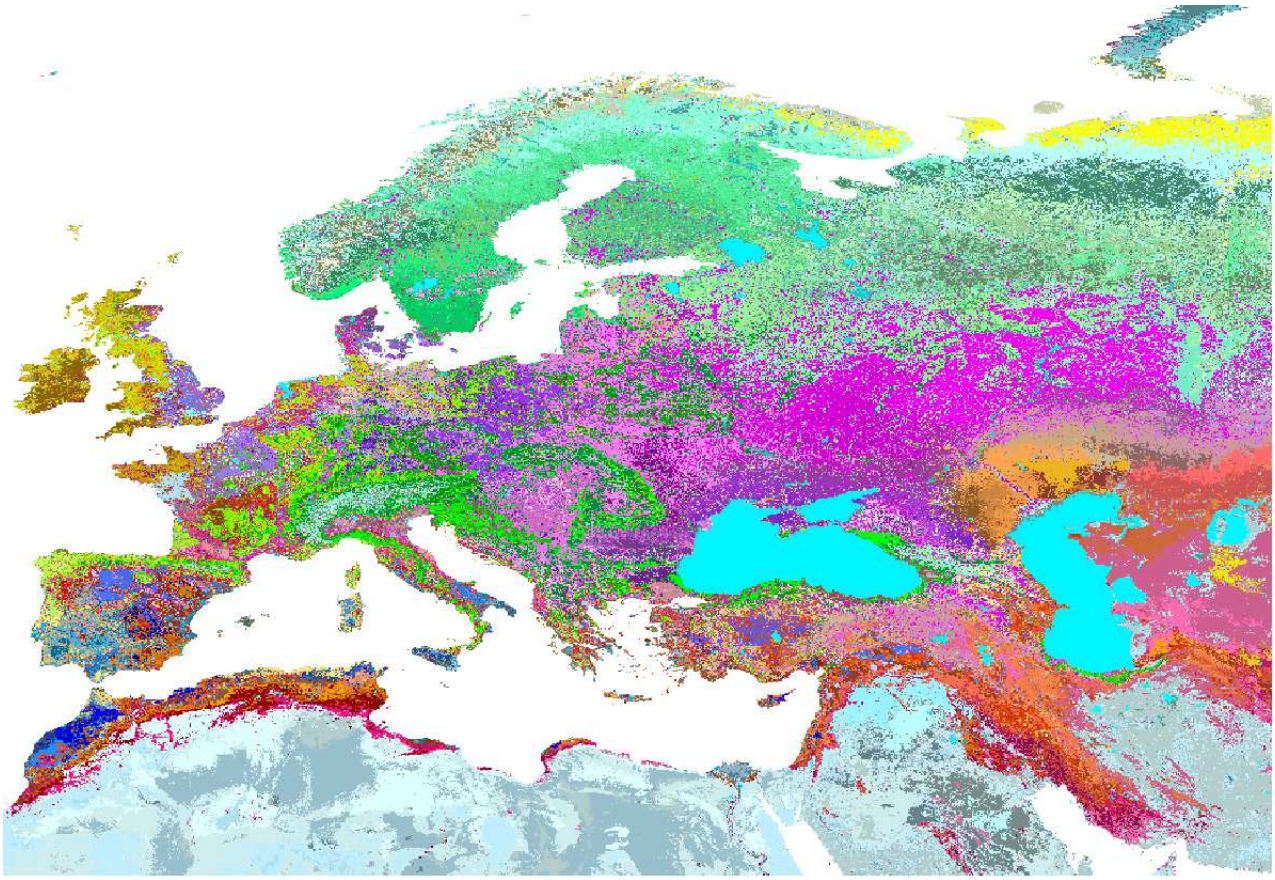

Figure 10.2: Ecoclimap-II C273 map on Europe (one color by class) (latlon projection)

To conclude, the Ecoclimap-II map comprises 273 classes (see fig. 10.2 for an illustration). The classification process combines both an automatic k-means algorithm on NDVI seven-years time series from SPOT/VGT and a more or less leaning constraint provided by an initial map built from existing land cover maps that are CLC2000 and GLC2000. The nomenclature of this map serves to contain the automatic classification and avoid the emergence of incoherent classes.
Note also that the use of seven-years time series data induces that the inter-annual variability is taken into account during the classification process.

10.1.5 Short description of covers

To summarize, it can be said that:

- Distribution of forests over the domain is quite linear and progressive, either on the geographic or on the NDVI profiles sides. The evolution follows a north-east to south-west axis.
- Crops are very regionalized, in areas with well-marked outlines; they doesn't seem to follow a strictly natural logic. Indeed, the human intervention plays a role for these kinds of covers.
- Distribution of shrubs and meadows is intermediate between forests and crops.
- Concerning bare land, snow, inland water and urban areas, resulting classes are very close to those of the initial map C76. Indeed, the NDVI classification doesn't allow to discriminate such types of

covers. However, the analysis of NDVI profiles is efficient to separate pure pixels from mixed ones, and to classify areas functions of the vegetation part of mixed ones. Nevertheless, maintaining such distinctions generates a very important amount of classes. That's why only few of these nuances are really integrated in C273, much with bare land and snow, just a little with inland water, not at all with urban areas. It could be interesting in the future to study the relevance of such distinctions.

Generally, ecosystems are rather homogeneous on large areas in the north continental, and very mixed in the mediterranean perimeter.

For practical purposes, it can be noted that classes are numbered from 301 to 573; sea and oceans present in the European domain take the number 1 from Ecoclimap-I.

10.2 Translation of covers in tiles and vegetation types

The next step is to define every new cover as a linear combination of the 4 tiles (types of surface) and the 12 vegetation types (inside the "nature" tile). The available sources are following:

- (a) Nomenclatures at 1-km resolution from CLC2000, GLC2000 (world, Europe, North Eurasia, Asia, Africa), Ecoclimap-I, C76 (initial map for the classification, see 10.1.1);
- (a)' The nomenclature at 100m resolution from CLC2000;
- (b) Agricultural statistics from Agreste on France, expressed in hectares, available department by department, since 1989. They comprise details about the types of crops;
- (c) a global map about the distribution of C4 vegetation, at 1-degree resolution, provided within the framework of ISLSCP2 and dating from 2003;
- (d) estimates of farm produce by european state, from the FAO;
- (e) data on the maize production by european country in 2003, available on website Maïsadour, in thousands of hectares.

The method is then the following:

- (a) each Ecoclimap-II cover is broken up among classes of considered other maps. Percentages of representation of the second in the first are listed and associated to the titles of the corresponding nomenclatures. The total percentage of the Ecoclimap-II cover in the considered map is indicated (in the case of Corine and GLC regional tiles, only a part of the domain is concerned).
- (b) For AGRESTE, department by department, quantities of forests, meadows, C3 crops, C4 crops, permanent crops and other types of covers are calculated. Values are averaged on the 1999-2006 spell of time. Resulting curves are plotted and overlain with the associated Ecoclimap-II curves, functions of the way of repartition of the covers in the 12 vegetation types.
- (c) The Ecoclimap-II C4 map is resampled at 1-degree resolution in order to compare with the ISLSCP2 map.
- (d) (e) The FAO and Maïsadour estimates haven't been exploited yet.

If the class is included in the CORINE area at more than 50%, the CORINE 100-m information is favoured, instead of 1-km nomenclatures. Amounts of C4, C3, meadows, forests, permanent crops are calibrated thanks to the AGRESTE curves, for well-represented classes on France. The ISLSCP2 map allows to give an idea about the C4 distribution outside France. Note that Agreste provides informations on irrigated surfaces that haven't been exploited yet.

10.3 Initialization of LAI profiles and other parameters

In Ecoclimap, as seen in tab. 9.1 and tab. 9.2, several parameters are initialized at the cover level.

10.3.1 Initialization of heights of trees, ground depths, irrigation and town parameters

First of them, heights of trees are set by using Ecoclimap-I values and the compositions of Ecoclimap-II covers into other nomenclatures (GLC, CLC, Ecoclimap-I). Concerning shrubs classes, a distinction is done between meadows and low-level trees.
Then, the ground depths are set by using exclusively the Ecoclimap-I information, the only available.
These two last parameters would gain by benefiting from other sources of information.
Then, the vegetation type "irrigated crops" is arbitrarily considered as composed of C4 crops only. In Surfex, the modelling of irrigation passes by four parameters (cf tab. 8.2): SEED, REAP, WATSUP and IRRIG. In Ecoclimap-I, by default these variables take constant values that are respectively: 10/05, 01/08, 30 and 1. In Ecoclimap-II, these default values are kept and defined as soon as the "irrigated crops" fraction is not null. It would be worth leaning on these values and precise them according to the classes.
Lastly, town parameters don't change in Ecoclimap-II: Ecoclimap urban classes are the same in the two versions and come directly from the CLC nomenclature.

10.3.2 Initialization of LAI

The LAI (Leaf Area Index) is defined as the ratio of total upper leaf (or needle) surface of vegetation divided by the surface area of the land on which the vegetation grows. The effective LAI seen by the satellite is not the same as the in-situ LAI used by ISBA: the latter is measured on the whole thickness of the vegetation whereas the satellite sees only the top of canopy and deduces the LAI by more or less performing algorithms. It notably often causes saturations for high LAI.

LAI by cover

Two satellite LAI have been examined for Ecoclimap-II: CYCLOPES (SPOT/VEGETATION) and MODIS. Algorithms leading from the satellite bands to the LAI are complex. Land cover maps are included, and the 7 satellite bands (in the case of SPOT) are used. CYCLOPES data range from 2000, January to 2004, December; MODIS data from 2000, March to 2006, December. As for the NDVI (see 10.1.2), a smoothing by pixel at the upper envelop of the LAI profiles is performed. This smoothing is debatable because it makes average LAI values by class very higher than these of rough LAI.
MODIS LAI, CYCLOPES LAI and SPOT/VGT NDVI are plotted by cover so as to be compared. The three products are quite correlated, but MODIS LAI values tend to be higher on forests. Given that MODIS LAI time series are longer and that higher values on forests seem more realistic, MODIS LAI are kept for Ecoclimap-II. Nonetheless, preconceptions relative to the smoothing could lead in the future to review this LAI and its range of values in particular, all the more because tests of smoothing with varying parameters give clearly different results.

Moreover, there is a mask with MODIS data that distinguishes not classed data, built areas, wetlands and marshes, permanent snow, ice and tundra, bare soil or sparse vegetation areas, inland water, missing data. These masked values can be interpolated in the time series, excluded or replaced by zero during the smoothing. It happens that missing data are very numerous at the end of 2000 and 2001, particularly for northern and continental classes. That's why, finally, LAI times series are kept only from 2002, January, in order not to damage average on all years. It appears necessary to replace masked values because of snow, bare soil or water by zero, since LAI are otherwise not realistic (what is seen during the disaggregation coming next). On the contrary, missing and not classed values are interpolated in the limit of 4 successive decades, but those which are not interpolated are ignored during the calculation of means by cover (acceptable insofar as they are not predominant).

Disaggregation of LAI by vegtype inside covers

	fraction of vegetation type									
vegtype	90-100%	80-90%	70-80%	60-70%	50-60%	40-50%	30-40%	20-30%	10-20%	0-10%
CONI	0	6	3	1	3	2	4	4	13	65
TREE	0	2	0	0	1	2	3	6	26	60
EVER	0	0	0	0	0	0	0	0	0	0
GRAS	0	1	4	2	7	10	14	16	17	29
TROG	0	0	0	0	0	0	0	0	0	100
PARK	9	2	0	0	2	0	2	0	3	83
C3	0	1	5	9	9	5	9	5	13	45
C4	0	0	1	1	0	1	0	0	2	95
IRR	0	3	5	3	0	2	3	2	2	81
SNOW	50	0	0	0	0	0	0	0	0	50
NO	3	2	3	4	6	8	6	11	22	35
ROCK	2	0	0	0	0	0	1	5	7	85
total	1	2	3	2	4	4	6	7	15	57

Table 10.1: Percentages of classes (calculated functions of the total numbers of classes by vegetation type) concerned by the fraction (columns) of each of the 12 vegetation types (lines)

nb of vegtypes or tiles n	1	2	3	4	5	6	7	8	9
nb of classes (vegtypes)	13	6	19	44	45	72	44	23	6
nb de classes (tiles)	126	94	53	0	/	/	/	/	/

Table 10.2: Number of classes comprising n vegetation types (second line) or n tiles (third line)

Remains to determine LAI by vegtype inside covers from LAI by cover. Given the complexity of classes in terms of vegetation types composition (see tab. 10.1 and tab. 10.2), an automatic LAI disaggregation technique is welcome. The principle of the applied method is the following:

- LAI 5-years profiles by cover are averaged in order to obtain the annual mean cycles.
- LAI from vegetation types NO, ROCK and SNOW are supposed null and constant.

- In each class, the main vegetation type is put apart. For each of the minority vegetation types, the LAI profile the closest according to the $\frac{distance}{correlation^2}$ criterion is searched, provided that it corresponds to a class where this vegetation type is majority.
- The profile found is taken from the profile of the initial class, weighted by its representation fraction into the class.
- One all minority vegetation types of the classes are thus processed, residual profiles of classes are obtained. Divided by the inverse of the fraction of the majority vegetation type, they are admitted to represent the pure majority profiles, in the classes.
- The whole operation is repeated, replacing initial classes profiles by the previously obtained pure profiles.
- A new set of pure profiles results, for majority vegetation types of classes. Plotting shows that the three profiles, initial (mixte), pure (first extimate), pure (second estimate) differ not much from one another.
- Lastly, 5-years LAI profiles are built by propagating the error between years and the average on the obtained pure profiles.

This method presents two problems:

- The seeking of approached classes only relies on profiles and not on the geographic localisation. Associations of classes coming from totally different climate areas are so expectable.
- The technique of subtracting the secondary profiles to deduce the main profile might produce negative LAI.

The first problem is corrected by introducing two climate maps (Firs on Europe, Koeppe et de Lond on the rest of the world). In the algorithm above, climate proximity is now favoured with the seeking beginning in the most represented climate area, next the second, etc. The second problem is solved by excluding a profile if its subtraction give negative values of LAI. If no suitable profile is found, this which gives the less negative values is linearly transformed in order to keep values just over zero.

This method presents the advantages that it relies only on the LAI profiles of covers, and doesn't create theoritical profiles. It's fast and supple (the longer step is to verify the spatial coherence of the origins of majority and minority profiles) and can be reprocessed in case of modifications of the distribution of classes among the 12 vegetation types. It ensures to diversify vegetation types profiles inside covers and guarantees the exact reconstitution of LAI covers profiles. However, it should be evaluated if the initial approximation between the cover profile and the main vegetation type profile doesn't produce too much bias in the definition of supposed pure profiles. But before, MODIS LAI also need to be validated.

10.4 Study of the discontinuity at the limits of the domain

For practical purposes, if the work area overflows the Ecoclimap-II domain, C273 is completed at its edges by Ecoclimap-I. First, north and major part of west of the domain, there is nearly only sea and ocean (apart from in New-Zemble, but the snow class Ecoclimap-II continues there in the snow class Ecoclimap-I). South and a little west, the boundary is located in the Sahara desert. Except from a possible discontinuity between

bare rock and bare soil, and between very sparse vegetated and desert areas, the impact is so minor. Remains the East to study: from northern Russian tundra to Central Asia deserts, by Russian forests, it's about quite homogeneous areas organized with latitude, what already dulls the discontinuity.
Classes, LAI by class and by vegetation type and vegetation types fractions on both sides are compared. Ecoclimap-II classes generally continue in Ecoclimap-I classes. LAI and fractions are often different, but these discrepancies are rarely enormous.
It's so chosen to begin tests with the straight discontinuity. Then, if the delimitation is too obvious, it will be possible to contemplate a version with a smoothed (but artificial) delimitation.

Chapter 11

Validation elements for Ecoclimap-II

Validation aspects relate to three fields:

- Ecoclimap-II new map has already been quite examined during the processing, through comparisons with other existing land cover maps (GLC, CLC, Ecoclimap-I - see 10.1.3 and 10.1.4). Other tests could be performed, for example a comparison with GlobCover, a global land cover map for the year 2005-2006 using ENVISAT MERIS fine resolution (300m) data, developed by ESA (European Spatial Agency) and distributed by Medias-France.

- Vegetation types fractions have been set in the light of existing land cover map nomenclatures. Other comparisons have been realized with AGRESTE and ISLSCP2 to calibrate values, but also a posteriori with Formosat on a square of 60km at the south-west of Toulouse, France. Formosat describes the land cover, year by year, on this area; the resolution is 20m. This map is produced by the CESBIO[1]. This last comparison gives encouraging results but also reveals the difficulty of different sources to agree: sources are sometimes contradictory, their charasterics and the geographic precision vary and are not necessarily easy to compare. However, the progressive use of more recent sources should allow to still refine this definition. Concerning specialized vegetation types thar are C4 crops, tropical grassland, irrigated crops, a lack of homogeneity inside the covers doesn't allow to get precise fractions. It could be interesting to make a potential new map with covers built by introducing entering informations about such characteristics.

- Difficulties have been met to validate other parameters initialized at the cover level: heights of trees, ground depths, LAI profiles and irrigation parameters. Indeed, complete and reliable sources aren't available. A prospect for the following is thus to find means of validating these quantites. Note again that the organization by covers yields a constraint (especially for irrigation) whose reliance could also be interrogated in the light of such new validating data.

[1] Centre d'Etudes Spatiales de la BIOsphere (spatial study of the biosphere center)

Chapter 12

Conclusion

Ecoclimap-II keeps the same general structure as Ecoclimap-I but several points have changed:

- The new covers relie on a k-means automatic classification process and on recent existing land cover maps (GLC2000, CLC2000);
- The vegetation types fractions and other cover-based parameters are consequently re-initialized, with help from several information sources (AGRESTE, ISLSCP2, land cover maps nomenclatures);
- The LAI profiles by cover come from MODIS satellite data, they are smoothed pixel by pixel;
- The LAI profiles by vegetation type inside covers are built through an original automatic disaggregation process in which only LAI profiles by cover step in;
- LAI profiles are available for the average of 5 years (2002-2006) or for each of these years.

Except from these discrepancies, other surface parameters are still likewise obtained. The geographic and by patch aggregation also remains. Several comparisons with other products have already been done but Ecoclimap-II now needs to be used in order to better qualify improvements and wastes in relation with the first version. Further evolution of the database is considered functions of users returns and of potential newly available validation data.

Part III

LAND SURFACE ANALYSIS

Chapter 13

Extended Kalman Filter

Contents

13.1 Introduction

The present description is based on the offline version of SURFEX v4.8 that runs on PC. One assumes that this version is currently running on your computer, if not, the first step is to install such version before trying to use the LDAS scheme.

13.2 Source code - creation of the binary

The source code has been provided to you in a tar file `SURFEX-EKF-SRC.tar`. You should untar the directories `VARASSIM` and `MYSRC` under the directory `$SURFEX_EXPORT/src`. Once it is done you will have in the directory `VARASSIM` the following files :

- `varassim.f90` : main program that performs the various steps of the assimilation : definition of initial perturbed states, reading of fields from SURFEX outputs, writing of fields necessary for the analysis, and finally the surface analysis.

- `choldc.f90` : Cholesky decomposition (part I)
- `cholsl.f90` : Cholesky decomposition (part II)
- `inverse_matrix.f90` : explicit computation of an inverse matrix after Cholesky decomposition.
- `trans_chaine.f90` : Transformation of an integer into a character .
- `get_file_name.f90` : gets the name of files for the current assimilation window.

In order to compile these routines and to get an executable `VARASSIM`, the file `Makefile.SURFEX.mk` (provided in the tar file) contains the following sequence of instructions :

```
#####################################################
# Source VARASSIM #
#####################################################
DIR_VARASSIM += VARASSIM
ifdef DIR_VARASSIM
DIR_SOURCE += $(DIR_VARASSIM)
endif
```

In the variable `PROG_LIST` defining the various main programs to be generated, `VARASSIM` has been added. You can then type `make` in order to generate the LDAS executable, to be located in the directory `$SURFEX_EXPORT/src/exe` (which is also where the other executables : `PGD`, `PREP` and `OFFLINE` are).

13.3 The EKF scheme

The tar file `SURFEX-EKF.tar.gz` contains a sample of all the required data and scripts to run the SURFEX-EKF LDAS. First, you need to have all the required data to run a ”normal” SURFEX integration : a file of *initial conditions* (e.g. `PREP.lfi` if you work with the LFI format) as well as a set of *forcing data* (e.g. `Forc_TA_YYYYMMDD_r12.txt` and `Params_config_YYYYMMDD_r12.txt` if you work with an ASCII format). If you want to run the LDAS over a long period of time the forcing should be split according to the length of your assimilation window and not to the actual period duration. Therefore if you have already run an offline integration without data assimilation (called an ”open loop” run), you should redo such exercise by splitting the forcing data set in a number of files corresponding to the duration of your integration divided by the length of the assimilation window (with the same unit for time). You should set the logical `LRESTART` to `TRUE` and copy the output file `SURFOUT.lfi` from a given SURFEX integration to the define the input file `PREP.lfi` of the next (see in the example of script `run_ekf.sh`).

In addition to the initial conditions and forcing files, you need *observation files*. Currently these files are written in ASCII and observations have been interpolated from the raw data on the model grid. There is one file per assimilation window that contains all types of observations that are located around the analysis time (end of the assimilation window [1]). The generation of this single file needs some preprocessing (this strategy could be revised in the future both in terms of data format and content). When an observation is missing at a given model grid point it is set to 999.0 (used to be the default of undefined values within SURFEX).

[1] Therefore for asynoptic data there is a mismatch between model and observation times. When considering short assimilation windows a simplified 2D-Var could appear more appropriate

13.4 The namelist

The standard namelist of SURFEX : `OPTIONS.nam` has to be complemented by options related to the LDAS EKF (done for you in the example provided):

```
&NAM_IO_VARASSIM
LPRT = F,
LSIM = F,
LBEV = F,
LBFIXED = F
/
&NAM_OBS
NOBSTYPE = 3 ,
YERROBS(1) = 1.0 ,
YERROBS(2) = 0.1 ,
YERROBS(3) = 0.4,
INCO(1) = 1,
INCO(2) = 1,
INCO(3) = 1
/
&NAM_VAR
IVAR = 1,
NVAR = 1,
XVAR_M(1) = 'WG2',
XVAR_M(2) = 'WG1',
XVAR_M(3) = 'TG2',
XVAR_M(4) = 'TG1',
PREFIX_M(1) = 'X_Y_WG2 (m3/m3) ',
PREFIX_M(2) = 'X_Y_WG1 (m3/m3) ',
PREFIX_M(3) = 'X_Y_TG2 (m3/m3) ',
PREFIX_M(4) = 'X_Y_TG1 (m3/m3) ',
XSIGMA_M(1) = 0.1,
XSIGMA_M(2) = 0.1,
XSIGMA_M(3) = 2.0,
XSIGMA_M(4) = 2.0,
TPRT_M(1) = 0.0001,
TPRT_M(2) = 0.0001,
TPRT_M(3) = 0.00001,
TPRT_M(4) = 0.00001,
INCV(1) = 1,
INCV(2) = 1,
INCV(3) = 0,
INCV(4) = 0,
SCALE_Q = 0.125,
/
```

Currently the EKF runs with the two-layer version of the ISBA scheme : it means that the control variables can be the four main prognostic variables of this scheme : the surface temperature T_s (`TG1`), the mean

surface temperature T_2 (TG2), the superficial volumetric water content w_g (WG1), the mean volumetric water content in the root-zone w_2 (WG2). The choice of the control variables is done by setting the corresponding element of the array INCV to one. The EKF should also run with the activation of the patches which means that in such circumstances the analysis of the prognostic variables will be done separately for each patch. Regarding the observations, three observation types are considered : screen level temperature and relative humidity, superficial soil moisture content. Like for the control variables, the elements of the array INCO control which type of observation one wants to assimilate.

13.5 Link with EKF equations

We consider a control vector $\mathbf{x}$ (dimension N_x) that represents the prognostic equations of the land surface scheme ISBA $\mathcal{M}$ (OFFLINE) that evolves with time as:

$$\mathbf{x}^t = \mathcal{M}(\mathbf{x}^0) \tag{13.1}$$

Therefore $N_x = 4$ and $\mathbf{x} = (w_g, w_2, T_s, T_2)$
At a given time t, a vector of observations is available $\mathbf{y}_o$ (with a dimension N_y) characterized by an error covariance matrix $\mathbf{R}$ (defined as $\overline{(\mathbf{y}_o - \mathbf{y}_t)(\mathbf{y}_o - \mathbf{y}_t)^T}$ where $\mathbf{y}_t$ is the true value of $\mathbf{y}$).
The observation operator $\mathcal{H}$ allows to get the model counterpart of the observations :

$$\mathbf{y}^t = \mathcal{H}(\mathbf{x}^t) \tag{13.2}$$

The operator $\mathcal{H}$ can be a vertical interpolation scheme for T_{2m} and HU_{2m} or a projection on the superficial soil moisture content w_g. In the current SURFEX-EKF the maximum dimension of the observation vector is $N_y = 3$. The forecast $\mathbf{x}$ at time t (written ${\mathbf{x_f}}^t$) is characterized by an background error covariance matrix $\mathbf{B}$ (defined as $\overline{(\mathbf{x_f} - \mathbf{x}_t)(\mathbf{x_f} - \mathbf{x}_t)^T}$ where $\mathbf{x}_t$ is the true value of $\mathbf{x}$).
Remark : In the SURFEX-EKF the observation operator $\mathcal{H}$ also includes the forward model propagation, that is :

$$\mathbf{y}^t = \mathcal{H}(\mathbf{x}^0)$$

A new value of $\mathbf{x}$ written ${\mathbf{x_a}}^t$ (the analysis), obtained by an optimal combination the observations and the background (short-range forecast), is given by :

$${\mathbf{x_a}}^t = {\mathbf{x_f}}^t + \mathbf{B}\mathbf{H}^T(\mathbf{H}\mathbf{B}\mathbf{H}^T + \mathbf{R})^{-1}(\mathbf{y}_o^t - \mathcal{H}({\mathbf{x_f}}^t)) \tag{13.3}$$

Since the observation operator can be non-linear, a new operator appears in this analysis equation : $\mathbf{H}$ (together with its transpose $\mathbf{H}^T$). It corresponds to the Jacobian matrix of $\mathcal{H}$ defined as :

$$\mathbf{H}_{ij} = \frac{\partial \mathbf{y}_i}{\partial \mathbf{x}_j} \tag{13.4}$$

This matrix has N_x columns and N_y raws. We use a finite difference approach where the input vector $\mathbf{x}$ is perturbed N_x times to get for each integration a column of the matrix $\mathbf{H}$, that is :

$$\mathbf{H}_{ij} \simeq \frac{\mathbf{y}_i(\mathbf{x} + \delta x_j) - \mathbf{y}_i(\mathbf{x})}{\delta x_j} \tag{13.5}$$

where δx_j is a small increment value added to the j-th component of the $\mathbf{x}$ vector (defined in the block &NAM_VAR of the OPTIONS.nam file by the values TPRT_M(1) (for w_2), TPRT_M(2) (for w_g),

`TPRT_M(3)` (for T_2), `TPRT_M(4)` (for T_g)).
The analysis state in characterized by an analysis error covariance matrix:

$$\mathbf{A} = (\mathbf{I} - \mathbf{KH})\mathbf{B} \tag{13.6}$$

where $\mathbf{K}$ is the gain matrix defined in the analysis equation by:

$$\mathbf{K} = \mathbf{BH}^T(\mathbf{HBH}^T + \mathbf{R})^{-1} \tag{13.7}$$

The analysis is cycled by propagating the time the two quantities $\mathbf{x_a}$ et $\mathbf{A}$ up to next time where observations are available :

$$\mathbf{x_f}^{t+1} = \mathcal{M}(\mathbf{x_a}^t) \tag{13.8}$$

$$\mathbf{B}^{t+1} = \mathbf{M}\mathbf{A}^t\mathbf{M}^T + \mathbf{Q} \tag{13.9}$$

This equation requires the Jacobian matrix $\mathbf{M}$ of the model $\mathcal{M}$, that is defined as (between time t and time $t = 0$):

$$\mathbf{M}_{ij} = \frac{\partial x_i^t}{\partial x_j^0} \tag{13.10}$$

A new matrix $\mathbf{Q}$ representing the model error covariance matrix needs to be defined.

13.6 Run script

You have a script `run_ekf.sh` (in `SURFEX-EKF/rundir` from the tar file `SURFEX-EKF.tar.gz`) that allows to run the EKF over a specified period. This script is the main driver of the assimilation, it does the looping over assimilation windows, gets the required data, stores outputs, creates temporary files, cleans directories, ... It operates in several steps (see flowshart in Figure 1):

- Step 0 : Calls `VARASSIM` in order to create perturbed initial conditions. This option is triggered by the logical `LPRT=T` in the namelist `&NAM_IO_VARASSIM`. A new perturbed file of initial conditions (`PREP.lfi`) is created. The initial background error covariance matrix **B** is defined and stored in a file `BGROUNDin0`.

- Step 1 : Runs SURFEX (`OFFLINE`) with the perturbed initial conditions (eq. (8))

- Step 2 : Calls `VARASSIM` in order to store the perturbed simulated observations and the perturbed evolved prognostic variables in temporary ASCII files (`OBSIMU` and `MDSIMU`). These values are read from the output file generated during the previous step. This option is triggered by the logical `LSIM=T` in the namelist `&NAM_IO_VARASSIM`.

- Step 3 : Redo steps 0 to 2 for each of the control variables that have been activated (both in `&NAM_VAR` with the array `INCV` and the script variable `vm` in `run_ekf.sh`). The integer `IVAR` in `$NAM_VAR` is defined in the script to know which the control variable is considered.

- Step 4 : Runs SURFEX (`OFFLINE`) with the reference initial conditions (eq. (8))

- Step 5 : Calls `VARASSIM` in order to store the reference simulated observations and the reference evolved prognostic variables in temporary ASCII files (`OBSIMU` and `MDSIMU`). These values are read from the output file generated during the previous step. This option is triggered by the logical `LSIM=T` in the namelist `&NAM_IO_VARASSIM`.

- Step 6 : Calls VARASSIM in order to evolve in time the **B** matrix (eq. (9)). This option is triggered by the logical LBEV=T in the namelist &NAM_IO_VARASSIM (done by the script). Store the evolved **B** matrix in an ASCII file BGROUNDout (for further use in analysis step). This step needs to read the various MDSIMU files generated during the previous steps (perturbed runs + reference run) and to compute in finite differences the Jacobian matrix **M** of the forward model (eq. (10)). This step is done even if LBFIXED=T, but in that case the results from this step are not used afterwards.

- Step 7 : Calls VARASSIM in order to perform the soil analysis : the corresponding switches are LSIM=F, LBEV=F and LPRT=F. Store the analysis for both the model state and the matrix of errors in the initial files for the next assimilation cycle - Go to step 0 until the maximum number of assimilation cycles is reached. During this step, the following instructions are done :

  – Read observations and perform a bias correction if required
  – Read simulated observations from reference and perturbed runs
  – Compute the covariance matrix **R** of observation errors
  – Compute the covariance matrix **Q** of model errors
  – Update the **B** matrix (eq. (9))
  – Compute the Jacobian of observation operator **H** in finite differences (eq. (5))
  – Compute the Kalman gain times the innovation vector (Cholesky decomposition) (eq. (3))
  – Perform the analysis and store the result in PREP.lfi file (for next cycle)
  – Get the Kalman gain in order to compute the covariance matrix **A** of analysis errors (eq. (6))
  – Store the matrix **A** in BGROUNDout file (for next cycle)

13.7 Management of dates

The dates defined as YYYYMMDDHH are evolved in time using the command smsdate that is a script that uses an executable decdate generated from the C program decdate.c using the command :
`gcc -o decdate decdate.c`
The script and the C program are available in the directory UTILITY of the tar file SURFEX-EKF-SRC.tar. If other tools are available in your computing environment you can use them accordingly.

13.8 Directory structure

A number of directories should be created and/provided :

- repforcing : Directory where the forcing data are stored (sample for one day provided in ASCII)
- represults : Directory where the results will be stored
- reprun : Working directory (script run_ekf.sh provided)
- repobs : Directory where the observations are stored (sample for one day provided in ASCCI)
- repnamel : Directory where the namelist is located (namelist OPTIONS.nam provided)

- `repanalyse` : Directory where the initial conditions are stored (`PREP.lfi` provided for the ALADIN-France domain on 01 July 2006 at 00Z)
- `repbin` : Directory where the binary files to execute SURFEX and the EKF are located

This structure has been created for you in the example provided in `SURFEX-EKF.tar.gz`. You will find in this tar file the script `run_ekf.sh` and a namelist `OPTIONS.nam`. Once you have created the executables `OFFLINE` and `VARASSIM`, the content of `SURFEX-EKF.tar.gz` should allow you to run one day of EKF assimilation of screen-level parameters every 6 hours over the ALADIN-France domain.

13.9 Matrix inversion using Cholesky decomposition

We want to find $\mathbf{x}$ such as :

$$\mathbf{y} = \mathbf{A}\mathbf{x}$$

where $\mathbf{A}$ is a symmetric positive definite matrix. It is decomposed as $\mathbf{L}\mathbf{L}^T$ where $\mathbf{L}$ is a lower triangular matrix. Once the $\mathbf{L}$ matrix has been obtained, the vector $\mathbf{z} = \mathbf{L}^{-1}\mathbf{y}$ is formed (output from `CHOLDC`), then using it as input in `CHOLSL` the vector $\mathbf{x} = (\mathbf{L}^T)^{-1}\mathbf{z}$ is computed.

Namelist block	Variable	Type	Description
NAM_IO_VARASSIM	LPRT*	**F**	to perform analysis
		T	to define δx_i and store $\mathbf{x} + \delta x_i$ at t=0
	LSIM*	**F**	to perform analysis
		T	to write the simulated observations $\mathcal{H}(\mathbf{x})$ and the evolved state vector $\mathbf{x}$
	LBEV*	**F**	to perform analysis
		T	to evolve of the $\mathbf{B}$ matrix
	LBFIXED	F	to evolve of the $\mathbf{B}$ matrix
		T	to keep the $\mathbf{B}$ matrix constant with time
NAM_OBS	NOBSTYPE	integer	Number of possible observation types *This value must be consistent with the obs file*
	YERROBS(1)	real	Observation error for T_{2m} in K
	YERROBS(2)	real	Observation error for RH_{2m} (no units)
	YERROBS(3)	real	Observation error for w_g (fraction of SWI)
	INCO(i)	integer	1 if observation type included 0 if observation type excluded
NAM_VAR	IVAR*	**1**	Control variable of interest
	NVAR*	**1**	Number of control variables (dimension of control vector)
	XVAR_M(i)	character	Control variable identifier in PREP file
	PREFIX_M(i)	character	Control variable prefix in PREP.txt file
	XSIGMA_M(1)	real	(Initial) BG error for w_2 (fraction of SWI)
	XSIGMA_M(2)	real	(Initial) BG error for w_g (fraction of SWI)
	XSIGMA_M(3)	real	(Initial) BG error for T_s (K)
	XSIGMA_M(4)	real	(Initial) BG error for T_2 (K)
	TPRT_M(1)	real	Size of perturbation of w_2 for finite Jacobians The perturbation δx writes $x\times$ TPRT_M
	TPRT_M(2)	real	Size of perturbation of w_g for finite Jacobians
	TPRT_M(3)	real	Size of perturbation of T_s for finite Jacobians
	TPRT_M(4)	real	Size of perturbation of T_2 for finite Jacobians
	INCV(i)	integer	1 if element of control vector included 0 if element of control vector excluded
	SCALE_Q	real	Definition of the matrix **Q** of model errors as fraction of the initial diagonal **B** matrix

Table 13.1: Description of each variable in the namelist OPTIONS.nam for the blocks relative to the Land Data Assimilation System. The elements with stars (*) should be kept at their value in bold - their actual values are defined by the script run_ekf.sh

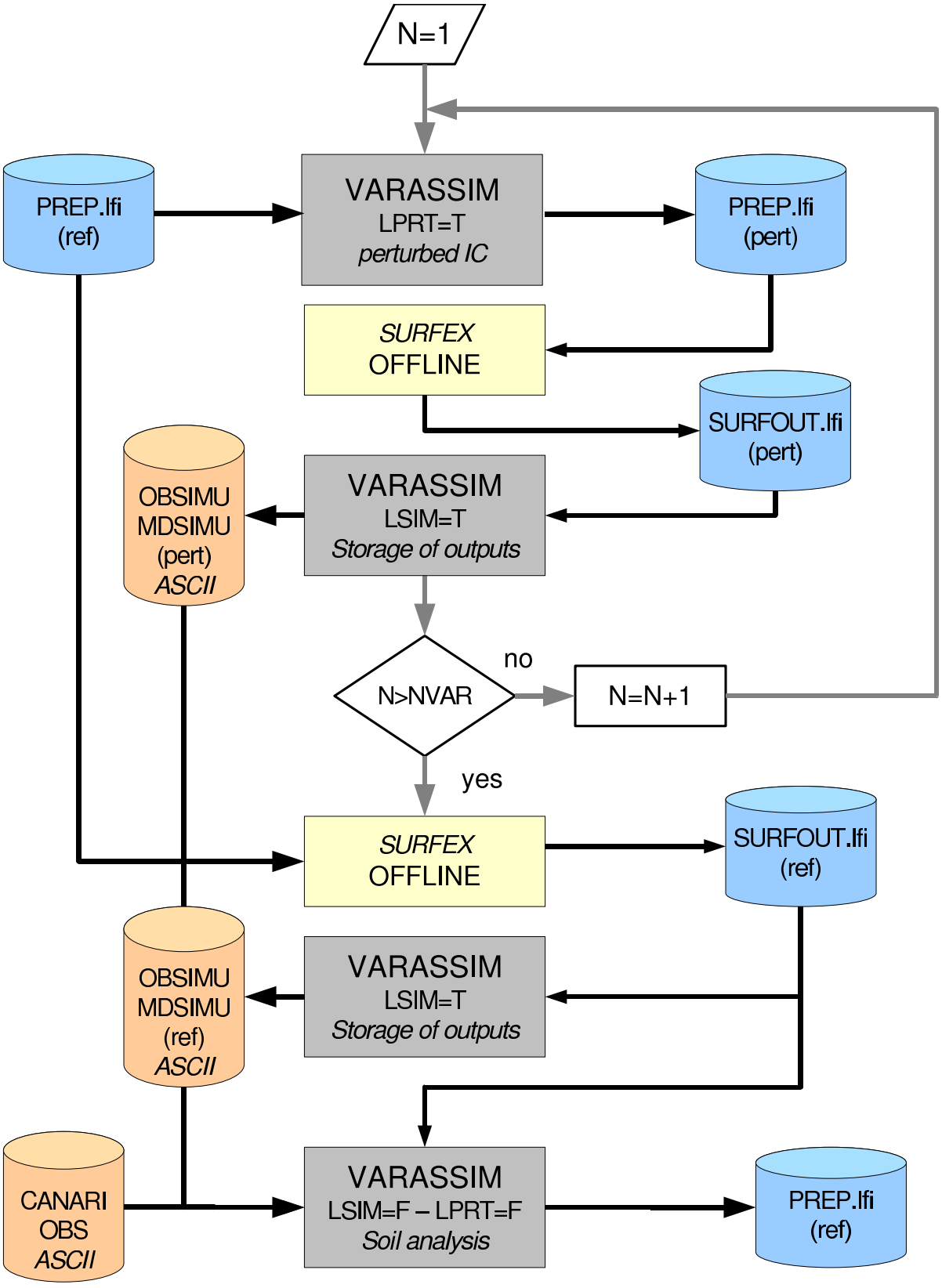

Figure 13.1: Flowshart of the EKF-SURFEX LDAS (corresponding to the various steps of the script `run_ekf.sh`) - NVAR corresponds to the dimension of the control vector.

Appendix: On the use of the EKF with the SURFEX "patch" option

13.9.1 Introduction

An EKF surface analysis scheme has been coded within SURFEX. The first version was not designed for the "patch" approach of the ISBA scheme. It has been recently extended to include such option that is compulsory when considering the ISBA-Ags scheme. The "patch" approach is similar to the "mosaic" land surface model of *Koster and Suarez* [1992] where the NATURE tile within a grid box is divided in a number of independent patches each having its own set of prognostic variables and surface energy and water balances. On the other hand, the forcing level for the fluxes and the meteorological variables is assumed to be identical for each individual patch. When aggregated values are needed (in particular to be given to the atmospheric model) a simple weighted average of each tile parameter is done as:

$$\overline{x} = \sum_{k=1}^{M} \alpha^k x^k$$

where α^k is the fraction occupied by the patch k within the NATURE tile and x^k the value of the parameter computed over this specific patch. Currently the number of patches M is set to 12.

13.9.2 Extended Kalman filter without patches

With only one patch, the dimension of the control vector $\mathbf{x}$ is equal to the number of prognostic variables to be initialized (N_x) (the analysis problem is solved independently for each invidual model grid point). The observation operator $\mathcal{H}$ projects this vector onto the observation space $\mathbf{y}$:

$$\mathbf{y} = \mathcal{H}(\mathbf{x})$$

This vector is then compared to the actual observation vector $\mathbf{y}_o$ to produce the innovation vector : $\mathbf{y}_o - \mathbf{y}$. The dimension of the observation vector is equal to the number of independent observations to be assimilated (N_y). The observations are interpolated on the model grid before analysis, which means that the observation operator does not include any spatial interpolation; this part is done in an independent pre-processing of the data.
The computation of Kalman gain requires the knowledge of the Jacobian matrix of the observation operator $\mathbf{H}$ defined by :

$$\mathbf{H} = \frac{\partial \mathbf{y}}{\partial \mathbf{x}}$$

or in finite differences :

$$H_{ij} = \frac{\partial y_i}{\partial x_j} \simeq \frac{y_i(\mathbf{x} + \delta x_j) - y_i(\mathbf{x})}{\delta x_j}$$

13.9.3 Extended Kalman Filter with patches

With M patches, the dimension of the control vector $\mathbf{x}$ is extended to $N_x \times M$.On the other hand the number of observations is still equal to N_y. The model counterpart of the observation $\mathbf{y}_o$ is assumed to be the average of the corresponding value $\mathbf{y}^k$ for each patch k:

$$\overline{\mathbf{y}} = \sum_{k=1}^{M} \alpha^k \mathbf{y}^k \tag{13.11}$$

Therefore, the innovation vector writes : $\mathbf{y}_o - \overline{\mathbf{y}}$.
For the computation of the Kalman gain, the dimension of the background error covariance matrix $\mathbf{B}$ has to be increased to the size $(N_x^2 \times M^2)$ whereas the observation error covariance matrix $\mathbf{R}$ keeps the same size $N_y \times N_y$. For each patch k, there is an observation operator $\mathcal{H}$ providing the simulated observation $\mathbf{y}^k$ from the control vector $\mathbf{x}^k$:

$$\mathbf{y}^k = \mathcal{H}(\mathbf{x}^k)$$

This relation states that the simulated observation over the patch k only depends upon the control vector over the same patch. This statement (independence of the patch columns) will greatly simplify the number of perturbed runs needed to compute the Jacobian matrix (which it is kept to N_x).

The actual observation operator combines the above relation with the spatial averaging over the patches:

$$\overline{\mathbf{y}} = \sum_{k=1}^{M} \alpha^k \mathbf{y}^k = \sum_{k=1}^{M} \alpha^k \mathcal{H}(\mathbf{x}^k)$$

from which the Jacobian matrix element H_{ij}^m can be deduced for the patch m :

$$H_{ij}^m = \frac{\partial \overline{y_i}}{\partial x_j^m} = \alpha^m \frac{\partial y_i^m}{\partial x_j^m}$$

This comes from the fact that the patches are independent, thus :

$$\frac{\partial y_i^k}{\partial x_j^m} = 0 \qquad when \quad k \neq m$$

By perturbing the component j of the control vector for all the patches ($k \in [1, N]$) by an amount : δx_j^k, the following Jacobian matrix column will be obtained:

$$H_{ij}^k = \alpha^k \frac{\partial y_i^k}{\partial x_j^k} \simeq \alpha^k \left[\frac{y_i^k(\mathbf{x} + \delta x_j^k) - y_i^k(\mathbf{x})}{\delta x_j^k} \right] \tag{13.12}$$

The initial control vector can be perturbed simultaneously for each patch because for two distinct patches m and k :

$$y_i^k(\mathbf{x} + \delta x_j^m) = y_i^k(\mathbf{x})$$

13.9.4 Conclusion

In this appendix I have shown that it is possible to extend the EKF coded within SURFEX for one patch for a set of M patches. The analysis equation and the methodology for getting the Jacobian matrix in finite differences are kept unchanged. In particular the number of perturbed integrations to be performed remains equal to the number of the control variables N_x and not to $N_x \times M$. This comes from the fact that the simulated observation is a linear combination of independent results from each patch, therefore they can be perturbed simultaneously. In practice the control vector needs to be enlarged from N_x to $N_x \times M$ (and accordingly the $\mathbf{B}$, $\mathbf{Q}$ and $\mathbf{A}$ matrices to $(N_x^2 \times M^2)$). The simulated observation needs to be computed from the weighted contribution of each patch (Equation 1) and the Jacobian matrix needs to be estimated in finite differences from Equation (2). These changes have been coded in the most recent version of the SURFEX-EKF and are available from the author.